COMMUTATION OF A BRUSHLESS MOTOR, USING POWER TRANSISTORS

GEORGE PAUL GOGUE

A THESIS

FOR THE DEGREE OF

DOCTOR OF PHILOSOPHY

THE UNIVERSITY OF ASTON IN BIRMINGHAM

DEPARTMENT OF ELECTRICAL AND

ELECTRONIC ENGINEERING

MARCH 1980

COMMUTATION OF A BRUSHLESS MOTOR, USING POWER TRANSISTORS

A THESIS

FOR THE DEGREE OF

DOCTOR OF PHILOSOPHY

G. P. GOGUE MARCH 1980

SUMMARY

The design and performance of a d.c. brushless motor and the application of power transistors to the commutation of the winding are considered in this thesis. The arrangement of a conventional d.c. motor is inverted and tappings from the commutated-winding are connected to bipolar switching circuits. The motor has a double-stator feature with identical windings in two lamination stacks. The field winding is also stationary. The interface between the motor and the power electronics comprises position sensors (opto-switches) connected to logic circuitry to decode the switching pulses. The supply voltage is provided by a thyristor bridge with control circuitry capable of performing IR compensation as well as starting the motor with an adjustable rate of rise of voltage.

The brushless motor has shunt characteristics. Speed control is very smooth and the response to changes in the supply voltage is quick. Maximum output torque is about 8.5 Nm when operating at 200 V with an efficiency of about 55%. Successful operation of the motor depends largely on the angle between the pole and winding axes at switching. This angle is optimised for maximum developed torque and for minimum peaks in the supply current. Safe operation of the transistor is also dependent upon the switching angle in limiting the current peaks. The switching losses are very small and reliability is enhanced by additional components in the bipolar circuit. This work shows that a truly brushless d.c. motor can be satisfactorily operated with an electronic commutator consisting of power transistors at medium values of voltage and current.

KEYWORDS: BRUSHLESS MOTORS; COMMUTATION;
POWER TRANSISTORS; VARIABLE-SPEED DRIVES.

ACKNOWLEDGEMENTS

The author acknowledges with gratitude the painstaking care and excellent supervision given by

Dr. M. J. Jevons,

Senior Lecturer in electrical engineering and supervisor of this research.

The author also acknowledges the help and advice of

Professor E. J. Davies,

Professor of electrical engineering (heavy current) at the University.

Many thanks are also extended to the technical staff of the department, especially

Messrs. B. Harrison, J. Partlow and L. Radford.

The author also acknowledges financial assistance provided by

The Government of the Republic of Iraq.

Last but not least, thanks to Kathy whose help has made completion of the project so much easier.

CONTENTS

CHAPTER 2 contd.

CHAPTER 3 MACHINE OPERATION

CHAPTER 3 contd.

CHAPTER 4 contd.

LIST OF TABLES

LIST OF FIGURES

CHAPTER 2 contd.

CHAPTER 3

CHAPTER 3 contd.

CHAPTER 3 contd.

CHAPTER 3 contd.

CHAPTER 4

CHAPTER 4 contd.

CHAPTER 6

CHAPTER 7

Note:

Some of the graphs have been reduced photographically, and this has resulted in 'awkward' scales. This, however, does not represent standard practice. The diagrams affected are:

Fig. No.	Page
3.45	123
3.46	123
3.47	125
3.48	125
5.10	220
5.11	221
5.21	235
5.22	235
5.27	237
5.28	237
5.31	240
5.32	240
6.23	282

LIST OF SYMBOLS

a	constant; depth of penetration, m
b	constant; pole-arc, mech. rad.
d	diameter of stator bore, m
e_c	e.m.f. induced in a coil of N turns, V
e_g	e.m.f. induced in a coil group, V
e_t	e.m.f. induced in one turn, V
f	frequency, Hz
h	maximum value of triangular waveform
i_C	instantaneous current in capacitor, A
i_D	instantaneous current in diode, A
i_1	instantaneous transistor collector current, A
i_w	instantaneous winding current, A
i_{in}	input current through diode D14, A
j	symbol for a particular part of the magnetic circuit
ℓ_a	axial length of one lamination stack, m
ℓ_g	air-gap radial length, m
ℓ_s	slot-width, m
m	number of tappings; constant
n	speed of rotation, rev/min; constant
p	constant; number of salient poles per stator section
q	specific electric loading, A.C./m
r	pole-arc/pole-pitch; length of torque arm, m
s	number of position sensors
t	time, s
t_d	delay time, s

t_f fall time, s

t_p pulse duration, s

t_r rise time, s

t_s storage time, s

t_w freewheel diode conduction period, s

v volume, m^3

v_w instantaneous winding voltage, V

y constant in mechanical loss expression

A constant; area, m^2

B_{av} average air-gap flux-density at stator surface, T

B_g maximum air-gap flux-density at stator surface, T

B_f air-gap flux-density due to field excitation, T

B_T total air-gap flux-density, T

B_w air-gap flux-density due to commutated-winding current, T

C capacitance, μF

C_B capacitor in base circuit, μF

C_o output coefficient, kW min/m^3

C_s capacitor across the d.c. supply, μF

E energy, J; e.m.f., V

E_b back e.m.f., V

E_{mean} mean value of e.m.f., V

E_{max} maximum value of e.m.f., V

E_{max1} maximum value of equivalent trapezoidal wave, V

E_{peak} peak value of actual e.m.f. wave, V

$E_{r.m.s.}$ r.m.s. value of e.m.f., V

F m.m.f., At

F_f field coil m.m.f., At

F_T total m.m.f., At

F_w commutated-winding m.m.f., At

H magnetising force, At/m

I_a total current to the ring commutated-winding, A

I_A anode current (SCR), A

I_B current in base circuit, A

I_c current in conductor, A

I_D current in opto-diode in base-drive, A; drain current (FET), A

I_g gate current (SCR), A

I_G gate current (FET), A

I_H SCR holding current, A

I_L SCR latching current, A

I_o winding current at turn-off, A

I_s supply current to star winding, A

I_w maximum winding current, A

I_1 collector current (transistor), A

I_{1F} collector current at instant of turn-off, A

K Carter's correction coefficient; friction torque, Nm

K_e eddy-current constant

K_f field form factor

K_h hysteresis constant

L inductance, H

L_w winding inductance, H

N number of turns

P_d power developed, W

P_i iron losses, W

P_l total losses, W

P_m mechanical losses, W

P_{tmax} maximum permissible power dissipation of transistor, W

P_1 peak value of equivalent squaré pulse of turn-on power loss curve, W

P_2 $V_{CE}I_1$ power loss, W

P_3 peak value of equivalent square pulse of turn-off power loss curve, W

R_a commutated-winding resistance between supply terminals, Ω

R_B resistor in base circuit, Ω

R_g resistance of one coil group, Ω

R_i reluctance of iron-path, H^{-1}

R_ℓ leakage reluctance, H^{-1}

R_{th} thermal resistance, °C/W

R_w winding resistance between diametrically opposite tappings, Ω

R_1 reluctance of section (1) of air-gap, H^{-1}

R_2 reluctance of section (2) of air-gap, H^{-1}

T pulse period, s; torque, Nm

T_a ambient temperature, °C

T_d developed torque, Nm

T_j transient junction temperature, °C

ΔT_j maximum temperature rise of transistor junction in one cycle of pulses, °C

$T_{j(max)}$ maximum permissible junction temperature, °C

T_ℓ loss torque, Nm

T_r reluctance torque, Nm

T_s saliency torque, Nm

T_{mb}	mounting base temperature, °C
U_o	e.m.f. constant, Vs/rad or Nm/A
V	voltage, V
V_{AK}	anode-cathode voltage (SCR), V
V_b	battery voltage, V
V_B	voltage across bipolar circuit, V
V_{BE}	base-emitter voltage, V
V_{CE}	collector-emitter voltage, V
V_{DS}	drain-source voltage (FET), V
V_{gK}	gate-cathode voltage (SCR), V
V_G	gate-voltage (FET), V
V_{ref}	reference voltage to OA1 in base-drive circuit, V
$V_{(RC)}$	voltage across RC in base circuit, V
V_s	supply voltage, V
V_{sr}	supply voltage to ring winding, V
V_{ss}	supply voltage to star winding, V
W_T	total work in motor, J
W_1	work done by a conductor in one lamination stack, J
Z_a	total number of current carrying conductors
Z_{th}	thermal impedance, °C/W
α	constant; SCR trigger angle, degree
β	constant
γ	constant; conductivity, S/m; angle between pole-axis and axis of ring winding, °(m)
γ_1	angle between pole-axis and axis of two pairs of coil groups (star winding), °(m)

δ	angle between pole-axis and tooth-axis, °(m); duty factor
η	efficiency, %
θ	angle between pole and coil axis, °(m)
λ	SCR conduction angle, degree
μ	permeability, H/m
ξ	damping factor
π	3.14159
τ	pole-pitch, °(m)
τ_w	winding time constant, s
ϕ_p	air-gap flux per pole, Wb
ϕ_t	flux embraced by one turn, Wb
ψ	flux linkage, Wb
ω	angular speed, rad/s; slot pitch, mm
ω_n	natural frequency, rad/s

CHAPTER 1

INTRODUCTION

1.1 The brushless motor

In a truly brushless motor, the commutator and brushes of a conventional d.c. motor are replaced by semi-conductor switches; both the commutated and the field winding(s) are in the stator, and the rotor has two sets of salient poles, one at each end.

The ease with which the speed/torque characteristics can be varied suggests numerous applications for the d.c. motor. But the design limitations and routine maintenance imposed by the commutator and brushes are a serious drawback. The same characteristics are available with the brushless motor and the particular limitations and maintenance problems are overcome.

The earliest record[1] of a brushless motor was in 1934 when thyratrons were used to control a 300 kW motor. From that time until the early sixties little development work was apparently done. When semi-conductors became commercially available, electronic commutation was applied to miniature and small motors only[2-5]. But in the seventies, with the development of very high rating semi-conductors[38], brushless motors with ratings up to 500 kW have been built[24].

1.1.1 General features

It is apparent from the literature that there are several designs for brushless motors[2-5,12-25]. The commutated-winding is either lumped[4,14,27] or distributed in slots[15,18]. Magnetic field excitation can be provided by either permanent magnets[2-4,12-20] on the rotor or stationary toroidal coils[21-24]. Either the commutated or the field winding is split into two sections for magnetic symmetry. In machines with a Lundell or clawpole-type solid rotor[21-24], there are two stationary field coils at opposite ends of the machine. Machines with a split commutated-winding placed in two sections of the stator have configurations very similar to several types of inductor alternator[9,10].

The tappings of the commutated-winding are connected to semi-conductor switches which are controlled in sequence to create a rotating magnetic field. The rotor rotates synchronously with the field and hence can develop a net torque. This is a distinctive feature of the d.c. brushless motor and necessitates rotor position-sensing, so that each switching device can be switched at the correct position of the rotor poles. The number of the solid-state switches does not have to be the same as the number of commutator segments in a conventional motor of similar rating, and is usually much smaller.

1.1.2 Stator winding and switching systems

Fig. 1.1 represents a ring winding with three tappings, each connected to two switching devices. The switching sequence given in Table 1.1 progresses the field clockwise in angular steps of 120°.

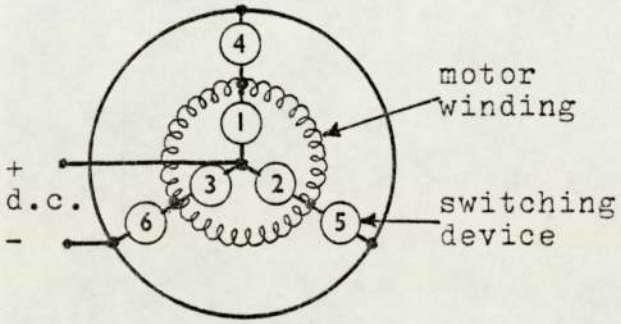

Fig. 1.1 Ring winding with 3 tappings

	Switches				
1	2	3	4	5	6
x				x	x
	x		x		x
		x	x	x	

x: switch closed

Table 1.1 Switching sequence for Fig. 1.1 for 1 cycle

As an improvement, the ring winding can be tapped at 6 points instead of 3, as shown in Fig. 1.2. The switching sequence is given in Table 1.2. Although the total number of switching devices is doubled, current is now uniformly distributed in the two sections of the winding, and the field step angle is shortened to 60°.

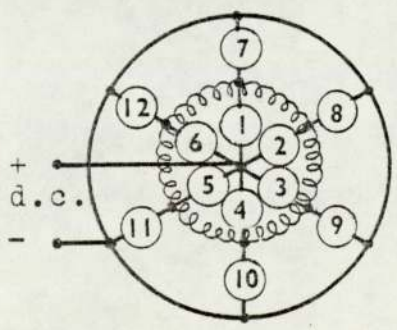

	Switches											
1	2	3	4	5	6	7	8	9	10	11	12
x									x		
	x									x	
		x									x
			x			x					
				x			x				
					x			x			

x: switch closed

Fig. 1.2 Ring winding with 6 tappings

Table 1.2 Switching sequence for Fig. 1.2

It is very easy with an electronic commutator to depart from the conventional ring winding and, for example, to use a star-connected type. Fig. 1.3 represents a star-connected winding with 3 tappings and 3 switching devices. Sequential switching is used with either one or two devices ON at any instant. Although this practice does not fully utilize the available copper, high winding currents can be permitted because of the reduced duty cycle.

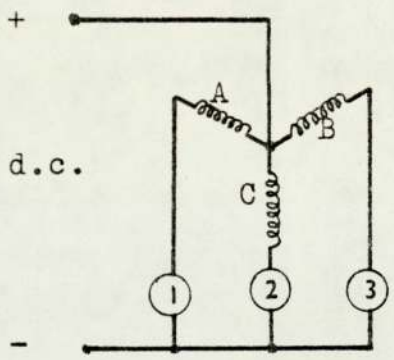

Fig. 1.3 Star-connected winding with 3 switching devices

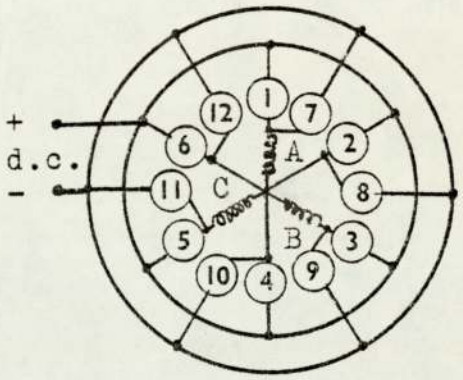

Fig. 1.4 Star winding with 12 switching devices

To allow for current reversal in the sections of a star-connected winding, switching devices can be connected to both ends of the sections with the centre points commoned, or the sections can be electrically separate as shown in Fig. 1.4. This is the type of winding used in the present study. The switching sequences could be the same as in Table 1.2 above. However, by 'half' stepping the winding, a much improved rotating field is produced. Part of the switching sequence is shown in Table 1.3.

Switches											
1	2	3	4	5	6	7	8	9	10	11	12
x									x		
x	x								x	x	
	x									x	
	x	x								x	x
		x									x
		x	x			x					x
			x			x					

Table 1.3 Half stepping sequence for Fig. 1.4 (part only)

For a given supply voltage and output power, the number of tappings is determined by the power rating of the available switching devices and the type of commutated-winding. The number of tappings determines the angular variation of the developed torque and of the back e.m.f.

Fig. 1.5 shows idealized torque/position characteristics with 2, 3, 4, and 6 tappings[8,16,28]. It is assumed in these diagrams that there is no armature reaction effect and the developed torque depends only on the angle between the commutated and field winding axes. The increase in mean torque with more than 6 tappings is marginal while the number of devices increases rapidly as seen from Table 1.4.

No. of tappings		m	2	3	4	6	8
No. of devices	Ring	2m	4	-	8	12	16
	Star-connected	m	2	3	4	6	8
	Star	2m	-	-	8	12	16
T_{min}/T_{max}		$\cos(\pi/m)$	0.0	0.50	0.71	0.87	0.92
T_{mean}/T_{max}		$(m/\pi)\sin(\pi/m)$	0.64	0.83	0.90	0.96	0.97
$(T_{max} - T_{min})/T_{mean}$			1.56	0.60	0.32	0.14	0.08

Table 1.4 Torque (p.u.) per cycle for various tappings

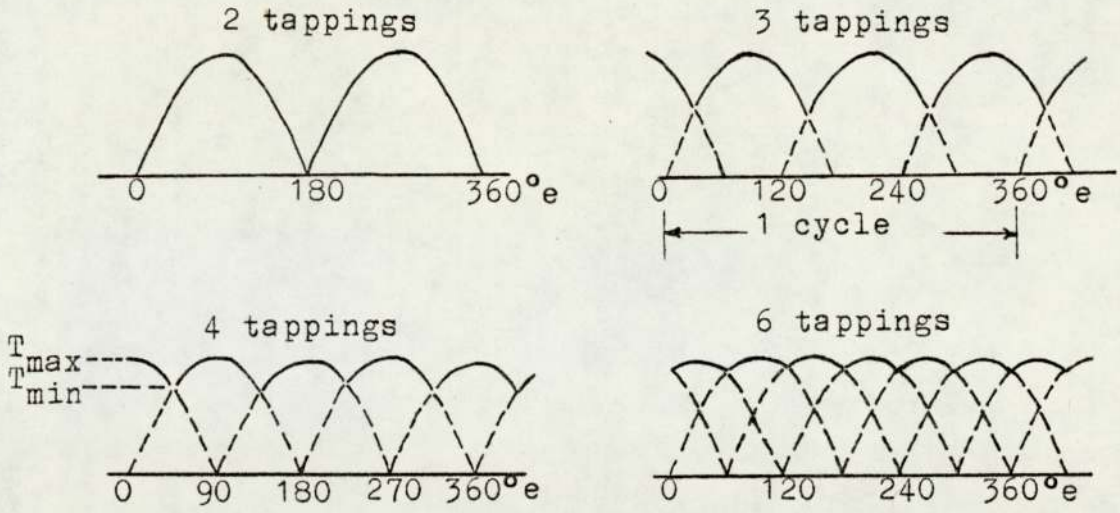

Fig. 1.5 Torque/position characteristics (single stepping)

1.1.3 Position sensing

Position sensors should not be affected by changes in speed, temperature, local magnetic fields or atmospheric conditions. Table 1.5 gives the principal features of the more common types of sensor.

Type	Principal features	Connection	References
Hall generator	Generated voltage is a function of magnetizing force and device current	Direct or through amplifiers	12, 26, 28, 29
Photo-electric cells	Sectored disc breaks a light beam	Direct or through amplifiers	5, 11, 21
Ferrite cores	Magnetized sectored disc causes changes in permeability	Through a circuit sensitive to inductance	14, 19
Proximity switch	Metal disc causes changes in inductance of coil	Changes in inductance actuate switch	15

Table 1.5 Position sensors

1.1.4 Advantages/disadvantages

Commutator sparking and maintenance have always made the conventional d.c. motor objectionable in certain applications. The brushless motor is free from sparking and can have the speed/torque characteristics of the conventional motor. Other advantages are:

(i) longer periods of maintenance-free operation,

(ii) acceptability in hazardous atmospheres,

(iii) less weight - excluding control gear,

(iv) lower acoustic noise,

(v) operation from a.c. and/or d.c. supplies[24],

(vi) reliability time constant at least twice the 'mean time before failure' of the conventional motor[41].

The main disadvantages are:

(i) more space to house the control circuits,

(ii) high cost due to semi-conductor devices (despite saving in commutator).

Diverse applications of the brushless motor include, for example, the space industry[3,14,19,34], servosystems[8,29,40], magnetic recording devices[16], Hi-Fi equipment[15,31], and variable speed drives[20,24].

1.2 Switching devices

Before semi-conductors became available in the early

fifties, bulky and expensive switching devices like the thyratron[1] and the ignitron[39] were commonly used. The unsophisticated and high-power control circuits are inappropriate in modern high-complexity applications where usually a large number of devices is required. These two devices are not, therefore, considered further.

In medium power applications, the electro-magnetic relay[42] was more suitable for switching in terms of size and economy. The control power as a percentage of the load power was much smaller than that required in other devices. But it proved impossible to use the relay in hazardous atmospheres and at high frequencies.

The important characteristics of 3 suitable switching devices of the same power rating[34-39] are compared in Table 1.6. The different features of the electro-magnetic relay limit its applicability to those situations where a short switching time, free from mechanical bounce, is not required. The comparison also shows that in switching circuits like the electronic commutator, semi-conductor switches are superior despite the complicated control circuitry required. In these circuits, the problem of electric coupling between the control circuit and the load circuit can be overcome by using opto-isolators.

Where fast and reliable switching is required, the relay is not competitive and the choice lies between the power transistor and the silicon controlled rectifier (SCR).

1.2.1 Power transistors vs. SCR's

	Electro-magnetic relay	SCR	Power transistor
Maximum power rating	700 V, 2 A	5 kV, 3 kA	3 kV, 500 A (ref. 38)
Control power	small	small	moderate
Leakage current	none	negligible	small
Turn-off time	2 ms	5 - 15 μs	less than 5 μs
Operation	bi-directional bi-stable	uni-directional bi-stable	uni-directional monostable
Commutation circuit	no	yes	no
Electric coupling between control and load circuits	no	yes	yes
Advantages	no heat sink, no protection circuits	no moving parts, long life, maintenance-free, ability to handle poor power factor, lighter, shock and vibration resistant, silent operation, cheaper, more compact, more reliable	
Disadvantages	imperfect contacts cause mechanical bounce, sparking can cause an explosion, continuous maintenance, frequency limitation	dv/dt and di/dt protection circuits, heat sinks	second breakdown limitations, snubber circuits, heat sinks

Table 1.6 Switching devices

Table 1.6 shows that power transistors and SCR's have many features in common. Power transistors, however, have a lower forward voltage drop and a shorter turn-off time. The monostable feature of power transistors makes

external commutation unnecessary since they remain ON until the control signal is removed. SCR's, in contrast, have to be commutated either naturally or by 'forced commutation'[22].

Manufacturer's data for a power transistor and an SCR of approximately similar power ratings is given in Table 1.7. The power required in the gate circuit of the SCR is much smaller than in the base circuit of the power transistor.

Device	Type	Main circuit			Control circuit			R_{jc}
		V (V)	I (A)	V_{on} (V)	V (V)	I	P (W)	(°C/W)
Transistor	WT5201	500	10	1.25 (1)	2 (3)	1.5 (5) A	3.0	1.0
SCR	THY500-12	500	12	1.85 (2)	2 (4)	50 (6) mA	0.1	1.8

(1) $V_{CE(SAT)}$ (3) V_{BE} (5) I_B

(2) $V_{AK(ON)}$ (4) V_{gK} (6) I_g

Table 1.7 Transistor vs. SCR (values at 25°C)

Power transistors are vulnerable to 'secondary breakdown'[44] which reduces the safe operating area. This becomes more likely at high working temperatures. RC snubber circuits must be used to avoid this type of failure. SCR's, although free from the secondary breakdown phenomenon, require snubber circuits to give protection from fast rates of rise of voltage and current.

Examples of other semi-conductor switching devices[39], with simple control circuits but limited rating, are the light-activated SCR and the gate-controlled switch.

Field effect transistors (FET) and, in particular, the VMOS type[43] are the most recently available switching devices. In Table 1.8, a 60 V VMOS device is compared with a power transistor and an SCR of the nearest available rating. The gate power listed for the SCR is the peak value at the start of the conduction period, whereas the figure listed for the VMOS and transistor is the continuous value of power during conduction. The FET allows direct interface to TTL and other MOS logic families. It is also free from secondary breakdown and can be switched in tens of nano-seconds. However, the highest operating voltage of the available VMOS FET's is less than 200 V (maximum current capability of 7 A).

Device	Type	Main circuit			Control circuit		
		V (V)	I (A)	V_{on} (V)	V (V)	I	P (mW)
VMOS	VN66AF	60(1)	2.0(4)	2.0(7)	10.0(10)	2.0 nA(13)	0.02
Transistor	2N3054	60(2)	1.0(5)	1.0(8)	1.7(11)	20.0 mA(14)	34
SCR	C6F	50(3)	1.6(6)	1.5(9)	0.5(12)	0.2 mA(15)	0.1

(1) V_{DS} (4) I_D (7) $V_{DS(ON)}$ (10) V_G (13) I_G

(2) V_{CE} (5) I_1 (8) $V_{CE(SAT)}$ (11) V_{BE} (14) I_B

(3) V_{AK} (6) I_A (9) $V_{AK(ON)}$ (12) V_{gK} (15) I_g

Table 1.8 Semi-conductor devices (values at 25°C)

All the above mentioned devices were considered for switching the present brushless motor. But for motor output powers of more than a few hundred watts, the choice lay between power transistors and SCR's. Because of the flexibility of power transistors, these were used in the switching circuitry of this project.

1.3 Object of the thesis

This thesis details the work carried out on a brushless d.c. motor, with power transistors forming the electronic commutator, and also the conclusions arrived at from various test results. The project has been divided into two major parts: the brushless motor and the power electronics. The topics of main interest are listed below.

(i) The design and operation of a truly brushless d.c. motor with no moving contacts. The double-stator feature is used for the first time in the construction of a motor of this size. Excitation to two fixed windings, the commutated-winding and the field coil, constitute a chance to study the specific magnetic circuit formed. The comparison with the conventional d.c. motor highlights the areas in which alterations in the design would bring about an improvement in the brushless motor performance.

(ii) The use of power transistors in the electronic commutator is attempted at considerably higher values of voltage and current than before. The feasibility of power transistors is thus investigated for switching a d.c. motor. There is also a considerable amount of investigation into the circuit requirements imposed by the power transistor, i.e., base-drive, protection, etc.

(iii) Interfacing the motor with the electronic

commutator is an exercise in position sensing technique and in logic circuitry. Construction of the 'logic unit' provides an insight into possible control circuits which would result in more flexible motor characteristics than those of a comparable conventional motor.

(iv) The 'IR' compensation, made possible with the controlled triggering of the SCR's in the power supply unit, adds a new dimension to the motor characteristics. A novel scheme in the generation of triggering pulses is used, resulting in a very satisfactory control over the rise in supply voltage when starting the motor. A great deal of experience is gained in the design and construction of the control circuitry in the power supply unit, and in the operation and protection of SCR's.

Several aspects of this work, and in particular, the machine design and the power electronics, were approached from the practical rather than the theoretical side. This was because of limited previous experience and, in some cases, the complexity and unreliability of theoretical calculation when based on insufficient information. However, the results and observations included in this thesis should be helpful in carrying out improvements on any similar project in the future.

1.4 Introduction to the following chapters

The two major parts of the thesis are distributed as follows: the motor design and operation are discussed in Chapters 2, 3 and 5, while the power electronics is explained in Chapters 4 and 6. More details are now given about the contents of each chapter.

1.4.1 The brushless motor

The specification and design of the brushless motor are given in Chapter 2, based partly on calculated values and partly on estimated parameters. Existing laminations, used in the construction of the motor, and a constraint on the physical dimensions were the starting point in the design. The design procedure is accompanied by an analysis of the theoretical aspects of the motor contrasted with those of the conventional d.c. motor. The areas of particular emphasis are the torque production mechanism and the magnetic circuit. The former helps in understanding the waveforms of developed torque given in Chapter 3, while the latter is essential in choosing an excitation level for the required values of flux-density in the air-gap.

The commutated-winding is constructed so as to permit different types of connection. The design procedure and the final layout and connections are given in Chapter 2.

The brushless motor operation is investigated in Chapter 3 with the aid of torque, e.m.f. and flux measurements as well as with no-load and load tests. To facilitate these tests prior to the construction of the electronic commutator, a mechanical arrangement of a faceplate commutator and brushes is used. Apart from normal motor operation as in the no-load and load tests, the machine was driven by an external prime-mover for the e.m.f. measurements, and manually rotated over parts of a revolution for some of the torque and flux measurements. The aims of Chapter 3 can be listed as follows:

(i) To investigate the effect on torque of ring and star type commutated-windings. Waveforms of torque are obtained with different groups of coils excited. This is done to understand how torque is developed and, later on, to decide between the ring and star windings as well as on the switching angle between pole and winding axes.

(ii) To measure the no-load and load losses and thus extrapolate the load characteristics beyond the limitations of the mechanical commutator for conditions similar to those with the electronic commutator.

(iii) To determine the air-gap flux-density distribution due to the current in either the field coil or the commutated-winding or in both. This identifies the teeth which are quicker to reach saturation than others and demonstrates the effect of armature reaction on the field form.

In Chapter 5, no-load and load tests are again performed but this time with the electronic commutator exciting a star type commutated-winding. Tests are also performed to demonstrate the effect of 'IR' compensation on the load characteristics. But prior to testing the motor, the effect of the switching angle between pole and winding axes on the winding current waveform is discussed at various values of load and excitation. This provides information leading to the choice of a suitable switching angle for the particular operating condition of the motor.

1.4.2 The power electronics

Chapter 4 gives the design and operation of the electronic commutator and the associated position sensing. The term 'electronic commutator' refers to the 3 bipolar circuits arranged to switch the current to the commutated-winding in a sequence and timing determined by the position sensing circuits.

Each bipolar circuit consists of 4 power transistors which are supplied from separate base-drive circuits. The base-drive circuit and its power supply are explained in detail. RC snubber circuits are connected across the power transistors to improve the switching loci, and the selection of the R and C values is based on the bipolar circuit requirements and the transistor ratings.

The operation of a bipolar circuit with snubber circuits described here is based on tests performed with the motor stationary, i.e., without back e.m.f. The dynamic performance of the bipolar circuits with normal operation of the motor, is explained with test results in Chapter 5.

The transistor losses are determined from the voltage and current wavforms at switching. Thermal calculations are also performed to predict the maximum power dissipation and temperature rise.

Position sensing consists of opto-switches and logic circuitry which together form the interface between the motor and the power electronics. The switching sequence is suitable for a star winding where two-thirds of the winding is excited. This is possible by having two of the three pairs of tappings connected to the d.c. supply at any moment. The details of the position sensing are given in Chapter 4 together with the electronic commutator.

Chapter 6 deals with the power supply unit which consists of a half-controlled SCR bridge and the associated electronic circuitry. Included in the latter is the generation of triggering pulses and control of the output voltage. Additional control circuitry limits the conduction angle of the SCR's so that motor voltage or current lies within a predetermined value.

The power supply unit is provided with transient suppressors in the form of filter circuits or surge protectors. A crowbar-thyristor is also connected across the power supply to protect the electronic commutator from sudden high voltages resulting from false triggering of the SCR's.

The protective measures in the power supply unit are taken to ensure that the electronic circuits are capable of withstanding fault conditions. The acceptable electrical starting conditions and the accuracy of the control as well as the satisfactory operation of the brushless motor over a wide range of speed are some of the important areas covered by the specification of a variable-speed drive.

CHAPTER 2

MACHINE DESIGN

2.1 Chapter outline

The specification of the brushless motor is given in this chapter and the motor is contrasted with a conventional counterpart[30]. Theoretical aspects (Section 2.3) of the study include the prediction of flux-density variation in the air-gap and the effect of armature reaction on it. Torque production mechanism is investigated and a reluctance model is devised for the motor. A preliminary design is carried out in Section 2.4 to determine the axial length of each lamination stack and the number of poles on the rotor. The m.m.f. calculations of the magnetic circuit are made in Section 2.5 to determine the required field ampere-turns. The commutated-winding design is explained in Section 2.6 and methods of connecting the winding sections are described.

2.2 Specification

It is intended for the motor to be a truly brushless d.c. motor with the switching of the commutated-winding synchronised with rotor position. The commutated-winding is to be designed (Section 2.6) to fit existing stator laminations with 36 slots and an internal diameter of 127 mm. To permit control of the field excitation, an

annular field coil (Section 2.5.2) is to be used instead of permanent magnets.

Both commutated-winding and field coil are to be supplied from a d.c. source, variable up to 200 V with a nominal maximum current of 10 A (Chapter 6).

The brushless motor is to have shunt characteristics and a variable no-load speed up to 1000 rev/min. Speed control is to be achieved by varying the voltage to the commutated-winding and/or the current to the field coil.

At 1000 rev/min the nominal full load output power is to be 1.05 kW corresponding with a shaft torque of 10 Nm. No value can be given for efficiency but as an estimate it is not likely to exceed 70%.

Maximum operating temperature of the winding is not to exceed 75°C in an ambient of 25°C. Only natural cooling is to be used and no ventilating ducts are to be provided in the lamination stacks.

2.2.1 Mechanical layout

The arrangement of a conventional d.c. motor was inverted so that tappings from the commutated-winding could be connected to stationary switching points. Magnetic symmetry on each side of the annular field coil was obtained by having two lamination stacks with similar

commutated-windings, connected in series. Figs. 2.1 and 2.2 show diagramatically a cross-section and an end-view of the motor, respectively.

The stator comprises two sections of unequal length which can be easily separated to gain access to the field coil, (v. Photograph 1b).

The principal dimensions (in mm) are:

Overall axial length between bearings	489.0
Outside diameter of stator	279.4
Outside diameter of laminations	203.2
Inside diameter of laminations	127.0
Thickness of each lamination	0.6
Axial length of each lamination stack	50.0
Air-gap length	0.25
Pole-piece height	19.1
Outside diameter of rotor-core	88.9
Inside diameter of rotor-core	44.5
Axial length of rotor-core	215.9
Thickness of brass sleeving	3.2
Diameter of shaft	38.1

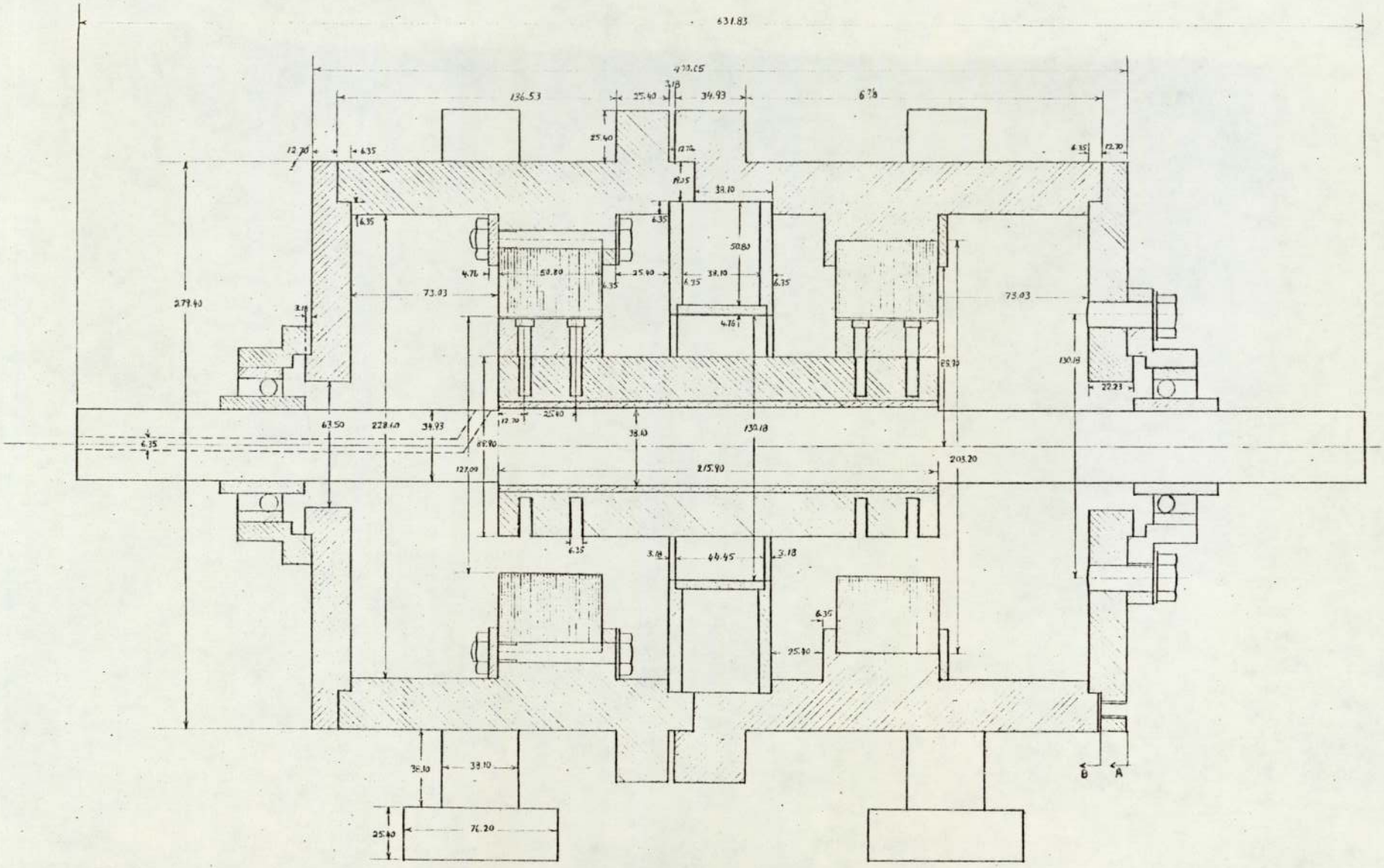

Fig. 2.1 Cross-section view of the brushless motor (dimensions in mm)

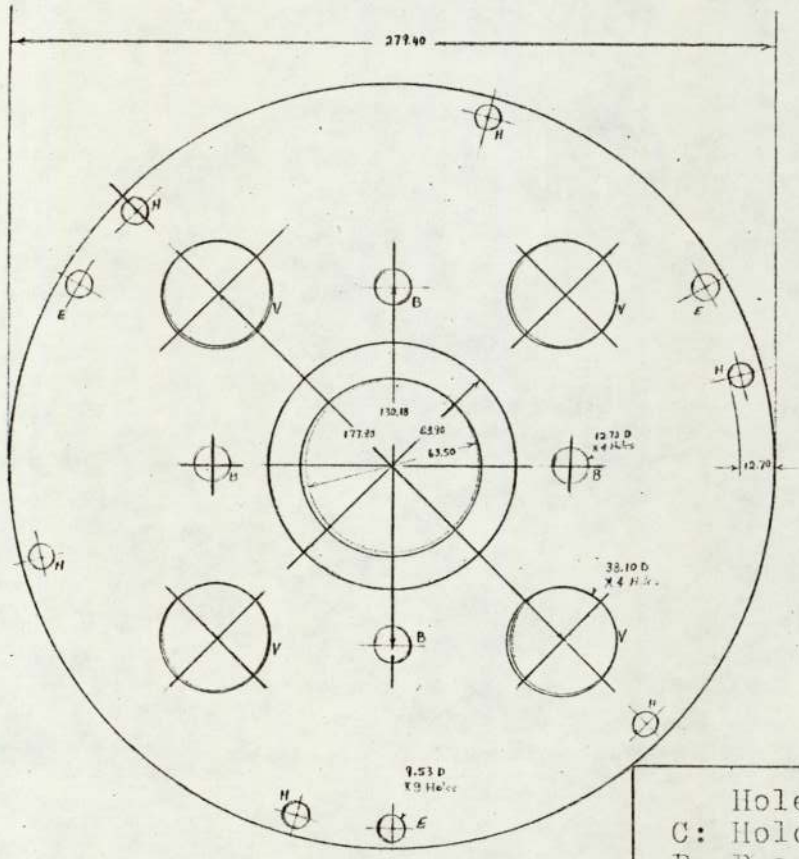

(a) End plate

Holes for:
C: Holding bolts
B: Bearing case
E: Extracting screws
G: Guide bolts
L: Laminations
V: Ventilation

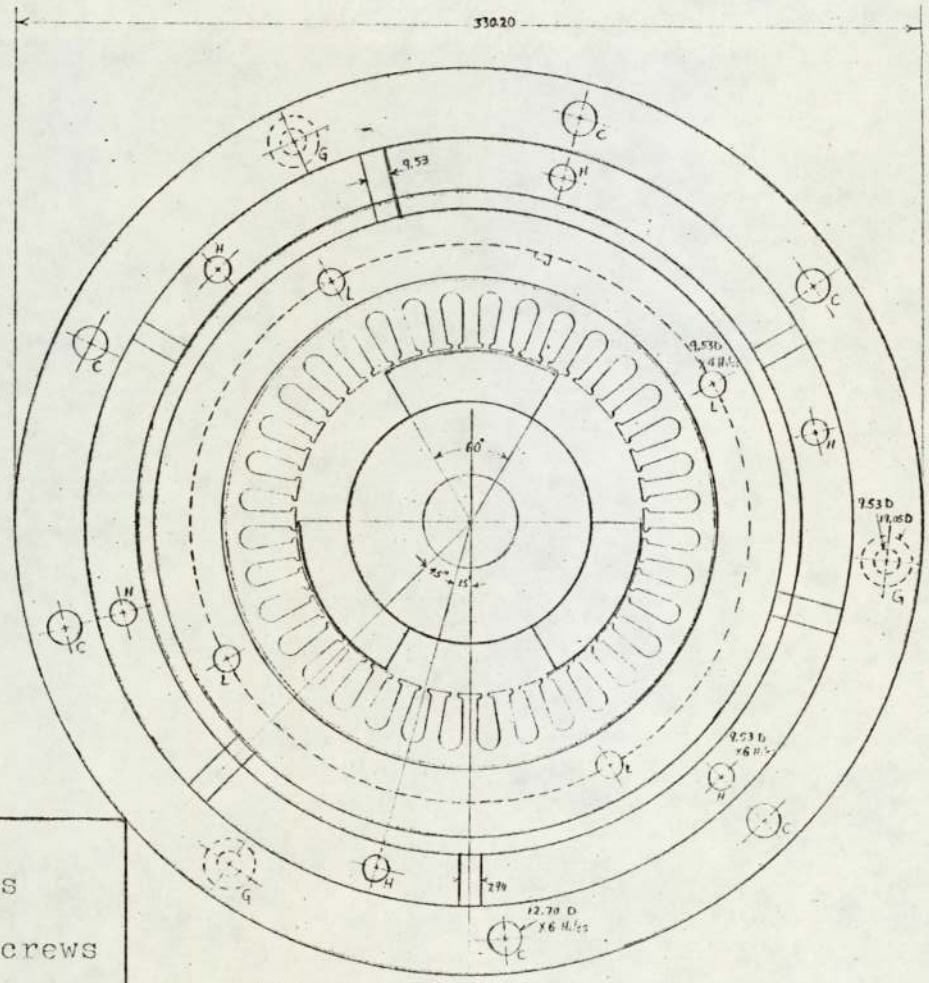

(b) End view of stator and rotor

Fig. 2.2 End view of the brushless motor (dimensions in mm)

2.3 Theory

Various features of the brushless motor are contrasted with those of a conventional d.c. motor of the same nominal rating. The output equation highlights the differences in the magnetic circuits and forms the basis for the winding design. A study of the flux-density variations in the air-gap is the design basis for the rotor poles and core.

2.3.1 Contrast with the conventional d.c. motor

The flux producing windings, namely the commutated-winding and the field coil, are both stationary in the brushless motor, whereas the armature winding in the conventional d.c. motor rotates as part of the rotor. In both motors, however, a certain angle must be maintained between the axes of flux produced by the two windings as the rotor rotates.

In the conventional motor, the separation angle is approximately constant because the field and brush axes are stationary. Small oscillations are caused by the movement of the brushes over the commutator segments. The equivalent in the brushless motor is the switching of successive tappings of the commutated-winding. Since the number of tappings is much smaller than the number of commutator segments, the axis of flux produced by the winding oscillates over a larger angle. Consequently the

changes in the separation angle between the two axes are larger in the brushless motor. This is reflected in the e.m.f. and torque waveforms as an increase in the high order harmonics. Typical waveforms for a ring winding are shown in Fig. 2.3.

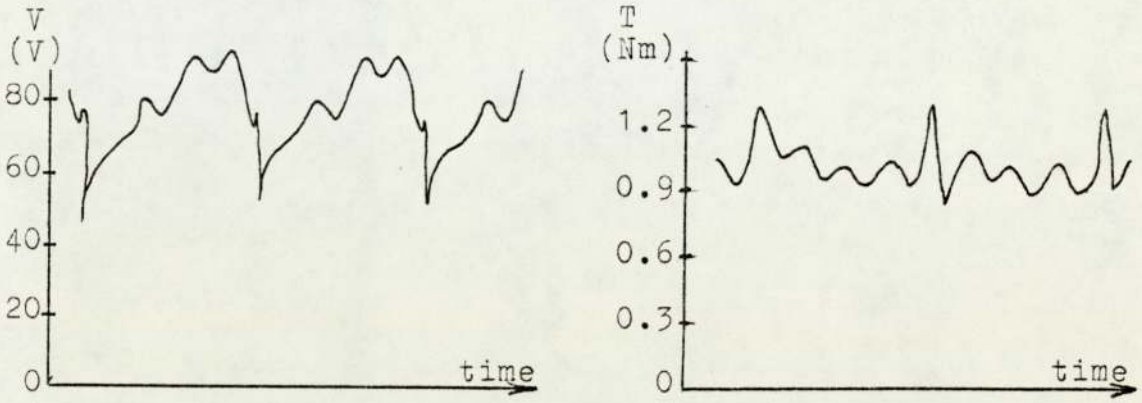

a) Generator: e.m.f. between brushes
F_f = 1050 At, E.M.F. = 80 V, n = 278 rev/min

b) Motor: torque waveform
F_f = 500 At, I_a = 1 A, n = 60 rev/min

Fig. 2.3 Typical brushless machine waveforms, $\gamma = -15^{\circ}$(m)

The main magnetic flux path in the two motors differs both in direction and length. The path is circumferential in the conventional motor whereas it is axial in the brushless motor, as shown in Fig. 2.4. This results in poles of opposite polarity at the ends of the rotor.

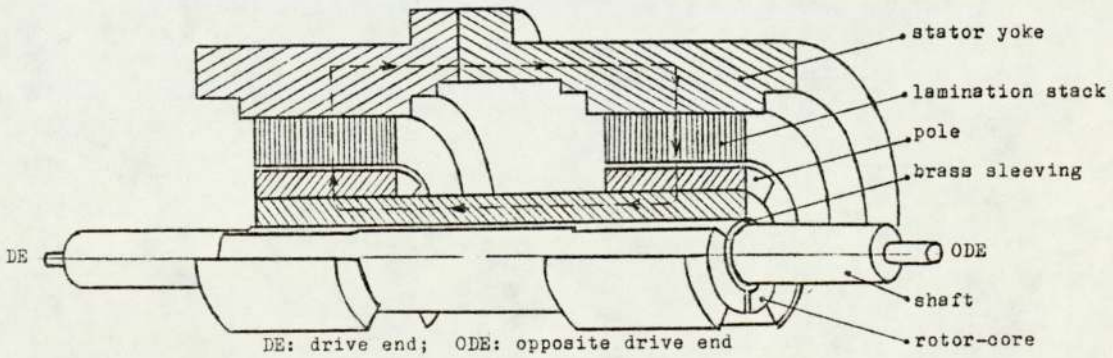

Fig. 2.4 Axial flux path in machine

The separation between the lamination stacks in the brushless motor is required for the field coil and the commutated-winding overhangs. The longer flux path means that more ampere-turns are required in a brushless motor than in a conventional motor of the same diameter at the air-gap, to obtain the same air-gap flux-density.

Consider a full-pitch coil of N turns in one lamination stack of the brushless motor. The e.m.f. induced in each turn is equal to the rate of change of magnetic flux linkage. The waveforms in Fig. 2.5 represent the flux-density at the stator surface, B_g, the flux ϕ_t embraced by one turn, and the induced e.m.f., 'e'. The turn is assumed close to the stator surface. The effect of slotting, fringing, and leakage on the flux-density waveform is neglected. Also, the relative magnetic permeability of the iron paths is assumed infinite. Hence, the waveform is rectangular and the interpolar flux-density is zero.

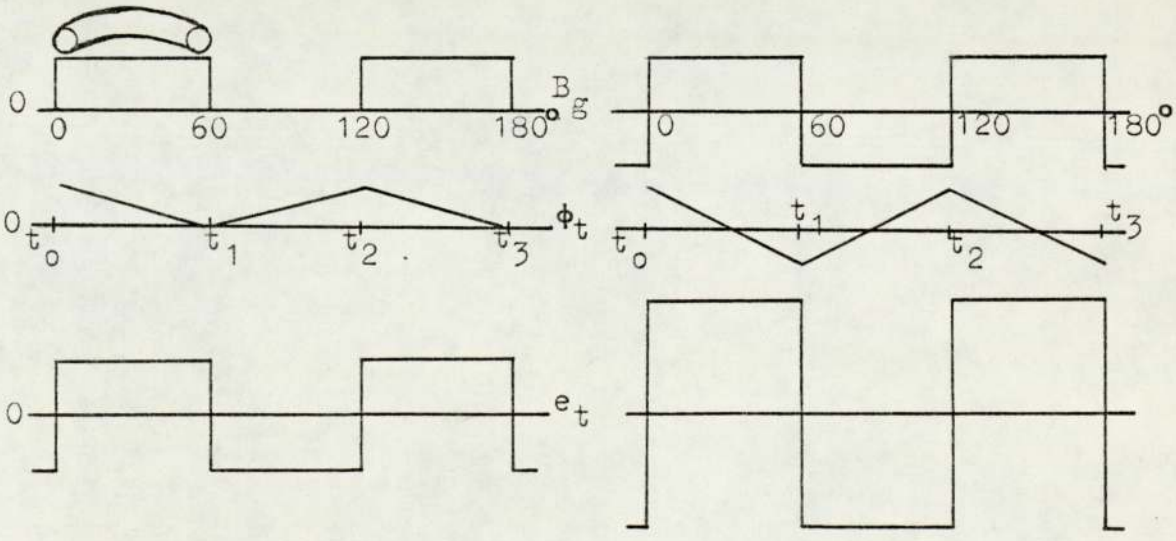

(a) Brushless motor (b) Conventional motor

Fig. 2.5 Flux linkage and induced e.m.f. in one coil

The e.m.f. induced is given by

$$e_c = 2pn\ N\phi_p/60 \qquad \text{(Appendix A1)} \quad (2.1)$$

In practice, e_c is not constant at the value calculated from Equation (2.1) but follows the variations in ϕ_p caused by slotting, fringing, the finite permeability of the iron etc. Speed too can vary over one revolution due to shaft misalignment, unbalanced magnetic pull, and reluctance torque.

In the conventional motor, the flux embraced by one turn changes direction with rotation since poles of opposite polarity alternately cover the coil. Fig. 2.5b shows that the rate of change of flux is twice that in the brushless motor, and, therefore, the e.m.f. induced is doubled.

Changing load current in the conventional motor results in undesirable sparking as the contact between the brush and commutator is broken. This phenomenon does not occur in brushless motors with electronic commutation since when the supply to a tapping is disconnected, a freewheel diode provides a path for the discharge current.

2.3.1.1 <u>The output equation</u>

The total developed power in watts is

$$P = (d^2 \ell_a)(q)\left(\frac{\pi^2}{60} B_{av}\ n\right) \qquad \text{(Appendix A2)} \quad (2.2)$$

where $q = \dfrac{I_c Z_a}{\pi d}$ (2.3)

At equal values of q, B_{av} and n, the ratio of output powers of the brushless and conventional motors is the same as the ratio of the respective $d^2\ell_a$. However, at equal diameters, ℓ_a must be the same for both to obtain equal output powers. That is, the axial length of the d.c. motor equals the axial length of one lamination stack in the brushless motor. The reason is that B_{av} in the interpolar zone of the brushless motor is practically zero and, therefore, the total magnetic loading per lamination stack is based on half the total number of poles.

Alternatively, if the d.c. motor has an axial length equal to the length of both lamination stacks of the brushless motor, the diameter of the former need only be about 70% of the brushless motor to produce the same output power. This, of course, does not include any increase in overall length to accomodate the field coil.

The specific electric loading, q, is assumed equal for both motors. But for two motors of the same diameter at the air-gap, it may not be possible to make q in the d.c. motor as high as in the brushless motor. Since the winding of the d.c. motor is in the rotor, the taper of the teeth is pronounced and a larger portion of the slot area is taken up by insulation. This limitation on q narrows the difference between the diameters of the two motors.

Table 2.1 contrasts the values of some parameters of the two motors at the following assumed values:

B_{av} = 0.7 T

ϕ_p = 2.3 mWb

I_a = 4.0 A

N = 50 turns/coil

n = 1000 rev/min

2p = 6

Parameter	Brushless Motor	D.C. Motor	Typical Value (30)	Unit
Magnetic loading	2 x 7	14	-	mWb
Total electric loading	2 x 7200	7200	-	A.C.
Specific electric loading, q	18000	18000	10000 to 20000	A.C./m
Output coefficient, C_o	2.07	2.07	1 to 3	-
$d^2 \ell_a$	2 x 0.82	0.82	-	$(10^{-3})m^3$
Power developed, P_d	1660	1660	-	W
Torque developed, T_d	15.8	15.8	-	Nm

Table 2.1 Comparison between motors of equal rating

The commutated-winding of the brushless motor and the armature winding of the d.c. motor are both assumed to be ring windings and, therefore, $I_c = I_a/2$. Since the windings are identical, the specific electric loading for both motors is the same. However, the total electric and magnetic loading for the brushless motor are, respectively, twice and equal to the values for the d.c. motor, due to the double-stator feature of the former. The $d^2 \ell_a$ of the brushless motor is also doubled for the same reason.

2.3.2 Armature reaction effect

The effect of current flow in the commutated-winding of a brushless motor is similar to that of the armature current in the d.c. motor. The result in both motors is a deformation of the flux-density curve B_f in the air-gap. The effect is more pronounced in the brushless motor since the three poles opposite the winding are of the same polarity. As seen in Fig. 2.6a, flux-density B_w produced by the commutated-winding is quasi-symmetrical about the winding axis.

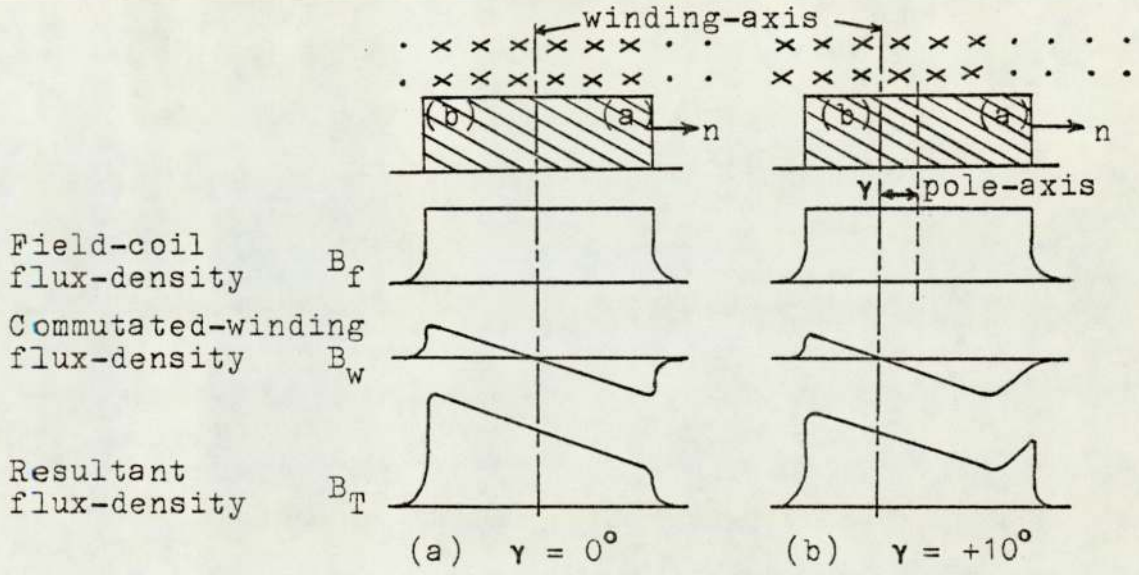

Fig. 2.6 Armature reaction effect on field form

Fig. 2.6b shows the flux-density waveform of the winding at a larger separation angle γ between the pole and the winding axes. For both values of γ the total flux-density, B_T, increases noticeably at one tip of the pole. (The curves of B_w and B_T can be compared with the experimental curves plotted in Figs. 3.60a and 3.61a, p. 142,

respectively.) This causes additional iron losses in the stator teeth opposite the pole. Naturally, a large increase in flux at the pole-tip drives that section of the pole into saturation, thus reducing the useful flux even further.

The m.m.f. produced by the commutated-winding, F_w, adds to the field coil m.m.f., F_f, at one pole-tip and subtracts from it at the other. Since F_w varies linearly over the pole-arc, the amount added or subtracted depends on r, the ratio of pole-arc to pole-pitch. It is highest in value when r is unity. Reducing r from unity means a reduction in the pole-face losses for the same flux-density distribution. But a reduction in r also means a smaller area at the pole-face. This results in higher flux-densities in the teeth leading to higher magnetic saturation and more iron losses.

The value of air-gap flux-density, B_w, due to the winding m.m.f., F_w, can be determined from Equation (2.4). α is the ratio of reluctance of the total iron path to that of one air-gap, and is plotted in Fig. A4.2, p. 304, to a base of F_w per pole per lamination stack. In Equation (2.4), α is divided by 2 since only half the iron circuit is considered.

$$B_w = \mu_o \frac{F_w}{(1 + \frac{\alpha}{2}) \ell_g K} \qquad (2.4)$$

To minimise the effect of large values of m.m.f. at the lagging pole-tip, b, the air-gap is made longer at the pole-tips by chamfering the poles. This reduces flux-densities B_f and B_w near the pole-tip and consequently the peak values of B_T are reduced.

Since the specific electric loading, q, is the distribution of ampere-conductors over the circumferential air-gap surface of the lamination stack, and armature reaction depends upon current flow in the winding, then armature reaction effect can be reduced by reducing q. This means either reducing the winding current or distributing the winding over a larger circumference, i.e. a larger stator bore is used. The latter is not possible with the present machine as the stator bore was fixed by the available laminations.

2.3.3 Flux-density variations in the air-gap

Conformal transformations are used in plotting the flux-density, B_f, at the stator surface of the air-gap (v. Appendix A3). The interpolar zone is assumed in one calculation to be one slot facing a smooth stator surface. Another calculation determines the changes in B_f between slots and teeth over the 60° pole-arc, for unsymmetrical placing of the slots about the pole-axis. The combined results are plotted in Fig. 2.7.

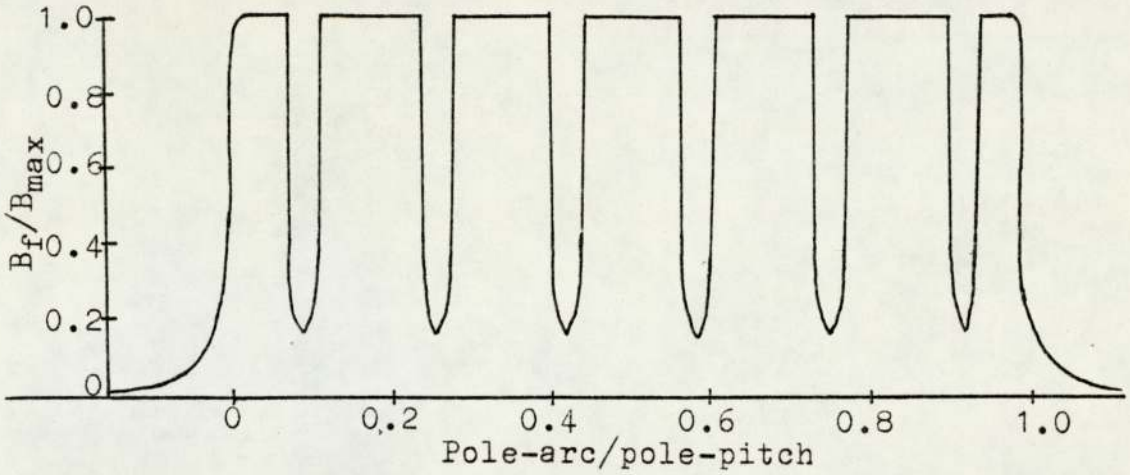

Fig. 2.7 Flux-density distribution in air-gap

This theoretical distribution of flux-density does not include the effect of armature reaction and fringing, nor does it allow for chamfering. The iron is assumed to have infinite permeability although in practice when iron is heavily saturated, flux-densities in the slots and interpolar zones tend to increase slightly.

Another effect of saturation is a more gradual rise and fall of flux-density at the pole-tips. Chamfering the pole-tips as in Fig. 2.8 also results in a flux-density waveform closer in shape to a sine wave. Owing to the finite permeability of the iron, a slight dip is noticed in the middle of the pole even with a gradual rise or fall of the flux-density at the pole-tips.

Fig. 2.9 shows the effect of chamfering the pole-tip on the field form. Since the iron is assumed unsaturated, the flux-density at the pole-tip may be taken to vary inversely with the air-gap length. The flux/pole

is reduced by about 10%. A slightly reduced pole-arc of 58°, used for some of the experimental work, does not alter the field form significantly.

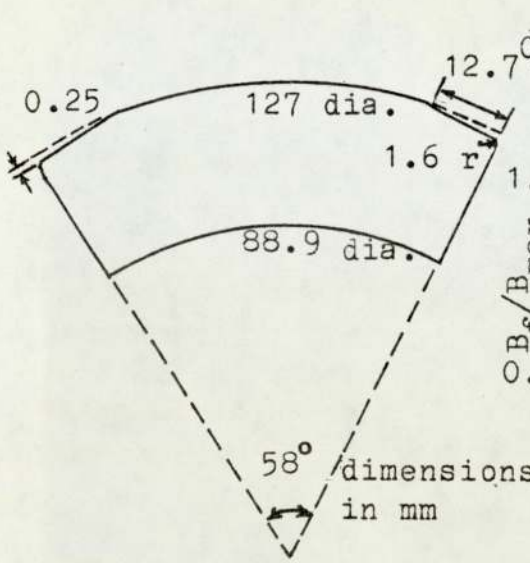

Fig. 2.8 A mild-steel chamfered pole

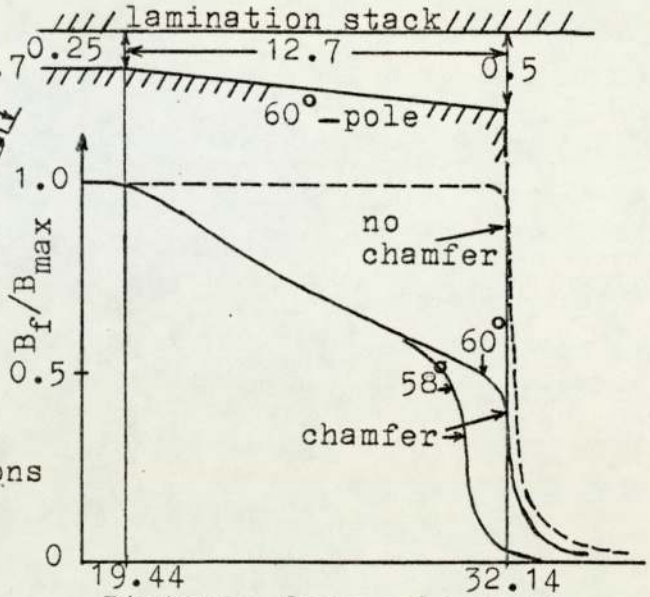

Fig. 2.9 Effect of chamfering on field form

In conventional d.c. motors, armature slots are skewed to reduce the high order slot harmonics in the induced e.m.f. waveform and to reduce the reluctance torque due to the slot openings. At this experimental stage it was more convenient to stagger the pole-pieces either side of an axial line by a quarter of a slot-pitch as in Fig. 2.10b.

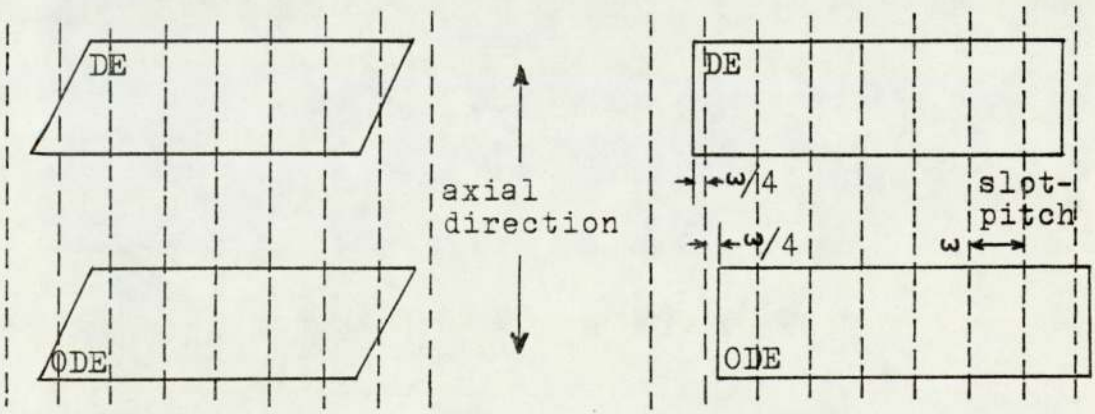

(a) Skewed poles (b) Staggered poles

Fig. 2.10 Pole alignment

2.3.4 Torque production

Developed torque has three sources:

(a) Reluctance effect of the rotor pole with the stator teeth and slots, whenever either or both the field and commutated-windings are excited.

(b) Saliency effect of the rotor poles, when the commutated-winding is excited.

(c) 'BℓI' effect created by field excitation and commutated-winding current.

2.3.4.1 Reluctance torque

The reluctance torque is dependent upon the slot/tooth configuration and on the air-gap flux. It causes the poles to seek a minimum reluctance position with the pole-tips opposite equal areas of tooth (shown hatched in Fig. 2.11), and, therefore, can be either clockwise or counter-clockwise.

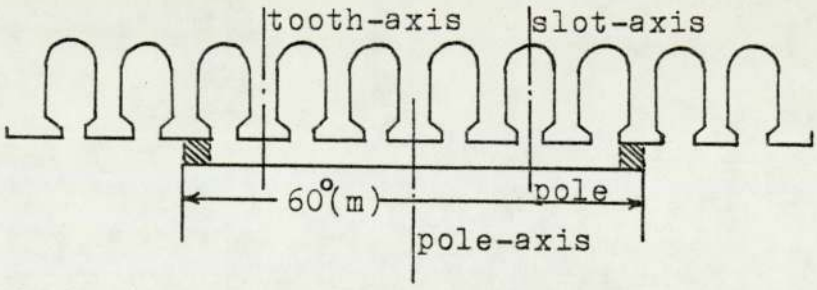

Fig. 2.11 Rotor pole and stator teeth

A semi-practical estimation of the magnitude of this torque was attempted using a resistance network model. The principal difficulty in constructing an accurate

analogue lies in the fact that the air-gap surfaces are assumed to be equipotentials. No account is taken of the m.m.f. for the iron parts of the magnetic circuit or the variation of magnetic potential near to the pole and tooth-tips. The maximum variation in air-gap reluctance is 4.5% giving a maximum torque of 13 Nm for a field excitation of 1050 At when the tooth and pole-tips are approximately in line. The maximum recorded reluctance torque for the same field excitation is only 0.76 Nm, (v. Fig. 3.4a, p. 67). Since the torque calculation is based on flux-densities in the pole and tooth-tips, which can be highly saturated, the average air-gap m.m.f., F_g, assumed, can be far in excess of the m.m.f. required to saturate the tips. For example, from Tables 2.3 and 2.4, pp. 46, 50, at F_f = 1050 At, F_g is 160 At, whereas a quarter of this value across the tips is sufficient to produce the measured value of torque.

2.3.4.2 Saliency torque

The stable position for saliency torque is when the pole-axis coincides with the axis of the commutated-winding. Using the principle of stored energy in the air-gap, a simplified model of the flux path is devised to determine the saliency torque ideally produced by one stator coil.

Fig. 2.12a depicts one full-pitch stator coil of N turns and a pole subtending $\pi/3$ radians (mechanical). The axis of this coil is in line with a similar coil in the other

lamination stack as shown in Fig. 2.12b. There are actually two components of the saliency torque corresponding with the two flux paths:

(i) across the air-gap, (1), into the rotor pole and returning by the air-gap, (2), as represented by the arrows in Fig. 2.12a;

(ii) across the air-gap, (1), through the rotor-core, across the second air-gap at the DE and back through the stator yoke as in Fig. 2.12b.

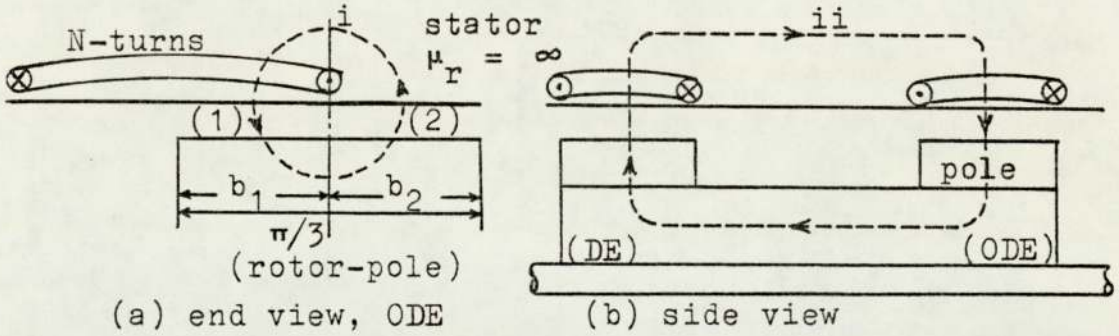

Fig. 2.12 Flux path diagrams

The physical representations of Fig. 2.12 are translated into an equivalent flux path model detailed in Appendix A4. It is shown that the saliency torque with 3 coils in each lamination stack displaced by 120°(m) is given by

$$T_s = \frac{3N^2I^2}{R\beta\pi/3} \cdot \frac{\frac{\alpha}{\beta} \quad \frac{b_2}{\pi/3}}{1 + \alpha/2\beta} \qquad \text{Nm} \qquad (2.5)$$

where

$$R = \frac{2K\ell_g}{\mu_o \ell_a d\pi/3} \qquad H^{-1} \qquad (2.6)$$

α, β and γ are empirical factors which modify the simplifying assumptions made in the derivation. α is introduced to represent the m.m.f. requirement of iron of finite permeability by additional air-gaps. To compensate

for the slotted air-gap surface and pole-tip fringing, the reluctance expressions are modified by a factor β chosen slightly greater than unity. γ is a correction coefficient for the shunt leakage path. Strictly, it is not a constant as it must depend upon b_1. But with the present simplifying assumptions, the value of γ is chosen to give zero torque when the flux linkage is maximum.

The values of α, β and γ were chosen so that there is a satisfactory correlation between calculated and experimental values of air-gap flux-density, B, and saliency torque, T_s.

For example, with three 50-turn coils in each lamination stack, each carrying 2.0 A, the constants are $\alpha = 2.0$, $\beta = 1.1$ and $\gamma = 23.1$. Carter's correction coefficient, K, in Equation (2.6) is taken as 1.26. The values of B and T_s are plotted in Fig. 2.13 to a base of $b_1/(\pi/3)$. The maximum value of torque is verified experimentally in Section 3.3.1, p. 65 .

The flux-density, B_1, at the stator surface opposite b_1 increases to a maximum as b_1 is reduced. But at $b_1 = 0$, i.e. when the pole uncovers the coil, B_1 must naturally fall to zero (apart from fringing). Similarly with B_2 at the stator surface opposite b_2 when $b_1 = \pi/3$. Apart from some leakage, the only flux path at $b_1 = \pi/3$ is that in Fig. 2.12b. Hence the flux-density in the rotor-core, B_c, is highest at $b_1 = \pi/3$. At this value of b_1, the

saliency torque, T_s, is minimum since it is the minimum reluctance position of the pole. The maximum value of T_s occurs at a value of b_1 close to zero. At negative values of b_1 the saliency torque is reversed in sign.

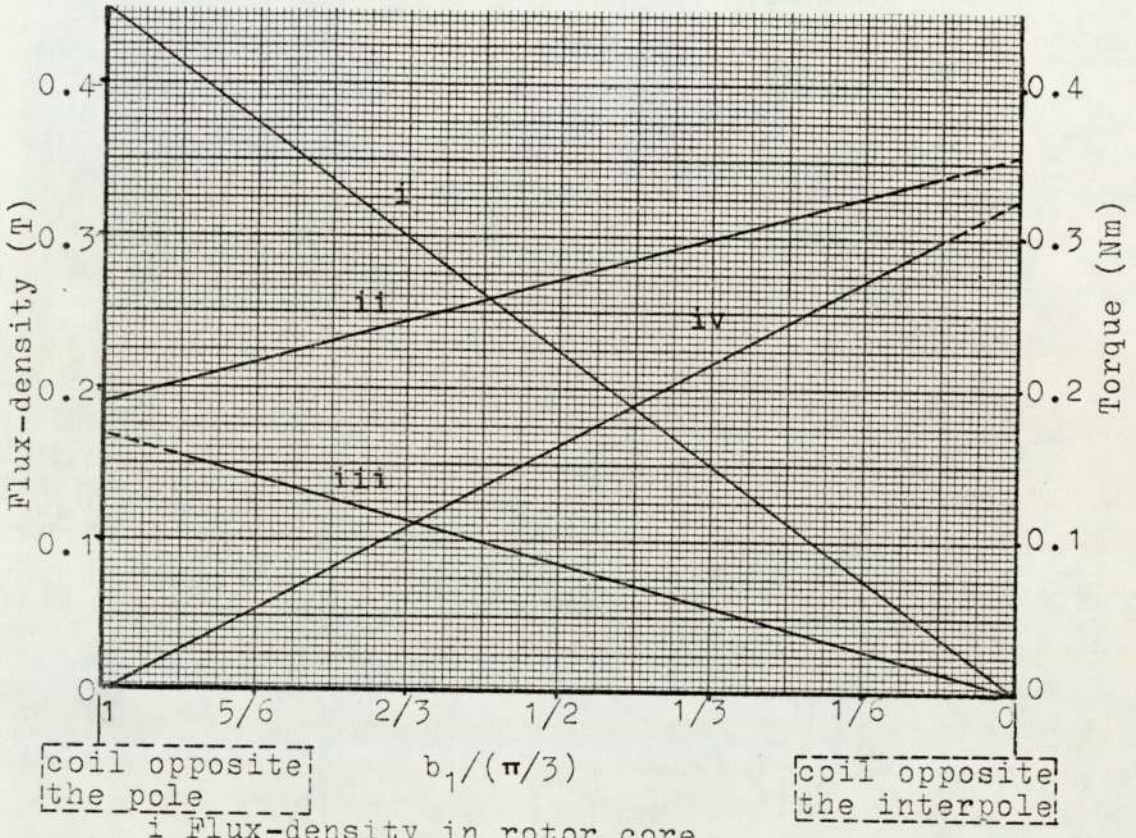

i Flux-density in rotor core
ii Flux-density B_1 opposite b_1
iii Flux-density B_2 opposite b_2
iv Saliency torque T_s

Fig. 2.13 Flux-densities and saliency torque corresponding with Fig. 2.12

2.3.4.3 'BlIr' torque

The third and largest source of developed torque is the 'BlIr' torque. This is obtained from the interaction of the magnetic field produced by the field coil and the current in the commutated-winding conductors. It is dependent on the angle of separation, γ, between the pole and the commutated-winding axes (Fig. 2.6, p. 30),

falling to zero at $\gamma = 0^{\circ}$. Apart from a uniform flux-density and a fixed current, constant torque requires a constant angle of separation. In a conventional d.c. motor, the variation in γ is minimal due to the large number of commutator segments. The variation is appreciable in a brushless motor, where there are usually a small number of tappings, giving rise to larger fluctuations between the maximum and minimum values of torque. A typical waveform of torque is given in Fig. 2.3, p. 25.

Using the ideal equation for developed power (Equation (2.2), p. 27) and the variation of torque for 'm' tapping points (Table 1.4, p. 5), the maximum value of the 'BℓIr' torque is

$$T_{max} = \frac{\pi}{2} (d^2 \ell_a)(qB_{av}) \quad \text{Nm} \qquad (2.7)$$

while

$$T_{mean} = \frac{m}{2} \sin \frac{\pi}{m} (d^2 \ell_a)(qB_{av}) \qquad (2.8)$$

and

$$T_{min} = \frac{\pi}{2} \cos \frac{\pi}{m} (d^2 \ell_a)(qB_{av}) \qquad (2.9)$$

The value of developed torque in Table 2.1, p. 29, can be determined from Equation (2.8) for m = 6. Also the minimum torque at this value of 'm' is 13% lower than the maximum value as was given in Table 1.4.

These formulae apply to the ring type commutated-winding. When a star winding is used, and not all the coils are energised, the values of torque are reduced.

2.4 Preliminary design

The cross-sectional area of the available slot is 140 mm^2. A 20% allowance is made for slot insulation, wedges and separators leaving 112 mm^2 for the winding. The copper area for a layered winding is only 78% of the winding area, and of the copper area an allowance of 5% must be made for the enamel insulation on the wire. This gives a maximum copper area of 83 mm^2, which corresponds to a slot loading of 290 A at a current-density of 3.5 A/mm^2.

The maximum copper area, however, cannot be utilized in practice due to the limited space for the overhang and to permit the coils to be changed easily. It was, therefore, found necessary to reduce the copper area to 40 mm^2. Meanwhile, the intermittent operation of each coil means that the current-density can be increased to 5.0 A/mm^2 without overheating. The slot loading is then 200 A, and for a lamination stack with 36 slots and an internal diameter of 127 mm, the specific electric loading is

$$q = \frac{200 \times 36}{\pi \times 0.127} = 18000 \quad A.C./m$$

Assuming that P = 1.05 kW, η = 70% and B_{av} = 0.7 T, the axial length of the lamination stack, ℓ_a, is determined from Equation (2.2), p. 27, as 44.87 mm. The lamination thickness is nominally 0.6 mm and hence each stack comprises 75 laminations. Allowing for a stacking factor of 0.9, the overall axial length of a lamination stack becomes 50 mm.

2.4.1 The pole-pieces

The two most important points that must be considered in choosing the number and dimensions of the poles are the effects on the operation of the motor and on the cost of the control circuits. A comparison is given in Table 2.2 contrasting the use of 4, 6, and 8 poles.

Parameter		Value			Unit
Number of poles, 2p		4	6	8	-
Pole-arc/axial length		1.99	1.33	1.00	-
Teeth minor loop magnetizing frequency (at 1000 rev/min)		33.3	50.0	66.7	Hz
Flux-density per pole (at a constant magnetic loading)		0.47	0.7	0.93	T
Flux-density in rotor-core		0.91	1.36	high	T
Armature reaction (at a constant total electric loading)		high	moderate	low	-
Inactive copper of commutated-winding		large	moderate	small	-
Steps in one revolution		12	18	24	-
T_{min}/T_{max} per rev	$\cos\left(\frac{\pi}{pm}\right)$	0.966	0.980	0.991	-
T_{mean}/T_{max} per rev	$\frac{pm}{\pi}\sin\left(\frac{\pi}{pm}\right)$	0.989	0.995	0.997	-

Table 2.2 Comparison with different numbers of pole ($m = 6$)

Normally in d.c. motor design the pole-arc is made approximately equal to the axial length, i.e. the poles

are approximately square. To limit the frequency-dependent iron losses to a low value, the frequency of the flux-density changes in the teeth is limited, in practice, to about 50 Hz.

If the number of tappings chosen from Table 1.4, p. 5, is 6, covering a pole and an interpole, then with 36 slots in the lamination stack, the number of steps per revolution is as given in Table 2.2. To obtain this rate of switching, the number of control circuits required is 6, regardless of the number of poles.

The work done per revolution is proportional to the number of poles, when the flux/pole and electric loading are constant. Hence the mean torque per revolution (in contrast with 'per cycle', in Table 1.4) is higher, for example, with 6 poles than with 4. Since the magnetic loading per lamination stack ($p\phi_p$) is assumed constant, the induced e.m.f. in a 50-turn coil of the commutated-winding is also constant, as seen from Equation (2.1), p. 27.

To maintain a whole number of slots between tappings, the 8-pole condition is ruled out. Table 2.2 and the subsequent discussion, point to 6 as the preferred number of poles in the present design.

2.5 The magnetic circuit

The m.m.f. requirements of the magnetic circuit at various values of air-gap flux-density are determined in this section. A discussion is included on the distribution of m.m.f. over the different parts of the magnetic circuit. The flux paths in the rotor-core are also discussed and design changes appropriate to a future motor are explained.

2.5.1 The magnetic characteristics

Annealed ring specimens[32] of the magnetic circuit materials are used in obtaining the magnetisation characteristics. Current reversal in a toroidal coil wound around the specimen causes flux changes which can be calculated from the e.m.f. induced in a search-coil. Fig. 2.14 shows the magnetisation characteristics of the 3 materials of the circuit.

The component parts of the machine are not annealed and calculations based on the curves underestimate the m.m.f. requirement.

2.5.2 The m.m.f. calculations

In view of the magnetic symmetry of the machine about the field coil, the total m.m.f. requirement is twice that per stator section. In Table 2.3, the flux-densities in the teeth, pole-pieces, and rotor-core are given at various

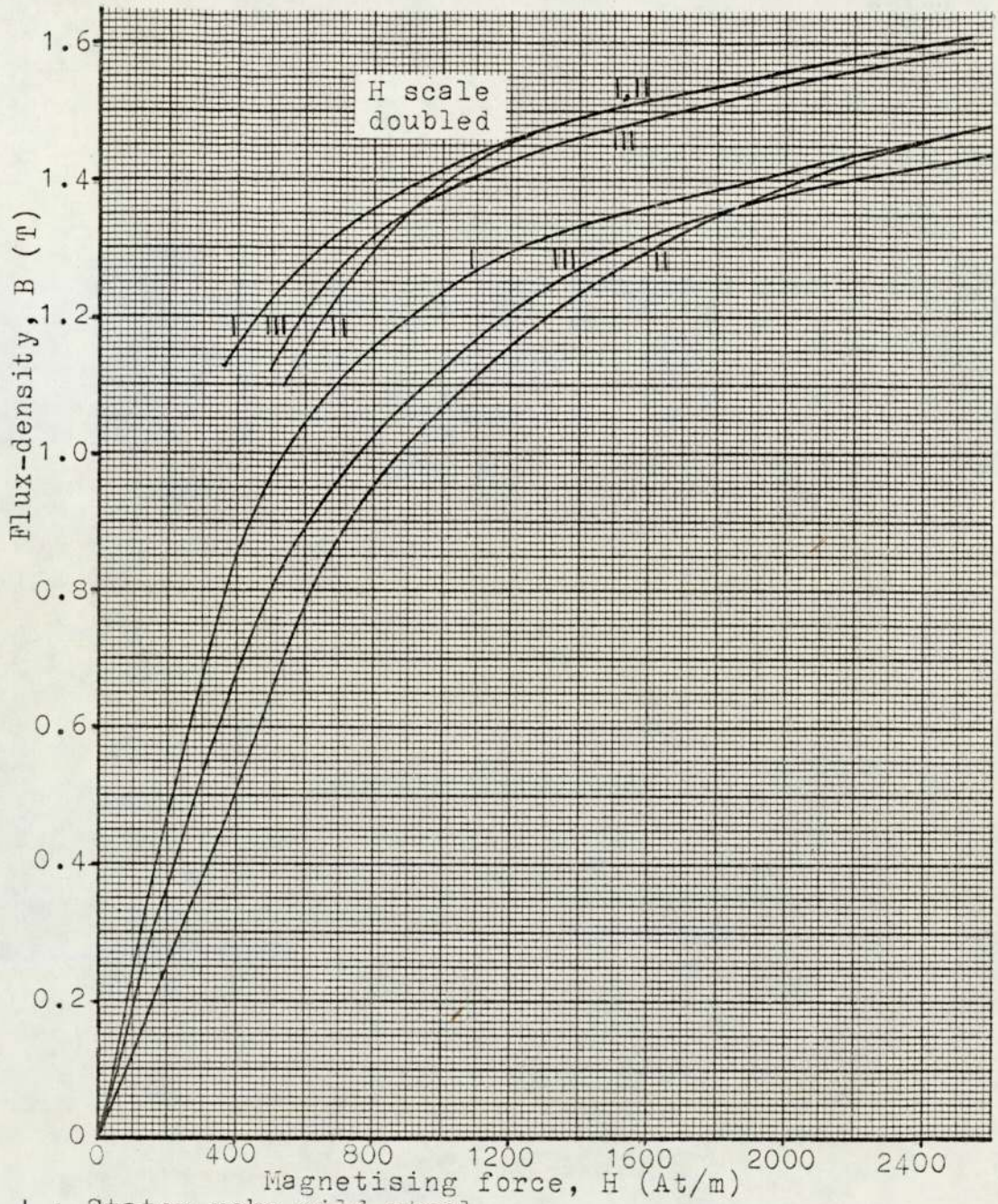

I : Stator yoke mild-steel
II : Rotor-core mild-steel
III : Laminations

Fig. 2.14 Magnetisation characteristics

values of air-gap flux-density, B_g. The corresponding values of m.m.f. for the different sections of the circuit and the total m.m.f. are also given in the table. Appendix A5 gives the relevant dimensions of these sections and the mean lengths of the flux paths.

Parameter		Value						Unit
Flux-density	air-gap, B_g	0.1	0.3	0.4	0.5	0.6	0.7	T
	tooth, B_t	0.23	0.7	0.93	1.16	1.4	1.63	T
	pole-base	0.144	0.43	0.58	0.72	0.86	1.0	T
	rotor-core, B_c	0.195	0.58	0.78	0.97	1.17	1.36	T
M.M.F.	air-gap	26	76	101	127	152	177	At
	teeth	3	7	8	23	46	135	At
	back of teeth	-	2	3	4	5	6	At
	pole	-	6	8	9	11	14	At
	stator yoke	-	6	8	9	11	14	At
	rotor-core	16	38	50	69	108	170	At
	half circuit	45	135	178	241	333	516	At
	total, F_T	90	270	356	482	666	1032	At

Table 2.3 Flux-density and m.m.f. values (solid rotor) (Values of F_T are plotted against B_g in Fig. 2.20, p. 51.)

It is assumed that the flux-density is uniform and that leakage paths, e.g. in the end plates, the space around the field coil and the interpolar zones, can be ignored. The air-gap length, ℓ_g, is uniform over a pole-arc, and Carter's correction coefficient[33] is used to allow for the effects of stator slots.

Due to the possible shaft misalignment at the bearings, the air-gap length opposite the 3 poles need not be the same. Additionally, in the experimental motor, there was some radial movement of the poles due to magnetic pull at high flux-densities.

In calculating the tooth m.m.f., a tooth is divided into 4 sections corresponding to the different cross-sectional areas. The flux-densities are consequently different and the highest value is between points B and D in Fig. 2.15. This is the value for B_t given in Table 2.3.

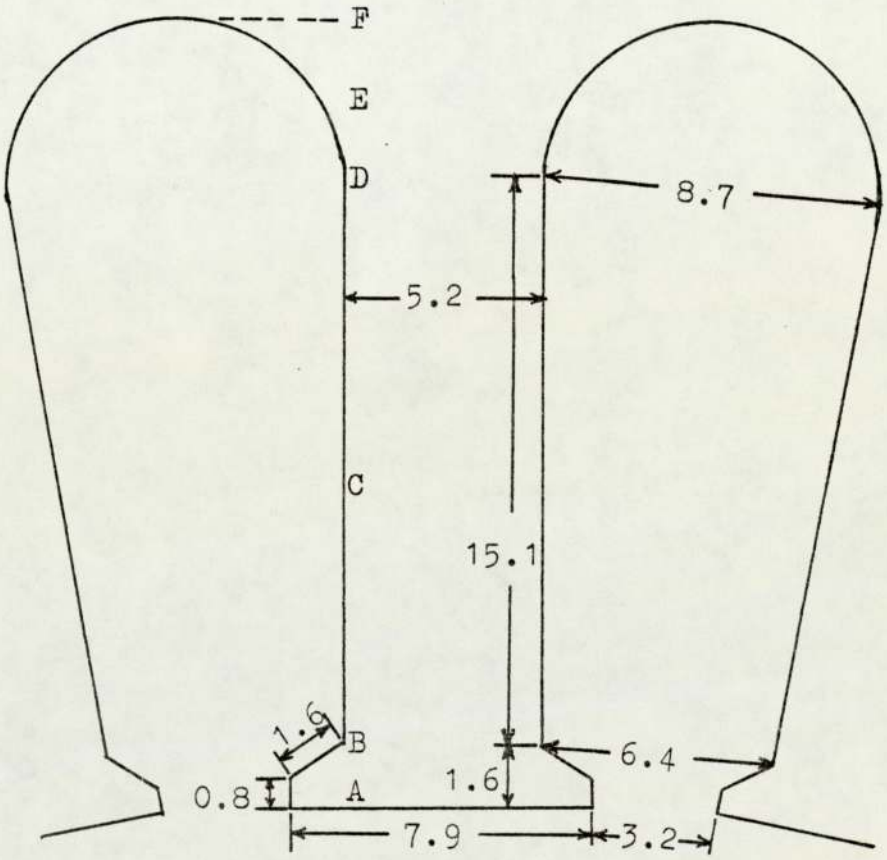

Fig. 2.15 Slot and tooth (dimensions in mm)

The flux path in the rotor-core is along the middle of the radial thickness, as shown in Fig. 2.16. Directly under the pole, the path is approximated to the arc of a circle. Strictly, however, flux-density tends to be higher around corners and in the outer sections of the core near to the poles. The total m.m.f. for the rotor-core is determined from the m.m.f. for the two sections of Fig. 2.16.

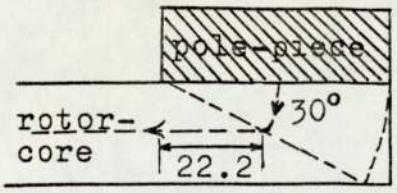

Fig. 2.16 Pole-piece and rotor-core

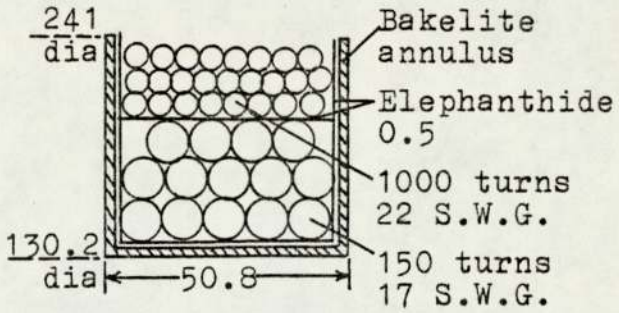

(dimensions in mm)

Fig. 2.17 Field coils and support

The three largest portions of the total m.m.f. are required by the rotor-core, air-gap, and stator teeth. At B_g = 0.7 T in Table 2.3, iron in the rotor-core and teeth is approaching saturation and a considerably larger m.m.f. is required to obtain a higher air-gap flux-density.

The total m.m.f. is provided by either of two annular field windings located midway between the two lamination stacks. One winding comprises 150 turns of 17 S.W.G. and the other, 1000 turns of 22 S.W.G. enamelled copper wire. The resistances of the coils at 20°C are 0.7 Ω, and 25.9 Ω, respectively. A cross-section of the two coils and the annulus supporting them is shown in Fig. 2.17.

2.5.3 Comments about the rotor-core

At high rotor-core flux-densities, some magnetic flux may cross into the stainless-steel shaft and use the end plates to complete the circuit. To minimize this, a 3.2 mm thick brass sleeving was inserted between the shaft

and the core. The depth of the core was limited on the inside by the shaft and on the outside by the depth of the poles and the diameter of the available laminations.

Although the path of the main flux is always axial as shown in Fig. 2.4, p. 25, flux produced by the commutated-winding can be partly circumferential. Since each lamination stack houses a complete winding with alternate polarity poles, part of the flux can use a shorter path through an adjacent pole-piece.

Fig. 2.18 shows the secondary paths for flux produced by one coil only. Ideally, when a complete winding is considered, these secondary fluxes cancel. In practice, however, it is not possible to cancel these fluxes completely due to variations in the air-gap lengths.

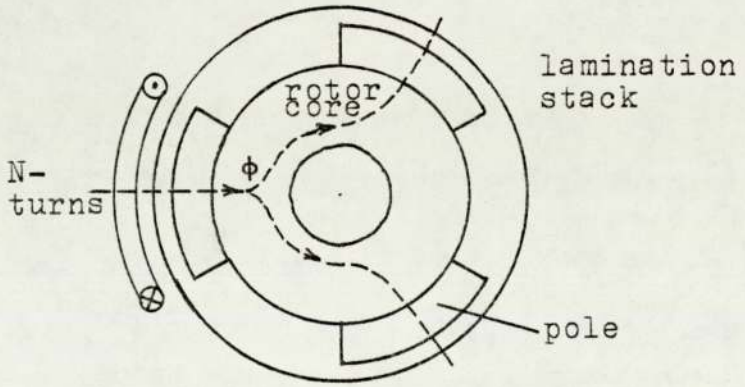

Fig. 2.18 Secondary flux paths in rotor

Axial slots were made in the interpolar zones of the core from one end to the other. Fig. 2.19 shows a top view and a cross-section of one end of the rotor-core. The slot between the poles (section A) is wider than section B

since the likelihood of secondary paths is more in section A. This segmentation eliminates the flux path shown in Fig. 2.18. Photograph 1a shows the segmented rotor-core and the pole-pieces.

Inserting a brass cylinder between the core and shaft, and segmenting the core, both result in a 16.5% reduction in the cross-sectional area of the iron. The flux-density and m.m.f. calculated for the reduced area are given in Table 2.4. The m.m.f. required for the rest of the magnetic circuit being the same as in Table 2.3, the total m.m.f. is determined and plotted in Fig. 2.20. The total m.m.f. is noticeably higher after segmentation due to the added requirement of m.m.f. for the rotor-core.

Parameter		Value						Unit
Flux-density	air-gap, B_g	0.1	0.3	0.4	0.5	0.6	0.7	T
	rotor-core, B_c	0.23	0.7	0.93	1.17	1.4	1.63	T
M.M.F.	rotor-core	20	48	80	110	190	615	At
	half circuit	49	145	208	282	415	961	At
	total, F_T	98	290	416	564	830	1922	At

Table 2.4 Flux-density and m.m.f. values (segmented rotor) (other parameters same as in Table 2.3, p. 46)

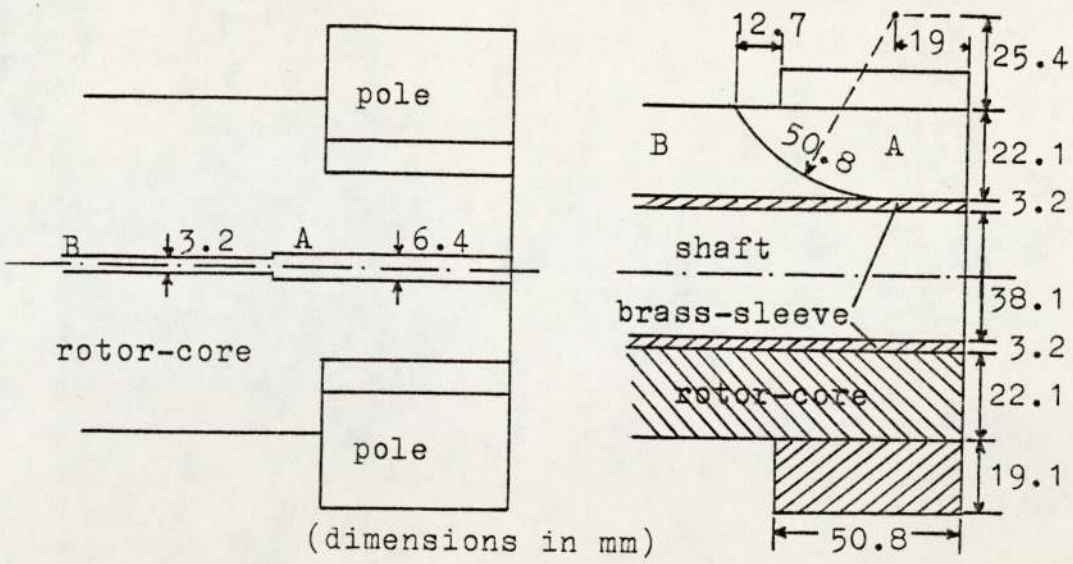

(a) Top view (b) Cross-sectional view

Fig. 2.19 Segmented rotor-core

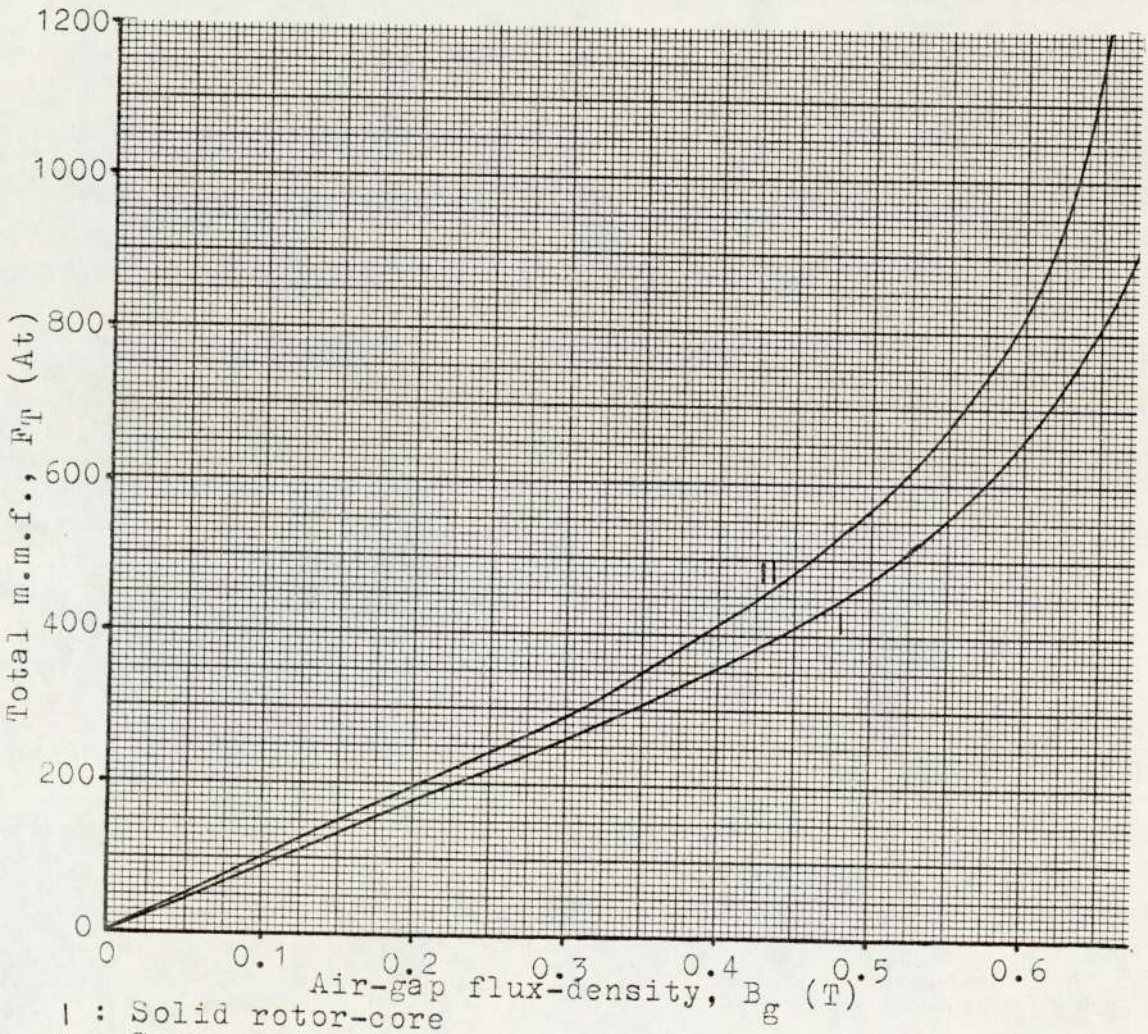

I : Solid rotor-core

II : Segmented rotor-core

Fig. 2.20 Total m.m.f. vs. air-gap flux-density

2.6 Commutated-winding design

Each 36-slot lamination stack is wound for 6 poles with full-pitch coils each of 50 turns. The double-layer winding must permit connections for the ring, star-connected and star windings, explained in Section 1.1.2, p. 3. Hence it is divided into 6 groups, each comprising 6 coils in one lamination stack. Fig. 2.21 shows one such group of coils, and the slot numbers which it occupies.

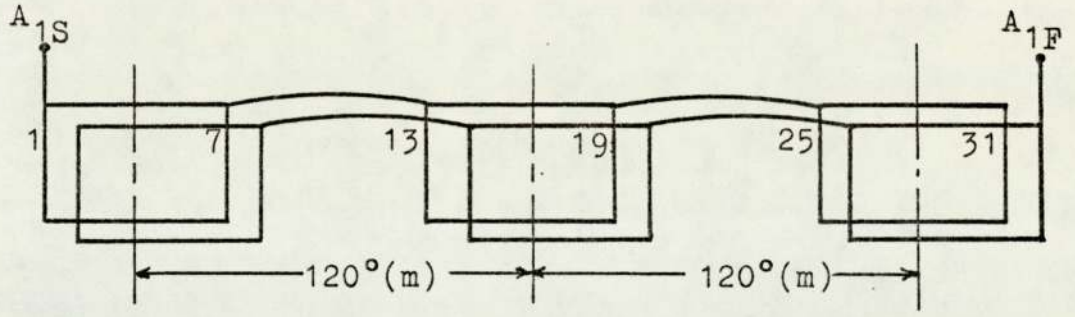

Fig. 2.21 Coil group A_1 in ODE lamination stack

The interconnections between the 6 coils are made inside the machine and only the start, S, and finish, F, of the group is brought out. A group in the other lamination stack is similarly distributed in the slots.

The developed winding diagram is given in Fig. 2.22 and the complete winding in the stator is shown in Photographs 2a and b. The start and finish of the six coil groups are brought to a mimic board in front of the machine with a layout similar to Fig. 2.23.

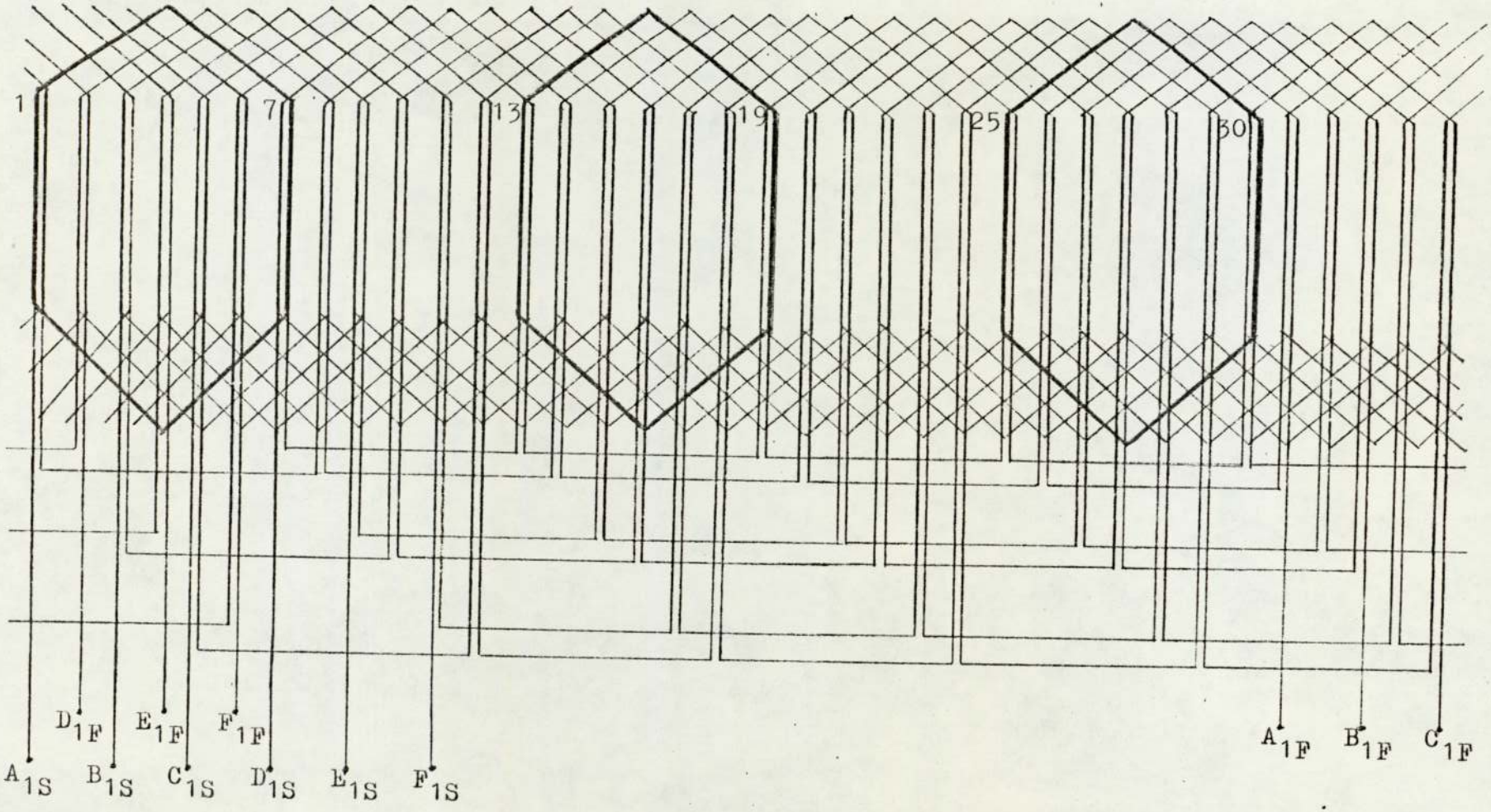

Fig. 2.22 Diagram of commutated-winding in ODE, 36 slots, 6 pole

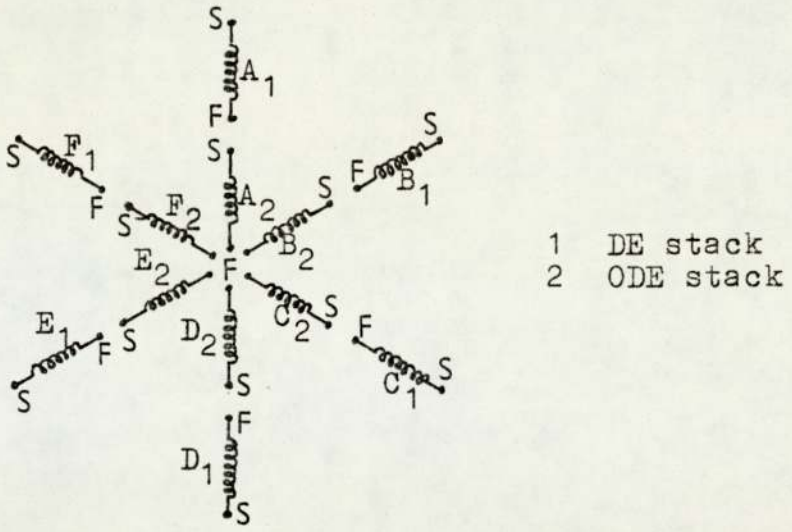

Fig. 2.23 Layout of winding on mimic board

A ring, star-connected or star winding can be obtained by connecting the terminals on the mimic board as in Table 2.5. The d.c. supply is then connected sequentially to the 6 tappings given in the table. Axially aligned groups, for example, A_1 and A_2 are connected in series for the 3 types of winding. But the start and finish of two such groups are arranged so that, when connected in series, one group produces a north pole and the other a south pole. These common connections are $A_{1F} - A_{2S}$, $B_{1F} - B_{2S}$, etc., $F_{1F} - F_{2S}$.

Winding	Connections	Tappings
Ring	$A_{2F} - B_{1S}$, $B_{2F} - C_{1S}$, etc., $F_{2F} - A_{1S}$	$A_{1S} - D_{1S}$, $B_{1S} - E_{1S}$ $C_{1S} - F_{1S}$
Star-connected	$A_{2F} - B_{2F} - C_{2F}$ etc.	A_{1S}, B_{1S}, C_{1S}, etc. to the connections in the middle
Star	$A_{2F} - D_{2F}$, $B_{2F} - E_{2F}$, $C_{2F} - F_{2F}$	same as for ring winding

Table 2.5 Connections corresponding to Fig. 2.23

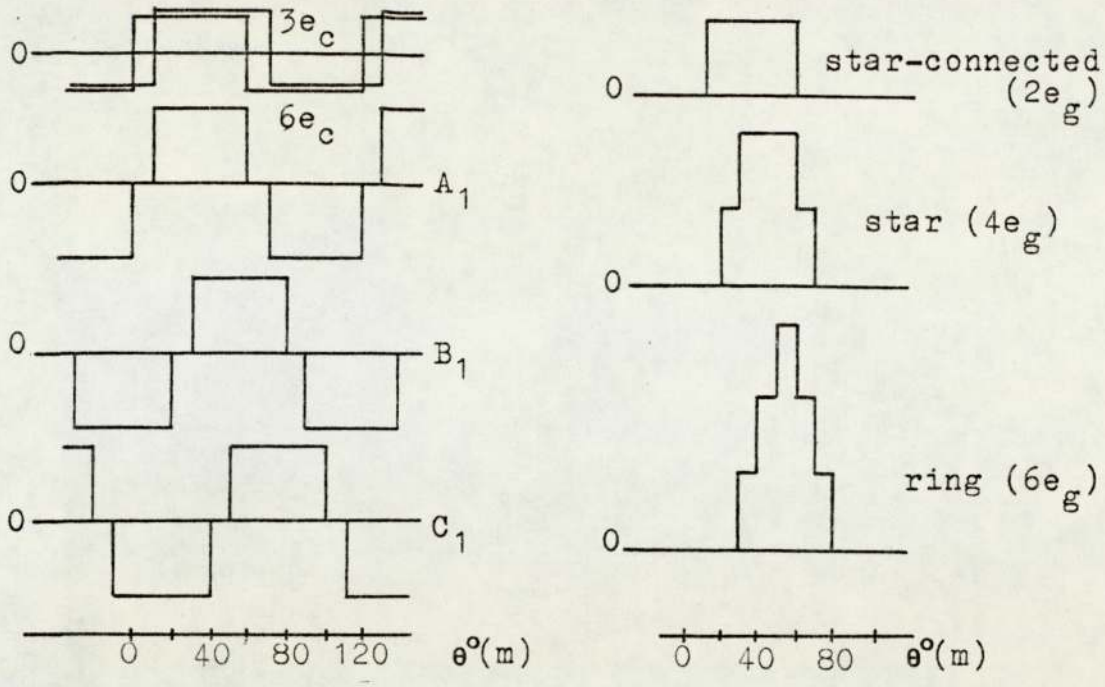

(a) e.m.f. in coil groups (b) e.m.f. induced between opposite tappings

Fig. 2.24 Diagrams of e.m.f.

For a given set of operating conditions the supply voltage to the commutated-winding tappings given in Table 2.5 must balance the e.m.f. induced between the tappings and the voltage drop due to the winding resistance.

The e.m.f. induced in one coil group, for example A_1, is common to all winding types. First, the e.m.f. induced in one coil is from Equation (2.1), p. 27:

$$e_c = 2pn\ N\ \phi_p/60$$

Therefore, for one coil group, the peak value of induced e.m.f. shown in Fig. 2.24 is

$$e_g = 12pn\ N\ \phi_p/60 \qquad (2.10)$$

At an air-gap flux-density of 0.7 T, the flux per pole with $2p = 6$ is 2.3 mWb. Assume a speed of 1000 rev/min

and that each coil has 50 turns. Substituting in Equation (2.10),

$$e_g = 69 \text{ V}$$

In Table 2.6, the peak value of the back e.m.f. of the winding is given for the 3 connections. The resistance, R_w, between tappings to which supply is connected, is given in terms of R_g, the resistance of one coil group.

Type of winding	E.M.F. (V)		R_w	Comments
Ring	6 e_g	414	3 R_g	High V
Star-connected	2 e_g	138	2 R_g	High I
Star	4 e_g	276	4 R_g	Moderate V, I

Table 2.6 Comparison between types of winding

It is seen from the comparison in Table 2.6 that a high voltage is required for the ring winding whereas a star-connected winding draws a high current for the same power rating. The star winding, however, requires only moderate values of voltage and current. This is a very important factor when considering the ratings of semi-conductor switches in the electronic commutator.

Fig. 2.24 also shows the ideal e.m.f. waveforms between opposite tappings for the 3 types of winding. If it is assumed that a connection is made for 10° either side of the peak value, then the ripple value is equal to e_g regardless of the type of winding. This value can be

reduced by offsetting the connection point and staggering the poles as will be explained in Section 3.4.1, p. 96.

In Section 2.4, p. 41, on the preliminary design, a slot electric loading of 200 A was decided upon. A conservative value of current chosen for the semi-conductor switches is 2 A. This is also the coil current, I_c, and hence the design requires 100 conductors per slot. For a double layer winding, a slot houses two coil sides of 50 conductors each. The copper area per slot is 40 mm^2 and, therefore, the conductor cross-section is $40/100 = 0.4$ mm^2. The nearest available wire gauge is 22 S.W.G. (0.711 mm diameter and 0.397 mm^2 cross-section).

The active length of conductor in each turn is $2 \times 50 = 100$ mm and the overhang is $2 \times 138 = 276$ mm. Hence the total length of copper in each 50-turn coil is $50(100 + 276) = 18800$ mm. The resistance of the copper wire is 42.64 Ω per 1000 m at 20°C. Therefore, the resistance of the coil is 0.8 Ω. Since there are 6 coils in a coil group then $R_g = 4.8$ Ω. (v. Table 2.6, p. 56). This is in agreement with the measured value.

The layout of a typical slot is shown in Fig. 2.25. An obvious drawback of the construction is the need for 4 overhangs for the windings in both lamination stacks: 73% of the conductor length is in the overhang. The additional overhangs increase the overall length of the machine and hence the m.m.f. required, particularly for the rotor-core.

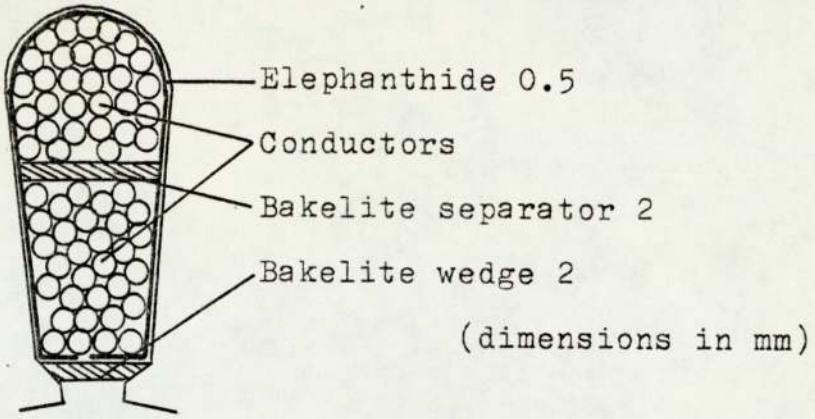

Fig. 2.25 Diagram of the slot and winding

In conventional machines, short chording by one slot-pitch reduces the coil inductance,and improves commutation. The coil-span is normally much greater than the pole-arc. In the present machine the coil-span is the same as the pole-arc and conditions are, therefore, different with regard to commutation which makes chording ineffective. Also with a star winding, because the coils are not energised all of the time, commutation can take place through a diode. Clearly the question of sparking does not arise in this machine when operated with the electronic commutator.

The inductance of the winding is estimated for the ring and star windings from the flux-density measurements as will be explained in Section 3.7.2.2.1, p. 146.

2.7 Comments

A theoretical comparison between the brushless motor of this project and the conventional d.c. motor is possible in view of the similarity between the two motors as can be seen from the specification and the mechanical design.

The shunt characteristics and the variable speed control are maintained, but due to the double-stator feature of the brushless motor, the total electric loading is twice the value for a d.c. motor of the same ratings. However, the total magnetic loading is the same for both motors since, in the brushless motor, the air-gap flux-density between rotor poles is practically zero. Compared with the circumferential flux path of the conventional d.c. motor, the longer axial path of flux in the brushless motor results in a higher m.m.f., especially in the rotor-core. This can be controlled by enlarging the cross-sectional area of the rotor-core, which, for the present motor, is limited by the existing stator laminations. The rotor-core is segmented axially to eliminate possible circumferential flux paths in each stator section.

The commutated-winding, which can be connected in several ways, e.g., ring, star etc., is designed for the available slot area, and for a reasonable value of the electric loading. The winding resistance depends upon the type of winding but is generally higher than that of a comparable d.c. motor, since there are twice as many coils in the brushless motor as normally required in a d.c. motor.

Torque production is investigated theoretically in this chapter and a model for determining the saliency torque is devised. This is complemented in the next chapter by experimental torque waveforms obtained with various combinations of winding coils.

CHAPTER 3

MACHINE OPERATION

3.1 Chapter outline

Several methods were used in measuring the torque developed by the machine under various conditions of excitation. The different methods complement each other in demonstrating the details of torque production. In Section 3.3, the final torque waveform was arrived at after experimenting with different numbers of coil groups of the commutated-winding. The same step by step procedure was followed in obtaining the waveform of e.m.f. induced in the winding. The e.m.f. was measured at several values of the commutation angle and the results are given in Section 3.4. Tests were performed on the machine when driven at a constant mean speed. No-load losses were determined from these tests as discussed in Section 3.5. Motor operation on no-load and on load is explained in Section 3.6 where a mechanical commutator was used. The commutated-winding connected to the commutator was, therefore, a ring type winding. A description of flux-density measurements and the results obtained are given in Section 3.7.

This chapter includes preliminary tests leading to the design and construction of the electronic commutator. Some of these tests were later refined and are discussed in Chapter 5.

3.2 Operation when driven at a constant mean speed

The test condition referred to in this section is used for the torque and e.m.f. measurements performed in Sections 3.3 and 3.4, respectively, as well as for the determination of losses in Section 3.5. The brushless machine was driven by a 1.1 kW d.c. motor while a d.c. supply was connected to the field coil and/or the coil groups in the commutated-winding.

A mechanical commutator was used only in the motor operation discussed in Section 3.6, but reference to it and the associated commutation angle is made in the preceding sections. The mechanical commutator consisted of an 18-segment faceplate commutator with a rotating brush-arm. The 6 tappings of the ring winding were connected to 6 successive segments. The 18 segments formed 3 groups mutually displaced by 120°(m). The brush-arm carried 4 roller brushes; two on the positive and negative rings and two on diametrically opposite segments as shown in Photograph 3b.

At this stage, it is useful to define the separation angle between the axes of the rotor pole and stator coils.

3.2.1 Relative position of rotor and stator axes

Fig. 3.1 shows one pole-pitch at the opposite drive end (ODE) of the machine. θ is the angle between the rotor

pole-axis and the centre-line of the leading coil of a coil group, assuming a clockwise direction of rotation. A coil group, e.g. A_1, has two coils (i) and (ii) per pole-pitch as shown in Fig. 3.1.

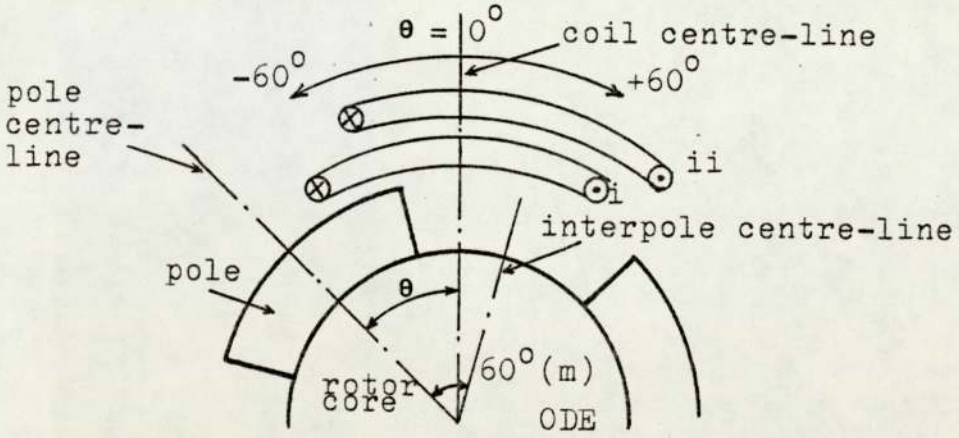

Fig. 3.1 Angle θ with respect to a stator coil

When the complete ring winding is energised, the angle referred to is that between the pole and winding axes, and is denoted by γ. Fig. 3.2 shows the positions of θ = 0° and γ = 0° with respect to each other. In both cases supply is connected to the tapping of coil group A_1. For easy reference, γ = θ + 5°(m).

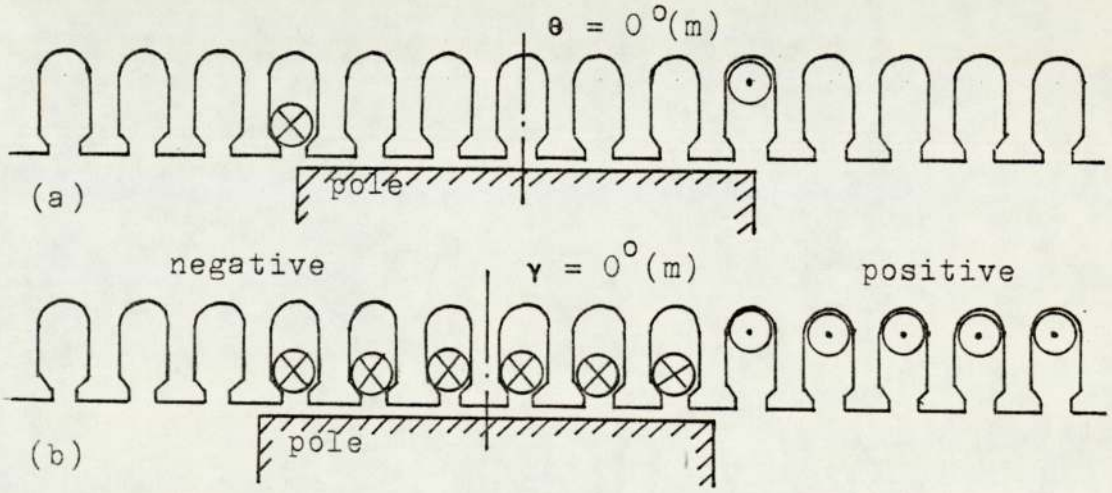

Fig. 3.2 Angles θ and γ

For completeness, Fig. 3.3 shows an idealised waveform of the e.m.f. induced between diametrically opposite tappings of the ring winding, and the corresponding values of γ (v. Fig. 2.24, p. 55). The peak e.m.f. is seen to occur at $\gamma = 0°(m)$ and $\pm 60°(m)$, i.e., when the pole and winding axes are either in line or separated by $180°(e)$.

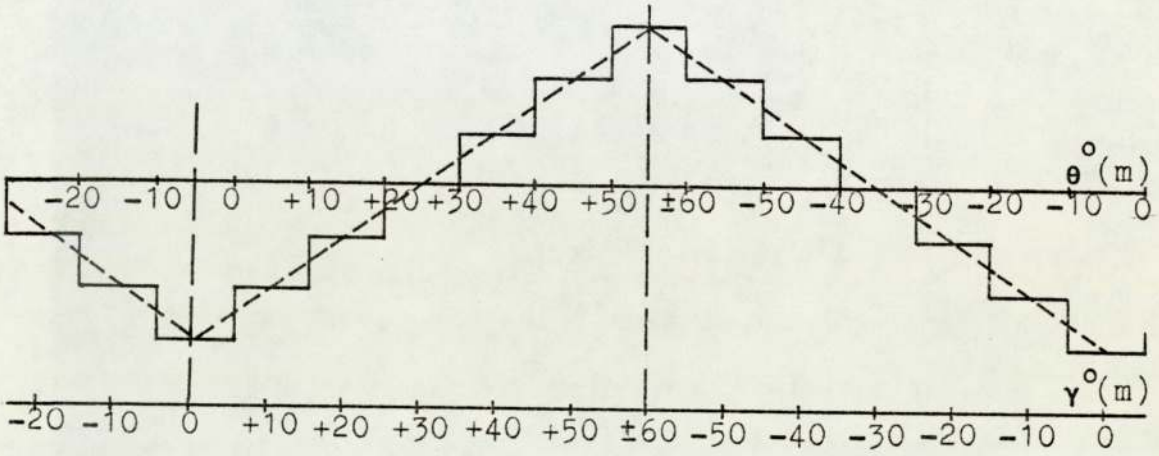

Fig. 3.3 Idealised e.m.f. waveform between opposite tappings of the ring winding

3.3 Torque measurements

The tests described in the following sections were performed with various numbers of commutated-winding coils excited, both with and without d.c. field excitation. Torque variations were also measured with field excitation only. These tests are referred to as static-torque measurements.

In Section 3.3.1, a balanced torque-arm was used in measuring the developed torque. A pointer was fixed onto the shaft to magnify the rotor movement by reading angular

positions of the rotor on a large scale of radius 0.3 m - 1°(m) corresponding to a pointer movement of 5.2 mm.

At each position of the rotor, the torque-arm was locked horizontally on the shaft. To counteract the developed torque, weights were placed on the tray at one end of the torque-arm to maintain the arm in the horizontal position.

Other static-torque tests were performed by manually rotating the shaft while torque variations were plotted on an X-Y recorder, and read directly on a digital voltmeter as described in Sections 3.3.2 and 3.3.3, respectively.

In these two sections as well as in Section 3.3.4, torque was measured with a strain gauge transducer coupled to the shaft. The signals from the transducer were amplified and then fed into a 100 Hz filter unit to remove an error signal caused by a fault in the transducer. Provisions are made in the filter unit for connections to an X-Y recorder/CRO and a digital voltmeter. The circuit diagram is given in Appendix A6.

Unlike the tests in the preceding 3 sections, the tests in Section 3.3.4 were performed with the brushless motor driven by a 1.1 kW d.c. motor. This was done to observe the effect of both excitation and the number of winding coils energised, on the developed torque.

3.3.1 Torque measurements with weights

Test no.	Field m.m.f. (At)	Stator coils*		Rotor poles (2p = 6) **	Source of torque ***	Fig. no.	Page no.
		Groups per lamination stack	Peak NI per 120°(m) of lamination stack (At)				
1	1050	-	-	B	a	3.4a	67
2	1050	-	-	C	a	3.4d	67
3	-	1	234	B	a,b	3.6a	69
4	-	1	234	C	a,b	3.6b	69
5	680	½	117	A	a,b,c	3.8	71
6	1050	1	234	B	a,b,c	3.9a	72
7	1050	1	234	C	a,b,c	3.9b	72
8	1050	Ring winding	702	C	a,b,c	3.10	73

* 1: one group of 6 series-connected coils in each lamination stack

½: one group of 3 series-connected coils in each lamination stack

** A: poles aligned, not chamfered, pole-arc 58°
B: poles aligned, not chamfered, pole-arc 60°
C: poles staggered, chamfered, pole-arc 58°

*** a: reluctance torque
b: saliency torque
c: 'B$_\ell$I$_r$' torque

Table 3.1 Torque tests with weights (I_a = 2.34 A)

The tests listed in Table 3.1 (except Test 5) were performed after the rotor-core was segmented (v. Section 2.5.3, p. 48). The sources of torque in each test correspond to those discussed in Section 2.3.4, p. 35. The peak m.m.f. of the stator coils is given in Table 3.1 per 120°(m) per lamination stack. The total current to the stator coils wherever applicable is 2.34 A, and the number of turns per coil is 50.

The variation in reluctance torque with angular position δ from Test (1) is shown in Fig. 3.4a. δ is the angle between a pole-tip and a tooth-axis (X). The torque curve is repetitive over a slot-pitch or 10°(m).

Peaks (i) and (ii) in Fig. 3.4a occur when the pole-tips are under teeth and slots respectively. The peaks are separated by a dip which occurs when the pole-tips are approximately opposite tooth-tips. The tooth-tips can reach magnetic saturation even at low values of excitation due to flux concentration when facing pole-tips. The occurence of torque peaks is, therefore, determined by the changes in flux distribution at the pole-tip, and hence by changes in the energy stored in the air-gap.

The variations in the peak value of reluctance torque, T_r, for pole type B (Fig. 3.4a) with field excitation is shown in Fig. 3.5. The variation with air-gap flux-density, B_g, is deduced from Fig. 2.20, p. 51, (B_g vs. NI for segmented rotor-core). The values of T_r vs. B_g are plotted in Fig. 3.5 and the following empirical relation describes this curve.

$$T_r = 0.205\ B_g + 1.15\ B_g^2 - 2.5\ B_g^3 + 5.0\ B_g^4 \qquad (3.1)$$

The reluctance torque waveform of Fig. 3.4b is the same as that of Fig. 3.4a but staggered by half a slot-pitch. The effect of staggering the poles on the reluctance torque is graphically determined in Fig. 3.4c by superimposing the above two curves, since this involves

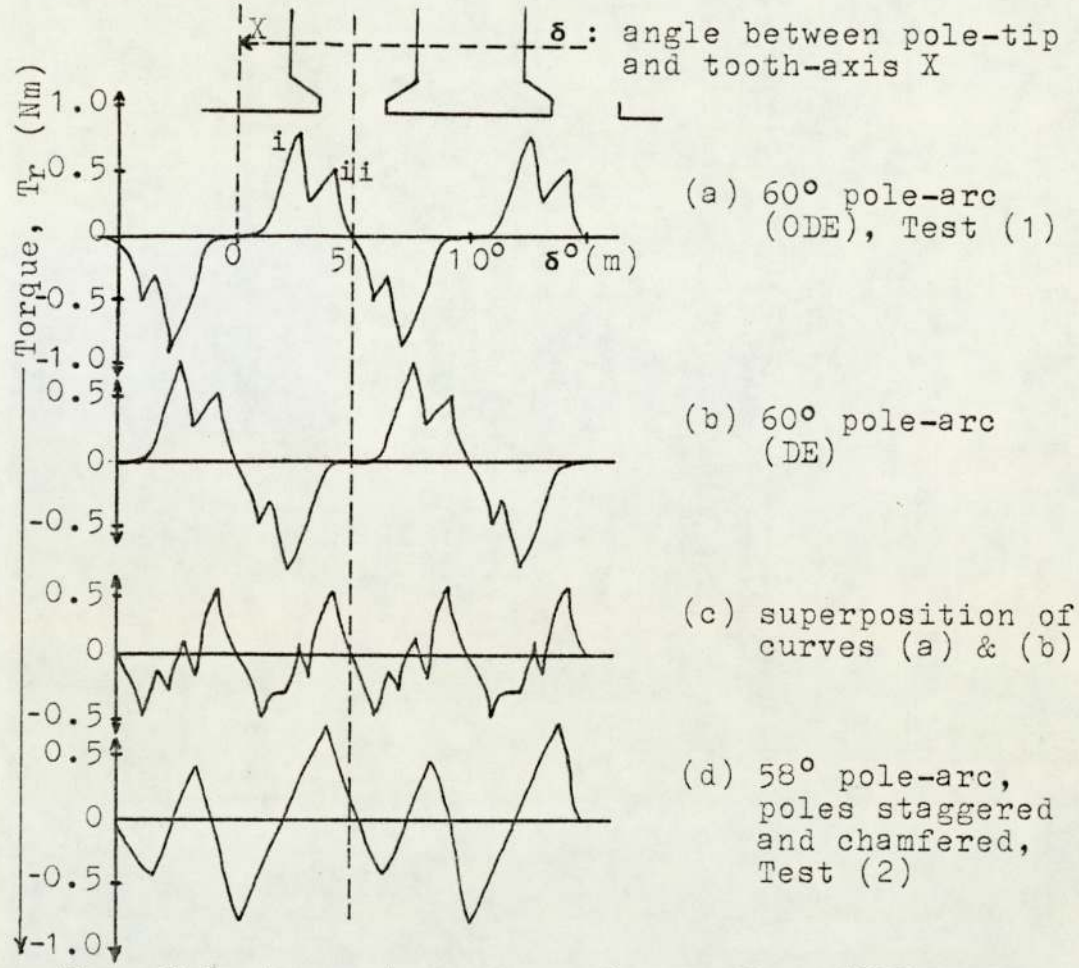

Fig. 3.4 Reluctance torque waveforms, F_f = 1050 At

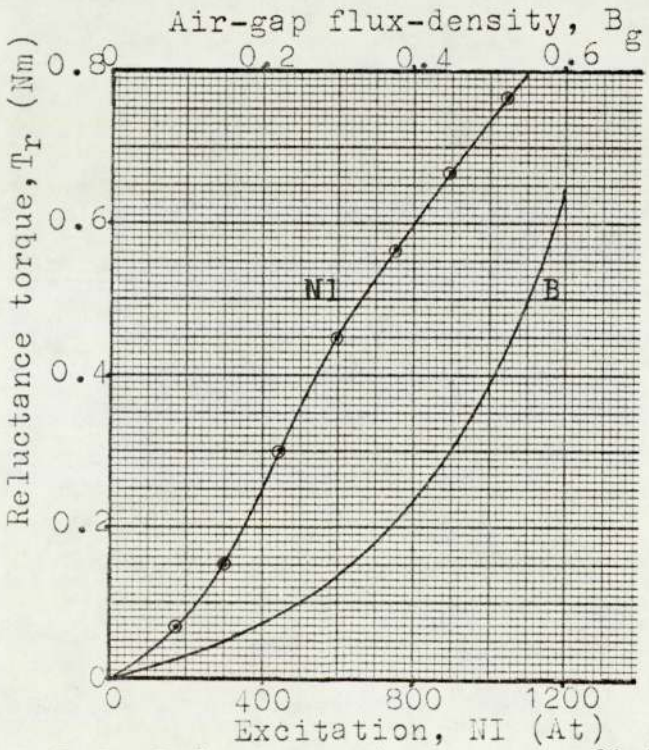

Fig. 3.5 Reluctance torque vs. field excitation and air-gap flux-density; poles aligned, 60° arc

separate air-gaps in the stator sections. The principal peak with aligned poles is eliminated by staggering the poles, leaving a smaller single peak as shown in Fig. 3.4c. The single peak is also apparent in the experimental curve of Fig. 3.4d (Test 2) although the poles here are chamfered and of 58° arc, (v. Fig. 2.8, p. 34).

There is no indication in the results from an analogue model (p. 35) of a minor peak in the torque curve. This can be explained with reference to the saturation in the tooth-tips, and to the misalignment of laminations and poles.

In Tests (3) and (4), one group of stator coils in each lamination stack, e.g. A_1 and A_2 is energised in the absence of field excitation. The values of torque are plotted in Fig. 3.6. There is symmetry about the line $\theta = \pm 4.0°$ for Tests (3) and (4) respectively; with values of θ on one side of this line giving rise to positive values of torque and on the other side negative values. Slot reluctance effect is seen as dips in the torque curve when the pole-tips are in the preferred positions opposite slots. At the particular values of θ, the pole-tips are facing the teeth/slots shown against θ in Fig. 3.6.

Saliency torque is the major part of the developed torque in Fig. 3.6 and is shown diagrammatically in Fig. 3.7. The conditions are similar to those in Test (3) i.e. with 60° aligned poles.

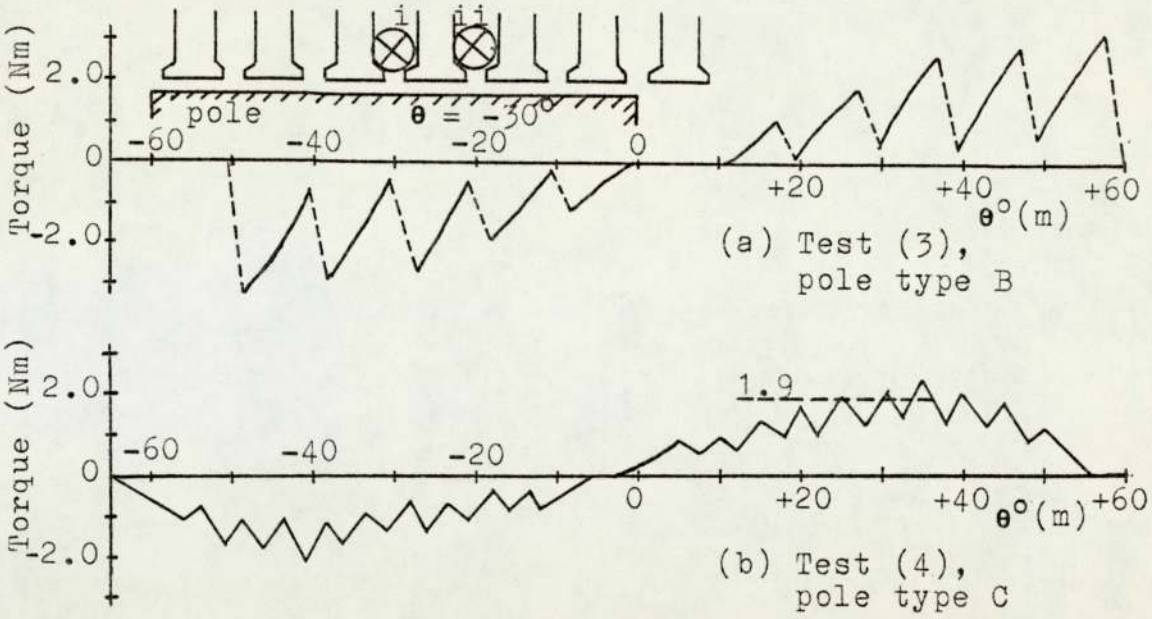

Fig. 3.6 Torque developed with one coil group only, F_a = 234 At/120°(m), I_a = 2.34 A

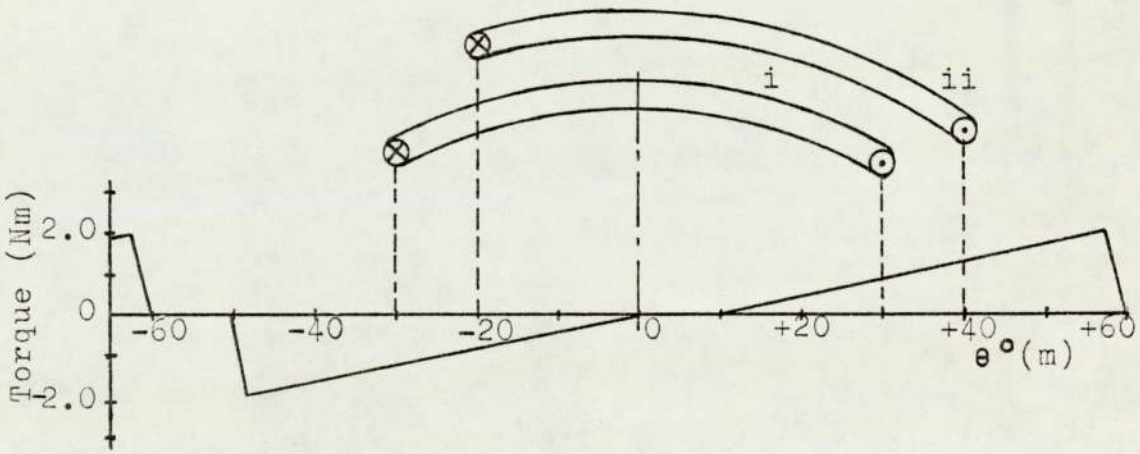

Fig. 3.7 Mean torque of Fig. 3.6a

It is noted that developed torque is zero when θ is 0° to 10° and -50° to -60°. This is the minimum reluctance position of the pole-piece with respect to the coils. Ignoring the torque variation due to reluctance torque caused by slotting, the mean torque in Fig. 3.7 varies

almost linearly with θ as expected from the theory of Appendix A4.

Saliency torque with half a coil group energised was determined in Section 2.3.4.2, p. 36, at a peak m.m.f. per 120°(m) of 100 At. The maximum value of torque was 0.33 Nm. Test (3) was performed with one coil group energised and a peak m.m.f. per 120°(m) of 234 At. The flux in the commutated coils is assumed to vary linearly with current at the low levels of excitation being considered. Since torque varies as the product of flux and current, it can be assumed to vary with $(\text{current})^2$ or with $(\text{ampere-turns})^2$.

The maximum torque in Test (3) can be determined as follows from the calculated value of 100 At.

$$T_{max} = 0.33 \times (\frac{234}{100})^2 = 1.81 \text{ Nm}$$

This value of torque is in good agreement with the maximum value in Fig. 3.7 at about $\theta = +60^{\circ}$(m).

Tests (5), (6) and (7) in Table 3.1 were performed with both commutated and field coils excited. Developed torque was, therefore, due to the 3 sources a, b and c.

In Test (5), half a coil group or 3 coils only per lamination stack were energised. The static torque developed is plotted against θ in Fig. 3.8 for full-pitch coils as well as for short and long-pitch coils. No definite increase in torque is seen when using short or

long-pitch coils compared with full-pitch coils. It is noticed that the peak and minimum torque values for the short and long-pitch coils occur at rotor positions approximately $\frac{1}{2}°$(m) either side of those for the full-pitch coils.

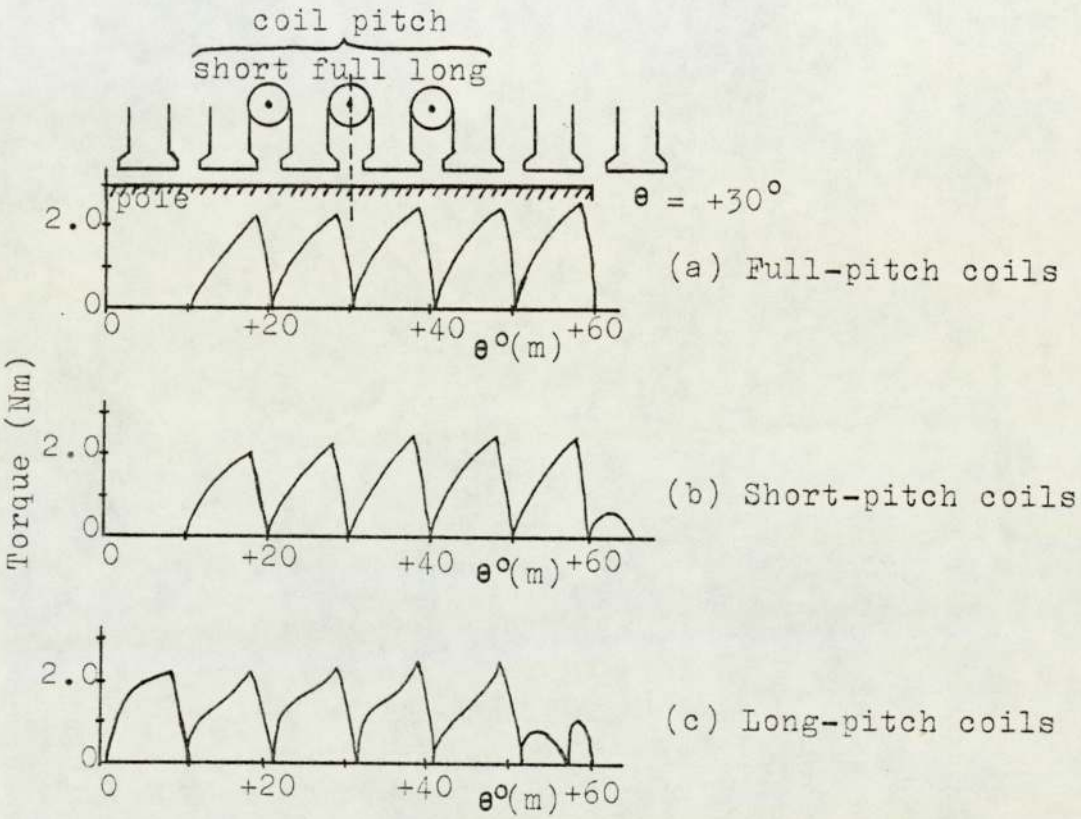

Fig. 3.8 Torque due to $\frac{1}{3}$ coil group per lamination stack, pole-pieces aligned and of 58° arc (type A), F_f = 680 At, F_a = 117 At/120°(m), I_a = 2.34 A, Test (5)

The minimum values of torque are zero and this is attributed to the slot reluctance torque which is more apparent when only one coil opposite each pole is energised as in Test (5). Minimum torque occurs when the pole-tips are facing slot openings.

Fig. 3.9 shows the results of Tests (6) and (7) with one group of stator coils excited. Staggering the poles in Test (7) resulted in a noticeable reduction in the fluctuation of torque compared with Test (6). Minimum torque as a percentage of maximum torque was increased from 10% to 50%.

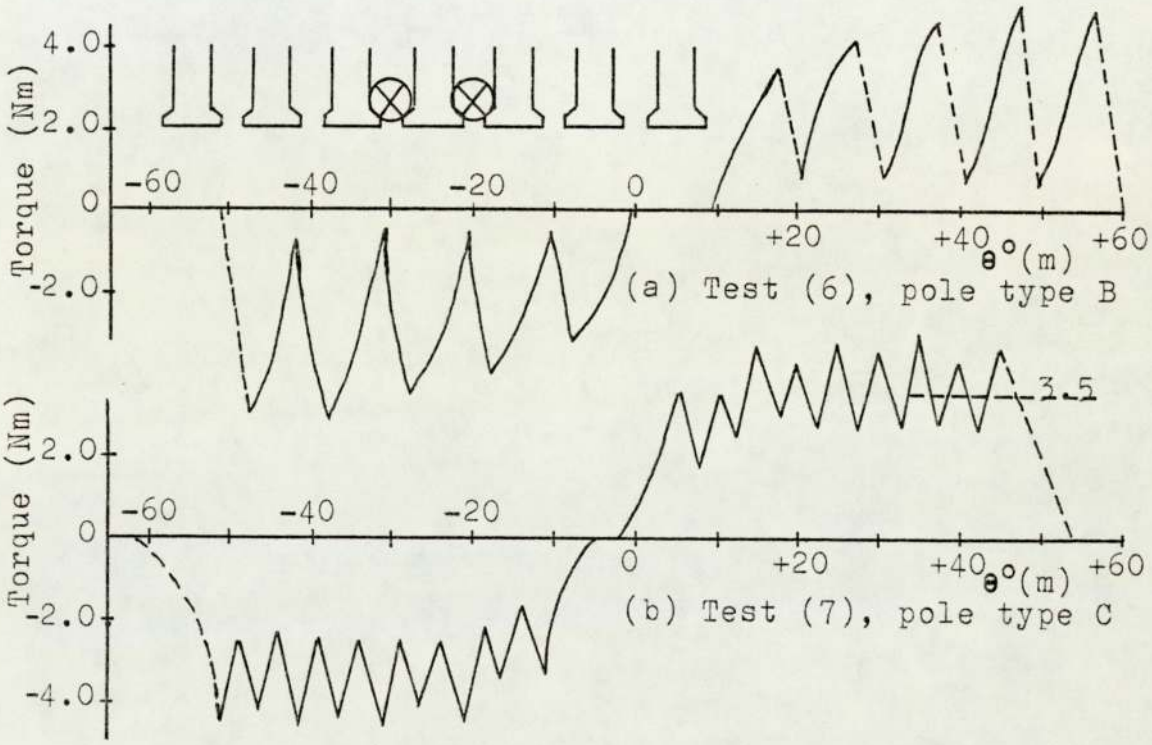

Fig. 3.9 Torque developed with one coil group and field coil excited, F_f = 1050 At, F_a = 234 At/120°(m), I_a = 2.34 A

Maximum torque with one coil group excited (Test 6) is approximately twice that with half a group (Test 5) since, for the same current, the ampere-turns are doubled. Apart from the reluctance and saliency torques, 'BlIr' torque is also developed in these tests. The difference between the values of field m.m.f. in the two tests does not affect the comparison greatly since the corresponding

air-gap flux-densities are close to each other (0.6 T vs. 0.635 T, v. two curves of Fig. 2.20, p. 51).

The complete ring winding and field coil are excited in Test (8), and the developed torque is plotted in Fig. 3.10 against θ. Since the rotor poles are staggered, slot reluctance effect causes the torque to fluctuate about a mean value over half a slot-pitch (5°(m)).

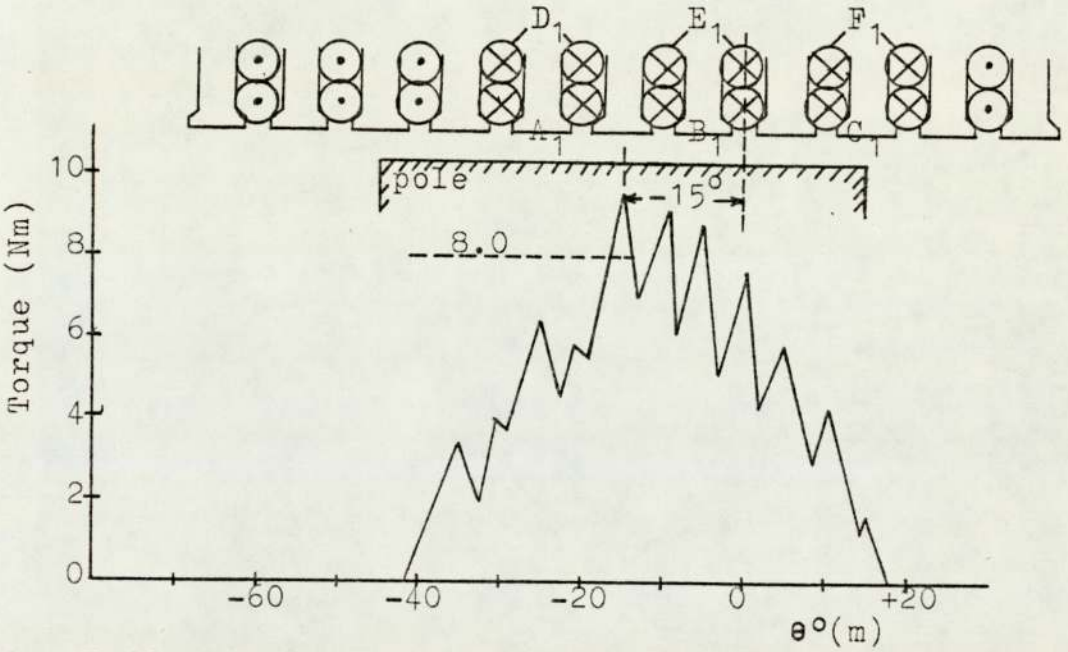

Fig. 3.10 Torque developed with ring winding and field coil excited, F_f = 1050 At, F_a = 702 At/120°(m), I_a = 2.34 A, poles staggered, 58° arc, type C, Test (8)

Ignoring the slot reluctance effect, the torque waveform can be taken as triangular with a peak torque approaching 8 Nm at about θ = -15°(m). In normal rotation, the continuous torque would be formed by the peaks of similar successive waveforms. The peak value of torque, however, may not be as high as in this test due to the absence of rotational eddy-current torques.

3.3.2 X-Y recorder waveforms

An X-Y recorder is connected as shown in the diagram of Fig. 3.11. A circular 1 kΩ potentiometer is mounted on the shaft at the ODE and connected to a low voltage (<5 V). The output voltage of the potentiometer which feeds the horizontal input of the recorder varies linearly with rotor position. The vertical input signal to the recorder is obtained from a strain-gauge transducer (v. Photograph 3a) via an amplifier and a 100 Hz filter unit (v. Appendix A6). A torque-arm fixed on the DE shaft extension was used to rotate the shaft slowly by hand.

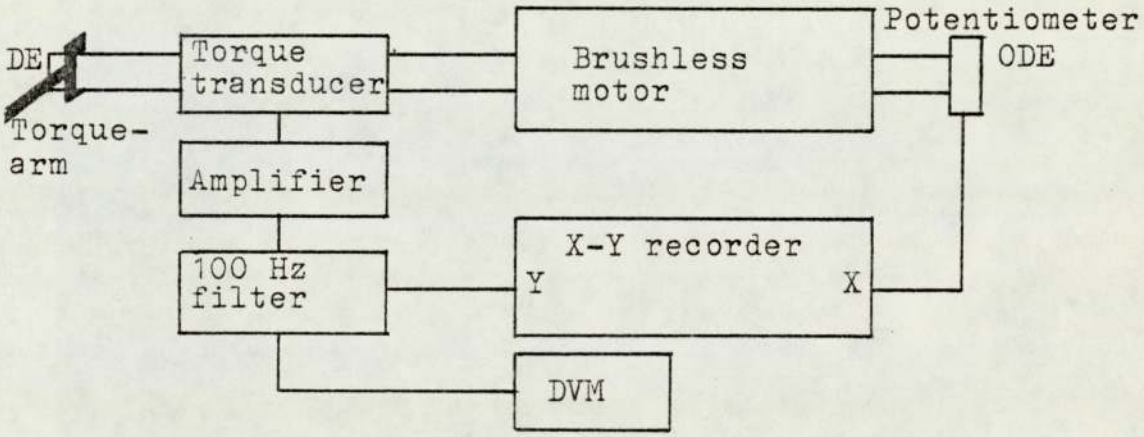

Fig. 3.11 Experimental set-up for torque measurement

Tests (2), (4), (7) and (8) in Table 3.1, p. 65, were repeated with the recorder. For these tests and for all other waveforms from the recorder, the poles were chamfered and staggered (type C). Other connections of the commutated-winding coils were experimented with, for example, 2 coil groups in parallel and 4 coil groups in series. The tests are listed in Table 3.2.

Test no.	Field m.m.f. (At)	Stator coils			Source of torque **	Fig. no.	Page no.
		Groups per lamination stack	Total current (A)	Peak NI per 120° (m) of lamination stack (At)			
1	450	-	-	-	a	3.13i	
	450	1	1.3	130	a,b,c	3.13ii	77
	450	2	1.3	260	a,b,c	3.13iii	
2	-	1	1.3	130	a,b	3.14i	
	450, 750	1	1.3	130	a,b,c	3.14ii 3.14iii	77
3	450	4*	2.6	520	a,b,c	3.15i	
	450	6	2.6	780	a,b,c	3.15ii	80
4	-	6	2.6	780	a,b	3.16i	
	150, 450, 750	6	2.6	780	a,b,c	3.16ii 3.16iii 3.16iv	80
5	450	6	2.6	780	a,b,c	3.17	82
6	450	4	2.6	520	a,b,c	3.18	82

* 4: parallel combination of two groups in series
6: parallel combination of three groups in series
** Same as defined in Table 3.1, p. 65
Pole type C: staggered, chamfered, pole-arc = 58°, 2p = 6

Table 3.2 Torque tests with X-Y recorder

The coil groups can be represented by Fig. 3.12 which is similar to Fig. 2.23, p. 54. Since a coil group in one lamination stack is always connected in series with another group axially aligned with it in the other stack, e.g. A_1 with A_2, reference will be made to the number of groups being excited in one lamination stack only for the particular test.

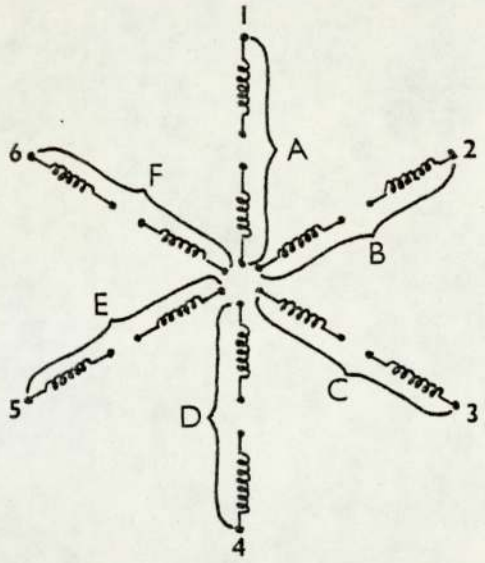

Fig. 3.12 Commutated-winding coils

Torque due to slot reluctance, with only the field coil excited, is shown in Fig. 3.13 (curve i). The two peaks of unequal height per slot-pitch (10°(m)) seen here and in Fig. 3.4d, p. 67, are due to the staggering of the poles.

The constant level of 0.25 Nm in Fig. 3.13 represents the torque required to overcome friction in the bearings. In the preceding Section 3.3.1, the rotor was not being rotated and hence the frictional torque was zero.

Fig. 3.14 (curve i) shows the developed torque due to the excitation of one coil group without field excitation. This curve is comparable to that of Fig. 3.6b, p. 69, for positive values of θ. Since the current in the commutated coils is the only source of air-gap flux, the ratio of torque in the two curves is the same as that of the (ampere-turns)^2.

$$\left(\frac{0.6}{1.9}\right) = \left(\frac{130}{234}\right)^2 = 0.31$$

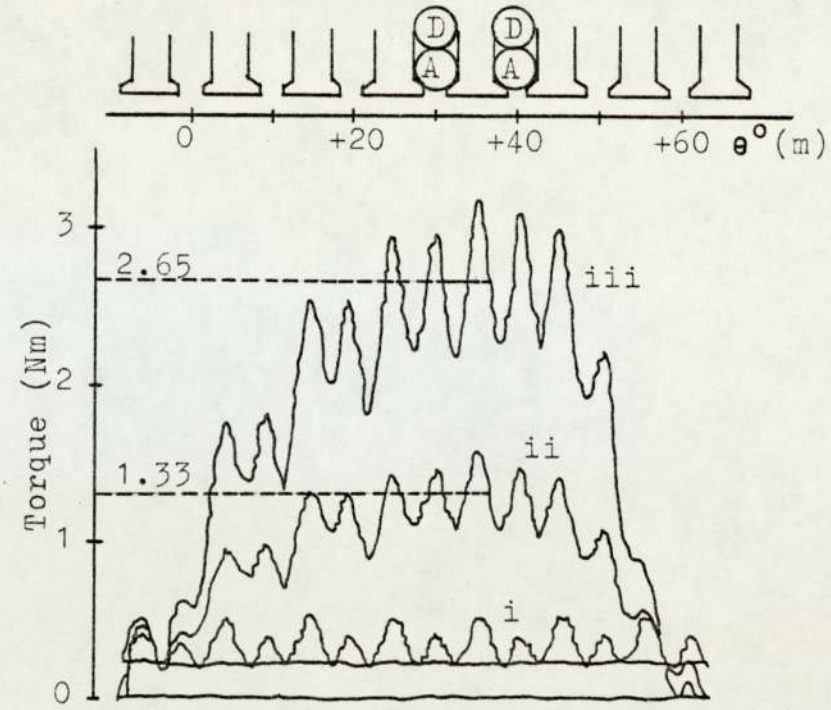

i : no coils excited — F_a : 0
ii : coil A excited — F_a : 130 At/120°(m)
iii : coils A and D excited — F_a : 260 At/120°(m)

F_f = 450 At, I_a = 1.3 A

Fig. 3.13 X-Y recorder torque waveforms, Test (1)

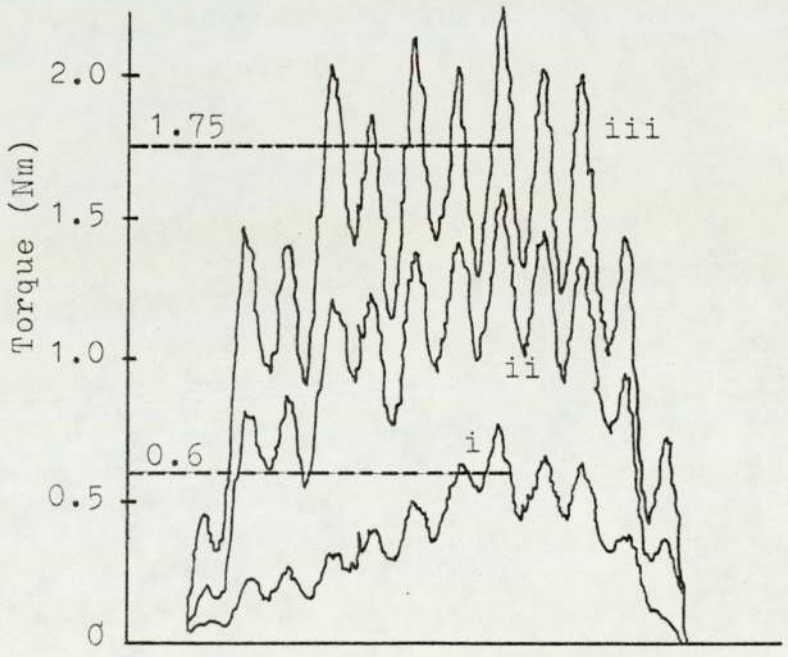

i : F_f = 0
ii : F_f = 450 At
iii : F_f = 750 At

coil A excited
F_a = 130 At/120°(m)
I_a = 1.3 A

Fig. 3.14 X-Y recorder torque waveforms, Test (2)

Fig. 3.14 also includes the torque curves for the same coil but with two different values of field excitation. The pattern of two peaks per slot-pitch (10°(m)) becomes more apparent at high excitations. Maximum torque in the 3 curves occurs at $\theta = +35°$(m), which agrees with those in Fig. 3.6b, p. 69, and Fig. 3.9b, p.72.

The following is a comparison between the curves of Fig. 3.9b and Fig. 3.14iii. The peak values of the mean torque for both curves are related to each other via air-gap flux-density B_g and commutated coils m.m.f., F_a, as given in Equation (3.2).

$$T_1 = T_2\left(\frac{B_{g1}}{B_{g2}}\right)\left(\frac{F_{a1}}{F_{a2}}\right) \qquad (3.2)$$

The values of B_g at the corresponding field excitation are read from Fig. 2.20, p. 51, (segmented rotor-core).

$$T_1 = 3.5\left(\frac{0.575}{0.635}\right)\left(\frac{130}{234}\right) = 1.76 \text{ Nm}$$

This result is in good agreement with the peak mean torque of Fig. 3.14iii.

Returning to Fig. 3.13, the same comparison can be carried out between curves (ii) and (iii). Since field excitation is constant, the ratio of torque is the same as the ratio of the respective commutated coils ampere-turns; 1:2.

Increasing the number of coil groups that are excited from 2 to 4 and then to all 6 of Fig. 3.12, results in the torque waveforms of Fig. 3.15. Although the ratio of

F_a for the two curves (i) and (ii) is 2:3, T_i is only slightly less than T_{ii} (<5%). The reason for this discrepancy (despite equal values of field excitation) is the proportional reduction in the air-gap flux due to armature reaction at the higher F_a. The position at which the peak torque occurs is shifted by 20°(m) since the axis of the flux which is produced by the coils is shifted as more coils are excited.

Fig. 3.16 shows torque waveforms obtained with the 6 coil groups excited for various values of field current. The peak value of the mean torque of curve (iv) can be calculated from that in Fig. 3.10, p. 73, which was obtained with weights.

$$T = 8.0\left(\frac{750}{1050}\right)\left(\frac{780}{702}\right) = 6.35 \text{ Nm}$$

This value agrees with that in Fig. 3.16.

For normal operation, the maximum value of rotational torque is obtained when only the peak torque over 20°(m) is considered. The coil groups of the commutated-winding are switched in sequence as the rotor rotates. This means that, at any moment, current flows in the commutated-winding in such a direction that operation is centred about the peak of the torque waveform.

Arranging the basic waveforms side by side as in Fig. 3.17, and selecting 20°(m) sections result in the waveform of the output torque. The tapping points to

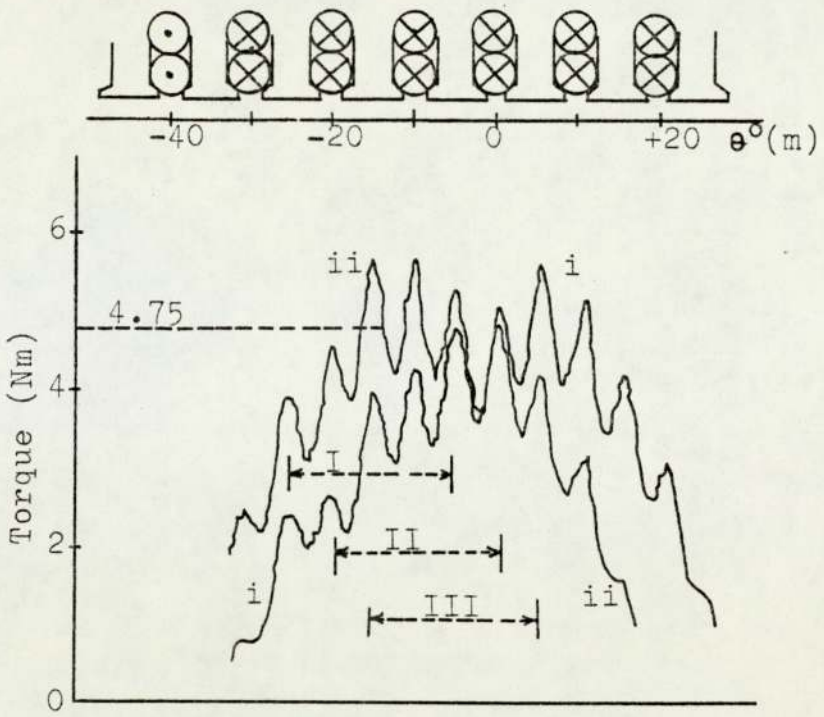

i : 4 coil groups F_a = 520 At/120°(m)
ii : 6 coil groups (Ring winding) F_a = 780 At/120°(m)

F_f = 450 At, I_a = 2.6 A

Fig. 3.15 X-Y recorder torque waveforms, Test (3)

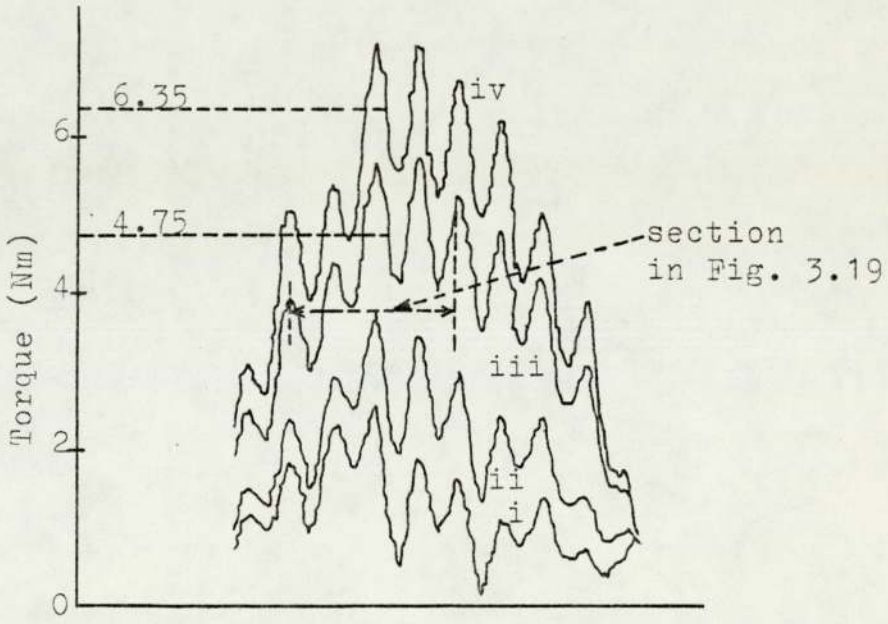

i : F_f = 0 iii : F_f = 450 At
ii : F_f = 150 At iv : F_f = 750 At
ring winding excited, F_a = 780 At/120°(m), I_a = 2.6 A

Fig. 3.16 X-Y recorder torque waveforms, Test (4)

which supply is connected are marked on the curves of Fig. 3.17 (v. Fig. 3.12, p. 76).

Similarly in Fig. 3.18, waveforms obtained with 4 coil groups only (v. Fig. 3.15i) are plotted side by side. Comparing the resultant with Fig. 3.17, the reduction in peak torque with 4 coil groups excited is less than 5%. This was seen previously in Fig. 3.15. However, in both Figs. 3.17 and 3.18, the peak-to-peak ripple as a percentage of the mean value is approximately the same and is equal to about 34%.

This comparison shows that at constant values of field excitation and total current, the loss in peak torque with 4 groups compared with that in 6 groups is marginal. Working with 4 groups is similar to having the star winding explained in Section 2.6, p. 52. This type of winding requires only moderate values of voltage and current, compared to the ring and star-connected windings.

3.3.3 Torque measurements using a digital voltmeter

The developed torque can also be deduced from the output voltage of the 100 Hz filter unit while the rotor is moved manually with the torque-arm. The tests were performed with the ring commutated-winding supplied via the commutator and brushes.

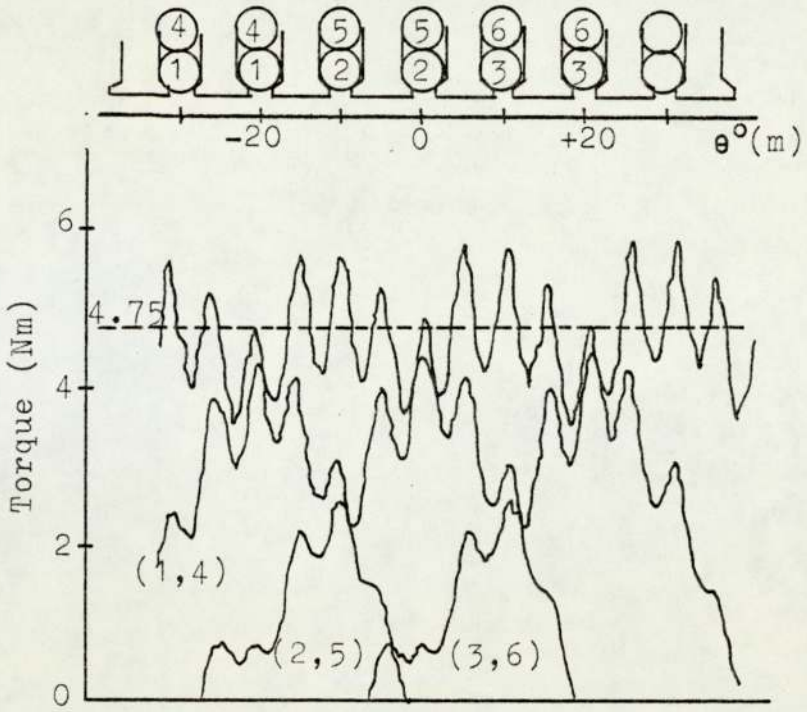

ring winding excited, F_f = 450 At, I_a = 2.6 A
F_a = 780 At/120°(m)

Fig. 3.17 X-Y recorder torque waveforms, Test (5)

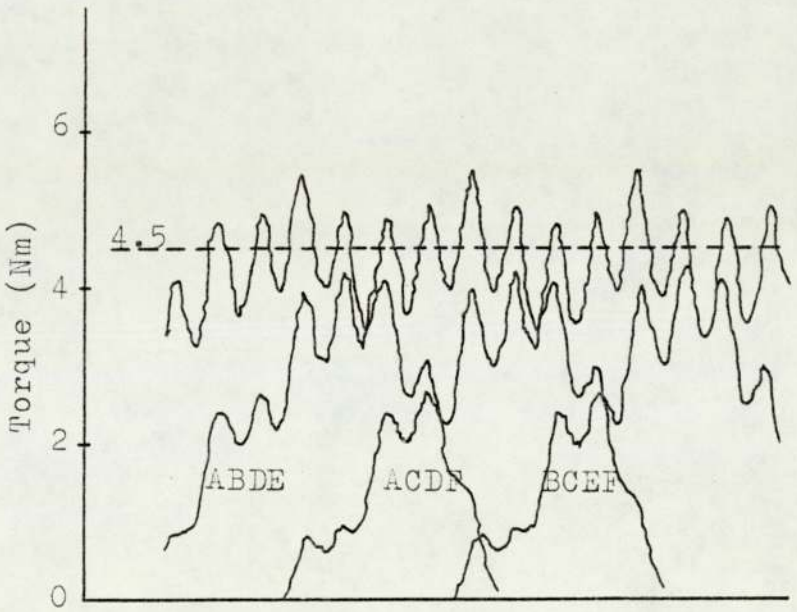

four coil groups excited, F_f = 450 At, I_a = 2.6 A
F_a = 520 At/120°(m)

Fig. 3.18 X-Y recorder torque waveforms, Test (6)

The values of torque measured correspond to successive points on a torque waveform of Fig. 3.16, p. 80, at a particular excitation. These values are plotted in Fig. 3.19 against θ, and the resultant waveform over 20°(m) is similar to that in Fig. 3.16 for the range of θ indicated.

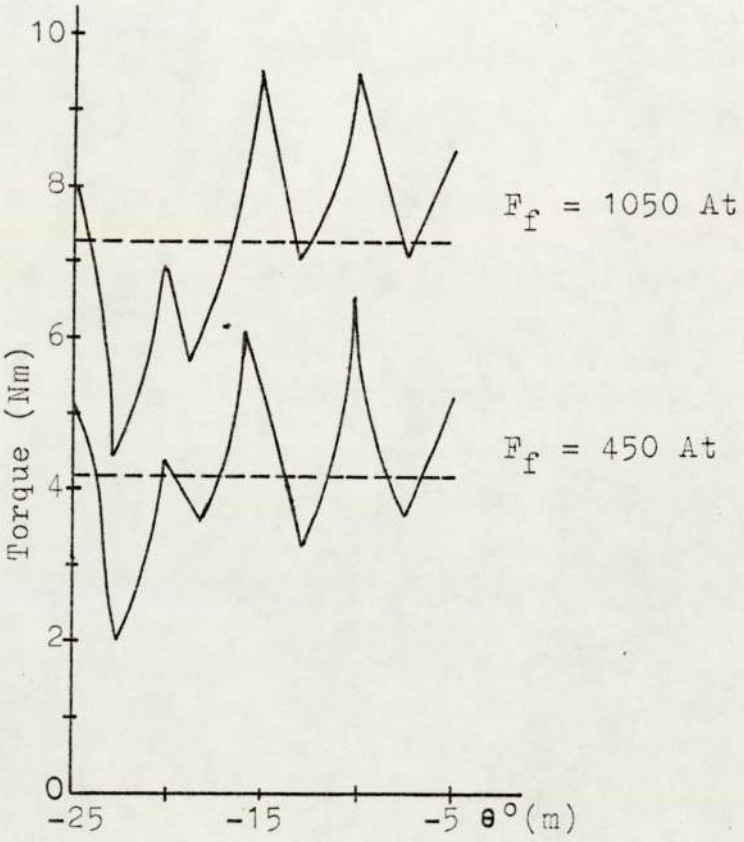

V_s = 50 V, F_a = 1005 At/120°(m), I_a = 3.35 A

Fig. 3.19 Torque variations using a DVM

Mean torque depends upon the point at which transition from one torque waveform to another occurs. Table 3.3 gives the mean value of torque at three different transition angles and two values of excitation, F_f. The three ranges of θ are marked in Fig. 3.15 curve (ii) for F_f = 450 At.

Range	θ°(m) setting	Mean torque per 20°(m) (Nm)	
		450 At	1050 At
I	-25	4.18	7.28
II	-19	4.08	8.01
III	-15	4.73	8.41

V_s = 50 V, I_a = 3.35 A, ring winding supplied via brushes, poles staggered and chamfered.

Table 3.3 Mean torque versus θ

The mean values of torque T_{mean} given in Table 3.3 are determined by measuring the area under the torque curve (e.g. Fig. 3.19 for $\theta = -25^{\circ}$). Fluctuations due to slot reluctance torque are appreciable, especially at low field excitations. Hence T_{mean} cannot be expected to vary linearly with θ nor to vary with θ in the same way at the two values of excitation.

3.3.4 Dynamic torque measurements

Dynamic torque was obtained as the voltage output of a strain-gauge bridge mounted on a hollow shaft, with the machine driven by a d.c. motor at a constant mean speed. Since an oscilloscope was used to display the torque waveforms, the graticule was calibrated in Nm/div. The traces shown in this section complement the curves and traces given in the preceding three sections as static measurements.

To minimise the smoothing effect of the moment of inertia, the traces were obtained at a low mean speed of about

70 rev/min. At low speeds the stepping action of the field due to the commutated coils current causes a noticeable cyclic variation of speed about a mean value. Hence to obtain a true variation of developed torque with angular position, the horizontal sweep of the oscilloscope was provided by a rotor-position-dependent voltage; the same arrangement as shown in Fig. 3.11, p. 74, for the X-Y recorder.

The output voltage from the 1 kΩ wirewound potentiometer is shown in Fig. 3.20a over one revolution where the departure from a linear rise with position is evident. This is demonstrated more clearly by differentiating (approximately) the displacement trace to give the trace in Fig. 3.20b, which shows the change in speed over approximately one revolution. The circuit of Fig. 3.21 was used.

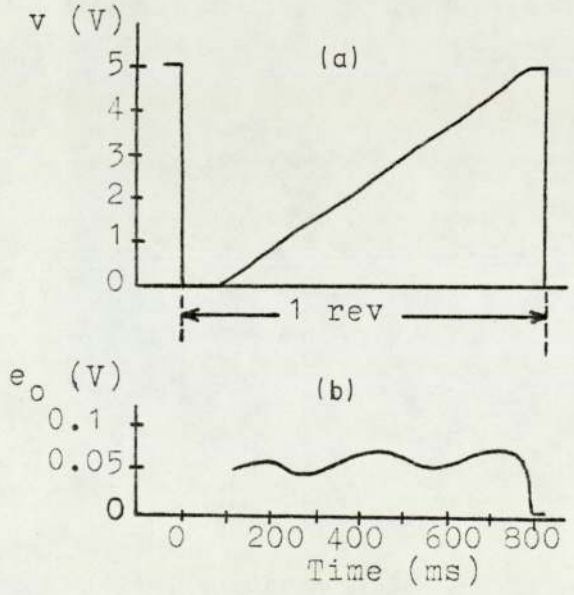

Fig. 3.20 Potentiometer output voltage and its derivative

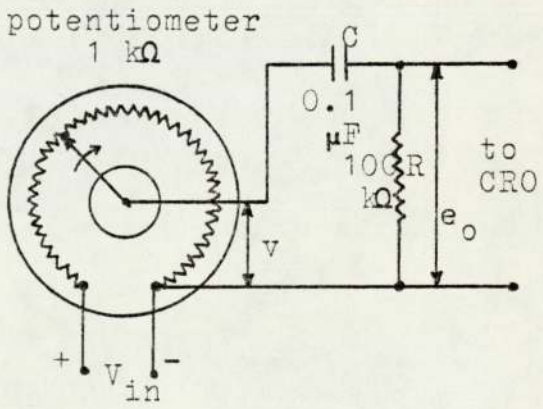

Fig. 3.21 Potentiometer connection for speed measurement

The voltage balance equation is:

$$v = (1/C)\int idt + iR \qquad (3.3)$$

Differentiating and rearranging the result:

$$e_o = RC\left(\frac{dv}{dt} - \frac{de_o}{dt}\right) \qquad (3.4)$$

The second term of Equation (3.4) only affects the start of the trace and otherwise can be neglected. The output voltage e_o is, therefore, proportional to the rate of change of v.

The maximum and minimum slopes of the curve in Fig. 3.20a are determined along with an average value over one revolution. These 3 values are given in Table 3.4 as volts per second. Values of speed at maximum and minimum slopes can be calculated by direct proportion with the mean experimental speed of 72.3 rev/min. Since fractions of a revolution are involved, the speed in Table 3.4 is also given in radians per second.

Value	Slope (V/s)	Speed n	
		(rev/min)	(rad/s)
Maximum	7.76	78.6	8.23
Average	7.14	72.3	7.57
Minimum	5.37	54.4	5.69

Table 3.4 Speed values from potentiometer output (values referring to Fig. 3.20a)

It is noted from the values of speed in Table 3.4 that the fluctuation between maximum and minimum is 2.54 rad/s. The average value is approximately 26% of this difference

below the maximum value and 74% above the minimum value.

The waveform of e_o given in Fig. 3.20b shows a difference between maximum and minimum values of 0.0225 V. Since the time constant of the differentiator in Fig. 3.21 is 0.01 s, the fluctuation in input causing this difference is 0.0225/0.01 = 2.25 V/s. This value is within 6% of the difference between maximum and minimum slopes in Table 3.4.

Input voltage V_{in} to the potentiometer equals 5.0 V, and therefore, the total change between zero and 5.0 V in Fig. 3.20a results in a change in Fig. 3.20b of 0.05 V, (RC = 0.01 s). This agrees with the average value of the curve in Fig. 3.20b.

The 1 kΩ potentiometer was later replaced by a toothed copper disc (353 mm diameter, 360 teeth) mounted on the shaft at the opposite drive end as seen in Photograph 4b. Signals from two opto-switches at the edge of a disc are fed to a staircase generator circuit to produce a rotor-position-dependent output signal.

Another advantage of working at a low speed in the following tests is in reducing the eddy-current torques associated with rotation. In any case, the mechanical construction of the potentiometer limits operation to low speeds.

The traces in Figs. 3.22 and 3.23 show the effect of excitation on the number of peaks per revolution in the torque waveform. The number of coil groups of the commutated-winding excited in each trace is different, and is treated separately.

(i) Coil groups A and D only:

Fig. 3.22 shows traces of the torque produced at three different values of field excitation. When the excitation is zero, as in (a), torque reaches the maximum value at 60° intervals of rotor position. The reason is that developed torque is saliency torque, and the successive axes of the coils excited, giving rise to this torque, are separated by 60°(m).

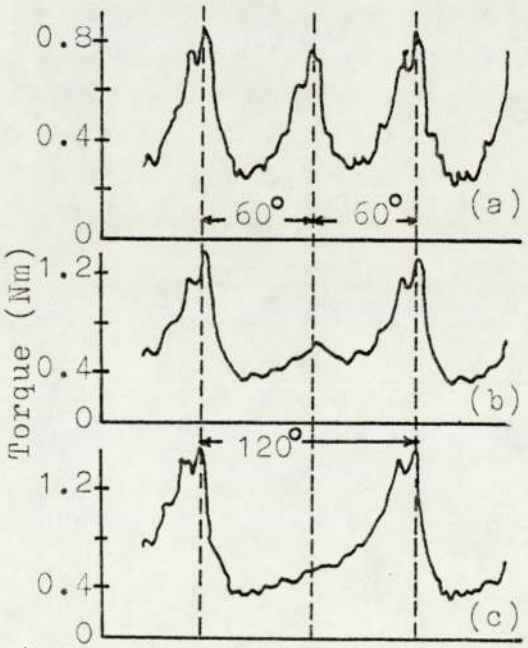

(a) F_f = 0
(b) F_f = 127 At
(c) F_f = 285 At

F_a = 260 At/120°(m)

Fig. 3.22 Torque due to coil groups A and D, I_a = 1.3 A

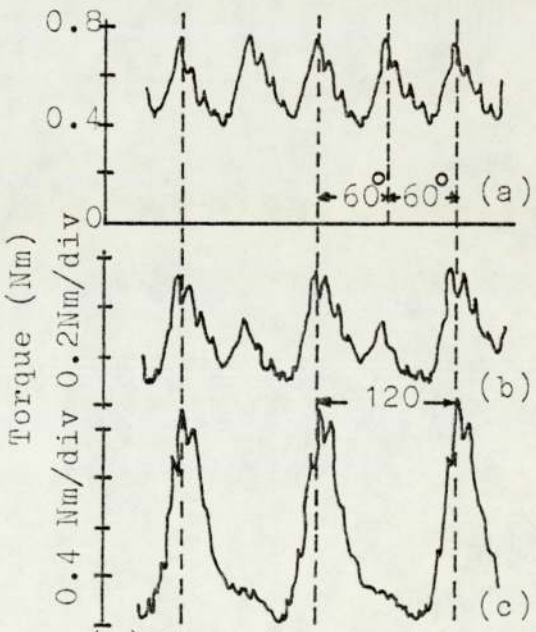

(a) F_f = 0
(b) F_f = 53 At
(c) F_f = 500 At

F_a = 390 At/120°(m)

Fig. 3.23 Torque due to ring winding, I_a = 1.3 A

At low values of field excitation, the 'BℓIr' torque developed assists certain peaks of saliency torque while reducing alternate ones. This is apparent in (b). Further increase in excitation as in (c) gives a peak torque twice that in (a), and alternate peaks are eliminated so that those remaining are 120°(m) apart. In terms of flux direction, the flux due to field excitation coincides with that from the commutated coils over 60° and opposes it over the following 60°.

The traces in Fig. 3.22 cannot be compared directly with curves obtained by weights or X-Y recorder due to the unrestricted rotation of the rotor. Since the machine is driven externally by a motor, developed and motor torques aid and oppose each other over successive arcs of rotor position.

Peak torque is more pronounced in the waveforms of Fig. 3.22 than in the X-Y recorder waveforms, but a comparison shows lower values of dynamic torque under equivalent excitations. For example, the torque for the conditions in Fig. 3.22c is determined from the value of torque in Fig. 3.13iii, p. 77, i.e.,

$$T = 2.65 \left(\frac{0.290}{0.425}\right) = 1.8 \text{ Nm}$$

Since the commutated coils m.m.f. is constant at 260 At, the ratio of torques is the same as the ratio of the air-gap flux-densities. However, the measured peak value from Fig. 3.22c is about 75% of 1.8 Nm. Torque requirements

for mechanical and eddy-current losses account for the difference between calculated and measured values of torque.

(ii) Complete ring winding:

Waveforms of torque were obtained at various values of excitation with the supply connected to diametrically opposite tappings of the ring winding. These waveforms are shown in Fig. 3.23 for one revolution and can be compared with the waveforms of Fig. 3.22. At zero excitation (trace a) the 6 peaks are due to saliency torque and are separated by 60°. As the field excitation is increased, alternate peaks are reduced and eventually eliminated as in traces (b) and (c).

For the same direction of rotation, the rate of change of developed torque is different in Fig. 3.22 from that in Fig. 3.23. The fast drop with two coil groups excited and the steep rise with the complete winding excited, are both due to the position of peak torque with respect to the position at zero torque.

Fig. 3.24 shows idealised torque waveforms for 2 and 6 coil groups excited. Positions (x) of peak torque and (y) of zero torque are determined from Figs. 3.13iii and 3.16iii, pp. 77 and 80. These positions depend on the flux-density distribution in the air-gap as will be seen from flux measurements in Section 3.7 (v. Figs. 3.59 and

3.61, pp.140 and 142). At positions (y), the air-gap flux-density distribution is symmetrical about the pole centre-line, and hence the net developed torque is zero, whereas at positions (x), flux-density at one pole-tip is maximum while it is minimum at the other pole-tip.

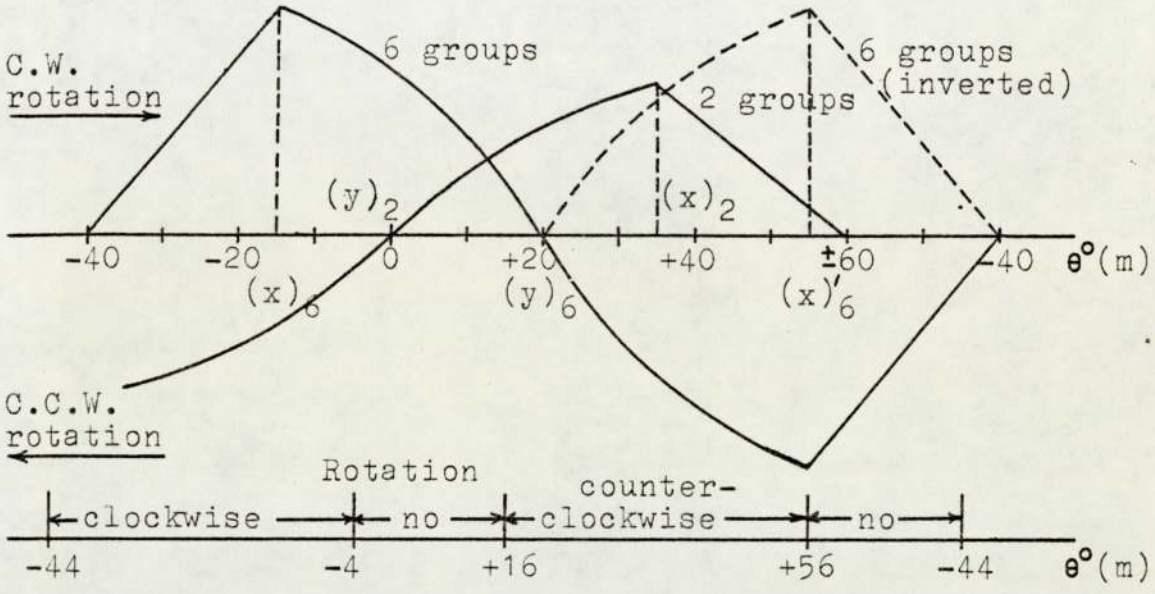

Fig. 3.24 Idealised torque waveforms: 2 and 6 coil groups excited (field coil also excited)

The 20°(m) shift between the (y) positions of the two curves corresponds to the shift between the axes of flux produced by the coils excited in both cases. For one direction of rotation, the preferred rotor positions (y) are on opposite sides of the peak positions (x) for the two curves. But if the field current is reversed in the case of 6 groups, the dashed curve in Fig. 3.24 is obtained. Thus the same angular shift is seen between the (x) and (y) positions, and also the two positions occur successively in the same direction of rotation.

3.3.4.1 Operation with a mechanical commutator

It was seen from Section 3.3.2, p. 74, that to obtain the maximum possible torque from the motor, either the current direction in certain coil groups must be changed or different groups must be connected as the rotor position changes. This is equivalent to the transition from one waveform to another in Figs. 3.17 and 3.18, p. 82.

The transition from one waveform to another is performed in the case of the ring winding by the mechanical commutator explained in Section 3.2, p. 61. The maximum speed of rotation is limited to 300 rev/min as the mechanical construction of the brush gear results in discontinuous contact at higher speeds. Owing to the shape of the brushes, the contact area with the segments is very small, thus placing a limit on the current to the winding.

The position at which the brush-arm is fixed to the shaft determines the portion of the torque waveform for the given tapping that is being connected to the supply. Since each commutator segment subtends $20^{\circ}(m)$, the portion of torque waveform considered also extends over $20^{\circ}(m)$.

It was found experimentally that a net torque can be developed only in the two zones indicated at the bottom of Fig. 3.24, with 6 groups excited (i.e., complete ring winding). Elsewhere, the reluctance torque is sufficient to cause cogging and thus prevent rotation.

In this test the machine is still driven with the direction of rotation opposite the preferred direction of the developed torque. Fig. 3.25a shows a torque waveform with the brushes set at $\theta = -25^{\circ}(m)$. At the same setting, another waveform was obtained using the X-Y recorder by placing complete waveforms side by side as outlined in Section 3.3.2, p. 74. The resultant waveform is shown in Fig. 3.25b. The same procedure is followed in constructing the waveform in Fig. 3.25c from that of Fig. 3.10, p. 73, obtained with weights.

The mean torques of the three waveforms in Fig. 3.25 can be related to each other via air-gap flux-density and commutated-winding ampere-turns. If the mean torque, T_a, in curve (a) is taken as 2.1 Nm, then T_b and T_c for curves (b) and (c) respectively are

$$T_b = 2.1 \left(\frac{0.425}{0.460}\right)\left(\frac{780}{300}\right) = 5.0 \text{ Nm}$$

and $$T_c = 2.1 \left(\frac{0.64}{0.46}\right)\left(\frac{702}{300}\right) = 6.8 \text{ Nm}$$

the above calculated values are in good agreement with the values read from curves (b) and (c).

Load tests using the mechanical commutator at various values of brush angle, excitation, and supply voltage are discussed in Section 3.6, p. 118.

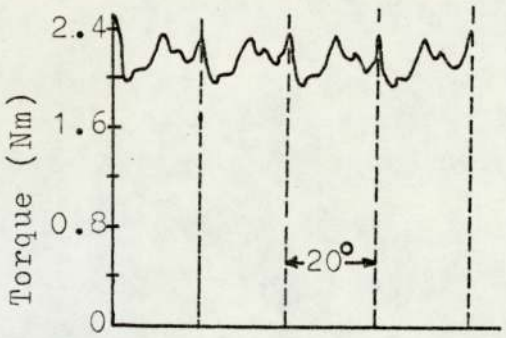

(a) F_f = 500 At, F_a = 300 At/120°(m),
θ = -25°, I_a = 1.0 A

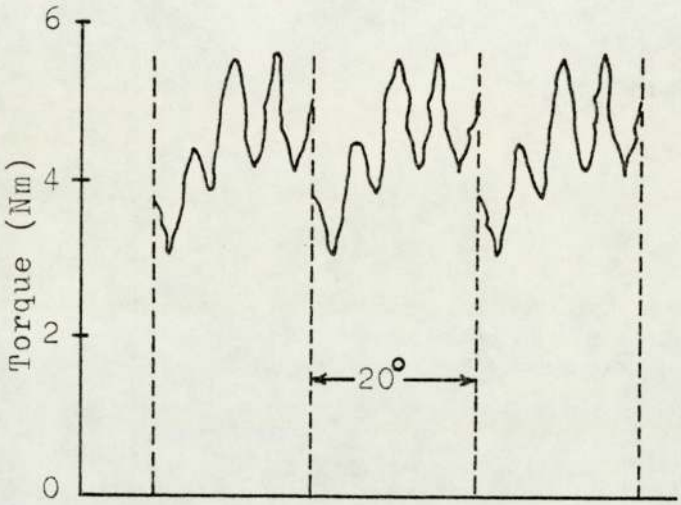

(b) F_f = 450 At, F_a = 780 At/120°(m),
θ = -25°, I_a = 2.6 A, (v. Fig. 3.15, p.80)

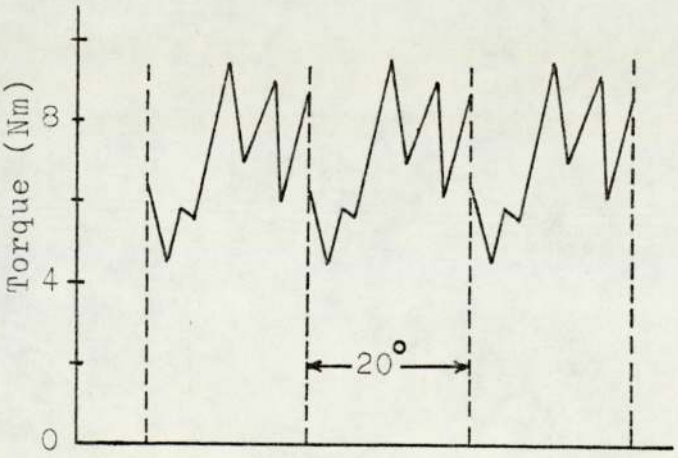

(c) F_f = 1050 At, F_a = 702 At/120°(m)
θ = -25°, I_a = 2.34 A, (v. Fig. 3.10, p.73)

Fig. 3.25 Torque waveforms with commutator

3.4 Induced e.m.f.

In this section as well as in the following sections, the commutated-winding excited is the complete ring winding. The tappings are connected to the commutator segments and the brush-arm is set at various positions with respect to the rotor.

In Section 3.2.1, p. 61, γ was introduced as the angle of separation between pole and winding axes. For a ring winding, angle γ is more suitable than θ and hence will be used throughout. ($\gamma^{o}(m) = \theta^{o} + 5^{o}$)

The waveforms of the e.m.f. induced in the stator search-coils and in the commutated-winding coils are given in Section 3.4.1 and the effect of the different types of pole on these waveforms is discussed.

Measurements of the r.m.s. values of the e.m.f. between opposite tappings and between brushes were made and the results are given in Section 3.4.2. The e.m.f. between brushes was measured at various values of brush-arm setting, i.e. angle γ. The effect of staggering and chamfering the poles on the waveforms and values of e.m.f. is also discussed in this section.

3.4.1 The e.m.f. waveforms

The e.m.f. waveforms shown in this section were obtained with the machine driven at constant speed and only the field coil excited. The waveforms are of the e.m.f. induced in search-coils and in the coils of the commutated-winding. Three different types of the 58°-arc rotor poles were used and the corresponding figure numbers are given in Table 3.5.

Parameter	Aligned poles (Type A)		Staggered poles		Staggered and chamfered poles (Type C)	
	Fig.	Page	Fig.	Page	Fig.	Page
e.m.f. in search-coil around tip of one tooth	3.26a	97	3.26a	97	3.29a	100
e.m.f. in search-coil around base of 6 teeth	3.26b	97	3.26b	97	3.29b	100
e.m.f. across coil group(s)	A_1 3.26c	97	A_1+A_2 3.27a	98	-	-
e.m.f. between opposite tappings of ring winding	3.26d	97	3.27b	98	3.29c	100

Table 3.5 The e.m.f. waveforms (F_f = 1050 At, n = 278 rev/min)

Fig. 3.26a shows the waveform of the e.m.f. induced in a search-coil, wound around the edge of one stator tooth adjacent to the air-gap. The peak value of e.m.f. is induced when either pole-tip only partly 'covers' the coil. The lower peak is obtained when the pole-tip starts to cover the coil, and the higher peak when it leaves the coil. The e.m.f. of either polarity can be determined from $N\frac{d\phi}{dt}$ while the flux linkage is changing

between zero and maximum value. Following that, the only change in flux linkage is due to the pole-tips crossing slot openings. This creates minor hysteresis loops which result in a higher value of flux per tooth when the pole eventually leaves the coil. Since a pole-tip takes the same time in crossing a coil in both covering or leaving the coil, the peak e.m.f. is higher when leaving the coil due to the larger flux linkage. When the coil is in the interpolar zone, there is hardly any flux linkage and, therefore, the induced e.m.f. is practically zero.

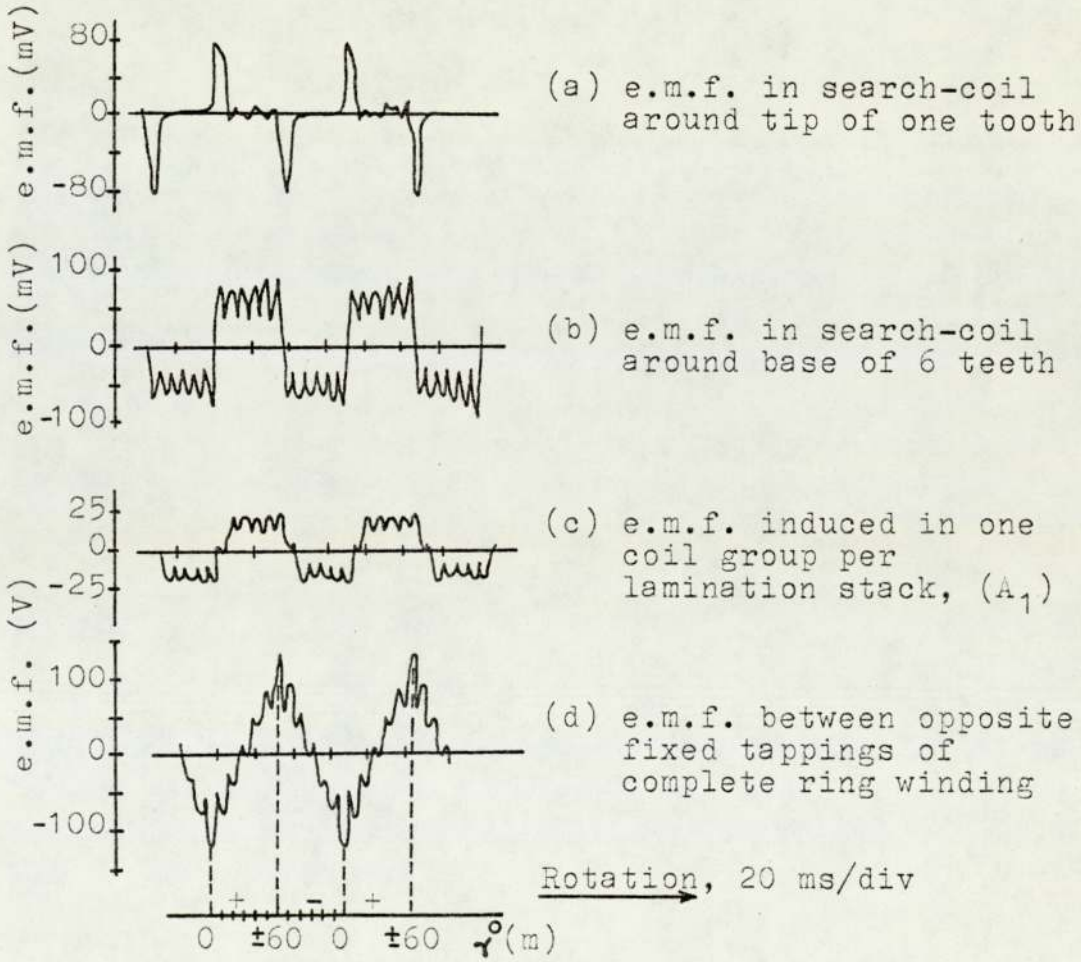

F_f = 1050 At, n = 278 rev/min, aligned 58° -arc poles

Fig. 3.26 Waveforms of e.m.f. with aligned poles

The waveform of e.m.f. between diametrically opposite tappings of the ring winding is triangular with marked ripples due to slot harmonics as seen in Fig. 3.26d. The principal slot harmonics are the 11th and 13th as seen from the results of an analysis given in Table 3.6.

Harmonic number	3	5	7	9	11	13
% of fundamental	12.7	5.7	4.5	5.4	19.3	6.4

Table 3.6 Harmonic contents of Fig. 3.26d (all values are positive)

An enlarged diagram of the e.m.f. waveform of Fig. 3.26d near the peak is given in Fig. 3.28a. The amplitude of the triangular waveform is about 100 V and hence the fundamental is 81.1 V. Harmonics, therefore, constitute 130.0 - 81.1 = 48.9 V, or 60% of the fundamental. In Table 3.6, the total harmonic content constitutes 54% of the fundamental since harmonics up to the 13th only are included.

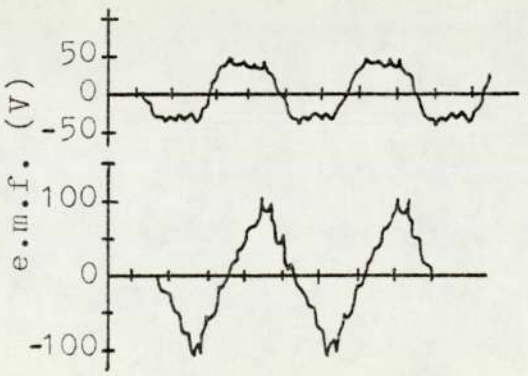

(a) e.m.f. induced in two coil groups in series, $A_1 + A_2$

(b) e.m.f. between opposite fixed tappings of the complete ring winding

Rotation, 20 ms/div

F_f = 1050 At, n = 278 rev/min

Fig. 3.27 Waveforms of e.m.f. with staggered poles

As seen in Fig. 3.27, staggering the poles by $\frac{1}{4}$ slot-pitch about a mean axis results in a noticeable reduction in the ripple. The amplitude of the equivalent trapezoidal waveform of Fig. 3.27b is about 90 V and hence the fundamental is $h_1 \frac{96}{11\pi^2} \cos \frac{\pi}{24} = 90(0.8767) = 78.9$ V, (v. Fig. 3.28b). The peak value of e.m.f. is about 110 V, and therefore, the harmonic content is 110 - 78.9 = 31.1 V or 28.3% of the fundamental which is less than half the value for aligned poles. The reduction in slot harmonics is also apparent in the waveform of the e.m.f. induced in the coil group(s) (Fig. 3.27a vs. Fig. 3.26c).

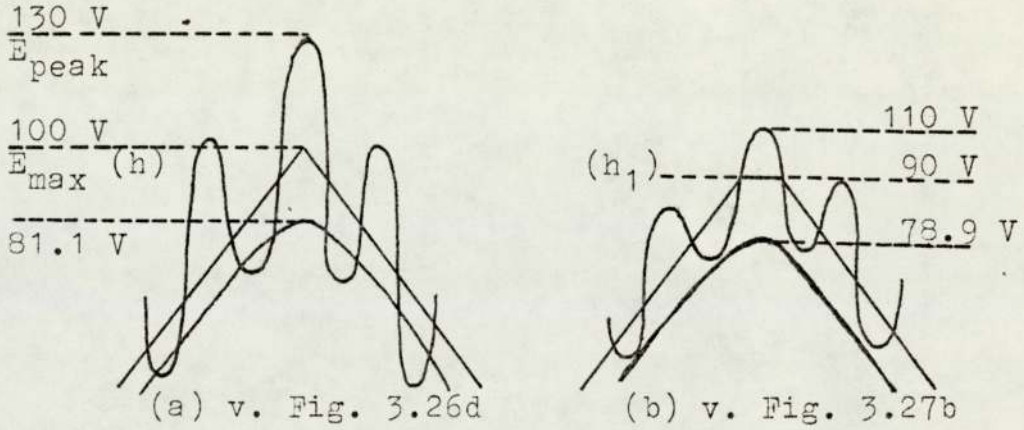

Fig. 3.28 Enlarged e.m.f. waveforms

Chamfering the poles as in Fig. 2.8, p. 34, results in the waveform of e.m.f. between opposite tappings shown in Fig. 3.29c. Here too, the amplitude of the fundamental of the trapezoidal waveform is 78.9 V, but the peak e.m.f. value is 95 V. The harmonic content, therefore, is only 16.1 V or 16.9% which is about a quarter the value for aligned poles.

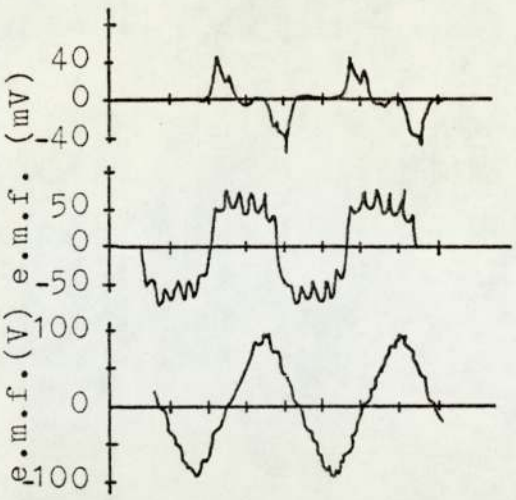

(a) e.m.f. in search-coil around tip of one tooth

(b) e.m.f. in search-coil around base of 6 teeth

(c) e.m.f. between opposite fixed tappings of the complete ring winding

Rotation, 20 ms/div

F_f = 1050 At, n = 278 rev/min

Fig. 3.29 Waveforms of e.m.f. with staggered and chamfered poles

Figs. 3.29a and b show a reduction in the e.m.f. induced in the stator search-coils shown in Figs. 3.26a and b, p. 97, due to the smaller rate of change of flux linkage at the pole-tips. Chamfering also accounts for the rounded corners of the waveform in Fig. 3.29b, i.e., a reduction in the higher order harmonics.

3.4.2 Measurements of e.m.f.

The r.m.s. values of the e.m.f. induced between opposite tappings of the ring winding and between brushes were measured with an electrodynamometer voltmeter while the machine was driven at a constant mean speed. The measurements were performed at various values of field excitation (both polarities) with aligned and staggered rotor poles.

A dynamometer voltmeter was used in these measurements for two reasons: it gives the same indication for a given continuous voltage as with the effective (r.m.s.) value of an alternating voltage, and it shows errors less than 0.5% up to 600 Hz. Thus error is minimised in measuring the e.m.f., which contains appreciable amounts of higher order harmonics. Measuring the mean value instead of the r.m.s., say with a moving-coil instrument, would not highlight the differences between aligned and staggered poles.

In measuring e.m.f. between brushes, tests were performed at various values of brush setting, i.e. separation angle γ between pole and winding axes. These angles refer to the commutated-winding coils at the opposite drive end (ODE) of the machine for both types of pole. However, with staggered poles, γ at the drive end (DE) is actually 5°(m) ahead of that at the ODE in the direction of rotation.

Prior to each measurement, the iron of the machine was demagnetised by cyclic reversal of the field current whilst reducing its value to zero. Errors due to remanent magnetism are thus minimised.

3.4.2.1 Induced e.m.f. between opposite fixed tappings

The tests in this section were intended to give an idea of the dependence of induced e.m.f. on excitation in both

value and polarity. Induced e.m.f. was recorded at a constant mean speed of 1000 rev/min as the field excitation was increased to a maximum of about 1200 At, and again as it was reduced to zero. This procedure was repeated with the field current reversed. The results are plotted in Fig. 3.30.

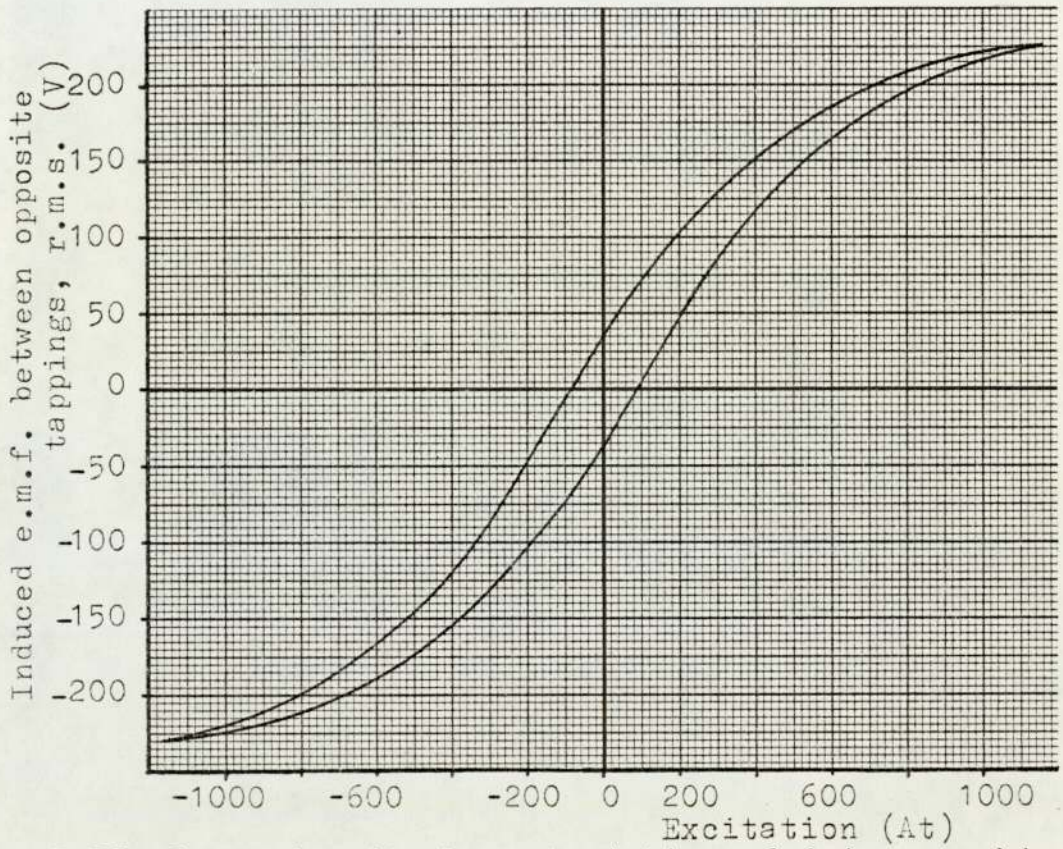

Fig. 3.30 Open-circuit characteristics of driven machine
n = 1000 rev/min, poles aligned, 58° arc

Fig. 3.31 shows the variation in r.m.s. value of e.m.f. against excitation of one polarity with aligned and staggered poles. From the e.m.f. waveforms in Section 3.4.1, p. 96, it was seen that staggering the poles reduces the slotting harmonics in the waveforms. This causes a corresponding reduction in the r.m.s. value of e.m.f. as in the case of an ideal machine.

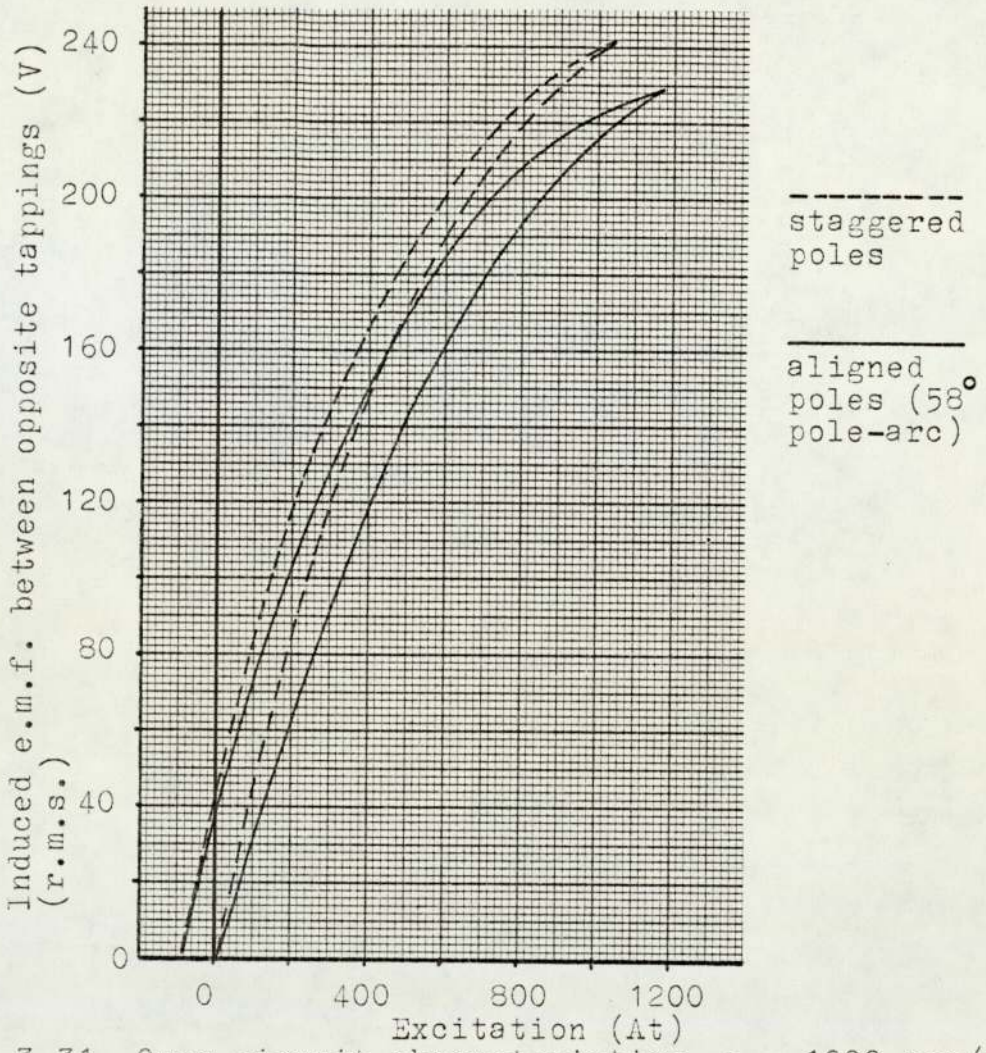

Fig. 3.31 Open-circuit characteristics, n = 1000 rev/min

However, the experimental curves in Fig. 3.31 show an increase in the r.m.s. value for staggered poles, which becomes larger as the value of excitation is increased, e.g., an increase of about 9% at 1050 At. This appears to be of magnetic origin but is otherwise inexplicable.

Table 3.7 gives the r.m.s. values of e.m.f. from Fig. 3.31 at several values of excitation for aligned poles. At the same values of excitation, the average air-gap flux-density, B_g, is read off from Fig. 2.20, p. 51, and the ratio of $E_{r.m.s.}$ to B_g is then determined.

F_f (At)	$E_{r.m.s.}$ (V)	B_g (T)	$E_{r.m.s.}/B_g$	$E_{max}/E_{r.m.s.}$
400	120	0.39	307.7	1.86
600	162	0.515	314.6	1.82
800	197	0.59	333.9	1.71
1050	222	0.64	346.9	1.65

Table 3.7 Flux-density and e.m.f. ratios
(n = 1000 rev/min, aligned poles)

The maximum value of the equivalent triangular waveform (E_{max}) for a ring winding equals $6e_g$ where e_g is the e.m.f. induced in one coil group (v. Fig. 2.24, p. 55). E_{max} is, therefore, determined from Equation (2.10), p. 55:

$$E_{max} = 36\ (2pn\ N\phi_p/60)$$

$$E_{max} = 36\ (6)(1000)(50)(3.29 \times \frac{58^\circ}{60^\circ} B_g)/60$$

$$E_{max}/B_g = 572.5 \qquad (3.5)$$

The ratio $E_{max}/E_{r.m.s.}$ can, therefore, be determined from Equation (3.5) and the values of $E_{r.m.s.}/B_g$ in Table 3.7. The results are given in Table 3.7 also.

This ratio can be determined experimentally at one value of excitation (1050 At) from Fig. 3.28a, p. 99, corrected to 1000 rev/min. Thus

$$E_{max}/E_{r.m.s.} = 100\ (\frac{1000}{278})/222 = 1.62$$

which is about 2% less than the calculated value.

In Appendix A7, the ratio $E_{max}/E_{r.m.s.}$ is mathematically determined as 1.73. Naturally the value of $E_{r.m.s.}$ in

this ratio does not include the slotting harmonics as is the case for the values in Table 3.7.

When staggered poles are used, the ideal e.m.f. waveform should be a trapezoidal waveform as seen from Figs. 3.27b or 3.29c, pp. 98 and 100. From Appendix A7, the ratio $E_{max1}/E_{r.m.s.}$ is equal to 1.604 where E_{max1} is the maximum value of the trapezoidal waveform and is equal to 91.7% E_{max} of the triangular waveform.

As seen in Fig. 3.28a, the peak value of the e.m.f., E_{peak}, is considerably higher than the maximum value of the triangular waveform, E_{max}. The ratio $E_{peak}/E_{r.m.s.}$ is determined in Appendix A7 as 2.12, assuming that the 11th and 13th harmonics are equal and together constitute the total harmonic at the peak of the e.m.f. waveform. If n is 12 slots per 120°(m), then the $n \pm 1$ harmonics are the slot harmonics which are the largest components.

3.4.2.2 Induced e.m.f. between brushes

Waveforms of the e.m.f. induced between the brushes are shown in Figs. 3.32 and 3.33 for aligned and staggered poles respectively.

These waveforms are actually 20°(m) repeated sections of the waveform of the e.m.f. induced between opposite tappings. The initial setting of the brush-arm with respect to the rotor determines which section of the

waveform is being considered. This is denoted by γ, the angle of separation between the pole and commutated-winding axes at the start of each section, i.e., when the brushes are connected to a pair of tappings via commutator segments. Comparison with Fig. 3.26d, p. 97, shows that to be consistent for the angles of γ considered, the sign of the e.m.f. waveforms in Fig.3.32 is negative.

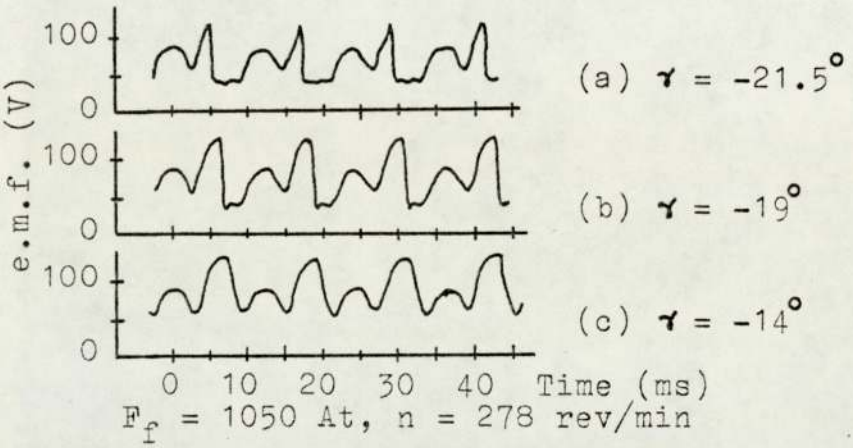

Fig. 3.32 Waveforms of e.m.f. between brushes (poles aligned, 58° arc)

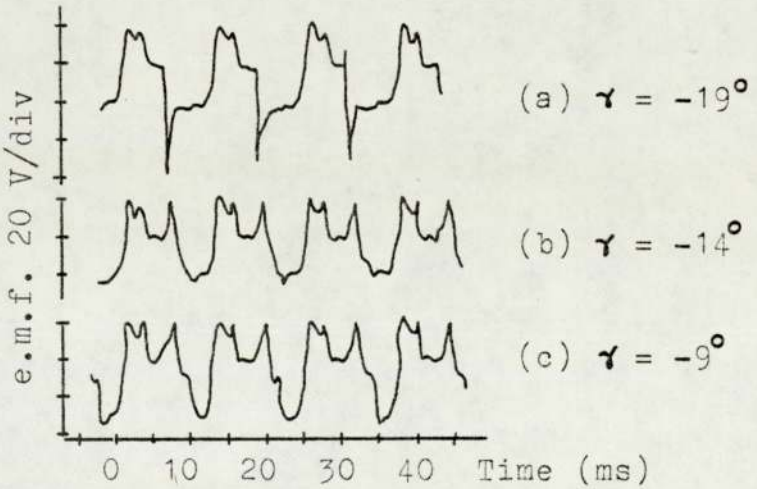

Fig. 3.33 Waveforms of e.m.f. between brushes (poles staggered) F_f = 1050 At, n = 278 rev/min

Fig. 3.33 shows waveforms of the e.m.f. between brushes with staggered rotor poles. The corresponding values of γ given, refer to those at the opposite drive end (ODE)

of the machine while at the drive end (DE), γ is 5°(m) ahead in the direction of rotation. Staggering the poles results in a considerable reduction in the ripple as seen from the waveforms and the values in Table 3.8.

γ°(m)	Aligned poles			Staggered poles		
	Fig.	$E_{r.m.s.}$	% ripple	Fig.	$E_{r.m.s.}$	% ripple
-21.5	3.32a	243	118	-	-	-
-19.0	3.32b	296	109	3.33a	300	91
-14.0	3.32c	337	85	3.33b	340	42
-9.0	-	-	-	3.33c	325	62

Table 3.8 Values of e.m.f. between brushes, (F_f = 1050 At, n = 1000 rev/min)

The values given in Table 3.8 for the ripple are $E_{max} - E_{min}$ as a percentage of the r.m.s. value of e.m.f. The highest r.m.s. values of e.m.f. and lowest percentage ripple for the two types of pole appear to occur at the same value of γ.

A theoretical comparison is carried out between the e.m.f. waveforms with the two types of pole. The assumption here is that the waveform of e.m.f. between opposite tappings is triangular with the slot harmonics neglected. Fig. 3.34 shows the triangular waveforms before and after staggering the poles as the sum of the two waveforms of height h/2, each corresponding to the winding in one lamination stack. The parameters of the waveforms given in Table 3.9 were determined at a different value of γ for the two types of pole. These values of γ result in a ripple in the waveform of e.m.f. between brushes that is

symmetrical about the peak value. Operation at these angles yields the highest mean and r.m.s. values of e.m.f. at a constant speed and excitation.

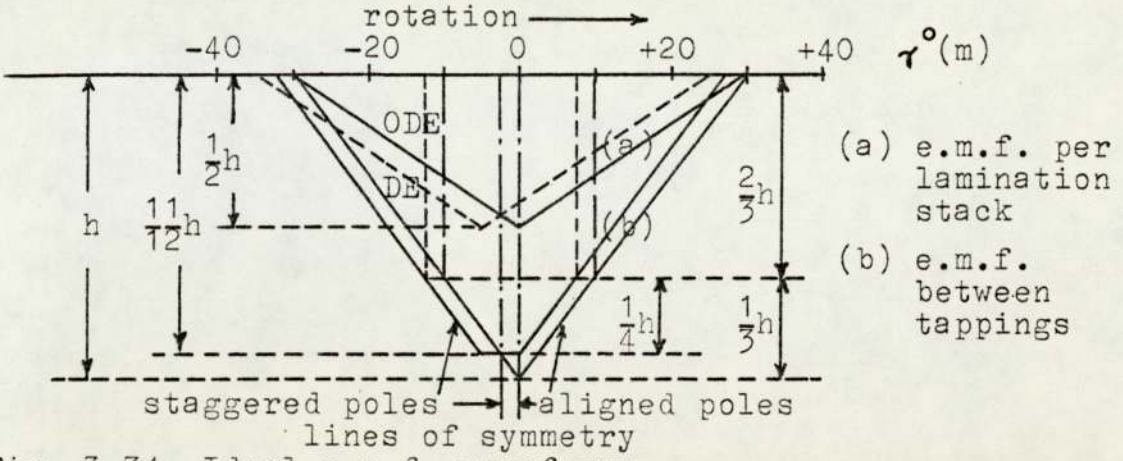

Fig. 3.34 Ideal e.m.f. waveforms

E.M.F. parameter		Aligned poles	Staggered poles
Maximum value between opposite tappings		h	0.917 h
Commutation angle, γ°(m)		-10	-12.5
Height of ripple		0.333 h	0.250 h
Ripple % of maximum		33.3%	27.3%
Mean value of ripple		0.167 h	0.156 h
E.M.F. between brushes	mean	0.833 h	0.823 h
	r.m.s.	0.839 h	0.827 h

Table 3.9 Parameters of waveforms in Fig. 3.34

Table 3.9 shows that if operation at a minimum ripple is desired, then decreases in the mean and r.m.s. values of e.m.f. are only 1.5% and 1.2%, respectively, when the poles are staggered.

The r.m.s. values of e.m.f. are plotted in Figs. 3.35 and 3.36 against excitation for aligned and staggered poles, respectively. In Fig. 3.35, the e.m.f. curves at γ equals -9° and -14° coincide with each other. The reason is that these values of γ are close to $\gamma = -10^{\circ}$ which gives the highest r.m.s. value of e.m.f. at a particular excitation. There is very little change in induced e.m.f. for 5° on either side of the position for which the waveform is symmetrical about the peak value.

The value of γ at which symmetry is retained with staggered poles is -12.5° as seen from Fig. 3.34. At this value of γ at the ODE, the equivalent value of γ at the DE is -7.5° since the poles at the DE are staggered by 5°(m) in the direction of rotation with respect to the poles at the ODE. Fig. 3.36 shows the r.m.s. values of e.m.f. between brushes with staggered poles versus excitation.

Figs. 3.37 and 3.38 show the variations in e.m.f. values with γ at the ODE at various values of excitation for aligned and staggered poles, respectively. Values of e.m.f. at constant excitation are only slightly higher with staggered poles over most of the values of γ. However, over the range of γ indicated, the effect of changing γ on the values of e.m.f. is less with staggered poles than with aligned poles.

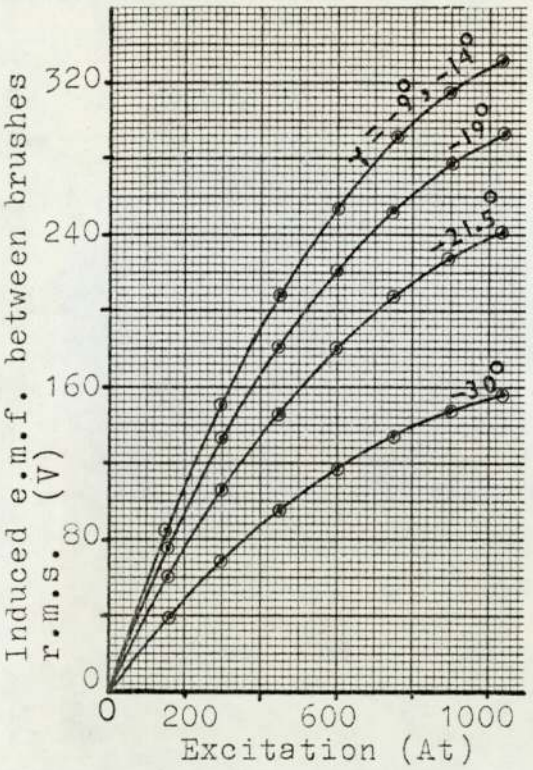

Fig. 3.35 E.M.F. vs. excitation, aligned poles

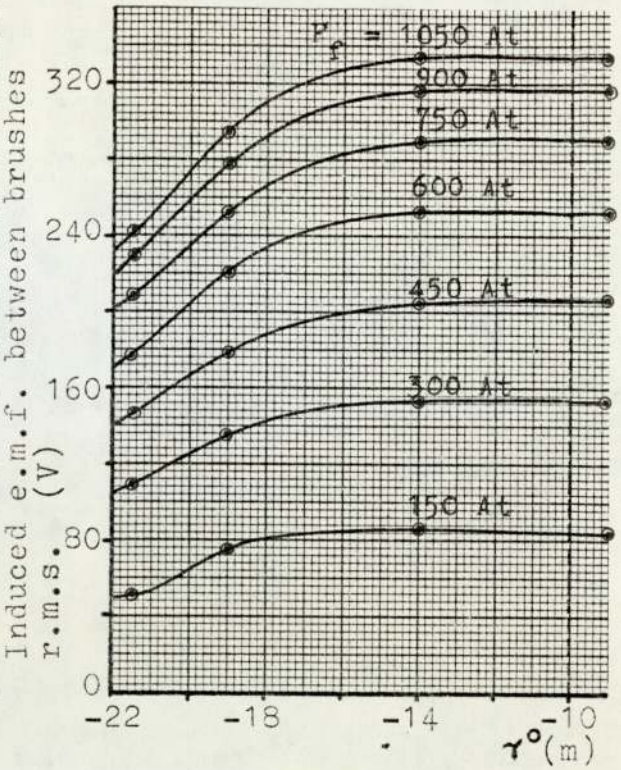

Fig. 3.37 E.M.F. vs. γ, aligned poles

n = 1000 rev/min

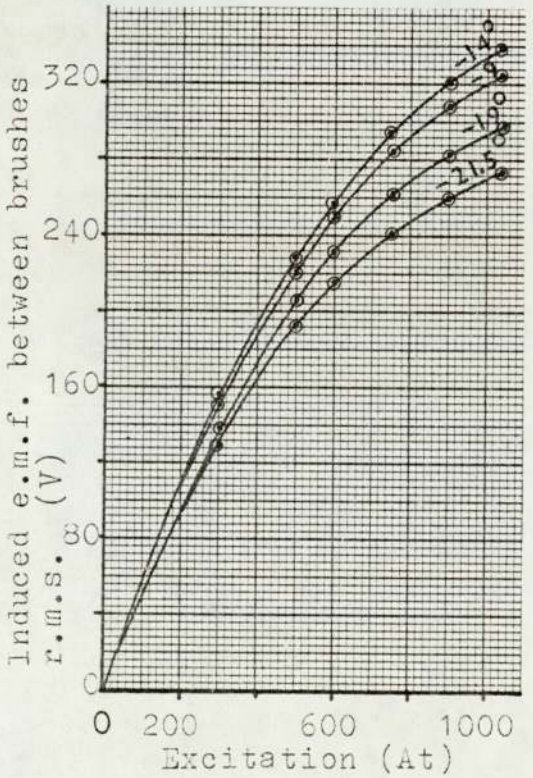

Fig. 3.36 E.M.F. vs. excitation, staggered poles

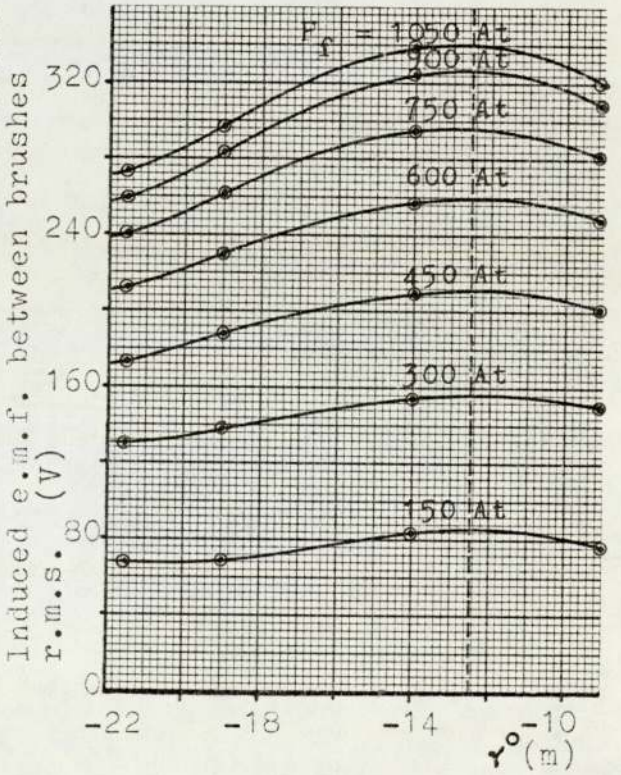

Fig. 3.38 E.M.F. vs γ, staggered poles

n = 1000 rev/min

At a constant excitation, say 1050 At, the r.m.s. values of e.m.f. at the axes of symmetry for the two types of pole are compared with each other. These values of γ, i.e. at -10° and -12.5° for aligned and staggered poles respectively, correspond also to the positions where minimum ripple occurs. It is noted that the r.m.s. value with staggered poles is higher than that with aligned poles by about 2.7%. This contradicts the prediction in Table 3.9.

The obvious difference between the two cases is in the e.m.f. waveform; a theoretical triangular waveform versus a waveform with slot harmonics. Also, changes in the magnetic circuit caused by staggering the poles can be responsible for the higher induced e.m.f. This was previously demonstrated in Fig. 3.31, p. 103, with the e.m.f. between opposite tappings.

The effect of magnetic saturation is seen in Figs. 3.37 and 3.38 as a smaller increase in e.m.f. with equal increments in the value of excitation.

3.5 No-load losses

On no-load, the losses are divided into mechanical, iron and electrical. The mechanical loss is determined by driving the machine with no current in either the field coil or commutated-winding, and the variation of the loss is shown in Fig. 3.39.

Exciting the field coil alone gives an indication of the iron loss at various values of field excitation and speed. The readings are plotted in Fig. 3.40 as the mechanical and iron losses versus speed.

The electric losses result from the field coil excitation, and the slight unbalance of the induced e.m.f.'s in the commutated-winding caused by differences in the coils and by magnetic unbalance. Field coil losses are determined from the coil resistance and current. The losses due to the commutated-winding circulating current are small and can be neglected - the induced e.m.f. between the open ends of the ring winding is 2.5 V at 300 rev/min with a field excitation of 1050 At. The power loss incurred at 1000 rev/min is only 2 watts.

3.5.1 Separation of mechanical losses

The mechanical losses of the machine can be divided into two parts: the bearing friction loss and the windage loss. Brush friction loss is not included in these tests since the brushes are lifted off the commutator.

Friction loss varies with n^y where n is the speed in rev/min and y is normally of the order of 1.5, depending upon lubrication and temperature rise of the bearings. Windage loss can vary with n^2 or n^3 and also depends upon the physical dimensions of the rotor. The surface of the rotor at the two ends consists of three polar projections

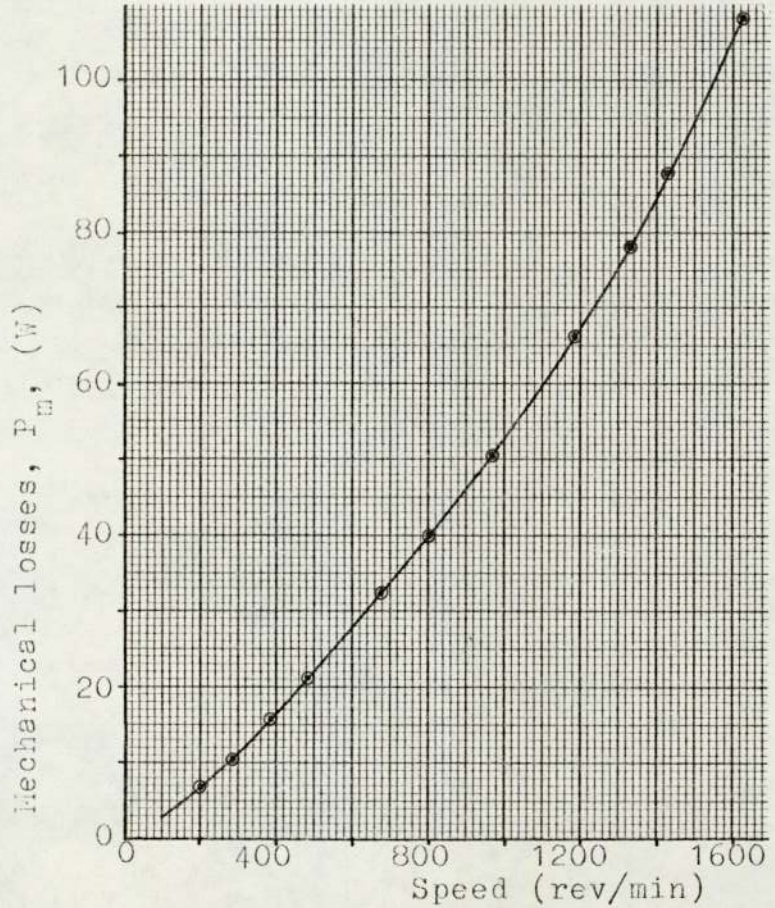

Fig. 3.39 Mechanical losses (without brushes)

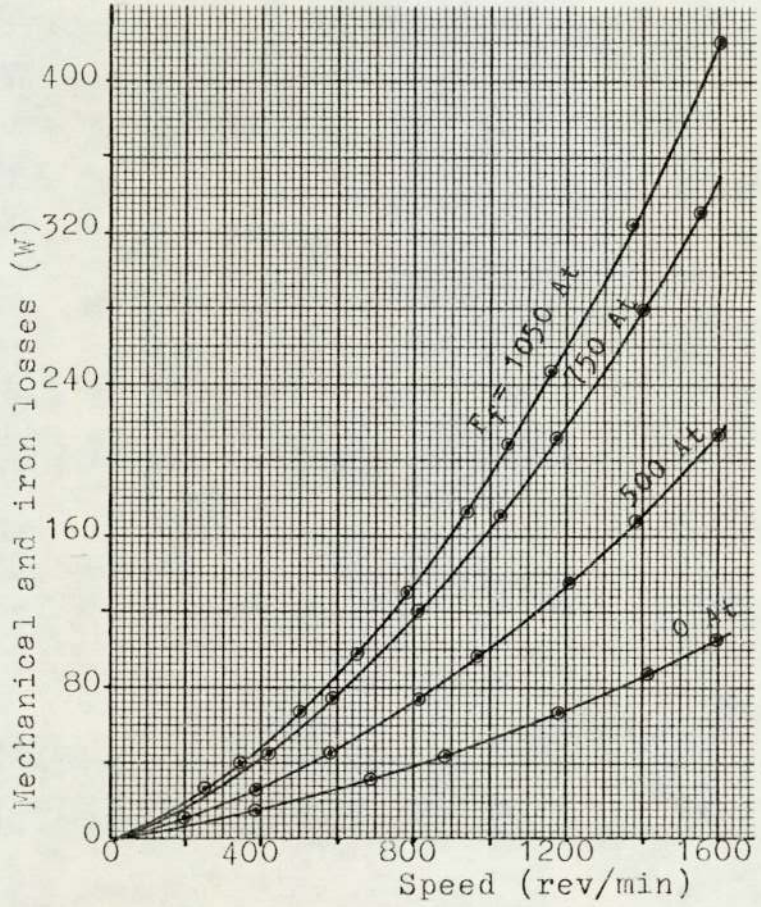

Fig. 3.40 Mechanical and iron losses (without brushes)

equally spaced around the core. The height of these projections is 15% of the rotor diameter at the air-gap, which is comparable to the ratio of slot depth to armature diameter in a conventional d.c. machine of similar diameter at the air-gap. Windage loss is normally a fraction of the friction loss especially in a small machine without a cooling fan.

Mechanical loss variations with speed are plotted in Fig. 3.39. For each of the following ranges of speed, the power loss is expressed as n^y, but at differing values of y.

$$\left.\begin{aligned} P_m &= 3.33 \times 10^{-3}\, n^{1.42} \qquad 0<n<500 \\ P_m &= 6.43 \times 10^{-3}\, n^{1.31} \qquad 500<n<1200 \\ P_m &= 0.30 \times 10^{-3}\, n^{1.74} \qquad 1200<n<1600 \end{aligned}\right\} \quad (3.6)$$

where P_m is in watts and n in rev/min. The changes in the value of y are attributed to the effect of windage which is included in the mechanical loss. For speeds below 100 rev/min, the mechanical loss can also be calculated from the friction torque (0.25 Nm) determined from the X-Y recorder waveforms in Fig. 3.13, p. 77.

3.5.2 Separation of iron losses

Iron losses result partly from flux pulsations due to (i) the movement of the pole-axis with respect to the commutated-winding axis and (ii) the change in reluctance as the pole-tips move across the teeth and slots. These losses are present in the lamination stacks and the poles

but not in the rotor-core and stator-yoke where the flux is uniform.

Since flux is unidirectional in the teeth, flux pulsations cause minor hysteresis loops. The number of these loops is three per revolution, corresponding to the three rotor poles. Iron loss in the teeth constitutes the major part of the loss in the stator laminations. Rotor pole movement causes rotational flux at the back of the teeth over an angle of almost 180°, but this results in a small power loss.

Iron loss in the poles depends upon the depth of penetration 'a' of flux pulsations at slot frequency.

$$a = \sqrt{\frac{2}{\omega \gamma \mu}} \qquad (3.7)$$

where the conductivity γ equals 7.82×10^6 S/m and the permeability μ is determined from the magnetisation characteristics at the particular air-gap flux-density. Values of 'a' are plotted against speed in Fig. 3.41 at two values of excitation corresponding to air-gap flux-densities of 0.46 T and 0.64 T.

The depth of penetration is not affected greatly by excitation since the flux-density in the poles does not normally reach saturation level. The maximum depth of penetration occurs at low speeds (60 to 70 rev/min) and is about 1 mm for a wide range of air-gap flux-density (0.46 T to 0.64 T). Hence the iron losses in the poles

due to slotting could be reduced by milling 1 mm grooves on the pole-face.

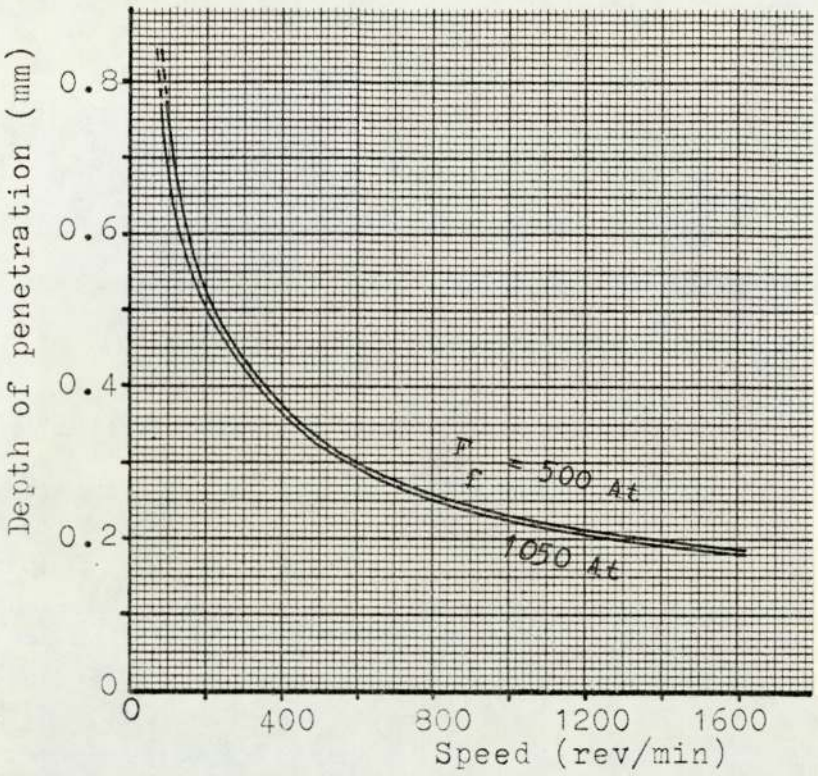

Note: Values of μ are based on average values of the air-gap flux-density.

Fig. 3.41 Depth of penetration of slot frequency component of air-gap flux

The iron losses are determined by subtracting the mechanical losses (Fig. 3.39) from the total losses (Fig. 3.40) and the results are shown in Fig. 3.42 at 3 values of excitation. These losses consist of hysteresis losses, P_h, and eddy-current losses, P_e, which are represented by the first and second terms respectively of Equation (3.8).

$$P_i = P_h + P_e = \sum_j K_{hj} B_j^{mj} f_j + \sum_j K_{ej} B_j^{nj} f_j^2 \qquad (3.8)$$

K_h and K_e are hysteresis and eddy-current losses constants, at flux-density B and frequency f, and j refers to the particular part of the magnetic circuit.

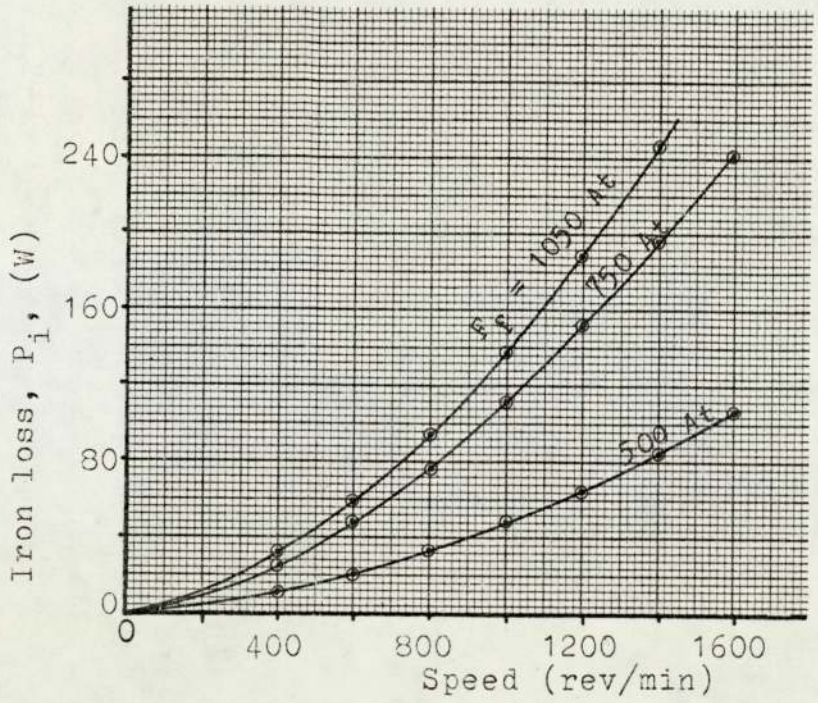

Fig. 3.42 No-load iron losses

The two parts of the magnetic circuit which experience these losses are the rotor poles and the laminations, but the values of flux-density are quite different. In the teeth, the flux-density is 2.33 times that at the surface of the rotor poles (v. Tables 2.3 and 2.4, pp. 46 and 50). Additionally, the frequency of the flux pulsations in the poles is slot frequency, whereas in the lamination stacks it is 1/12 of the slot frequency.

Therefore, each of the terms of Equation (3.8) consists of two terms, one for the poles and another for the laminations.

$$P_h = K_{h1} B_g^{m1} (12f) + K_{h2} (2.33\ B_g)^{m2} f \qquad (3.9)$$

$$P_e = K_{e1} B_g^{n1} (12f)^2 + K_{e2} (2.33\ B_g)^{n2} f^2 \qquad (3.10)$$

Subscript (1) refers to the poles and subscript (2) the

laminations. Iron losses were determined at the 3 values of excitation only (Fig. 3.42), and the values available are not sufficient to determine the constants m1, m2 and n1, n2 with sufficient reliability.

It is however, possible to determine the dependence of P_h and P_e on speed from Fig. 3.42. The losses in watts for the 3 values of excitation are given in the following expressions.

$$\left.\begin{aligned} P_i &= 1.3\left(\frac{n}{100}\right) + 0.35\left(\frac{n}{100}\right)^2 \qquad 500\ \text{At} \\ P_i &= 3.0\left(\frac{n}{100}\right) + 0.79\left(\frac{n}{100}\right)^2 \qquad 750\ \text{At} \\ P_i &= 4.2\left(\frac{n}{100}\right) + 0.96\left(\frac{n}{100}\right)^2 \qquad 1050\ \text{At} \end{aligned}\right\} \quad (3.11)$$

Hence the hysteresis loss is greater than the eddy-current loss for speeds less than 400 rev/min and vice versa above 400 rev/min.

3.6 Motor operation

Use of the faceplate commutator and brushes limits the speed of rotation and the commutated-winding current to values much lower than those in the specification. Mechanical losses are higher than those given in Fig. 3.39, p. 113, since brush friction is now included.

Despite these disadvantages, the tests in this section demonstrate the effect of γ on the load characteristics. In addition, the waveforms of voltage and current in the

machine could be studied before the electronic commutator was constructed. The rotor poles in the no-load and load tests are staggered and chamfered. For comparison, waveforms are included for both staggered and aligned poles.

3.6.1 No-load test

A no-load test was performed on the motor at one value of γ and excitation. The commutated-winding current I_a and the speed n are plotted in Fig. 3.43 to a base of supply voltage V_s. A voltage of 15 V is required to overcome the stiction torque.

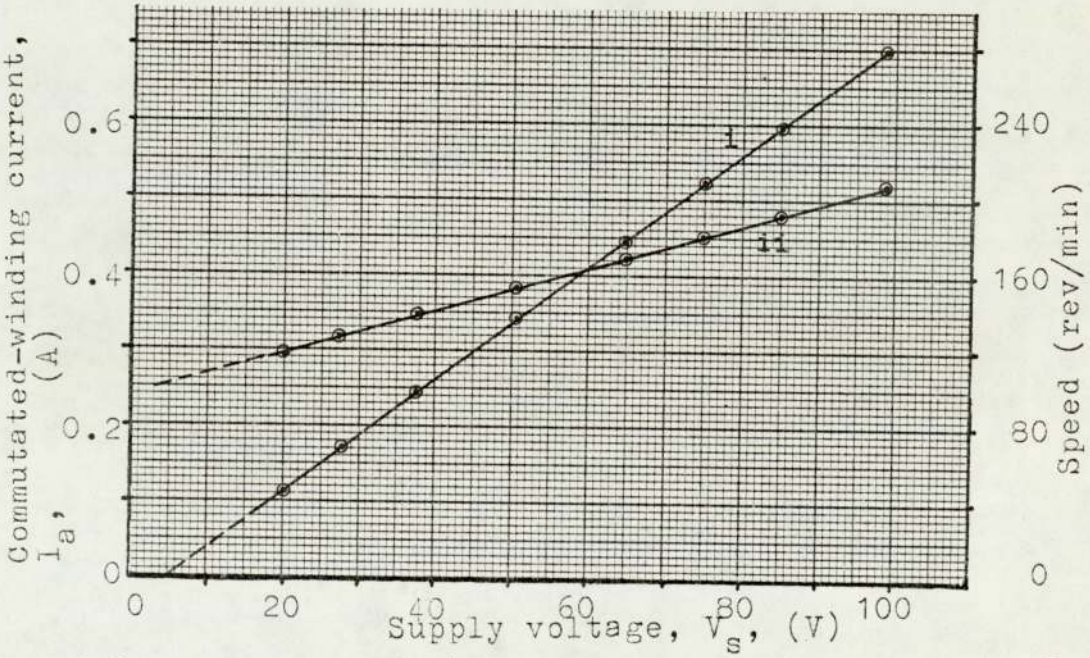

(i) speed (ii) commutated-winding current, I_a

Fig. 3.43 No-load test, F_f = 1050 At, γ = -10°(m), poles staggered and chamfered

An expression for the developed torque can be obtained from e.m.f. Equation (3.12) together with the expressions

for I_a and n in terms of V_s from Fig. 3.43. The e.m.f. equation is

$$V_s = U_o \omega + I_a R_a \qquad (3.12)$$

where U_o is the e.m.f. constant, and ω is the speed in rad/s.

At no-load, the motor develops enough torque to cover the mechanical and iron losses plus the friction of the brushes. Hence developed torque is

$$T = \frac{EI_a}{\omega} = U_o I_a = A\omega + K \qquad (3.13)$$

where A and K are constants.

Equations (3.14) and (3.15) for I_a and n are obtained from Fig. 3.43.

$$I_a = 2.8 \times 10^{-3} V_s + 0.24 \quad \text{(A)} \qquad (3.14)$$

$$n = 2.93 V_s - 12.7 \quad \text{(rev/min)} \qquad (3.15)$$

The values of the constants were determined from the above 4 equations. Thus U_o = 3.1 Vs/rad and the torque equation is

$$T = 28.28 \times 10^{-3} \omega + 0.78 \quad \text{(Nm)} \qquad (3.16)$$

At 200 rev/min, the torque is 1.37 Nm and the developed power is therefore, 28.78 W. From Fig. 3.40, p. 113, the mechanical and iron losses at 1050 At and 200 rev/min are 20 W, leaving 8.78 W for brush friction.

The value of R_a was calculated as 17.18 Ω whereas the ring winding resistance is $3R_g = 3(4.8) = 14.4\,\Omega$

(v. Table 2.6, p. 56). The difference between the two values is 2.78Ω and this is equivalent to a voltage drop across the brushes of about 1.25 V.

Based on the total loss curve at 1050 At in Fig. 3.40, p. 113, and the value of the e.m.f. constant U_o, the supply current I_a is predetermined at no-load with the motor operating with the electronic commutator instead of the brushes.

$$I_a = \frac{P_\ell}{U_o \omega} \qquad (3.17)$$

The supply voltage V_s is then determined from Equation (3.12) with R_a equal to the commutated-winding resistance only, i.e., 14.4 Ω. The values of I_a and n are plotted to a base of V_s in Fig. 3.44. These curves were determined for a field excitation of 1050 At at which value the iron is well into saturation and the no-load speed at a particular V_s is a minimum. The curves are unique to a brush setting, or separation angle γ, at commutation, of -10°(m).

The r.m.s. value of e.m.f. between brushes is $U_o\omega$ and is equal to 325 V at 1000 rev/min. This value is in good agreement with that read off from Fig. 3.38, p. 110, at 1050 At and γ = -10°(m).

The values in Fig. 3.44 were based on the loss curve of the machine when driven. Hence the effect of the commutated-winding field on the field form due to the

field excitation is not included. However, the additional iron loss resulting from the deformation of the field form is negligible due to the small value of I_a at no-load.

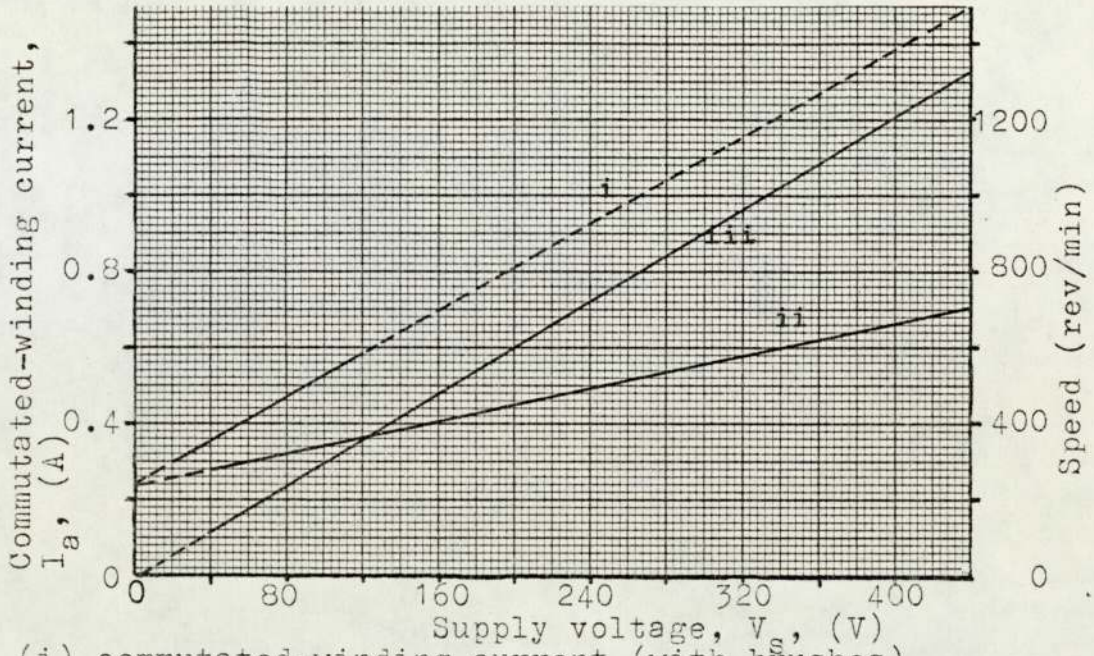

(i) commutated-winding current (with brushes)
(ii) commutated-winding current (no brushes)
(iii) speed (no brushes)

Fig. 3.44 Theoretical values at no load (electronic commutator), F_f = 1050 At, γ = -10°(m)

3.6.2 Load tests

Speed, torque and commutated-winding current were recorded at various values of excitation, supply voltage and separation angle γ. The results are plotted in Figs. 3.45 and 3.46, and a typical torque waveform is shown in Fig. 2.3b, p. 25.

Fig. 3.45 shows the approximately linear relation between torque and commutated-winding current I_a for constant excitation. This is more apparent at low values of I_a

where armature reaction does not have a noticeable effect on the field from. Torque varies with flux per pole ϕ_p and I_a, and hence varies linearly with I_a provided that ϕ_p is not affected by armature reaction.

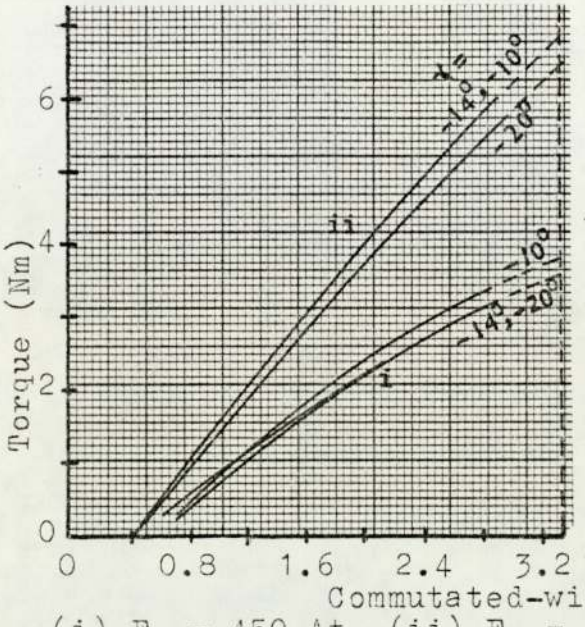

(v. page xviia)

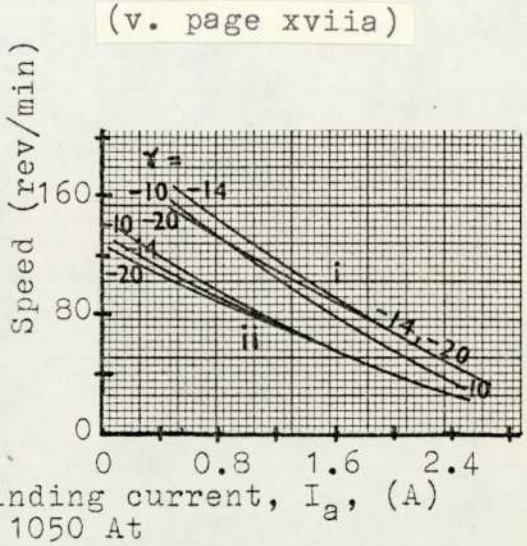

(i) F_f = 450 At, (ii) F_f = 1050 At

Load tests, V_s = 50 V, staggered and chamfered poles

Fig. 3.45 Torque curves

Fig. 3.46 Speed curves

At an excitation of 1050 At, the torque values at $\gamma = -10^\circ$ and -14° are approximately the same since the e.m.f.'s induced between the brushes at these values of γ are almost equal (v. Fig. 3.38, p. 110).

However, at a lower field excitation of 450 At, the effect of armature reaction is more pronounced, for the same value of I_a. Hence the axis of symmetry in Fig. 3.38 is shifted in the direction of rotation resulting in the peak e.m.f. occuring at a value of γ closer to -10° than to -14°. In Fig. 3.45 this is seen as lower values of torque at -14° than at -10° for an excitation of 450 At.

The curves in Fig. 3.45 are extrapolated to I_a = 3.35 A so that values of torque which are given in Table 3.10 can be compared with those in Table 3.3, p. 84. The values of output torque in Table 3.10 are between 10% and 20% less than those at corresponding conditions in Table 3.3. This is the result of rotational losses (mechanical and iron).

$\theta°$(m)	$\gamma°$(m)	Mean torque (Nm)	
		450 At	1050 At
-25	-20	3.6	6.5
-19	-14	3.6	6.9
-15	-10	3.8	6.9

Table 3.10 Mean torque versus θ and γ (V_s = 50 V, I_a = 3.35 A)

Fig. 3.46 shows the variation of speed with commutated-winding current for three values of γ at two values of excitation. Speed varies inversely with air-gap flux and hence is higher at low values of excitation. Speed is also dependent upon the angle γ but in an opposite manner to that of the torque variation with γ in Fig. 3.45, particularly at high values of current. The variation of speed with current is non-linear as seen from Fig. 3.46, and Equation (3.12), p. 120, cannot be applied to the motor on load. U_o in Equation (3.12) is constant provided that air-gap flux remains unchanged. However, on load, armature reaction reduces the air-gap flux, and this reduction depends to a great extent on the initial amount of flux at no-load.

To predetermine the load characteristics from the available results, U_o is assumed constant at the value obtained on no-load (Section 3.6.1, p. 119). The value of U_o at 1050 At was 3.1 Vs/rad and therefore, at 450 At:

$$U_o = 3.1 \left(\frac{0.425}{0.640}\right) = 2.06 \text{ Vs/rad (or Nm/A)}$$

0.425 T and 0.640 T correspond to 450 At and 1050 At, respectively (v. Fig. 2.20, p. 51).

The values of speed are determined for various values of current I_a at a constant supply voltage using Equation (3.12), p. 120. To exclude the effect of the brush resistance, the value of R_a is made equal to 14.4 Ω which is the resistance of the ring commutated-winding only.

Speed was calculated for 4 values of supply voltage and at two values of excitation, and the results are plotted to a base of I_a in Fig. 3.47. The curves are linear due to the assumption of a constant value for U_o.

(v. page xviia)

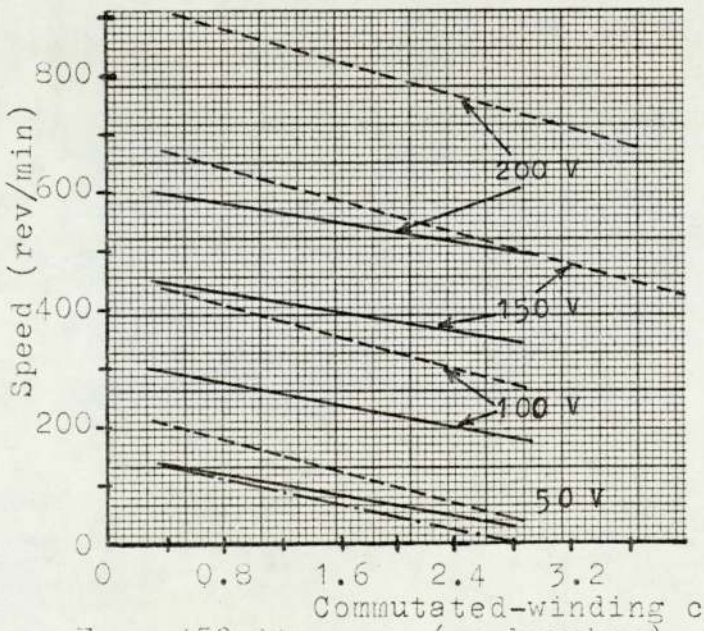

Fig. 3.47 Theoretical speed curves

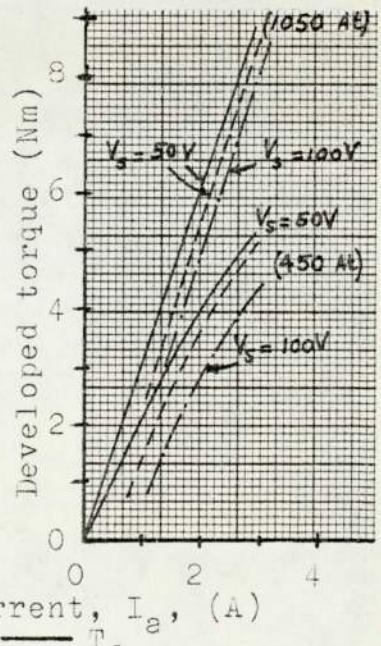

Fig. 3.48 Torque curves

The developed torque, T_d, was determined from the curves in Fig. 3.47 by subtracting the winding copper loss from the input power.

$$T_d = \frac{1}{\omega}\left(V_s I_a - I_a^2(14.4)\right) \qquad \text{Nm}$$

The values obtained are plotted in Fig. 3.48. The output shaft torque would be lower than T_d by an amount equivalent to the mechanical and iron losses. This reduction is greatest at high values of I_a due to the considerable iron loss expected on load.

Although the curves in Fig. 3.48 were determined for V_s equal to 50 V and 100 V, these curves can be extended for higher voltages too, since the reduction in developed torque would be small. But the shaft torque would be reduced by a greater amount since both mechanical and iron losses are higher at higher supply voltages.

The broken curves in Fig. 3.48 represent the developed torque minus the torque required to equalise the no-load iron losses and the mechanical losses. The expressions for the iron losses in Equation (3.11), p. 118, can be rewritten in terms of ω as follows

$$\left.\begin{aligned} P_i &= 0.124\ \omega + 0.0032\ \omega^2 \quad (W) \quad 500\ \text{At} \\ P_i &= 0.286\ \omega + 0.0072\ \omega^2 \quad (W) \quad 750\ \text{At} \\ P_i &= 0.401\ \omega + 0.0088\ \omega^2 \quad (W) \quad 1050\ \text{At} \end{aligned}\right\} \quad (3.18)$$

The torque required for the iron loss is $T_i = P_i/\omega$ and for the mechanical loss $A\omega$, where A is equal to 28.3×10^{-3}

(Equation (3.16), p. 120). The total loss torque T_ℓ is, therefore,

$$\left.\begin{aligned} T_\ell &= 0.124 + 0.0315\ \omega \quad (\text{Nm}) \quad 500\ \text{At} \\ T_\ell &= 0.286 + 0.0355\ \omega \quad (\text{Nm}) \quad 750\ \text{At} \\ T_\ell &= 0.401 + 0.0371\ \omega \quad (\text{Nm}) \quad 1050\ \text{At} \end{aligned}\right\} \quad (3.19)$$

The expression for T_ℓ at 500 At is used to determine the torque curve at 450 At, since it is the nearest value available. The error involved is small since the air-gap flux-density is only 8% higher at 500 At. The values of speed ω in the calculation were obtained from Fig. 3.47 at two values of supply voltage V_s.

The shaft torque that would be obtained with the electronic commutator would be even lower than these calculated values since the iron losses on load are higher than the theoretical values.

3.6.3 Voltage and current waveforms

Fig. 3.49 shows typical waveforms of voltage and current of the brushless motor on load. The voltage between a tapping and one of the supply terminals changes between V_s and zero as shown in Fig. 3.49a. Each of the 6 tappings is connected to the supply twice per cycle for a time equivalent to 1/18 of a revolution.

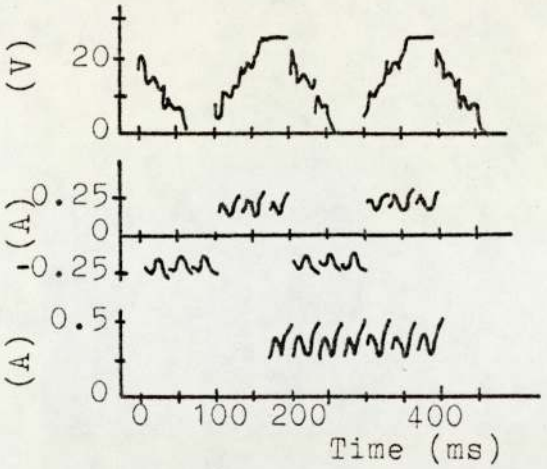

(a) voltage between a tapping and a supply terminal

(b) current I_c in the ring winding

(c) commutated-winding current I_a

Fig. 3.49 Voltage and current waveforms, aligned poles V_s = 25 V, F_f = 450 At, I_a = 0.32 A, n = 100 rev/min, $\gamma = -14^\circ$ (m)

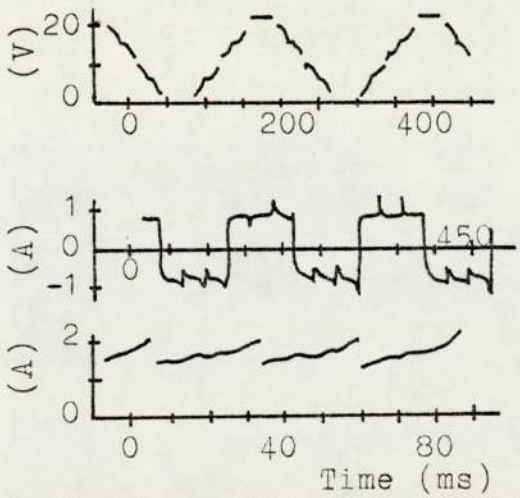

(a) voltage between a tapping and a supply terminal: V_s = 25 V, n = 90 rev/min

(b) current I_c: V_s = 50 V, n = 115 rev/min, I_a = 1.5 A

(c) current I_a: same as in (b)

Fig. 3.50 Voltage and current waveforms, staggered and chamfered poles, F_f = 450 At, $\gamma = -14^\circ$ (m)

The supply is momentarily interrupted as the brushes cross the 0.6 mm gap between commutator segments. It was not possible to eliminate these spikes by connecting resistors between the segments without affecting the behaviour of the motor. However, since this problem is associated with the mechanical commutator only, it is not considered further.

Reversal of the supply to radially opposite tappings by the action of the commutator and brushes results in current reversal in the ring winding as seen in Fig. 3.49b. Discontinuities due to the gaps between segments can be seen in the current waveforms also. The total commutated-winding current, I_a, to the brushes is unidirectional and is equal to twice the value of current I_c in the ring winding as shown in Fig. 3.49c.

Fig. 3.50 shows waveforms of voltage and current with the poles staggered and chamfered but at the same values of $\gamma = -14^\circ$ as in Fig. 3.49. A noticeable reduction in the ripple is achieved in all the waveforms by staggering the poles. This means a reduction in the iron and copper losses caused by current pulsations.

3.7 Flux-density measurements

The flux-density measurements are divided into two groups:

(i) with the machine prevented from rotation, and

(ii) with the machine either driven or operating as a motor.

The first group of tests is discussed in Section 3.7.2 where the test methods used are current reversal and incremental movement. A fluxmeter is used in both methods to give direct readings of flux from the e.m.f. induced in search-coils.

In the second group of tests where the machine is rotating (Section 3.7.3), the e.m.f. induced in the search-coils is first integrated and then displayed on an oscilloscope. The positions of the search-coils are given in Section 3.7.1.

3.7.1 Search-coil positions

Single-turn search-coils (42 S.W.G.) were wound around 12 consecutive teeth in the lamination stack at the opposite drive end (ODE). Fig. 3.51 shows the positions with respect to the 'starts' of the commutated-winding coil groups.

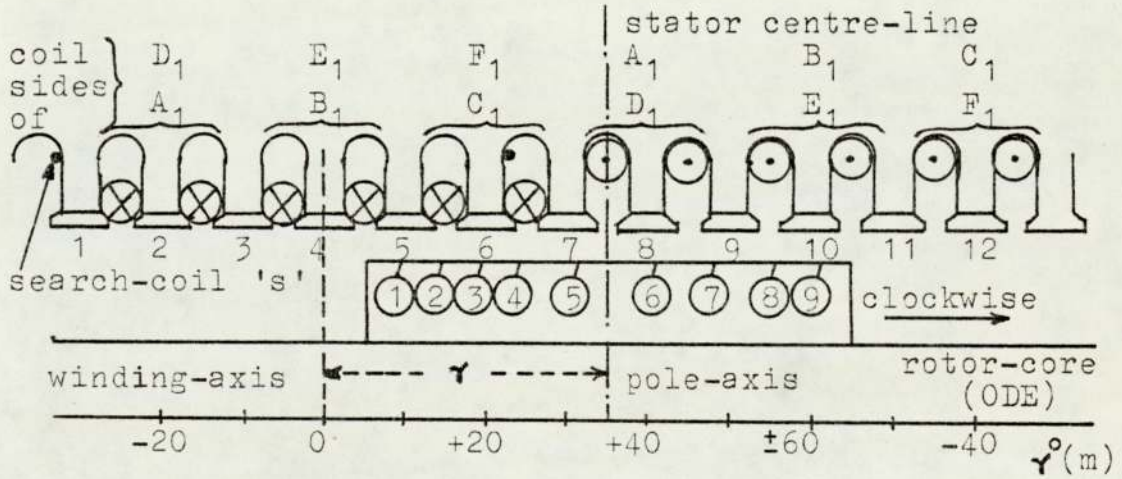

Fig. 3.51 Search-coil positions

The search-coils are positioned around the parallel-sided parts of the teeth (point B in Fig. 2.15, p. 47). From the m.m.f. calculations in Section 2.5.2, p. 44, the flux-density is highest at this part of the tooth.

Fig. 3.52 shows the search-coil layout on the pole-face. Single-turn coils (48 S.W.G.) were distributed over the 60° arc. The dimensions of the coils as well as the gaps between them are given in the figure.

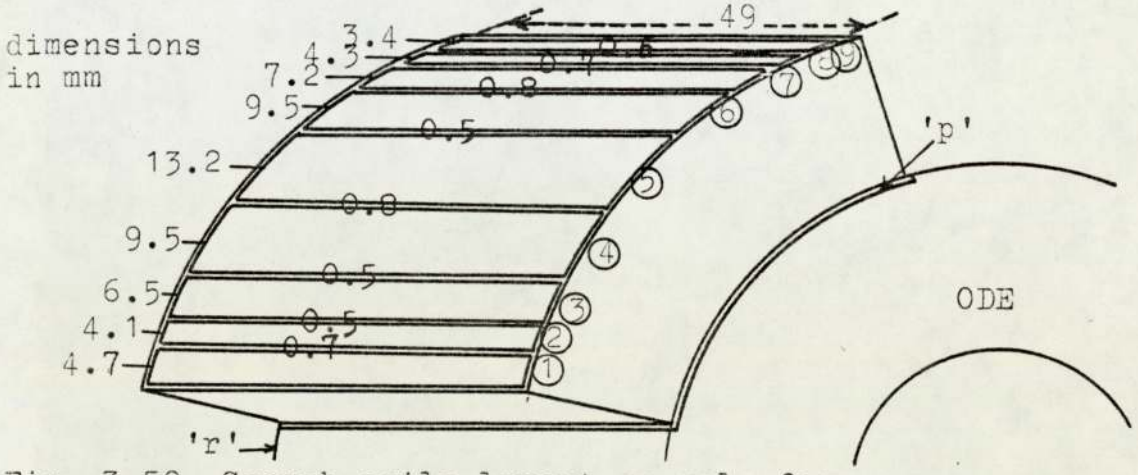

Fig. 3.52 Search-coils layout on pole-face

Owing to the thickness of the copper wires used in the search-coils and the gaps between the coils, the overall area enclosed by the search-coils is less than the surface area of the pole. This, however, does not affect the flux-density calculation since it is done for each search-coil separately.

Three search-coils were also placed in the lamination stack, separated by 120° (m) from each other. Each coil was wound around the base of 6 teeth, and one such coil 's' is shown in Fig. 3.51.

Another single-turn search-coil 'p' was wound around the base of a pole-piece, adjacent to the rotor-core surface. To check the changes in flux-density in the rotor-core,

a search-coil 'r' was wound around the core between the poles at one end and the machine centre-line. Search-coils 'p' and 'r' are shown in Fig. 3.52.

3.7.2 Static measurements

In these tests, flux was measured with a fluxmeter manually adjusted to a minimum drift position for the particular range setting. The iron of the magnetic circuit was demagnetised prior to each measurement to minimise remanent magnetism.

The tests performed can be subdivided according to the method of flux production, i.e., current reversal or incremental movement of the rotor. Test results for the first method lead to actual values of flux-density whereas the second method provides information only about the manner in which the flux-density is changing.

In both methods the magnetic effects were observed in the 12 teeth (Fig. 3.51, p. 130), under 4 conditions:

(i) half a coil group excited,
(ii) one coil group excited,
(iii) the complete ring winding excited, and,
(iv) the ring winding and field coil excited.

Additionally, in the current reversal method, magnetic effects were observed in the search-coils on the pole-face. Measurements were also taken with only the field coil excited.

3.7.2.1 Current reversal method

Depending upon the particular test, either the field coil current or the commutated-winding current (or part of the winding) was reversed with a change-over switch. The direction of e.m.f. induced in all search-coils was noted for a known polarity of flux linkage, i.e., with a pole facing the particular search-coil while only the field coil was excited. The underlying assumption in the current reversal method is that the magnetisation of iron is symmetrical for both directions of m.m.f.

The measurements of the flux-densities at the pole-surface are discussed separately from those of the flux-densities at the stator teeth in the following two sub-sections.

3.7.2.1.1 Flux-density on pole-surface

Fig. 3.53 shows the changes in flux-density in each of the search-coils on the surface of the pole over 10°(m) (one stator slot-pitch) of rotor movement and at an excitation of 1050 At. The frequency of the flux-density pulsations is equal to the slot frequency, and the amplitude of these pulsations can be up to 2.5 times the minimum value. This means that during normal operation as a motor the iron of the poles experiences minor hysteresis loops of magnetisation at slot frequency, giving rise to losses.

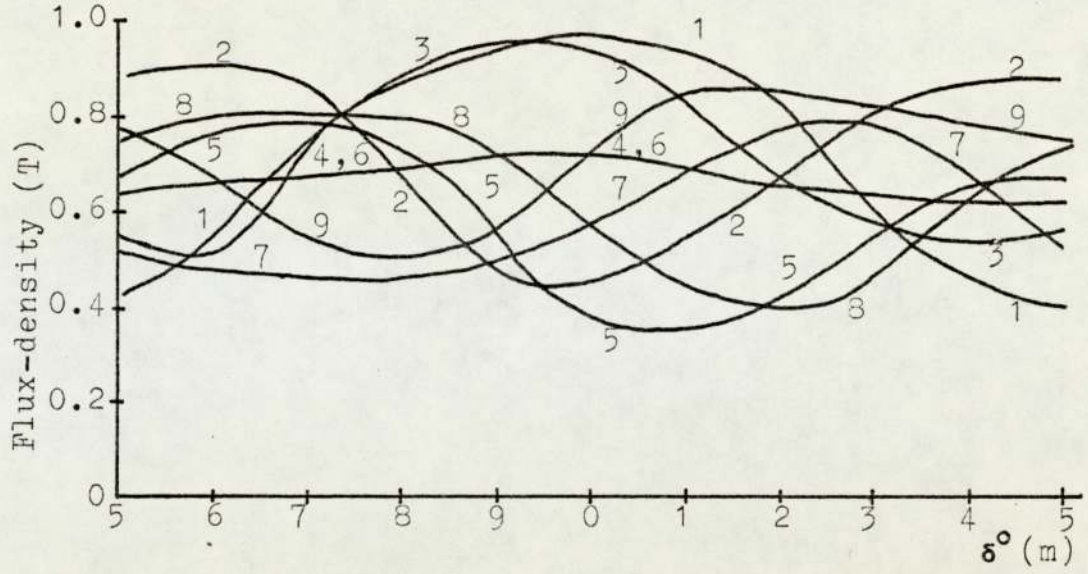

Fig. 3.53 Flux-density at pole-face, F_f = 1050 At

Dividing the total flux linkage of all the search-coils by the total area of the search-coils on the pole-surface gives the average radial flux-density (B_{av}). B_{av} does not vary greatly over 10° of rotation as seen from Fig. 3.54. δ is the angle between the pole-tips and the tooth centre-line.

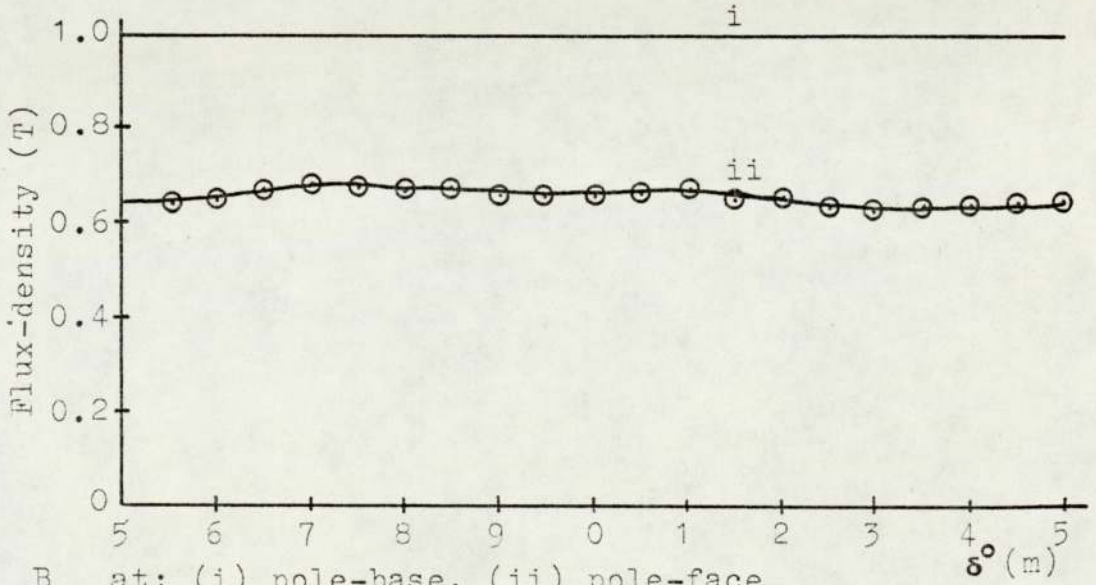

B_{av} at: (i) pole-base, (ii) pole-face

Fig. 3.54 Average flux-density per pole, F_f = 1050 At

The flux-density at the base of the pole is also plotted in Fig. 3.54 as a constant value obtained from the test. The cross-sectional area at the base of the pole is 30% less than at the surface. But B_{av} at the base is increased further by the leakage flux between the stator teeth and the sides of the pole. Leakage accounts for about 4% of the flux at the base of the pole.

At $\delta = 0^{\circ}$ the pole-tips are facing the centre-lines of teeth. This is a position of minimum reluctance where the reluctance torque due to slotting is zero (Section 2.3.4.1, p. 35). In Fig. 3.55a, the average flux-density over search-coil area is plotted at $\delta = 0^{\circ}$ to construct the field form on the pole-surface. Although the pole surface area is divided into large parts corresponding with the search-coils, the variation in flux-density, B_g, is still apparent. B_g is still highest at the pole-tips decreasing towards the centre-line.

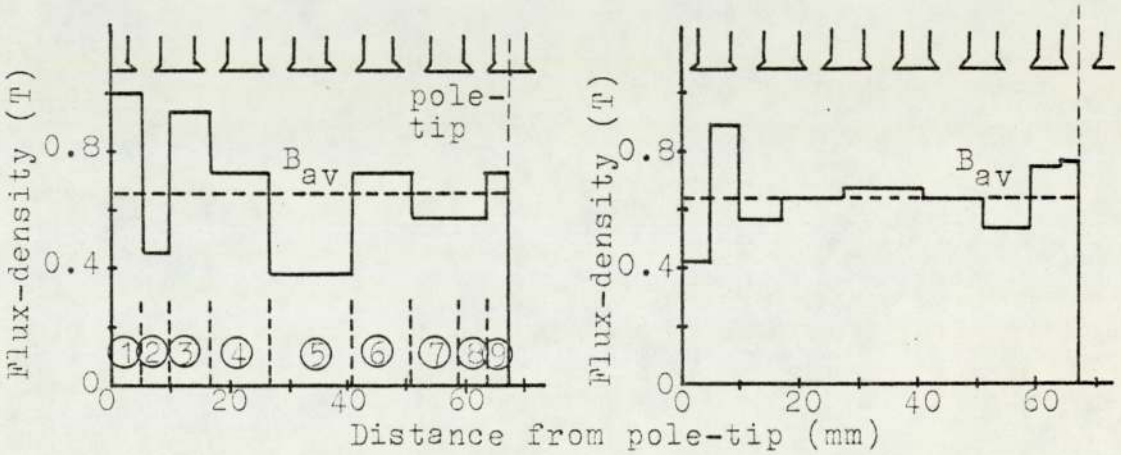

(a) $\delta = 0^{\circ}$ (m), stable position

(b) $\delta = 5^{\circ}$ (m), unstable position

Fig. 3.55 Field form at pole-face, 1050 At

In contrast, Fig. 3.55b shows the field form at $\delta = 5^{\circ}$, i.e., pole-tips facing the centre-lines of slots, where the rotor position is unstable. B_g at the middle of the pole is higher than for the stable position. However, both distributions are non-symmetrical about the pole centre-line. This is due to the unequal areas of search-coils on either side of the centre-line. Instability at $\delta = 5^{\circ}$ results from the slightest difference in magnetic pull between the two pole-tips.

Fig. 3.56 shows the field form at the pole-surface due to the current in 3 series coils per lamination stack, displaced by 120°(m), (i.e., half a coil group). In Fig. 3.56a the axis of the pole coincides with that of the coil and this represents the minimum reluctance position. Saliency torque at this position is zero as discussed in Section 2.3.4.2, p. 36.

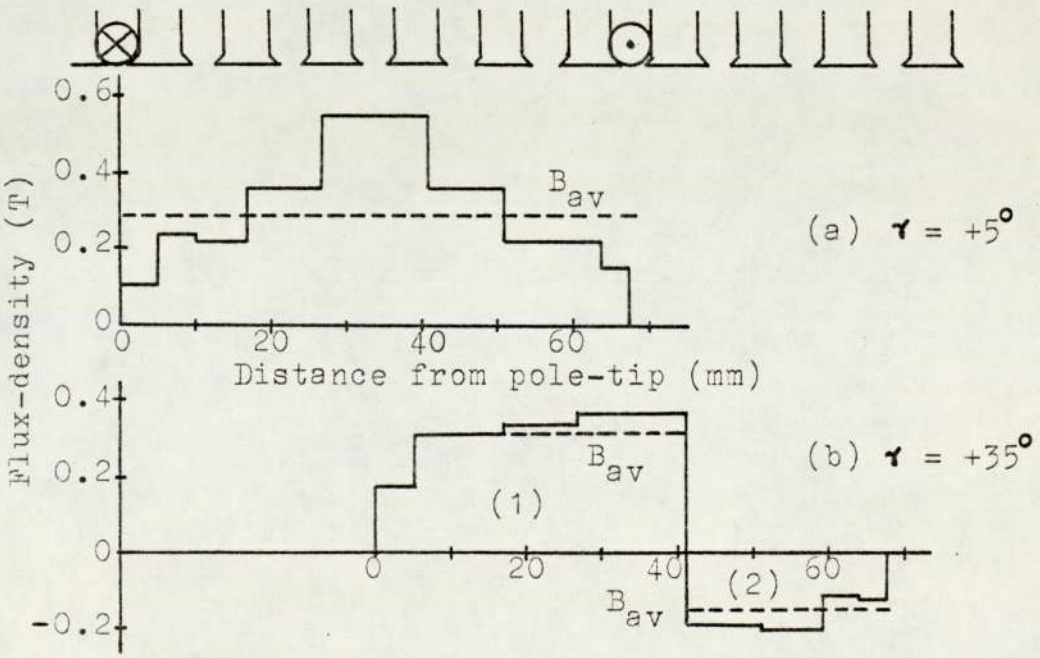

Fig. 3.56 Field form at pole-face with one coil excited, F_a = 118 At/120° (m), I_a = 2.36 A

With the pole rotated by 30°(m), i.e., half the coil-span, the flux-density distribution becomes that of Fig. 3.56b. Apart from a reduction in the value of flux-density, the direction of flux under the coil is opposite to that outside it. This is caused by the local flux path (i) shown in Fig. 2.12, p. 37. From test results, the flux at the pole-surface outside the coil is about 35% that opposite the coil. The ratio of the flux-densities at the two equal parts of the pole-surface obtained from the curves of Fig. 2.13, p. 39, at $b_1/(\pi/3) = 1/2$, is

$$B_2/B_1 = 0.085/0.272 = 31.3\% \qquad (3.20)$$

The experimental and calculated values are in good agreement considering the assumptions in determining the curves in Fig. 2.13.

The values of B_{av} in Fig. 3.56b are higher than those in the above Equation (3.20) since this test was performed at a higher m.m.f. (18%). Also, parts (1) and (2) of the pole-surface in Fig. 3.56b are not equal although the coil side is along the pole centre-line.

3.7.2.1.2 Flux-density in stator teeth

The flux-density B_t in the stator teeth is measured with only the field coil excited as well as for the conditions listed in Section 3.7.2, p. 132. The field form is drawn for each condition at two values of γ, +5° and +35°. The experimental values of B_t are higher than those of B_g on the pole-face for the same condition of excitation.

This is due to the small cross-sectional area of the flux path in the teeth before spreading out on the pole-face. From Table 2.3, p. 46, B_t is approximately equal to 2.33 B_g.

(i) Field coil only excited

Fig. 3.57 shows the flux-density distribution in the teeth with a field excitation of 1050 At. This measurement was performed at the same conditions as for Fig. 3.55b, p. 135. However, the distributions are different from each other since they refer to different parts of the magnetic circuit.

Flux fringing at the tooth-tips is one reason for the difference in field form. Another reason is the flux linkage between the teeth in the interpolar zone and the search-coils on the pole-face.

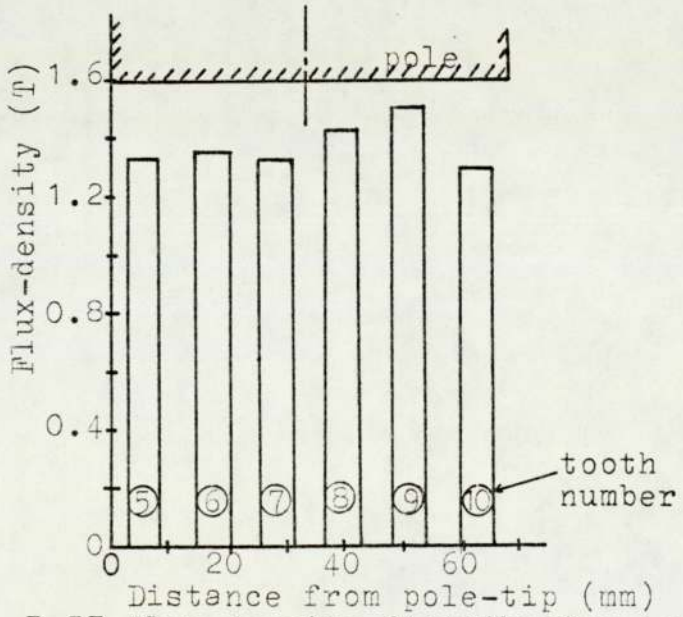

Fig. 3.57 Flux-density distribution in teeth due to field excitation, F_f = 1050 At, δ = +5° (m)

(ii) Half a coil group excited

The values in Fig. 3.58 were obtained under the same conditions as in Fig. 3.56. The field-distributions are considerably different at $\gamma = +5^{\circ}$ for much the same reasons given above in (i). B_t is slightly lower in the teeth opposite the middle of the pole than in those near the coil sides, since the latter also carry flux which takes a local path in the lamination stack without crossing the air-gap. However, the distribution is more uniform in the teeth than on the pole-face.

At $\gamma = +35^{\circ}$, the flux-density distributions in the two figures are similar but due to the smaller cross-sectional area in the teeth compared with the pole-face, B_t is higher than B_g.

(iii) One coil group excited

Exciting one coil group in each lamination stack resulted in the flux-density distribution given in Fig. 3.59. B_t in the teeth between adjacent coil sides is reduced to almost zero while B_t in the teeth embraced by the coils is almost doubled in comparison with Fig. 3.58. Since the iron is still unsaturated in these measurements, the flux-density varies linearly with m.m.f., which is doubled in Fig. 3.59. B_t in the teeth not shown in the diagrams is negligibly small.

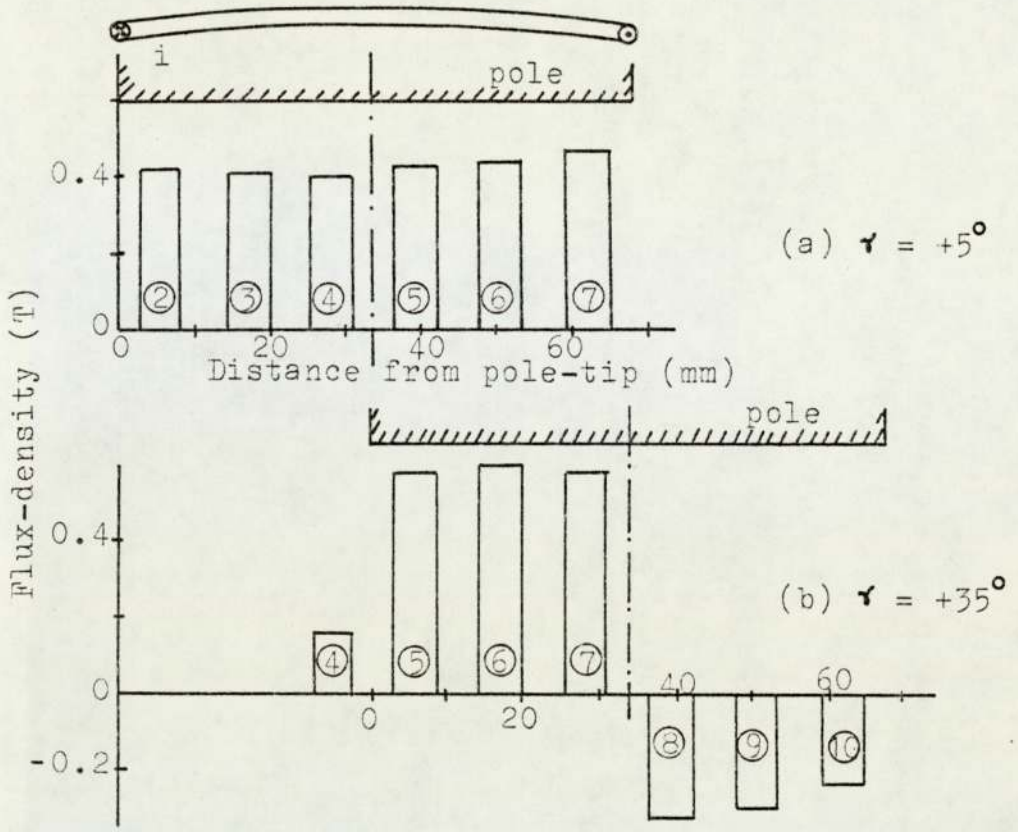

Fig. 3.58 Field form due to current in ½ coil group, F_a = 118 At/120° (m), I_a = 2.36 A

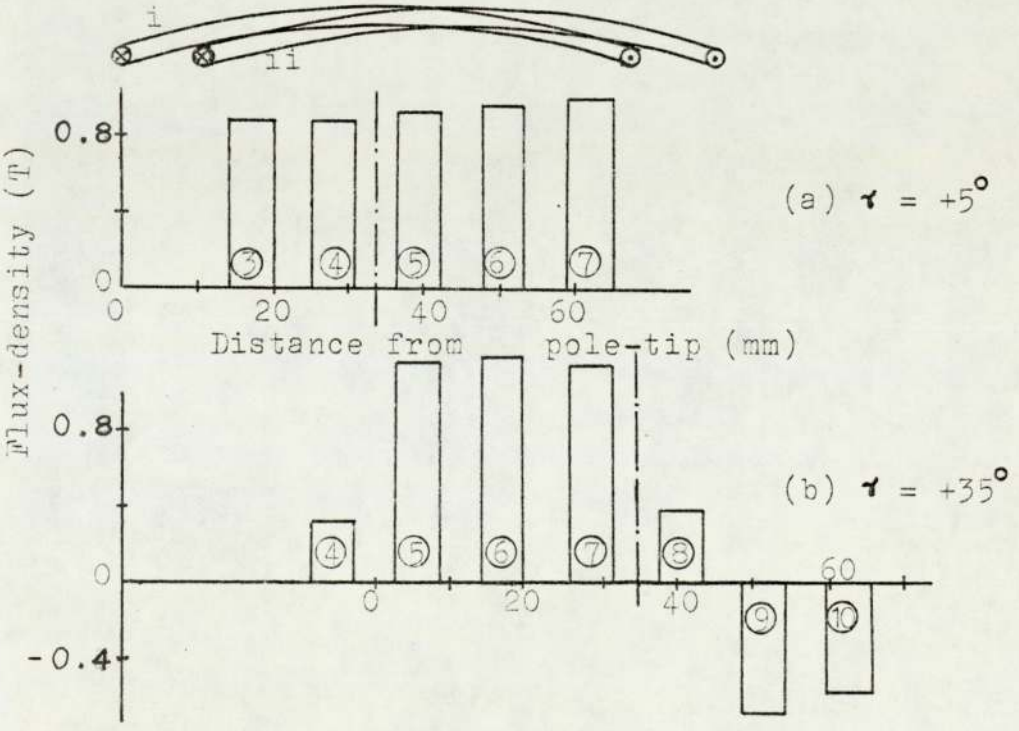

Fig. 3.59 Field form due to current in one coil group, F_a = 236 At/120° (m), I_a = 2.36 A

(iv) Complete ring winding excited

The flux-density distribution due to current in the ring winding is plotted in Fig. 3.60. The pole centre-line and winding-axis are shown in the figure. The familiar triangular distribution can be seen with its minimum value at the tooth along the winding-axis. At an excitation of 708 At per 120°(m), the iron is reaching saturation and hence the relation between m.m.f. and B_t is non-linear when compared with Fig. 3.59.

(v) Ring winding and field coil excited

The values of flux-density in Fig. 3.61 were obtained by reversing the currents in both commutated-winding and field coil. The total flux produced by the two currents results in a high value of B_t opposite one pole-tip and a low value opposite the other. From Figs. 3.61a and b at $\gamma = +5°$ and $+35°$, it can be seen that at $\gamma = 0°$, the maximum value of B_t opposite one pole-tip would be the highest possible while it would be almost zero opposite the other pole-tip. This suggests the maximum value of the 'BlIr' torque at $\gamma = 0°$. But since connecting a particular pair of tappings to the supply entails the same direction of m.m.f. due to the winding current for 20°(m) of rotor movement, then maximum torque would be obtained if operation is maintained for 10°(m) either side of this position. Hence it is similar to operating the motor at a brush setting angle of -10°(m). This

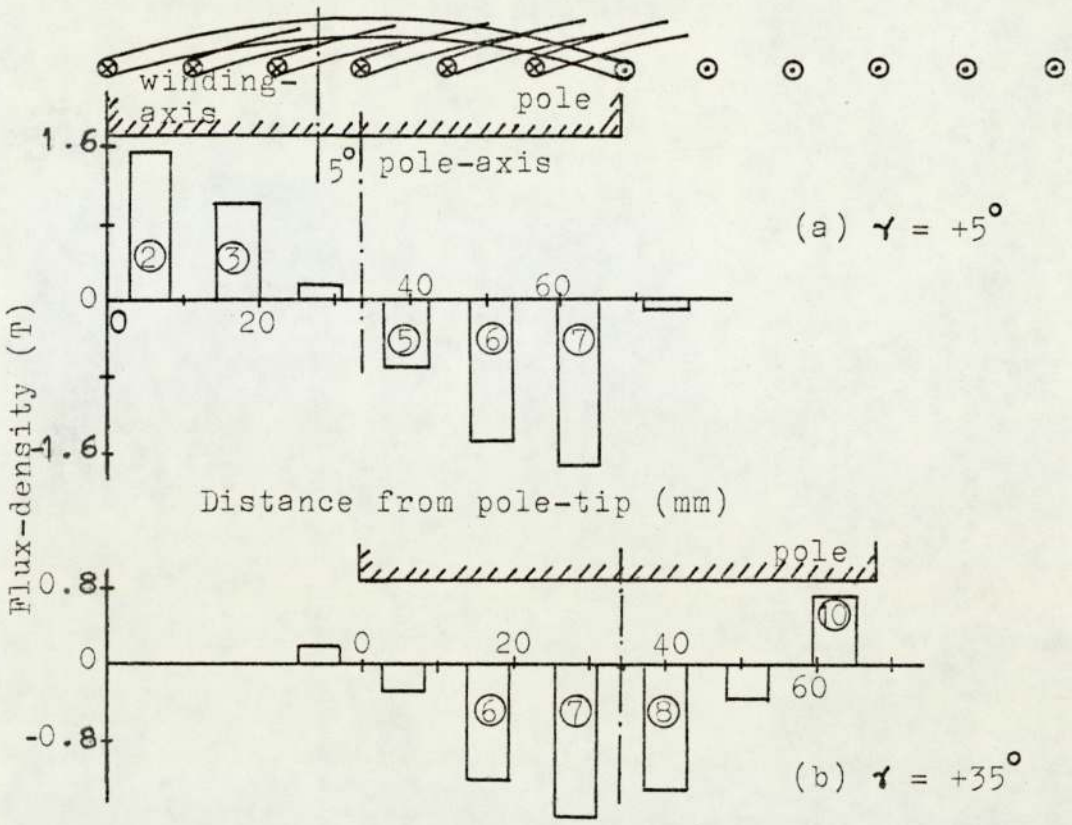

Fig. 3.60 Field form due to current in the complete ring winding, F_a = 708 At/120° (m), I_a = 2.36 A

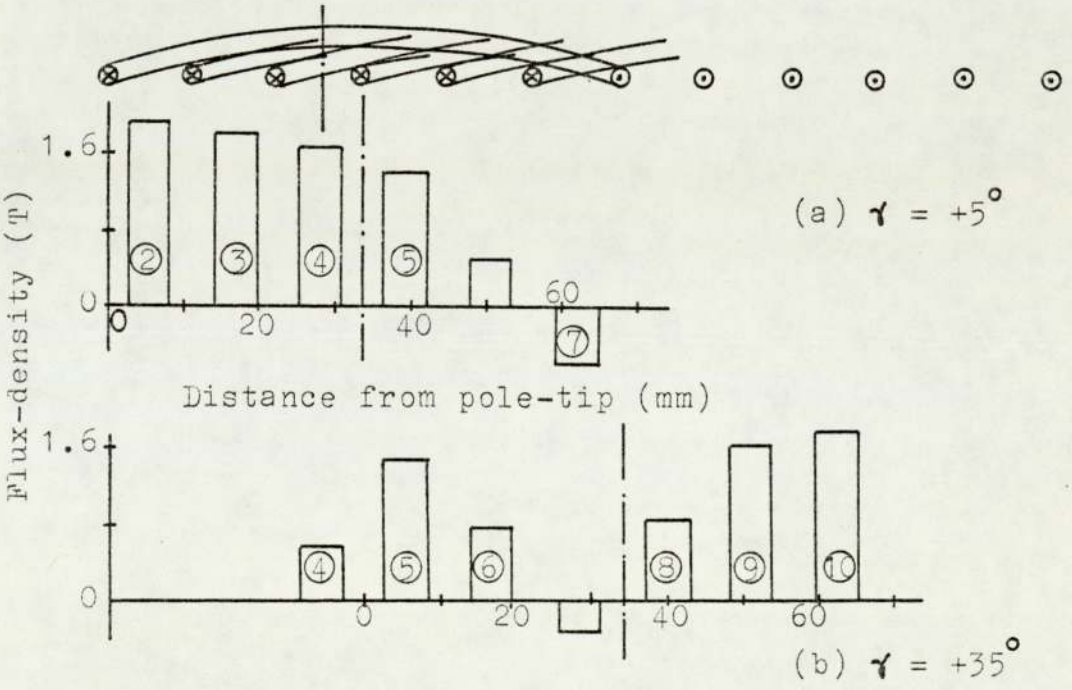

Fig. 3.61 Field form due to current in ring winding and field coil, F_f = 1050 At, F_a = 708 At/120° (m), I_a = 2.36 A

agrees with the e.m.f. curves versus γ in Fig. 3.37, p. 110, where the e.m.f. between brushes is a maximum at the same value of $\gamma = -10°(m)$.

3.7.2.2 Incremental movement method

The values of flux are read on a fluxmeter connected to the search-coils around the teeth, while the rotor is rotated manually over 120°(m) with the excitation maintained at the particular condition. The flux-density in the teeth is determined after correcting the values of flux by adjusting B_t in a tooth in the interpolar zone to zero, since there is very little leakage flux in this zone. The curves were also corrected for the drift in the fluxmeter by equalising the values of B_t at the start with those at the end of each run.

Figs. 3.62 to 3.65 show the flux-density variations in the teeth over 120°(m) of rotor movement for the 4 conditions of excitation given in Section 3.7.2, p. 132. These waveforms can be used to plot the distribution at any value of γ. An example is given in Fig. 3.66 at $\gamma = +5°$ and $+35°$ based on the curves of Fig. 3.65. The similarity between Fig. 3.66 and the distributions in Fig. 3.61, which was obtained by current reversal, is very marked.

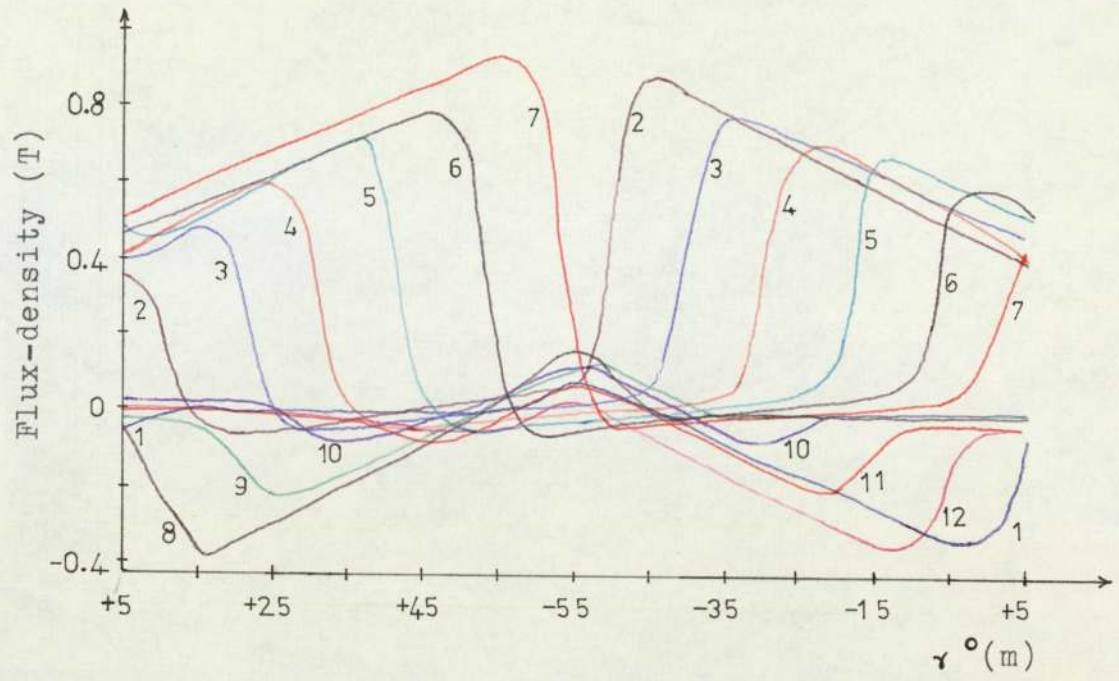

Fig. 3.62 Flux-density in teeth ($\frac{1}{2}$ coil group excited), F_a = 118 At/120°(m), I_a = 2.36 A

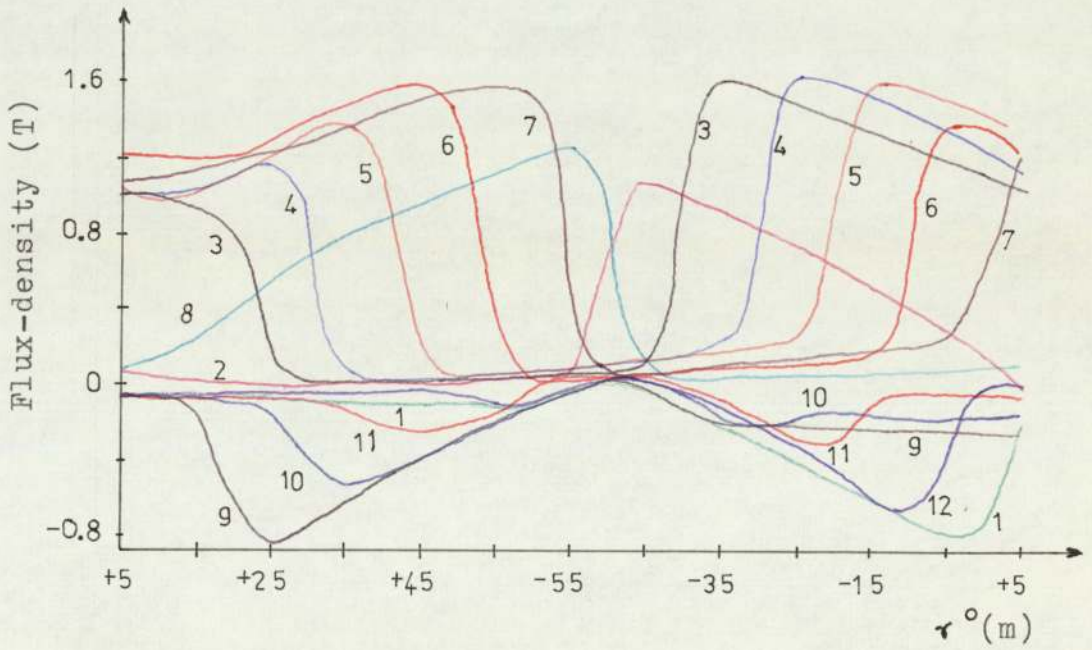

Fig. 3.63 Flux-density in teeth (one coil group excited), F_a = 236 At/120°(m), I_a = 2.36 A

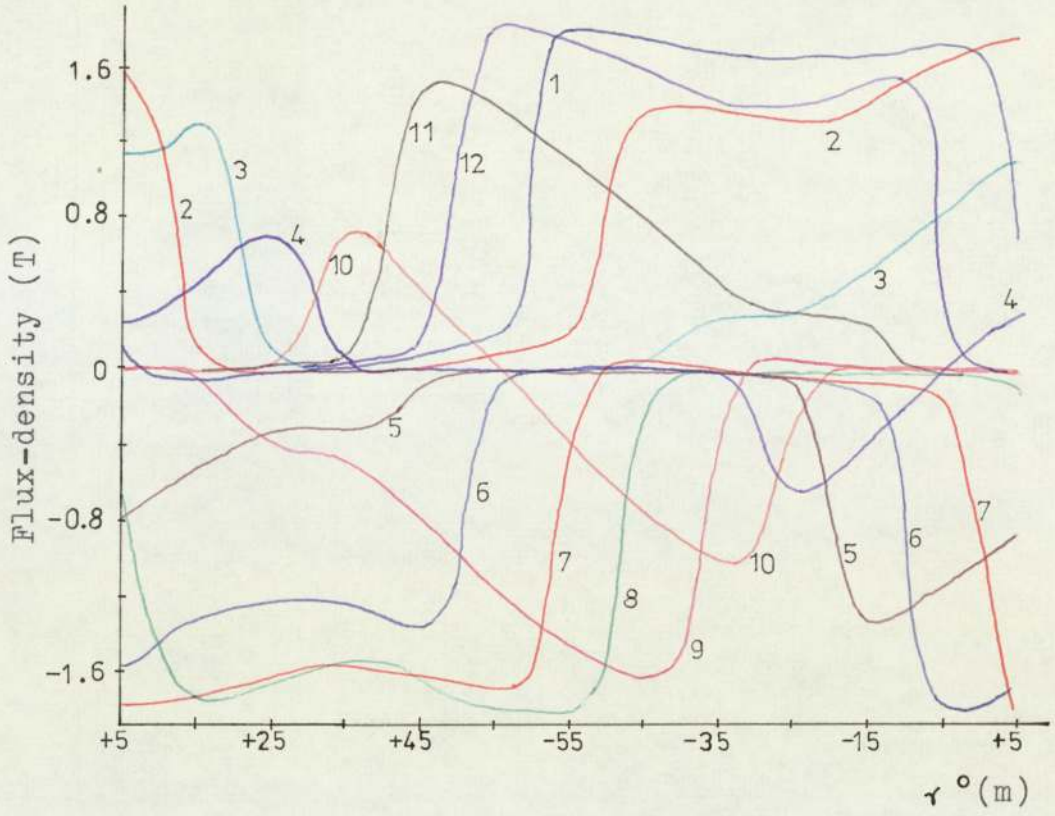

Fig. 3.64 Flux-density in teeth (complete ring winding excited), F_a = 708 At/120° (m), I_a = 2.36 A

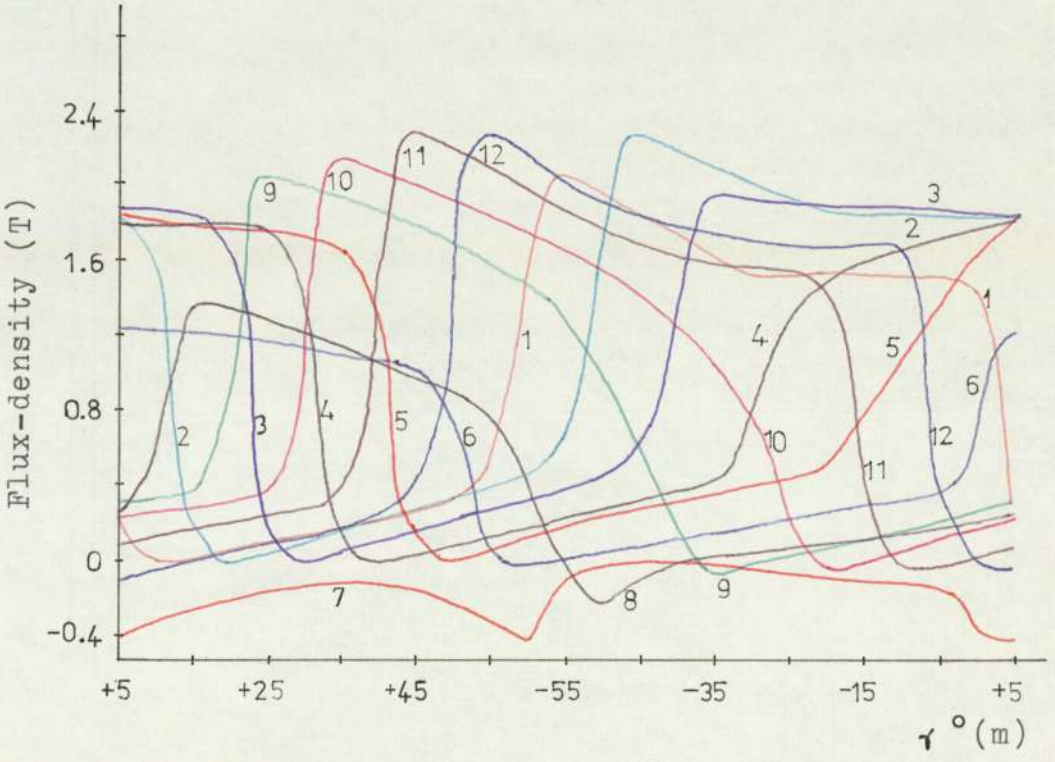

Fig. 3.65 Flux-density in teeth (ring winding and field coil excited), F_f = 1050 At, F_a = 708 At/120°, I_a = 2.36 A

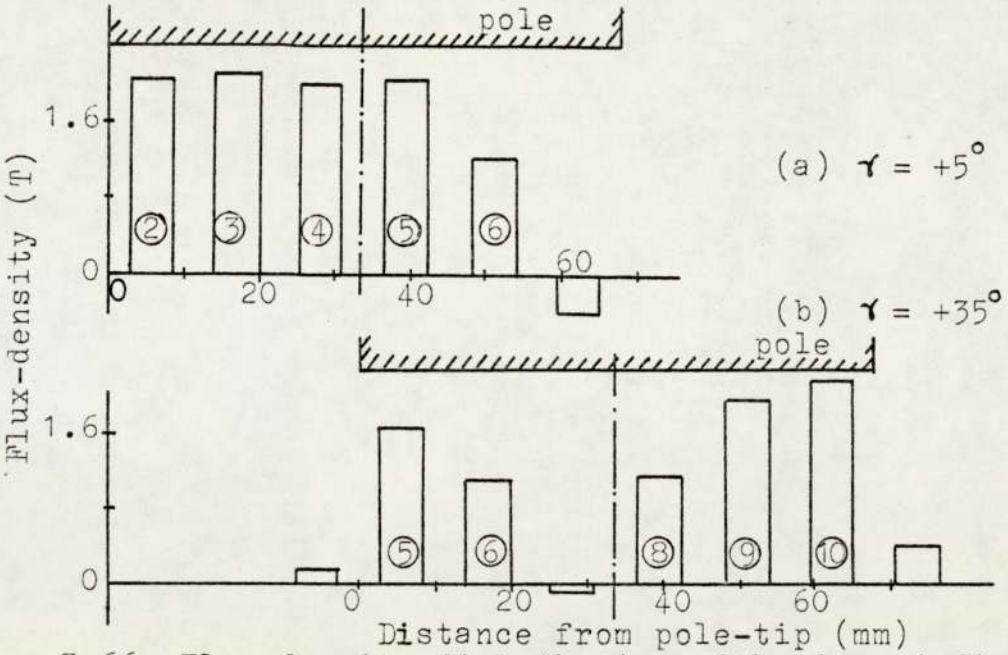

Fig. 3.66 Flux-density distribution with ring winding and field coil excited; values obtained from Fig. 3.65 (incremental movement method)

3.7.2.2.1 Winding inductance

The inductance of the ring winding is estimated using the curves of the flux-density in the teeth given in Fig. 3.65. For each position of the rotor poles, the total flux embraced by the coils of groups A_1, B_1 and C_1 is determined by adding the values of flux through the appropriate teeth (v. Fig. 3.51, p. 130). This procedure is then repeated for groups D_1, E_1 and F_1. The inductance of each of the two combinations of coil groups is determined by multiplying the flux values by the number of turns (N = 50) and dividing by the winding current (I_w = 1.18 A). The total inductance of the ring winding between diametrically opposite tappings is then determined by adding in parallel the inductance values of the two

combinations. The values of the inductance are plotted in Fig. 3.67 (curve i) against rotor position and are seen to vary between 0.92 H and 0.82 H over 120°(m).

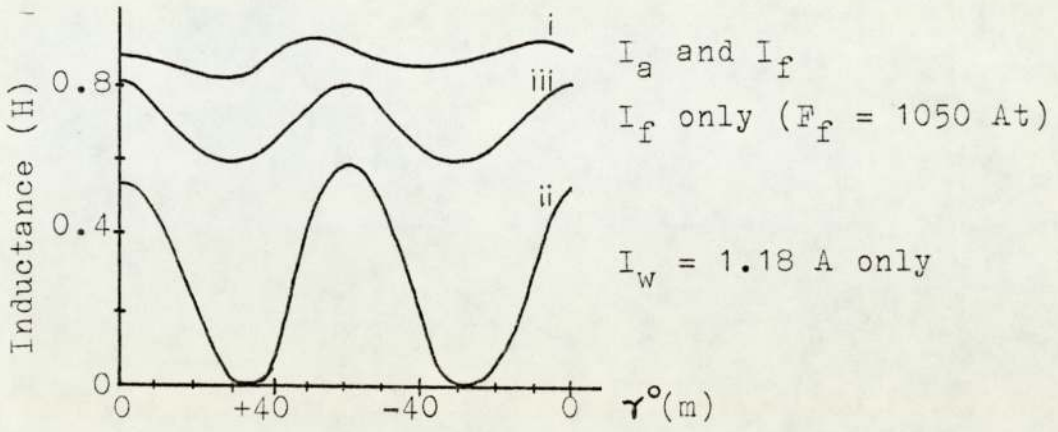

Fig. 3.67 Ring winding inductance

The same procedure is repeated to determine the inductance from the flux-density curves of Fig. 3.64 which was obtained with the commutated-winding only excited. The resultant values are plotted in Fig. 3.67 also (curve ii). Due to the absence of field excitation, the total flux embraced by each combination of coils, e.g., A_1, B_1 and C_1, becomes zero at a particular rotor position. This results in the total inductance between opposite tappings reaching zero twice in 120°(m) of rotor rotation.

The inductance is also determined with the field winding only excited. The values of flux-density in the teeth are obtained from Fig. 3.57, p. 138, and the total flux embraced by the coils is determined at different positions of the rotor poles. The values of inductance are then plotted in Fig. 3.67 (curve iii).

The inductance curves in Fig. 3.67 for the 3 conditions of excitation have two minimum and two maximum values which occur at rotor positions separated by 60°(m), corresponding to a pole-arc (or to a coil-span). Under normal operation of the motor, the variation between maximum and minimum inductance as shown in curve (i) is about 10% of the maximum value.

Fig. 3.68 shows the inductance curves obtained with the same procedure as above, for the 3 conditions of excitation, but for two coil groups, e.g. A and D, in series. These coil groups represent the section of the star winding connected to one of the 3 bipolar circuits of the electronic commutator. This, however, is not an exact representation of the star winding inductance since, in this calculation, the flux embraced by coil groups (A, D) is produced by the current in all the coils of the winding whereas for a star winding this flux would be due to current in $\frac{2}{3}$ of the winding only. The values of inductance for the coil groups (A, D) in a star winding would, therefore, be lower than in Fig. 3.68 by about $\frac{1}{3}$.

The variation in the inductance in Fig. 3.68 (curve i) with both commutated-winding and field coil excited is about 20% of the maximum value. The curves in Fig. 3.68 also apply to the other two pairs of coil groups, i.e., (B, E) and (C, F), for the same rotor position γ°(m).

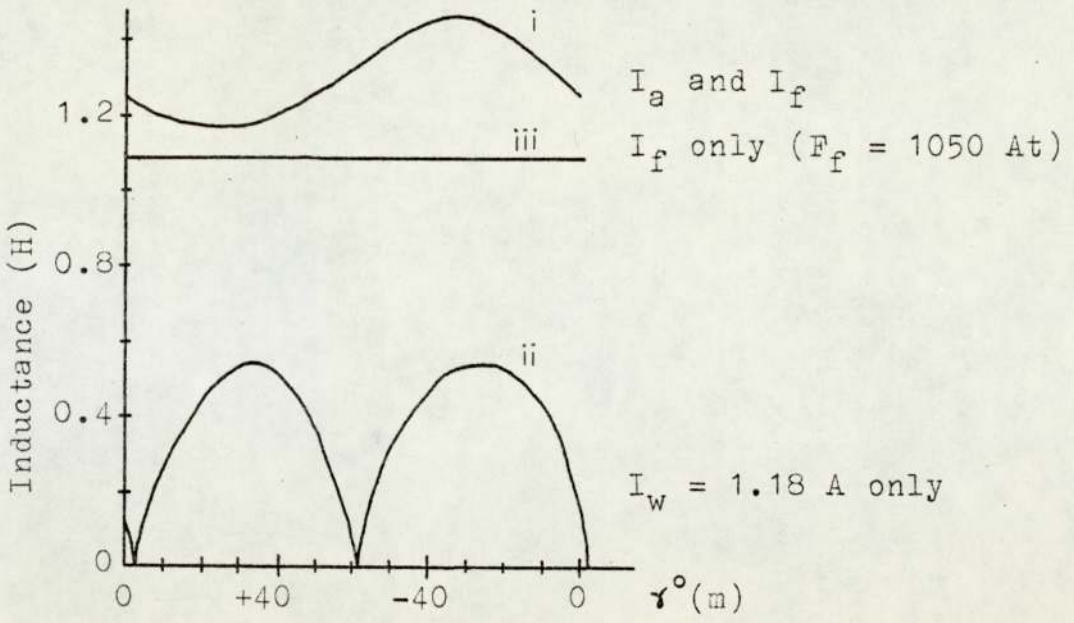

Fig. 3.68 Inductance of coil groups (A, D) in series

Curves (i) in Figs. 3.67 and 3.68 are approximated to sine functions of the angle γ as in the following expressions,

$$L_w = K_1 + K_2 \sin 6\ (75^\circ - \gamma) \qquad \text{Ring} \qquad (3.21)$$

$$L_w = K_3 + K_4 \sin 3\ (300^\circ + \gamma) \qquad \text{Star} \qquad (3.22)$$

where K_1 to K_4 are constants and L_w is the inductance of the winding between opposite tappings. If the winding current is assumed constant then the torque developed by the motor can be determined from the following expression.

$$T_d = -\frac{1}{2} I^2 \frac{dL_w}{d\gamma} \qquad (3.23)$$

Hence

$$\frac{dL_w}{d\gamma} = 6\ K_2 \cos 6(75^\circ - \gamma) \qquad \text{Ring} \qquad (3.24)$$

$$\frac{dL_w}{d\gamma} = -3\ K_4 \cos 3(300^\circ + \gamma) \qquad \text{Star} \qquad (3.25)$$

The values of γ at the maximum and minimum values of T_d can be determined from Equations (3.24) and (3.25) substituted in Equation (3.23). The ideal torque curve is plotted for both types of winding as in Fig. 3.69. The points of maximum and minimum torques obtained from the experimental curves of Fig. 3.15, p. 80, are also marked in the diagram. It should be noted that the curves in Fig. 3.15 were obtained with staggered poles whereas those in Fig. 3.69 are based on measurements with aligned poles. However, the correlation between the theoretical and actual variation is still satisfactory.

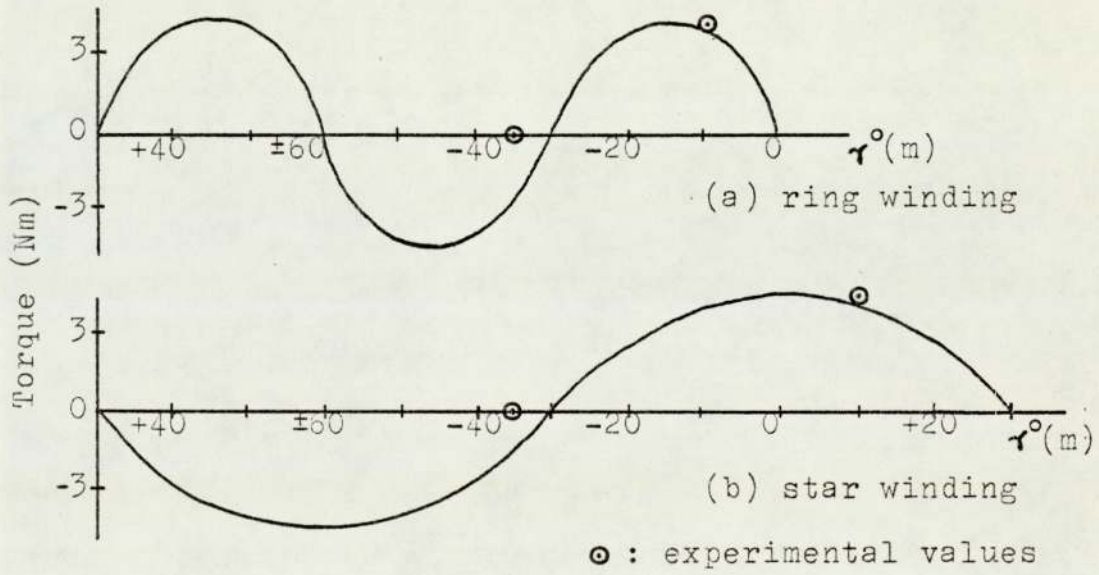

Fig. 3.69 Ideal torque curves

3.7.2.2.2 Flux-density at pole-base

The flux at the pole-base was measured with search-coil 'p' (v. Fig. 3.52, p. 131) connected to the fluxmeter. The values of flux-density are plotted in Fig. 3.70 over 120°(m) of rotor movement. With the commutated-winding

coils only excited, minimum flux-density occurs at γ between -50° and -60° depending upon the number of coils excited. At these positions, flux due to the current in the coils follows a local path only, consisting of the laminations, the air-gap and the poles. The curves in Fig. 3.70 are an indication of the flux-density variation in the rotor-core.

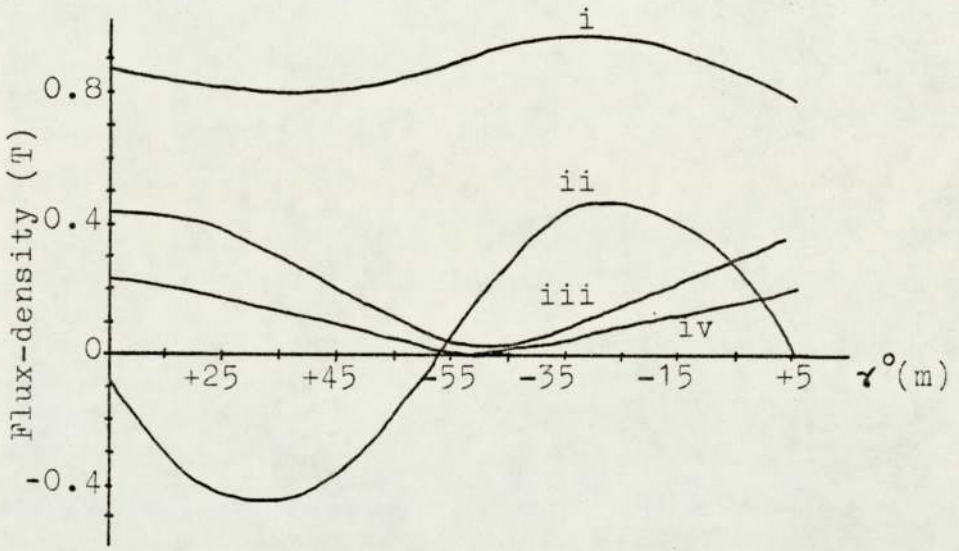

(i) ring winding and field coil excited, F_f = 1050 At, F_a = 708 At/120° (m)
(ii) ring winding only excited, F_a = 708 At/120° (m)
(iii) one coil group excited, F_a = 236 At/120° (m)
(iv) one-half coil group excited, F_a = 118 At/120° (m)

Fig. 3.70 Flux-density at pole-base

The flux-density curve with both ring winding and field coil excited shows a variation between 0.8 T and 1.0 T with flux constantly taking the path through the rotor-core. This variation is attributed to the effect of the changing flux due to the ring winding current on the unidirectional flux due to the field coil.

3.7.3 Dynamic measurements

These measurements refer to the evaluation of flux-density on the pole-face and in the teeth while the machine is rotating. The e.m.f. induced in the search-coils is integrated and then displayed on an oscilloscope. The integrator uses an operational amplifier with R and C equal to 0.1 MΩ and 0.1 μF, respectively.

The widths of some of the search-coils on the pole-surface are multiples of a slot opening. Search-coils 9, 3, 6 and 5 have widths approximately equal to 1, 2, 3 and 4 slot openings. The waveforms of the e.m.f.'s induced in these coils are, therefore, similar to each other. The reason for this similarity is that flux linkage, upon which the e.m.f. depends, changes by the same amount as a search-coil crosses a slot opening, regardless of the width of the coil. The similarity is only slightly lost if the search-coil width is not a multiple of a slot opening.

Fig. 3.71 shows the waveform of e.m.f. induced in search-coil no. 9 and that of the integrated e.m.f. The waveforms in Fig. 3.71 are typical of those of the other search-coils mentioned above. Due to equal changes in the flux linkage, the integrated waveforms as well as the e.m.f. waveforms are similar.

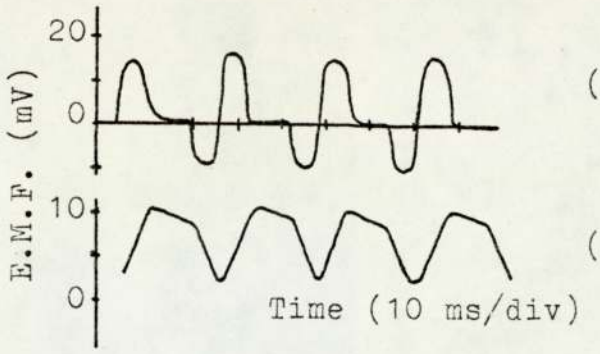

Fig. 3.71 Waveforms of search-coil no. 9 (v. Table 3.11)

The average radial flux-density in the stator teeth can be determined from the integrated e.m.f. waveform. Errors in the electronic integrator cause the higher frequency components to be attenuated resulting in a calculated value of flux lower than the actual value. This error can be minimised by performing the measurements at low rotor speeds thus reducing the actual frequency of the high order harmonics such as those due to slotting.

The flux-density is equal to

$$B = \frac{e_o RC}{A} \qquad \text{(Tesla)} \qquad (3.26)$$

where e_o is the peak voltage of the integrated waveform, A is the search-coil area and R, C are the values of integrator components.

The waveform of the e.m.f. induced in a search-coil around a tooth is shown in Fig. 3.72 along with the integrated waveform. The minor peaks seen between the two main peaks of the e.m.f. waveform are due to slotting. The integrated waveform is not rectangular because of hysteresis in the iron and these minor peaks.

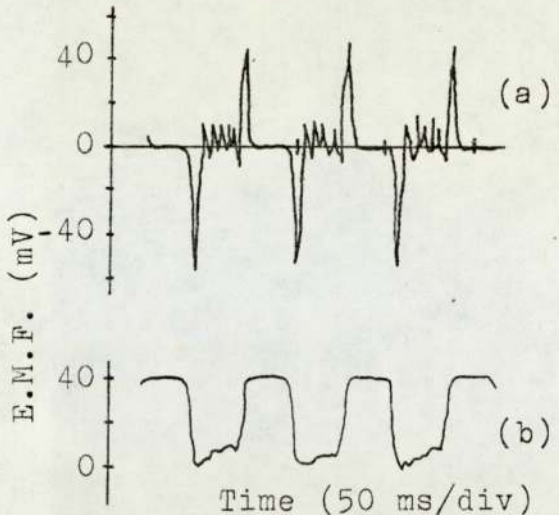

(a) waveform of e.m.f. induced in the search-coil
(b) waveform of the integrated e.m.f.

Fig. 3.72 Waveforms of search-coil around one stator tooth

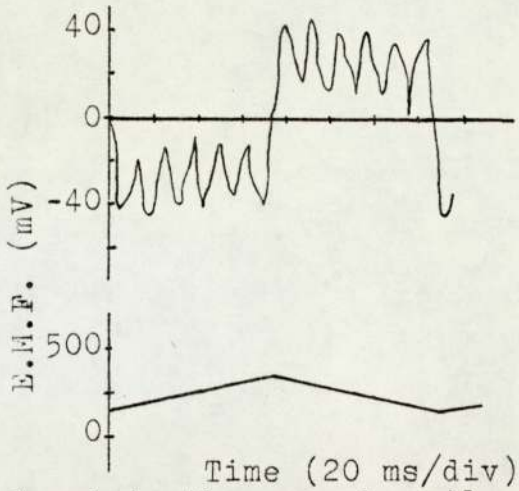

Fig. 3.73 Waveforms of search-coil around base of 6 teeth

Fig. 3.73 shows the waveform of e.m.f. induced in search-coil 's' wound around the base of 6 teeth (v. Fig. 3.51, p. 130), and the integrated e.m.f. waveform.

The waveforms in Figs. 3.71, 3.72 and 3.73 were obtained with the machine operating as a motor, at different values of supply voltage and excitation as given in Table 3.11. The values of e_o and flux-density are also given in the table as determined from Equation (3.26) with R = 0.1 MΩ and C = 0.1 μF.

Search-coil	Fig.	V_s (V)	F_f (At)	I_a (A)	n (rev/min)	e_o (mV)	A (mm^2)	B (T)
No. 9	3.71b	22	450	0.40	73	8	163.2	0.23
Tooth	3.72b	60	1050	0.68	174	40	235.9	0.85
6 teeth	3.73b	50	1050	0.43	135	250	4028.0	0.31

Table 3.11 Waveforms of e.m.f. in search-coils

3.8 Comments

The angle θ is more suitable for tests involving certain coils of the commutated-winding, whereas angle γ is suitable when the complete winding is excited. These two angles are related by the following expression: $\gamma = \theta + 5^{\circ}(m)$. The torque waveforms show that peak torque is about 5% less when operating with a star winding (4 coil groups) than with a ring winding (6 coil groups) for the same conditions of excitation. This means that the motor can operate at moderate values of supply voltage, which is advantageous with power transistors in the electronic commutator.

Torque is developed with the angle γ set between $-44^{\circ}(m)$ and $-4^{\circ}(m)$, for one direction of rotation. However, maximum torque is developed with γ between $-20^{\circ}(m)$ and $-10^{\circ}(m)$. Measurements of back e.m.f. also indicate that the largest values are obtained for the same range of γ, resulting in the maximum developed torque. The rotor poles are axially staggered from each other by half a slot-pitch resulting in e.m.f. and torque waveforms with a considerable reduction of the harmonics at the peak values.

As expected, the mechanical losses of the brushless motor are very small (about 50 W at 1000 rev/min). But the iron losses increase very rapidly with load, reducing

the efficiency and limiting the operating range of the motor.

Flux measurements indicate that for normal motor operation the stator teeth experience a continuous change in the magnitude but not direction of flux. This results in minor hysteresis loops in the iron giving rise to eddy-current and hysteresis losses.

The values of winding inductance based on the flux-density measurements show that the inductance varies within 10% of the maximum value for a ring winding and within 20% for a star winding. The average values for the two windings are about 0.9 H and 1.3 H, respectively.

CHAPTER 4

ELECTRONIC COMMUTATOR

4.1 Chapter outline

The term 'electronic commutator' refers to the group of power transistors used in switching the d.c. supply to the commutated-winding of the brushless motor. The 12 transistors used form 3 units and each is referred to as a bipolar circuit. The operation of one bipolar circuit is discussed in Section 4.2. The operation of the power transistor as a switch is explained in Section 4.3, and reference is made to stepping motor control circuits[6-8] where transistors are extensively used. The details of the base-drive are also given in this section. To improve the switching operation of the transistors, RC snubbers are used as described in Section 4.4. Section 4.5 deals with rotor-position sensing by opto-switches, and the decoding of switching pulses for speed measurement and transistor gating. The operation of the 'logic unit' is also explained in this section.

4.2 The bipolar circuit

In Chapter 3, the brushless motor was tested with a ring type commutated-winding which was convenient for the mechanical commutator used. However, from the torque measurements in Section 3.3, p. 63, it was found that at the same field excitation and winding current, the

reduction in the peak torque developed with a star winding is less than 5% of the value with a ring winding. Also, the discussion in Section 2.5, p. 44, showed that a star winding requires lower values of supply voltage than the ring winding, because of the lower values of e.m.f. induced between opposite tappings at similar excitations and speeds.

Table 2.6, p. 56, shows that the back e.m.f. with the star winding is 2/3 that with the ring winding. Also, by having <u>two</u> pairs of diametrically opposite tappings connected in parallel with the supply at any moment, the resistance R_a between the supply terminals is $R_w/2$. Hence R_a is equal to $2R_g$ and is, therefore, 2/3 the resistance with the ring winding.

To demonstrate the relation between the type of winding and the supply voltage V_s necessary, voltage balance Equation (4.1) is used,

$$V_{sr} = E + I_a R_a \qquad (4.1)$$

where V_{sr} is the supply voltage to the ring winding.
If the power developed is kept constant, then the supply voltage V_{ss} to the star winding is,

$$V_{ss} = \tfrac{2}{3}E + (\tfrac{3}{2}I_a)(\tfrac{2}{3}R_a) \qquad (4.2)$$

Note that, to obtain the same developed power, the winding current, I_a for the star winding is multiplied by 3/2. Subtracting (4.2) from (4.1) shows that the supply voltage can be reduced by (1/3)E when a star winding is used.

An example of the star winding was given in Section 1.1.2, p. 3, together with the possible switching sequences. It is seen from Tables 1.2 or 1.3 that the polarity of the supply to the diametrically opposite tappings must be reversed once every cycle. To facilitate this reversal, two switching devices are connected to each tapping point. Fig. 4.1 shows this connection for one pair of tappings only.

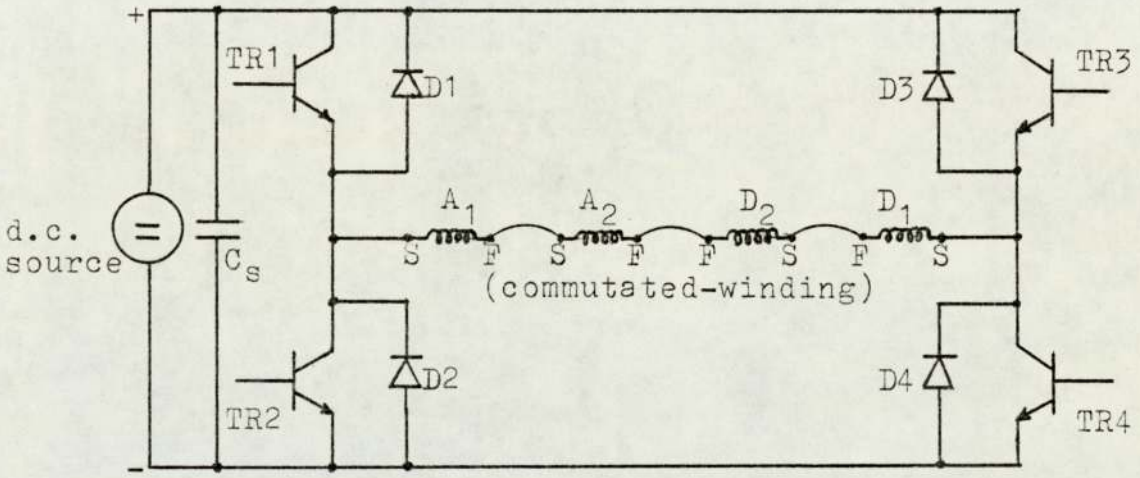

Fig. 4.1 Bipolar drive circuit

The bipolar driver of Fig. 4.1 allows current to flow from A_{1S} to D_{1S} when TR1 and TR4 are ON, and from D_{1S} to A_{1S} when TR2 and TR3 are ON. Each of the 4 transistors remains ON for a definite period of time depending upon the speed of rotation of the motor. This is achieved by controlling the base-drive circuit of the transistors. It is not essential that the turn-on instants of the two transistors of each pair are synchronised, since current can only flow in the winding when both transistors are ON.

At turn-off, the fast-recovery freewheel diodes (Westinghouse type SF5N12, V_{RRM} = 500 V, t_{rr} = 0.2 μs, $I_{F(DC)}$ = 12 A) across the transistors provide a path for the discharge current from the inductive winding. For example, when TR1 and TR4 are turned off, diodes D2 and D3 become forward biased and allow current to flow back into the supply. When D2 and D3 are conducting, the collector-emitter voltage, V_{CE}, of the transistors in parallel with them, i.e. TR2 and TR3, is reversed. This is permissible due to the low forward voltage drop across the diodes.

The electronic commutator requires 3 bipolar circuits for the complete commutated-winding. These are connected in parallel across the supply. Photograph 7a shows the positions of 4 power transistors of one bipolar circuit and the associated base-drives.

The supply in this chapter is the same as in Chapter 3, i.e., a 30 kW d.c. generator with a variable shunt field current. A large capacitor C_s is connected across the supply to provide a path for the discharge current of the winding at turn-off.

4.2.1 Circuit operation

To test each of the drive circuits independently, without driving the brushless motor, transistors TR1 and TR4 in Fig. 4.1 are turned on and off by a timer unit, (v. Appendix A8). The length of the switching pulse, t_p,

is controlled by the unit and can be varied between 1.10 ms and 1.11 s. Idealised waveforms of the collector-emitter voltage V_{CE} across the 4 transistors are shown in Fig. 4.2.

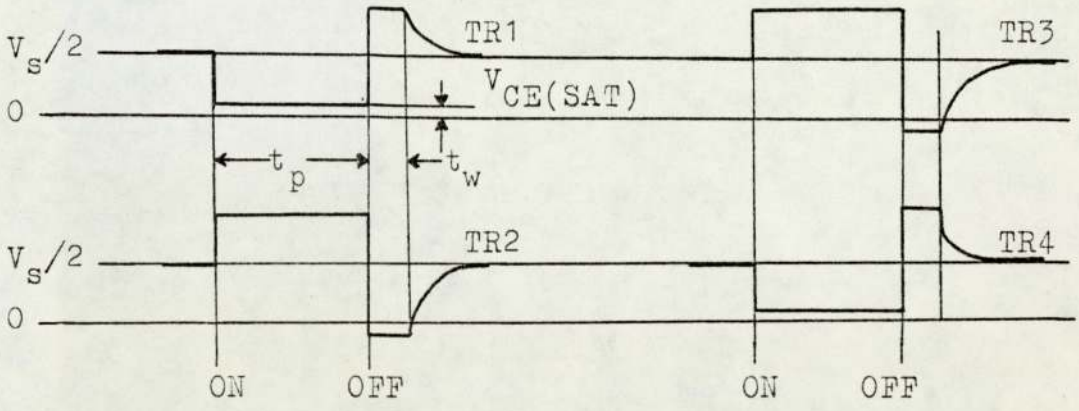

Fig. 4.2 Collector-emitter voltages across the transistors in Fig. 4.1

When the 4 transistors are OFF, the supply voltage V_s is shared equally by the two transistors of each pair, i.e., $V_{CE} = V_s/2$. For the period t_p, transistors TR1 and TR4 are ON and the saturated collector-emitter voltage $V_{CE(SAT)}$ is about 1.2 V. The voltage across either TR2 or TR3 is, therefore, $V_s - V_{CE(SAT)}$.

At turn-off, the freewheel diodes D2 and D3 are forward biased and hence V_{CE} for TR2 and TR3 is slightly negative. The freewheel diodes conduct for the time t_w as shown in Fig. 4.2. The period t_w is a function of the winding current I_w at t_{OFF} and the time constant, τ_w, of the winding.

Fig. 4.3 shows the winding current I_w for various values of t_p. Since there are 3 switching cycles per revolution,

and a transistor pair (e.g., TR1 and TR4) is switched on for $\frac{1}{3}$ of the cycle, then the relation between the speed n and t_p is

$$n = \frac{60}{3 \times 3t_p} \quad \text{(rev/min)} \qquad (4.3)$$

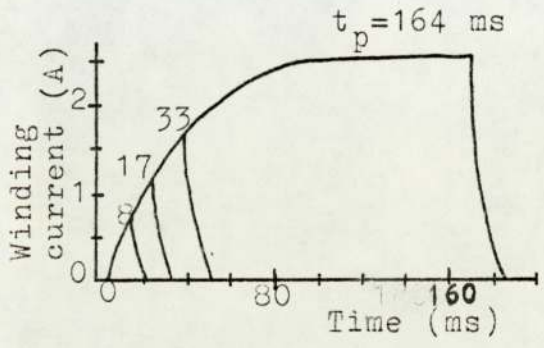

Fig. 4.3 Winding current for various t_p

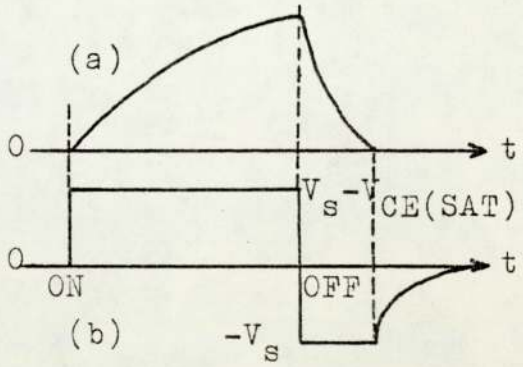

(a) winding current, i_w
(b) winding voltage, v_w

Fig. 4.4 Winding current and voltage waveforms

The values of n corresponding with those of t_p given in Fig. 4.3 are listed in Table 4.1.

t_p	164	33	17	8	ms
n	40.7	202.0	392.2	833.3	rev/min

Table 4.1 Values refer to Fig. 4.3

The equation of the current i_w at turn-on is

$$i_w = \frac{V_s}{R_w}\left(1 - e^{-(R_w/L_w)t}\right) \quad \left(\text{neglecting } V_{CE(SAT)}\right) \qquad (4.4)$$

The time constant τ_w of the winding determined from Fig. 4.3 at i_w equal to 63.2% of the maximum current I_w, was 32 ms. The voltage across the winding rises to the

maximum value in few micro-seconds, which is negligible in comparison with τ_w. From Table 2.6, p. 56, the resistance R_w between opposite tappings of a star winding is $4R_g$ or 19.2 Ω. The winding inductance, L_w, at this rotor position is, therefore, 32 x 19.2 = 614 mH at I_w = 2 A.

At turn-off, the voltage across the winding has the same value as before but it is reversed in polarity as seen in Fig. 4.4. This is because, at turn-off, the freewheel diodes D2 and D3 in Fig. 4.1 are conducting and the tappings are effectively reversed with respect to the supply terminals. The equation of the current curve at turn-off is

$$i_w = \frac{V_s}{R_w}\left(2e^{-(R_w/L_w)t} - 1\right) \qquad (4.5)$$

The time t at which current i_w is zero is equal to $\tau_w(\ln 2)$. The experimental value is less than this because of a slight overshoot in the value of v_w when the polarity changes at t_{OFF}. The induced e.m.f., E, in the winding cannot cause current to flow back into the supply through diodes D1 and D4 since E is less than the supply voltage V_s.

Additions to the bipolar circuit of Fig. 4.1, include a 120 kΩ, 0.5 W resistor connected across the collector-emitter junction of each transistor. These resistors suppress the pick-up power frequency e.m.f.'s across the junction. Since the resistors are permanently connected,

the result is a continuous, but negligible power loss in the electronic commutator, e.g., 1.0 W at V_s = 200 V.

'Klip-Sels'[47] comprising 6 cells were connected between the supply terminals across each bipolar circuit. The clipping voltage of each non-polarized stack is about 375 V.

4.3 Power transistors

Triple-diffused NPN silicon power transistors are used in the bipolar circuits. The manufacturer's technical specification is given in Appendix A9. The power transistors operate in class 'D' mode (v. Fig. 4.5a).

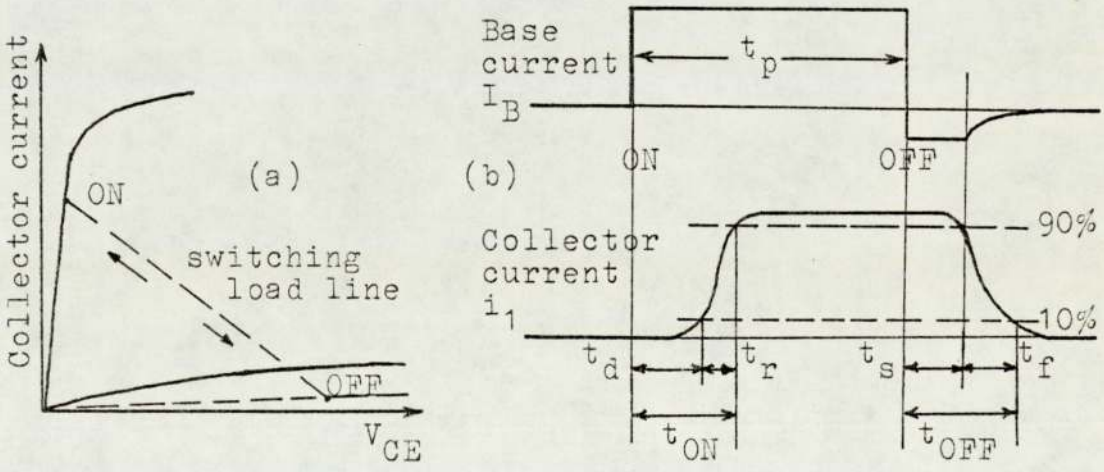

Fig. 4.5 Class 'D' transistor operation

To minimise the leakage current in the OFF state, the base-emitter junction is reverse biased by making V_{BE} negative. However, an excessive negative voltage increases the turn-on time by introducing a delay time

during which the emitter junction capacitance charges up to zero volts[35,36]. The turn-on time consists of the delay and rise times (t_d and t_r) while the turn-off time consists of the storage and fall times (t_s and t_f) as shown in Fig. 4.5b. The turn-off time of a transistor is usually longer than the turn-on time and the aim is to keep both times small to minimise the switching losses.

The requirement in the bipolar circuit of Fig. 4.1, p. 159, is for two transistors with different voltage levels to be switched together. This could be done with a slave circuit[45] which requires careful voltage level setting. Alternatively, each power transistor can be provided with an isolated base-drive, switched from a common triggering signal. The second method, which is used in this work, is more expensive but offers interference-free operation of the electronic commutator.

The base-drive comprises a power supply, an op-amp, and a base circuit which are explained in the following sub-sections. Photograph 7b shows one base-drive unit.

4.3.1 Base power-supply

The ±15 V and +5 V rails of the power-supply are obtained from the 250 V a.c. mains via a step-down transformer, a full-bridge rectifier and integrated circuit d.c. regulators as represented by the schematic diagram of Fig. 4.6.

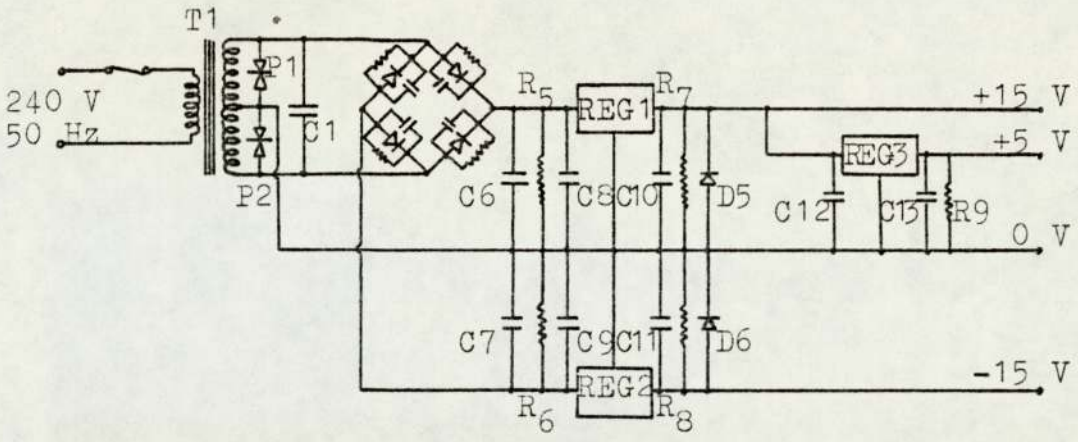

Fig. 4.6 Base-drive power supply

(i) Selenium 'Klip-Sel' voltage surge protectors, P1 and P2, with a limiting voltage of 46 V, are connected across the transformer secondary. The resistance of these Klip-Sels drops considerably as the voltage and/or frequency increase(s), thus providing a low impedance path for any high-voltage transients originating from the supply or generated by switching. Capacitor C1 (0.47 μF) is also connected across the transformer for transient suppression.

(ii) Parallel RC circuits (200 kΩ, 0.01 μF) are connected across the diodes of the bridge rectifier for protection from surges when the voltage across the diodes reverses polarity.

(iii) Resistors R5 and R6 are connected across the output terminals of the bridge to maintain diode conduction at light loads and to discharge the smoothing capacitors. The 10 kΩ resistor results in a continuous power loss of only 0.9 W, which is negligible.

(iv) Smoothing of the rectified waveform is achieved by 1000 μF capacitors C6 and C7 across the output of the diode bridge. The amount of smoothing is not critical because the voltage regulators can operate at a high percentage of ripple; typically within 58% of the maximum input voltage.

(v) To ensure stability of the regulators, the input terminals are bypassed near the integrated circuit package with 4.7 μF Tantalum capacitors, (C8, C9 and C12).

(vi) Regulators 1 and 2 are 1.5 A, 15 V positive and negative d.c. monolithic regulators (LAS 1515 and LAS 1815), respectively, and regulator 3 is a 1.5 A, 5 V positive regulator (LAS 1505).

(vii) High-current diodes D5 and D6 are connected across the output of the ±15 V regulators to protect the regulators from reverse voltages and potential latch-up problems.

(viii) 10 kΩ resistors R7, R8 and R9 maintain the regulators loaded permanently and also provide a discharge path for the 1000 μF capacitors C10, C11 and C13.

4.3.2 Operational amplifier

The second part of the base-drive consists of the integrated circuits and the operational amplifier, shown diagramatically in Fig. 4.7.

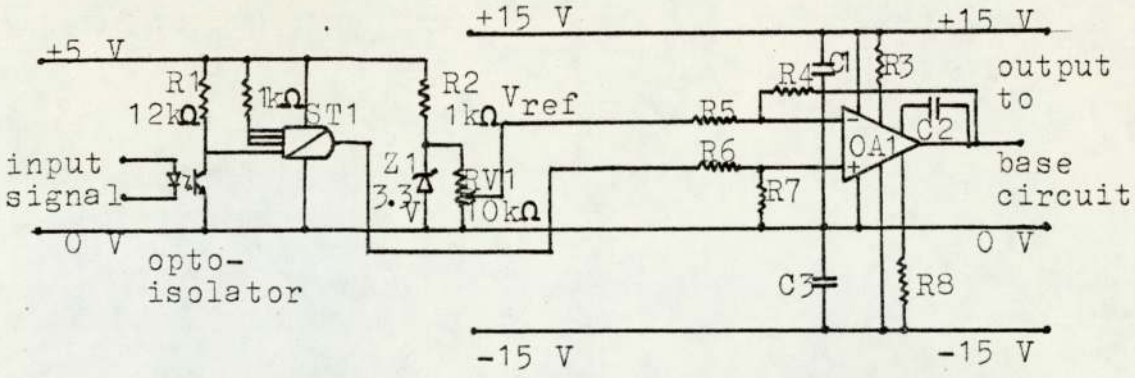

Fig. 4.7 Operational amplifier schematic diagram

An opto-isolator provides the electric isolation required between switching signals and the base circuit of the power transistor. A logic '1' signal to the input of the isolator results in a logic '1' at the output of the Schmitt trigger ST1.

OA1 is a power operational amplifier (National Semiconductor LH0021CK) with a maximum output current of 1.0 A and a slew rate of 3.0 V/μs. The amplifier is connected for differential operation with a closed loop gain ratio of 10/3.9. There are two reasons for using an amplifier in the circuit.

(i) The power level of the input signals is much lower than that required by the base circuit. The input impedance of the amplifier is typically 1 MΩ, and hence would not load the Schmitt trigger.

(ii) The base-emitter voltage V_{BE} of the power transistor is to be reversed when the transistor is OFF. This is easily done with the differential amplifier by adjusting the reference voltage V_{ref} connected to the inverting input.

The time delay between the arrival of the switching signal at the input, and the output of OA1 reaching a maximum value depends on the switching time of the 3 IC's in Fig. 4.7. The output voltage rise times of the Schmitt trigger ST1 and the operational amplifier OA1 are about 1.0 μs and 5.5 μs, respectively. These values are fixed by the components themselves, and do not depend on the external circuit.

The fall time of V_{CE} for the opto-transistor depends upon the signal current I_D in the opto-diode. A high value of I_D would ensure a short fall time but would reduce the lifetime of the device. Hence a moderate I_D of about 6 mA was chosen giving a fall time of about 17 μs. The total delay, therefore, between the signal and the output of OA1 reaching the maximum value, is about 23 μs. This is shown in Fig. 4.8a for an input signal which rises to the maximum value in less than 1 μs.

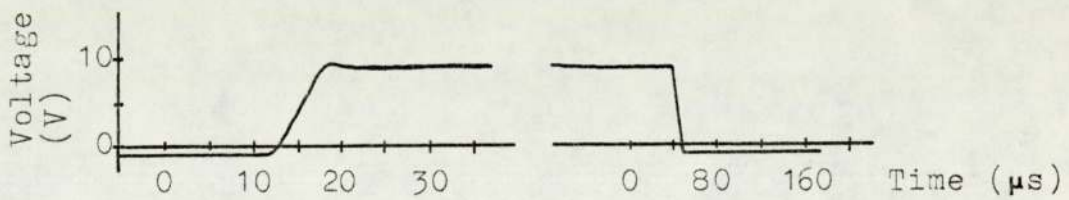

(a) turn-on (b) turn-off

Fig. 4.8 Output voltage of OA1 (I_D = 6mA)

Turn-off time depends on the rise time of the opto-transistor and on the fall time of OA1. It takes about 40 μs for V_{CE} of the opto-transistor to become high enough for ST1 to change state. The fall time of OA1 is about

8 μs (v. Fig. 4.8b). The total turn-off time is, therefore, about 48 μs which is more than twice the turn-on time.

4.3.3 Base circuit

The output from OA1 is connected to the base terminal of the power transistor as in Fig. 4.9.

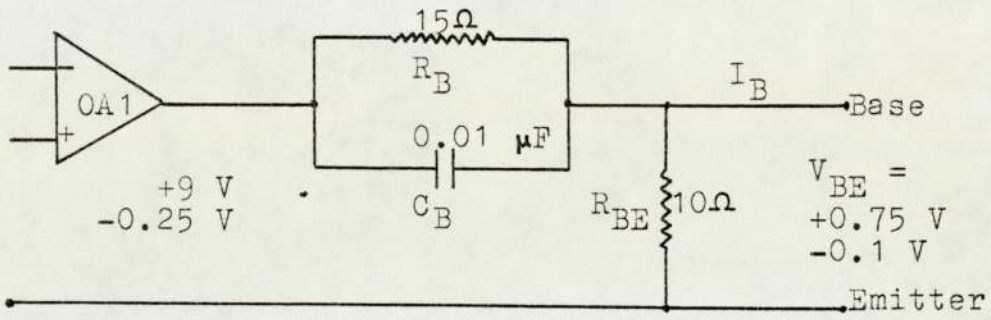

Fig. 4.9 Base circuit

R_B is chosen so that the base current I_B is about 0.55 A. This value is sufficient to operate the transistor in the saturated region for the maximum collector current I_1 expected. Waveforms of I_B and V_{BE} are shown in Figs. 4.10 and 4.11, respectively, at turn-on and turn-off.

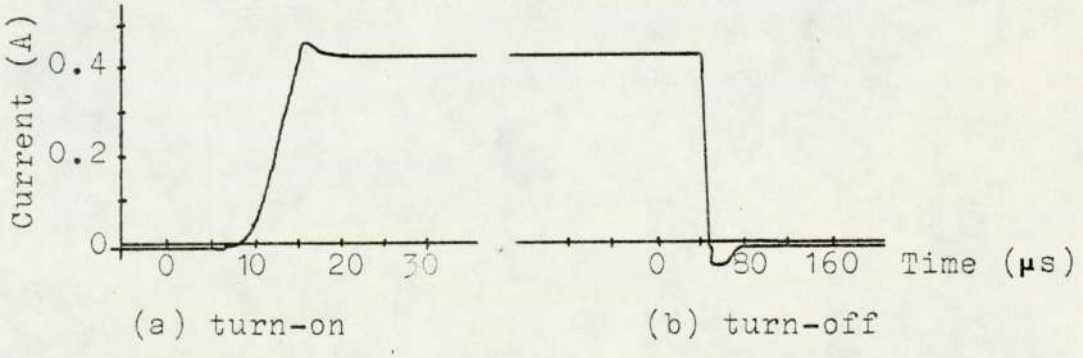

Fig. 4.10 Transistor base current, I_B

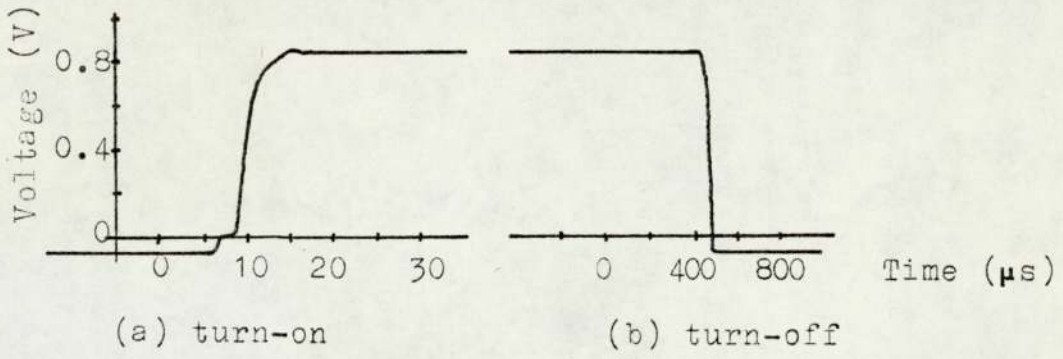

(a) turn-on (b) turn-off

Fig. 4.11 Base-emitter voltage, V_{BE}

The value of C_B was determined experimentally for the maximum value of collector current by observing the waveforms of V_{CE} and V_{BE}. The storage time at turn-off can be reduced with C_B, but a limit is set by the onset of oscillations in the base-emitter voltage.

The RC circuit in Fig. 4.9 affects the switching time in two ways:

(i) The rise time t_r, reduced by the overshoot in I_B and seen in Fig. 4.10a as the steepness of the forward base pulse, is preserved by the capacitor C_B.

(ii) The storage time t_s is reduced by the RC circuit. The capacitor reverse biases the base-emitter voltage thus aiding the reverse base-drive. This results in a fast fall of I_B to zero followed by a reversal in direction as seen in Fig. 4.10b. A large negative value of I_B assists the collector current in removing the minority carriers thus reducing t_s.

The base-emitter resistance R_{BE} reduces the possibility of transistor instability, which results in leakage current variation with temperature, and also increases the $V_{CE(SUS)}$ to 500 V. Parasitic oscillations in the base circuit are eliminated by this damping resistor.

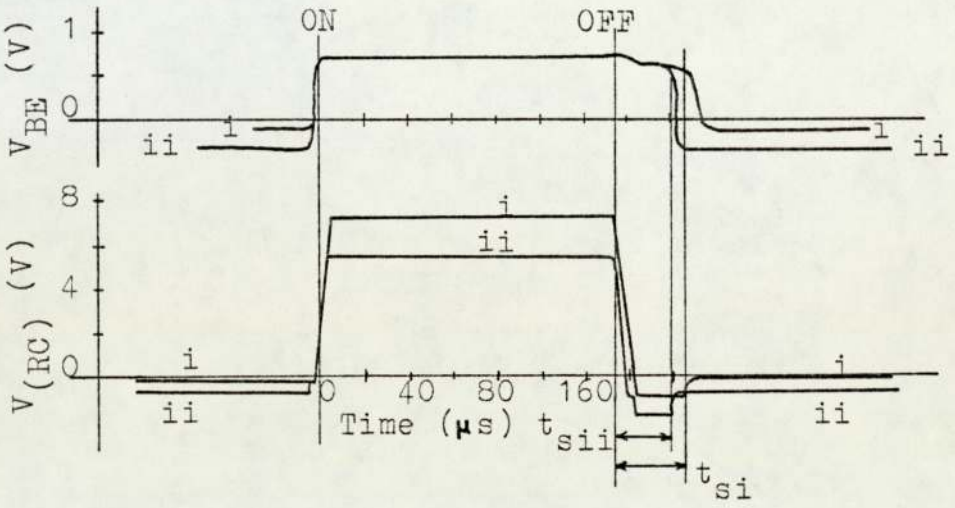

Fig. 4.12 Voltages in base circuit

Fig. 4.12 shows waveforms of V_{BE} and the voltage across the RC circuit, $V_{(RC)}$, at turn-on and turn-off. The curves (i) and (ii) correspond to two settings of the reference voltage V_{ref} to the inverting output of amplifier OA1 in Fig. 4.7, p. 168, resulting in the negative and positive voltages given in Table 4.2.

Curve	V_{OA1}	V_{BE}	$V_{(RC)}$
i	-0.25	-0.1	-0.15
ii	-1.0	-0.3	-0.70
i	+8.00	+0.75	+7.3
ii	+6.35	+0.75	+5.6

Table 4.2 Voltages in base circuit (in volts) (v. Fig. 4.12)

A large negative base bias at turn-off (as in (ii)) reduces both the storage time t_s and the fall time t_f. The reduction in the positive voltage drop across RC, i.e. $V_{(RC)}$ in (ii), results in a fall in the forward base current I_B. This is corrected by adjusting the value of R_B.

4.4 The snubber circuit

Switching the inductive winding with the circuit of Fig. 4.1, p. 159, causes the voltage across the transistors being switched off, e.g., TR1 and TR4, to reach values several times that of the supply voltage V_s. This is unacceptable since the normal operating voltage must then be reduced well below the maximum $V_{CER(SUS)}$.

An alternative method of reducing the turn-off voltage is to connect snubber circuits across the power transistors. A discussion of the choice of suitable values of components is given in Section 4.4.4.

Apart from improving the reliability of the power transistors by controlling the I_1/V_{CE} loci, switching losses are also reduced by the use of snubber circuits. A further reduction in losses is made possible by the reduction of switching times as will be explained in Section 5.3, p. 216.

4.4.1 Turn-off loci

Fig. 4.5a, p. 164, showed the switching locus at turn-off with a resistive load. This is reproduced together with typical loci for capacitive and inductive loads in Fig. 4.13a. Here the inductive locus is limited by the freewheel diodes.

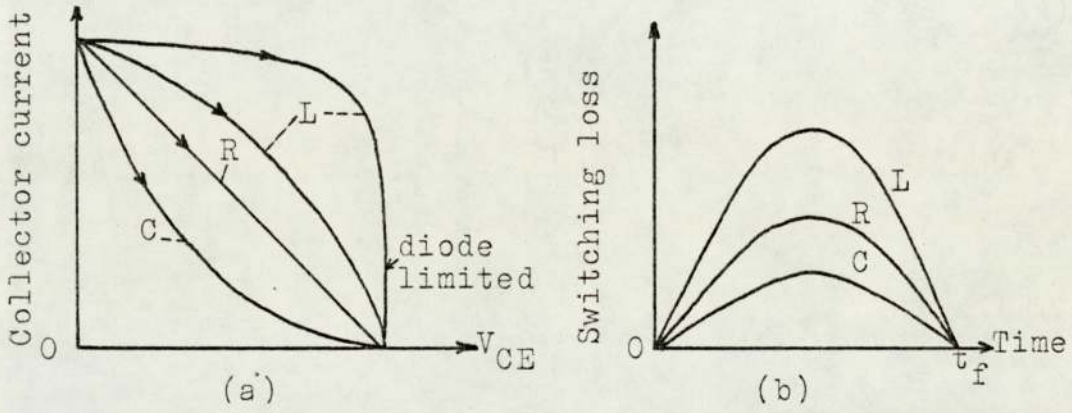

Fig. 4.13 Turn-off loci and losses with R, L and C loads

The power loss at turn-off equals $V_{CE}I_1$ for the time duration t_f. This is shown in Fig. 4.13b for the three types of load. It is evident that a capacitive load causes the least switching loss, has the best switching locus, and is least likely to cause secondary breakdown. Hence if the switching losses normally associated with the inductive winding are not to be dissipated in the transistor, the switching locus must be made to appear as much capacitive as possible. This is achieved by the snubber circuits as explained in the following Section 4.4.2.

4.4.2 Operation of the snubber circuit

The simplest snubber circuit consists of a combination of resistor, diode and capacitor. More complex versions comprise a combination of more than one of these components and can sometimes include several small inductors. References 48 to 52 give several connections of these components across each power transistor. In this project, the snubber circuits are connected as shown in Fig. 4.14. Each circuit has two time constants: a very short one through the diode and a much longer one through the resistor.

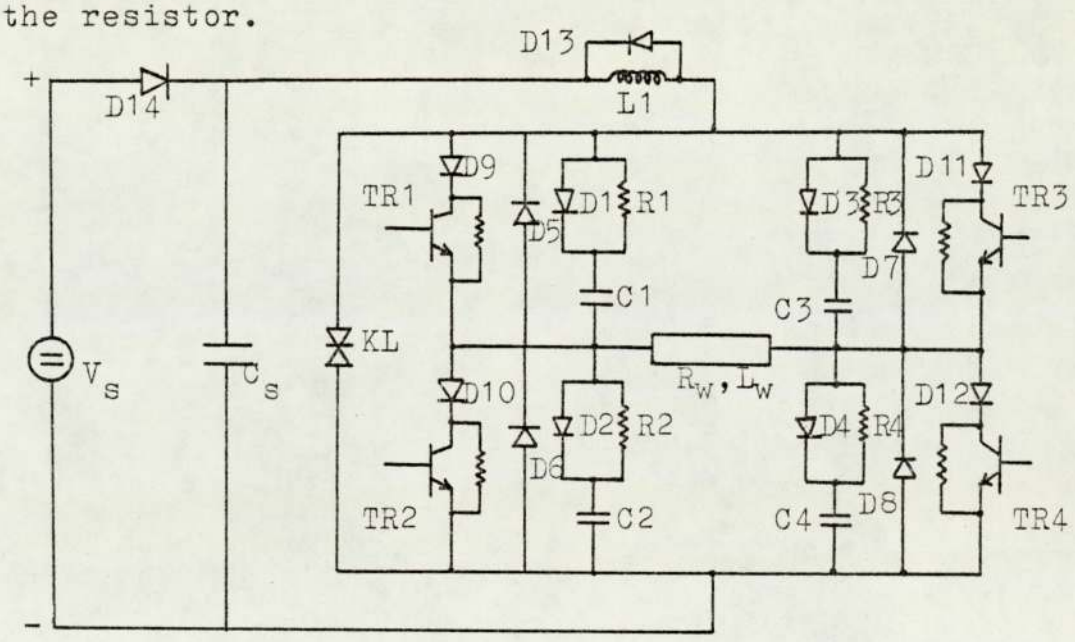

Fig. 4.14 Complete bipolar circuit

Fig. 4.15 shows waveforms of voltage and current of the transistor pair TR1 and TR4, and of the associated snubber circuits at turn-off. The winding current i_w remains practically constant during the time taken for

the transistor to turn off (typically few micro-seconds). The collector current i_1 falls rapidly to zero, being transferred to the snubber capacitors, (I_{C1} and I_{C4}). The voltage V_{CE} is held at a low value by the snubber capacitors, which require a finite time to charge, and hence V_{CE} is still quite low when the collector current has collapsed.

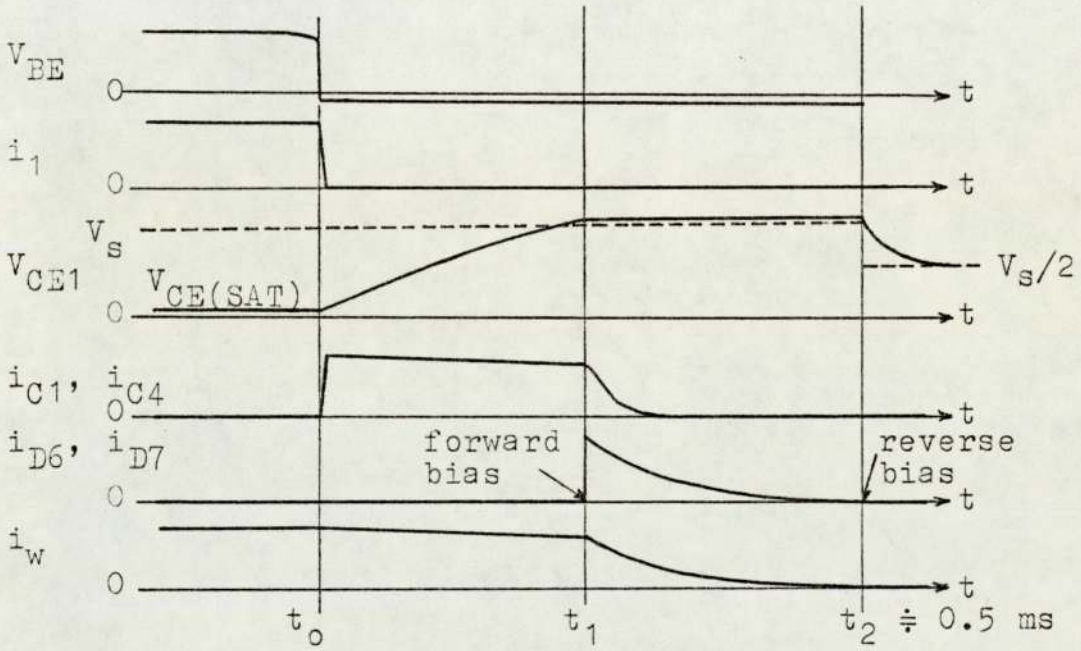

Fig. 4.15 Turn-off waveforms

Winding current continues to flow through the snubber capacitors until V_{CE} is slightly above V_s. Then the freewheel diodes D6 and D7 become forward biased, providing a path for the discharge current of the winding back into the capacitor C_s connected across the supply. The decay current through the freewheel diodes is determined by the winding inductance and resistance, and the capacitor C_s as shown in Fig. 4.16. The initial conditions in the circuit are the capacitor voltage V_s and the current I_o in the winding inductance.

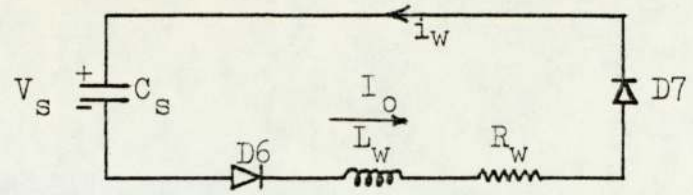

Fig. 4.16 Current path at t_1 after turn-off

$$i_w = I_o\, e^{-\xi\omega_n t} \cos\left(\omega_n\sqrt{1-\xi^2}\right)t - \left(\frac{V_s}{L_w} + \xi\omega_n I_o\right)\frac{e^{-\xi\omega_n t}}{\left(\omega_n\sqrt{1-\xi^2}\right)}\sin\left(\omega_n\sqrt{1-\xi^2}\right)t \qquad (4.6)$$

The damping factor is $\xi = \frac{1}{2} R_w\sqrt{\frac{C_s}{L_w}} = \frac{\omega_n C_s R_w}{2}$

and the natural frequency is $\omega_n = \frac{1}{\sqrt{L_w C_s}}$

The forward voltage drop across the freewheel diodes is neglected in Equation (4.6) for simplicity. The other assumption is that the winding inductance L_w remains constant during turn-off.

V_{CE} rises after turn-off to the maximum value with a slight non-linearity caused by the slightly decreasing winding current. The rate of change of V_{CE} with time is given approximately by $I_o/2C1$.

After the freewheel diodes become reverse biased at t_2 (Fig. 4.15), V_{CE} across each transistor returns to $V_s/2$. The shape of the curve is determined by the snubber capacitors and the current paths when charging and discharging, as will be explained from the experimental results in Section 4.4.5.

4.4.3 Effect on turn-on

At turn-on, the bipolar switching circuit of Fig. 4.14 behaves like the circuit shown in Fig. 4.17.

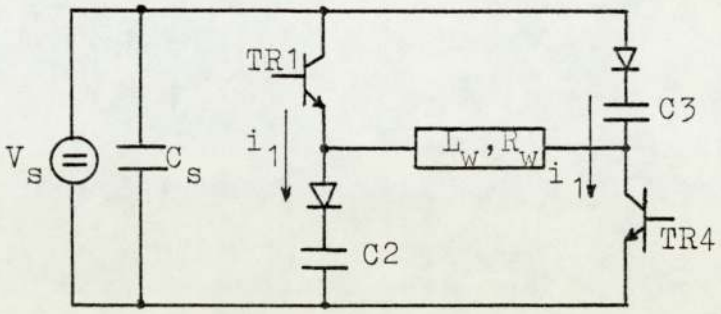

Fig. 4.17 Bipolar circuit at turn-on

The winding inductance is large, and during the first few micro-seconds after switching, it can be assumed infinite. The transistor current is then limited only by its own saturated impedance and the wiring impedance. Hence a large current, sufficient to destroy the transistor, flows until the capacitors have charged up to almost the supply voltage V_s. The capacitor voltages cause a potential difference between the tappings of the winding and the winding current rises exponentially. The two effects can be separated because the time constant of the capacitor charging circuit is of the order of micro-seconds while that of the winding is of the order of milli-seconds.

To limit the initial surge current to a safe value, a resistor or inductor can be connected in series with the snubber diode. A resistor of several hundred ohms would be required and would result in a large power loss at

turn-off when the winding current is transferred from the transistor to the snubber circuit. A resistor would also increase the charging time of the capacitor at turn-off, impeding the effectiveness of the snubbers. An inductor would eliminate the 'short-circuit effect' of the snubbers, but it would also cause unacceptable oscillations in V_{CE} at turn-off, with voltages reaching several times the supply voltage.

As an alternative, a small inductor L1 connected in series with the supply would reduce the high turn-on transients. The turn-off process need not be affected if a diode D13 is connected in reverse parallel across the inductor as shown in Fig. 4.14. This is done to provide a path for the winding discharge current.

4.4.4 Selection of values

The 'short-circuit effect' of the snubbers mentioned in the previous section is illustrated in Fig. 4.18 by waveforms of transistor TR1 collector current i_1 at turn-on. The amplitude of the initial transient increases with the value of snubber capacitor C2.

This transient current includes the discharge current of the parallel capacitor C1 which is controlled by the resistance R1. Fig. 4.19 shows the effect of varying R1 with constant C1 and C2. The discharge current is naturally small at high values of R1.

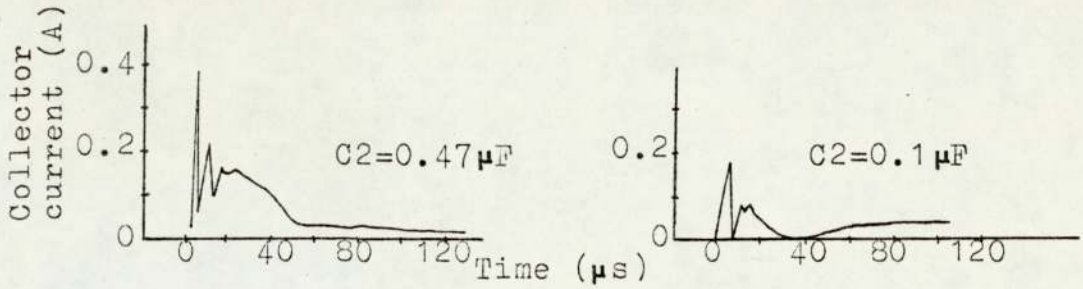

Fig. 4.18 Effect of snubber capacitor, V_s = 17 V, R1 = 1 kΩ

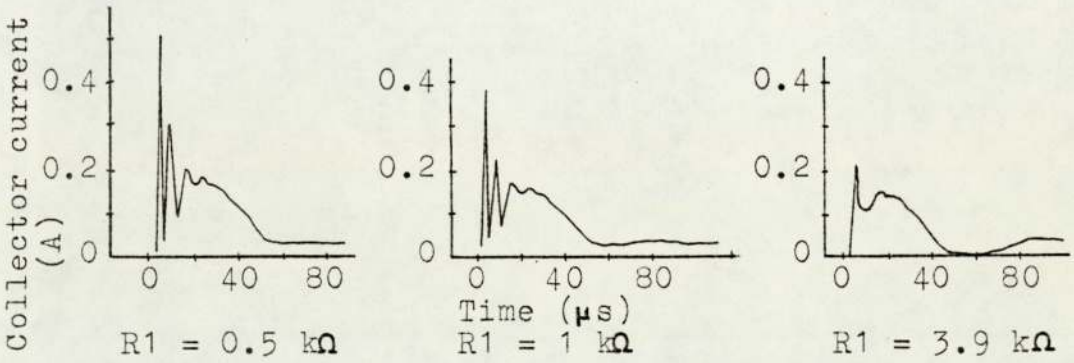

Fig. 4.19 Effect of snubber resistor, V_s = 17 V, C2 = 0.47 μF

To limit the transient current due to the 'short-circuit effect', a 1.3 mH air-core inductor L1 is connected in series with the supply. Fig. 4.20 shows that at V_s = 17 V, the peak transient is reduced by $\frac{2}{3}$ the value without the inductor. It is also apparent there, that the rate of rise of collector current i_1 is greatly reduced by the addition of the inductor.

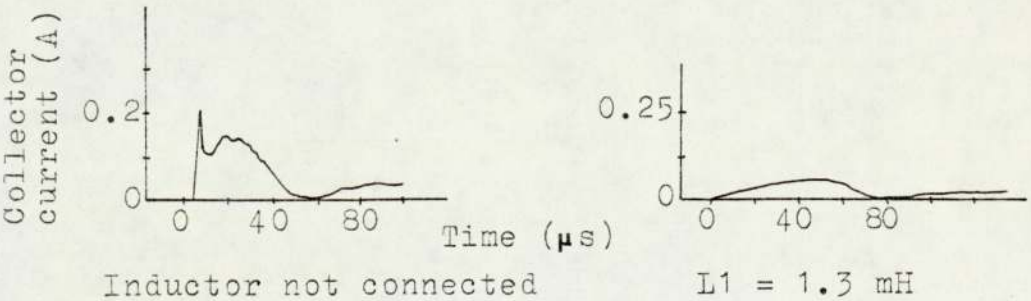

Fig. 4.20 Effect of series inductor, V_s = 17 V, R1 = 3.9 kΩ, C1 = 0.47 μF

The waveforms in Fig. 4.21 were obtained at turn-off for two values of snubber capacitor C1. In Fig. 4.21a, the maximum value of V_{CE} is closer to the supply voltage V_s at high values of C1. The rate of rise of V_{CE} with time is also reduced at high values of C1, allowing the winding current to flow in the snubber circuit for a longer time as seen in Fig. 4.21b. It was mentioned in Section 4.4.2 that the freewheel diodes D6 and D7 cannot conduct after turn-off unless V_{CE} becomes slightly higher than V_s. Between the instant of turn-off and the time of freewheel diode conduction, the winding current is carried by the snubber circuit instead of the transistor.

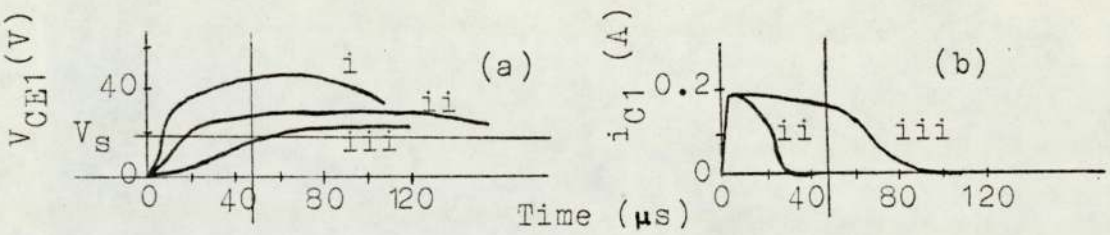

(i) no snubbers, (ii) C1 = 0.1 μF, (iii) C1 = 0.47 μF

Fig. 4.21 Turn-off waveforms

Immediately after turn-off, the snubber capacitor charges up to a voltage of $I_o t_f/2C$ in excess of $V_{CE(SAT)}$, where I_o is the winding current at turn-off and t_f is the fall time of the transistor. The fall time is typically 1 μs and for I_o = 2 A and C at say 0.5 μF, the additional voltage is 2 V. The value of $V_{CE(SAT)}$ at 2 A is, from Appendix A9, about 0.25 V, and hence the voltage to which the snubber capacitor charges immediately after turn-off is 2.25 V.

Following that, the time taken for C to charge up to a value slightly higher than V_s is CV/I_o. This time period is shortest when the supply voltage is lowest, say 20 V. Therefore, V = 20 - 2.25 = 17.75 V, and t = 0.5 (17.75)/2 = 4.4 μs. This means that the shortest time period between turn-off and freewheel diode conduction is about 5 times the fall time of the transistor.

The value of R of the snubber circuit must be high enough to limit the discharge current of the capacitor through the transistor at turn-on. But it should not be so large that the capacitor is not fully discharged by the end of the switching cycle. It is satisfactory in practice to have a discharge time constant about 30% of the shortest period a transistor is ON.

At the top speed of 1000 rev/min, the operating frequency of the power transistors is 50 Hz. The ON time is, therefore, 6.7 ms and τ_{RC} would be 0.3 (6.7) = 2 ms. Since C was determined as 0.5 μF, then R = 4 kΩ.

In the circuit of Fig. 4.14, p. 175, the values of the snubber circuit components are:

C1 = 0.47 μF

R1 = 3.9 kΩ

τ_{RC} = 1.83 ms

4.4.5 Experimental results

The results of tests performed on the bipolar circuit of Fig. 4.14 are divided into turn-on and turn-off.

4.4.5.1 Turn-on

The transient collector current at turn-on is shown in Fig. 4.22 at 3 values of supply voltage. The peak value of current is dependent upon the supply voltage V_s, and a relation between i_1 and V_s can be given based on the curves of Fig. 4.22.

$$\text{Peak transient } i_1 = V_s/285 + V_s/2R1 \qquad (4.7)$$

The first term of Equation (4.7) depends upon the impedance of the current path in the circuit of Fig. 4.17, p. 178 and the second refers to the discharge current of C1 (Fig. 4.14).

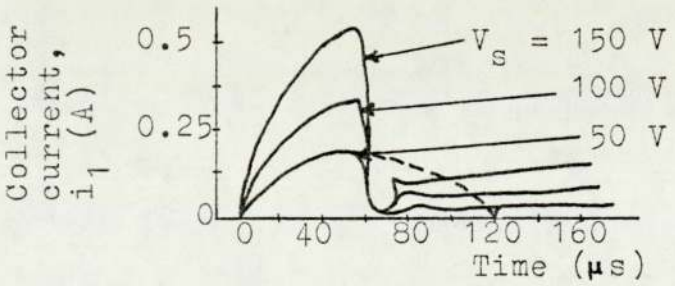

Fig. 4.22 Effect of supply voltage on turn-on, R1 = 3.9 kΩ, C2 = 0.47 μF

Capacitor C_s across the supply is essential at turn-off but it affects the turn-on transient. At high values of C_s, the voltage across the bipolar circuit is less

affected by turn-on and thus remains almost constant. This results in higher transient values at turn-on, but in a shorter charging time for the snubber capacitor C2. The value of the capacitor used as C_s was 10 μF. Larger values cause little further change to the switching transients.

Fig. 4.23 shows waveforms of voltage and current at turn-on in more detail. The supply voltage drops slightly while capacitor C2 charges up from $V_s/2$ to V_s. The series inductor L1 causes a gradual rise in the transient current and the voltage drop across it is equal to:

$$V_{L1} = V_s - V_{C2} - V_d \qquad (4.8)$$

where V_d is equal to the saturation voltage V_{CE} of transistor TR1 plus the forward voltage drops across diodes D9 and D2.

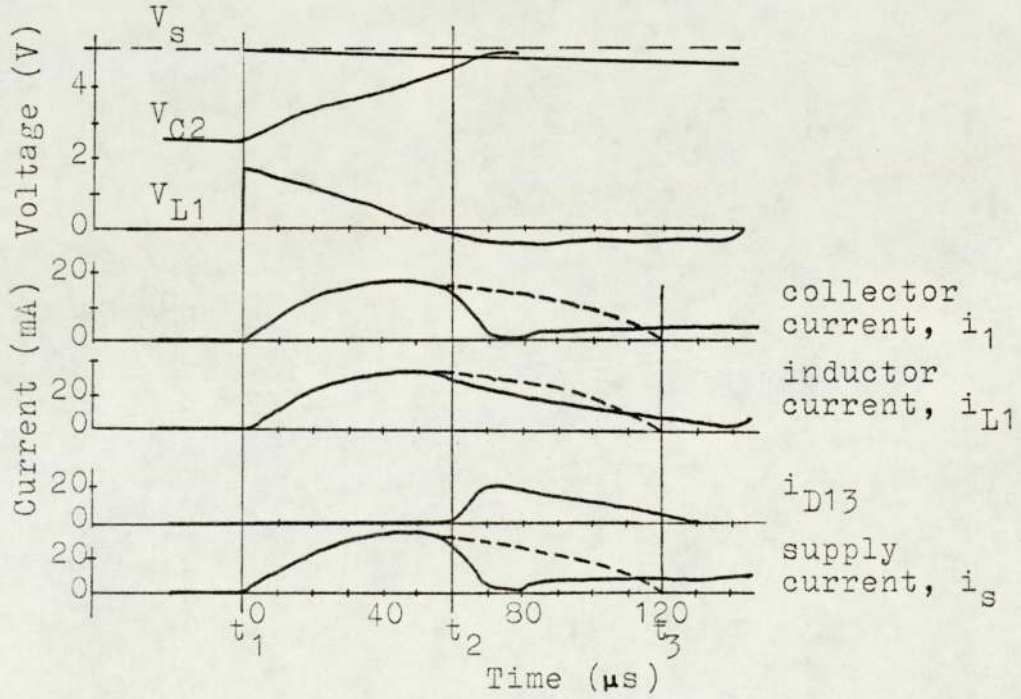

Fig. 4.23 Turn-on waveforms, V_s = 5 V

The collector current i_1 continues to rise until V_{C2} exceeds V_s by a certain amount, enough to forward bias diode D13. V_{C2} can exceed V_s in the oscillatory circuit formed by L1 and C2. Current, therefore, circulates in the inductor L1 and diode D13 connected across it, resulting in the sudden cessation of the transient current i_1. Following that, transistor TR1 carries the winding current only, i.e., $i_1 = i_w$.

Diode D13 remains conducting for about 80 μs, depending upon the values of the components used in the circuit. During this period, current in the inductor L1 is higher than that in diode D13 by the small amount of the winding current i_w as can be seen from the waveforms. If diode D13 is disconnected, the transient currents would fall off gradually to zero along the dotted curves in Fig. 4.23. The time period t_1 to t_3 can be determined from the values of L1 and C2. Thus

$$t = \pi\sqrt{(L1)(2C2)} \qquad (4.9)$$

$$t = \pi\sqrt{(1.3 \times 10^{-3})(2 \times 0.47 \times 10^{-6})} = 110\ \mu s$$

This is approximately the same as the time period in Fig. 4.23. The value of C2 is doubled in Equation (4.9) since two snubber capacitors, C2 and C3, are being charged simultaneously at turn-on.

4.4.5.2 Turn-off

After transistors TR1 and TR4 are turned off, the respective snubber capacitors C1 and C4 gradually charge up to slightly above the supply voltage. Fig. 4.24 shows the rise in V_{CE} across TR1 versus time for various values of i_1 at turn-off, while the winding current is being carried by the snubber circuit. The initial rate of rise of voltage (V/t) is equal to (i_1/C), and if C is constant, this is proportional to i_1.

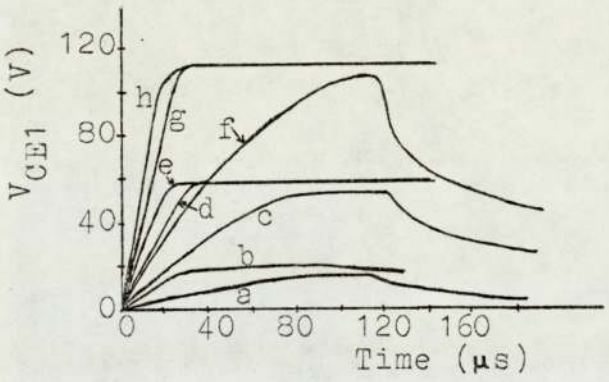

	i_1	V_s
a	0.29 A	17 V
b	0.4 A	
c	0.57 A	50 V
d	0.73 A	
e	0.87 A	
f	0.72 A	100 V
g	1.0 A	
h	1.22 A	

Fig. 4.24 Collector-emitter voltage at turn-off, R1 = 3.9 kΩ, C1 = 0.47 μF

In Fig. 4.25, line (i) represents the theoretical relation between (V/t) and the current, and line (ii) is the mean of the values obtained from the experimental curves of Fig. 4.24. For a particular value of i_1 the experimental rate of rise of voltage is less than the theoretical value since the winding current, which is i_1 at the instant of turn-off, decreases slightly as the snubber capacitors charge.

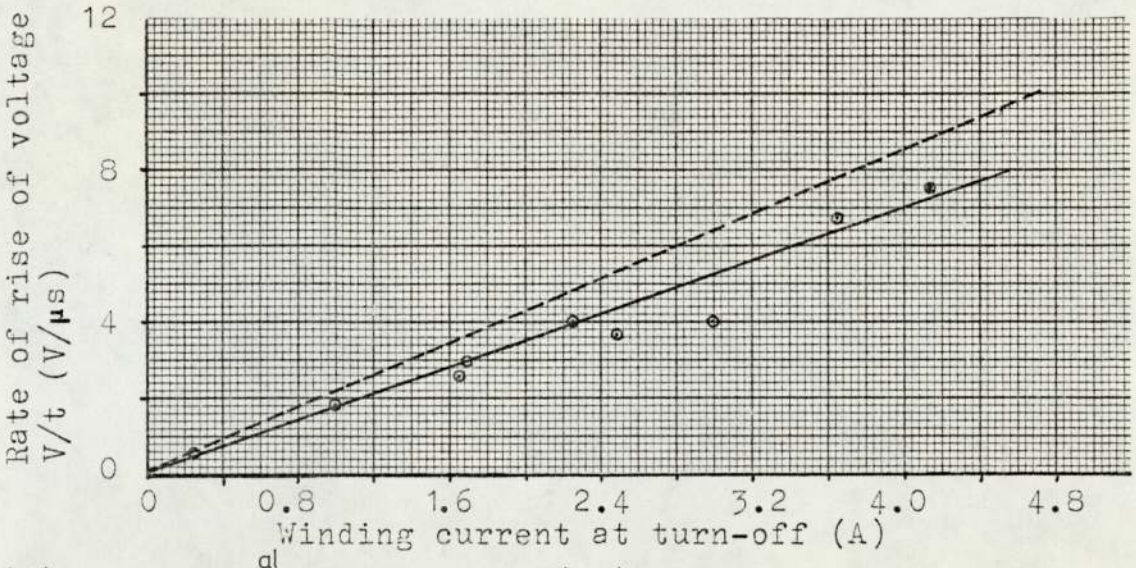

(i) Theoretical curve ----- (ii) Experimental curve ——

Fig 4.25 Rate of rise of voltage vs. winding current

The waveforms in Fig. 4.26 were obtained at various points of the bipolar circuit of Fig. 4.14, p. 175, at turn-off. The time intervals marked on the waveforms are as follows:

t_1 : the start of the fall time of TR1 and TR4.

t_2 : freewheel diodes D6 and D7 become forward biased.

t_3 : voltage across the bipolar circuit, V_B, is higher than V_s; the current i_{C1} in the snubber capacitor starts to fall; the current i_{D13} starts to rise.

t_4 : peak values of current are reached in the freewheel diodes D6 and D7, the diode across the inductor D13, and in C_s connected across the supply.

t_5 : diode D13 is reverse biased; the input current i_{in} (through diode D14) is zero.

In the interval t_1 to t_2 the voltage V_{CE} across TR1 is rising as capacitor C1 is charging. At t_2, V_{CE} is sufficiently above V_s for D6 to be forward biased and the

discharge current starts to rise. Between t_3 and t_5, the voltage V_B across the bipolar circuit is higher than the supply voltage V_s and, therefore, diode D13 across the inductor is forward biased. This is similar to the interval t_2 to t_3 at turn-on in Fig. 4.23, p. 184. But at turn-off, current circulating between diode D13 and inductor L1 stops after some time and the inductor as well as the diode carry the discharge current back into the capacitor C_s across the supply.

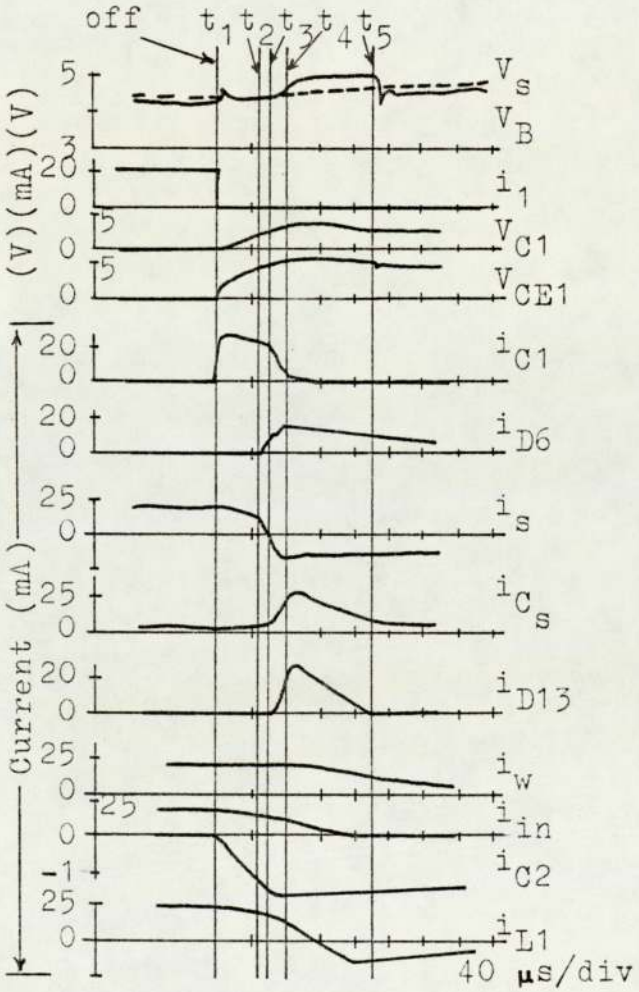

Fig. 4.26 Turn-off waveforms

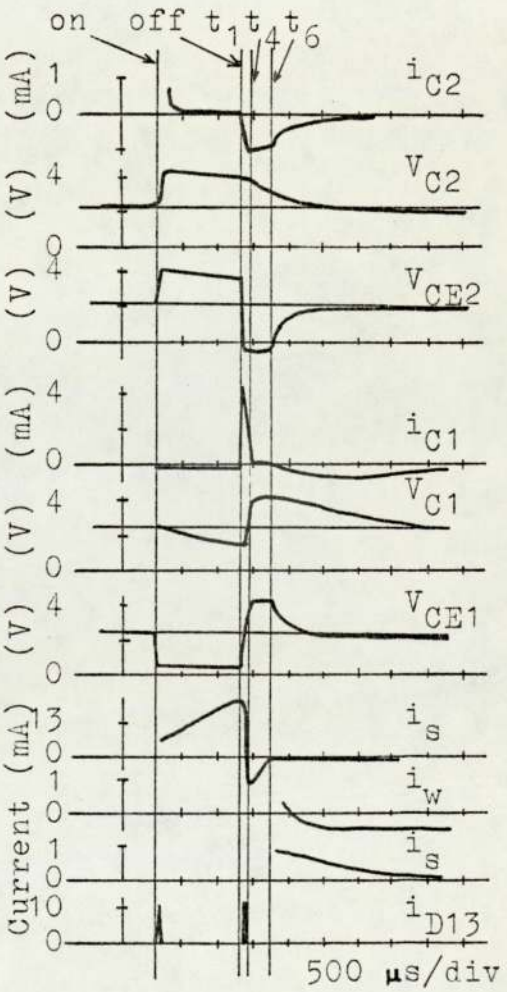

Fig. 4.27 Turn-on and off waveforms

Since, in these tests, only one bipolar circuit is connected to the supply, then the only path for the discharge current is through capacitor C_s. For the time

period after t_5, the discharge current through D6, D7, L1 and C_s decays to zero taking a considerably longer time than t_1 to t_5.

The waveforms in Fig. 4.27 demonstrate what happens some time after the initial period in Fig. 4.26. At time t_6, freewheel diode D6 conduction ends and it remains for the snubber capacitors to adjust the voltages across them to half the supply voltage.

From the instant of turn-off at t_1, capacitor C2 along with capacitor C3 starts to discharge from a voltage of $V_s - V_{CE(SAT)}$ through the winding. Due to the high snubber resistances, the voltage across C2 is still above $V_s/2$ even at t_6, at which time C1 starts to discharge from V_s. Therefore, from t_6 onwards, both C1 and C2 (also C3 and C4) are discharging into C_s, and the difference between the currents is carried by the winding (i_w).

4.4.5.3 Switching with back e.m.f.

In this section, the turn-on and turn-off waveforms examined are those obtained when there is a back e.m.f. in the winding at switching. Since the shaft is not rotating, this e.m.f. is simulated by a battery, giving a choice of magnitude and polarity with respect to the supply voltage. To observe the effect of e.m.f. on

turn-off by increasing the discharge current of the winding, the battery is connected as shown in Fig. 4.28 with the battery voltage V_b higher than the supply voltage V_s.

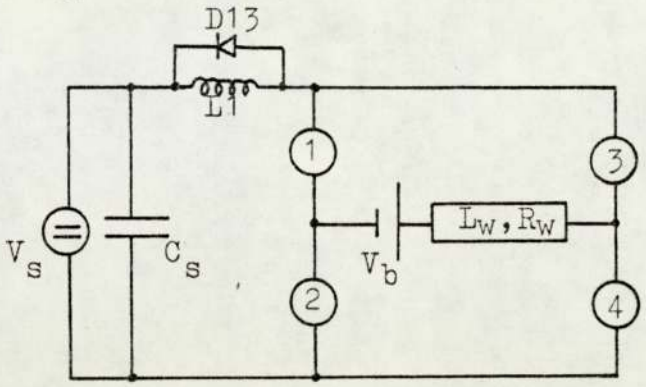

Fig. 4.28 Battery connection

Since the battery is connected prior to switching transistors TR1 and TR4 on, the voltage across each of the 4 transistors is not $V_s/2$ as was the case in Fig. 4.27. There are actually 3 minor circuits with the battery and winding common to all. Two of these circuits are formed by a snubber capacitor and a freewheel diode each, i.e., C1 - D7 and D6 - C4, and the third is formed with the supply capacitor C_s, i.e., D6 - D7 - C_s. These circuits result in a voltage across TR2 and TR3 equal to the freewheel diodes forward voltage drop (about 0.3 V) and the remainder of V_b appears across transistors TR1 and TR4, (v. Fig. 4.14, p. 175).

Fig. 4.29 shows some of the waveforms at turn-on, with V_s = 5 V and V_b = 12 V. The peak value of the transient current i_1 is higher than in Fig. 4.23, p. 184, where no battery was connected. The reason is that capacitor C2

(and C3) must charge up to a higher voltage, i.e., 11 V, as seen from the waveforms of voltage V_B across the bipolar circuit.

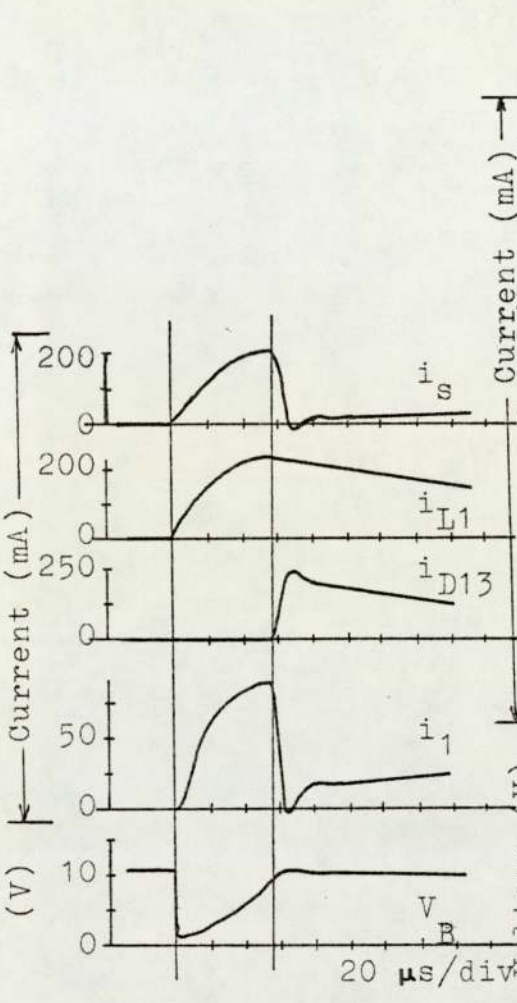

Fig. 4.29 Turn-on waveforms V_s=5V, V_b=12V

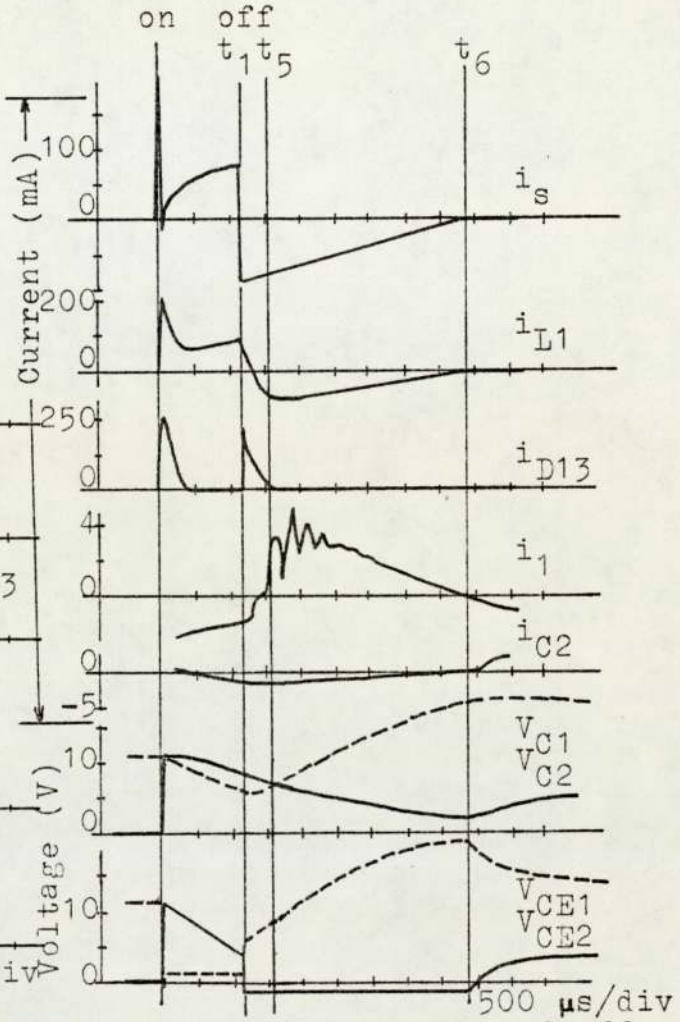

Fig. 4.30 Turn-on and off waveforms, V_b=12V

In the waveforms of Fig. 4.30, turn-off is also shown, and the points t_5 and t_6 correspond to those in Figs. 4.26 and 4.27, p. 188. At t_5 the diode D13 across the inductor is reverse biased and at t_6 the freewheel diodes are reverse biased. The time interval between t_5 and t_6 is longer than in Fig. 4.27 since the winding current (or i_s) is higher at turn-off.

The high voltage across the two capacitors C1 and C2, immediately after turn-on, is followed by a gradual discharge to $V_{CE(SAT)}$ and $V_s - V_{CE(SAT)}$, respectively. This becomes clear when the transistors remain ON for a longer period as in Fig. 4.31a and b. An important difference between Figs. 4.31b and 4.27 is the maximum value to which V_{CE1} (and V_{C1}) builds up after turn-off.

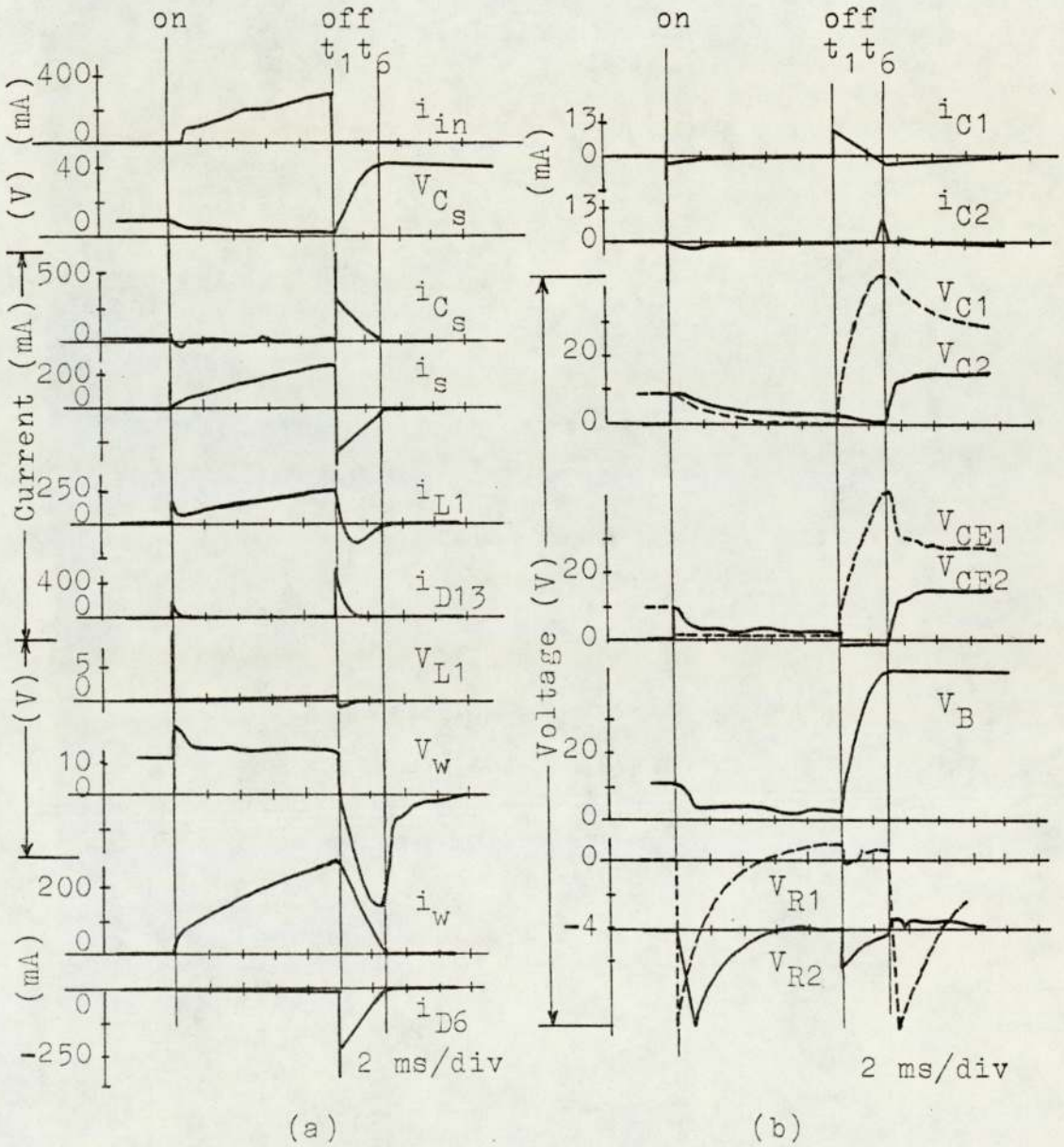

Fig. 4.31 Turn-on and turn-off waveforms with back e.m.f., V_s = 5 V, V_b = 12 V

4.5 Position sensing

In this section, the layout of the rotor-position-sensors is given together with the associated logic circuits. The facilities available in the logic unit, which is intermediate between the sensors and the power transistors, are also detailed here.

Based on the comparison between various types of position sensor given in Table 1.5, p. 6, it was decided to use opto-switches in the present work. With sufficient amplification the outputs from the opto-switches can be used to drive the power transistors directly. The logic unit, however, provides more flexibility and improves control over the operation.

Transistor-Transistor-Logic (TTL) is used since it is cheap and available in various combinations enabling a large system to be created by direct interconnection. The integrated circuits (IC's) used are of the dual-in-line (DIL) type, 7400 series. The operation of the logic gates is described in the following quotation:

> 'The output of a gate is guaranteed to be less than 0.4 V or greater than 2.4 V in the logical '0' and '1', respectively. Similarly the threshold is guaranteed to lie between 0.8 V and 2.0 V.'[53]

A stabilized 5 V (±2.5 mV) power supply is used for reliable operation of the IC's (v. Photograph 5b).

4.5.1 Layout of the opto-switches

The slotted opto-switch used comprises an infra-red light-emitting-diode and a silicon opto-transistor both housed in a plastic package. The specifications for the diode are $V_D max$ = 1.7 V, $I_D max$ = 50 mA, and for the opto-transistor $V_{CEO} max$ = 60 V, $V_{CE(SAT)}$ = 0.2 V, h_{FE} = 30, $t_r = t_f$ = 5 μs, P_d = 150 mW. A 3 x 8 mm slot permits the infra-red beam to be broken thus changing the output logic state from '0' to '1'. A schematic diagram of an opto-switch is shown in Fig. 4.32. To avoid reducing the lifetime of the opto-diode, the diode current I_D is limited to about 14 mA. A 1 kΩ resistor in the collector circuit of the opto-transistor is adequate for current limiting since the output terminal is connected to a Schmitt trigger only.

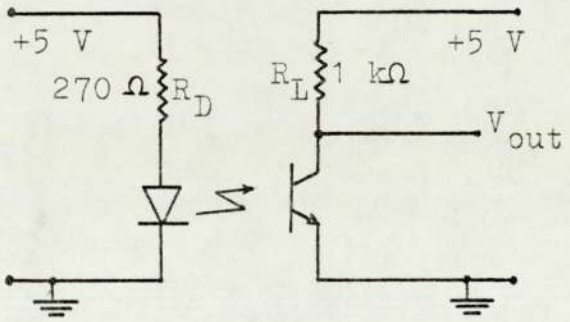

Fig. 4.32 Schematic diagram of an opto-switch

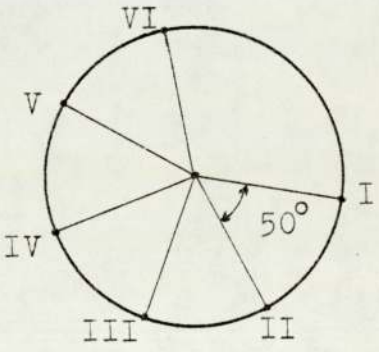

Fig. 4.33 Opto-switch positions

The opto-switches used were fixed on a 203 mm diameter aluminium disc mounted on the end plate of the brushless motor at the opposite-drive-end (v. Photograph 4b). Six switches (I to VI) were distributed around the disc at 50°(m) intervals, as shown in Fig. 4.33.

The infra-red beam was broken by the rotation of 3 cylindrical sectors fixed horizontally to another aluminium disc mounted on the shaft. The 60°, 1 mm thick sectors were equally spaced at a diameter of 152.4 mm. The 10° difference between the arc of the sectors and the separation angle between opto-switches produces 6 pulses over one third of a revolution (120°(m)) as seen in Fig. 4.34.

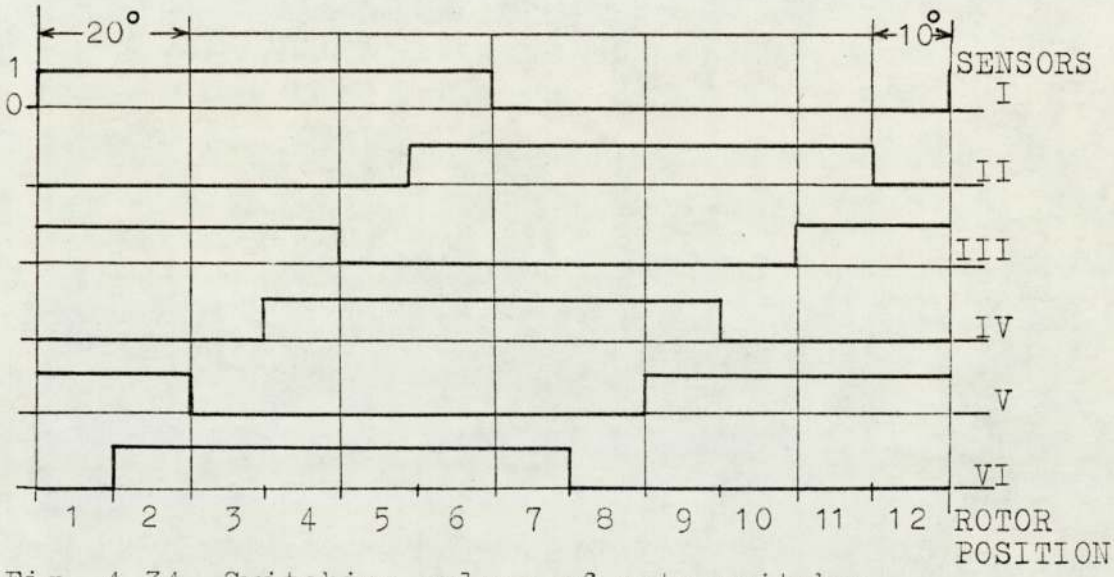

Fig. 4.34 Switching pulses of opto-switches

4.5.2 Switching pulses

As a general rule, 's' sensors with $\tau(1 - \frac{1}{s})°$ spacing give the position of the rotor to within $(\tau/s)°$ and give 2s outputs. Therefore, with s = 6 opto-switches, and a pole-pitch τ of 60° (represented by the aluminium sectors), the spacing between switches is 50°(m) as explained in Section 4.5.1. This number of switches gives the rotor position to within 10° or one slot-pitch, and provides 12 outputs. The use of 6 switches

demonstrates the 'walking code' which changes by one bit at each step, as demonstrated by Fig. 4.35 and Table 4.3.

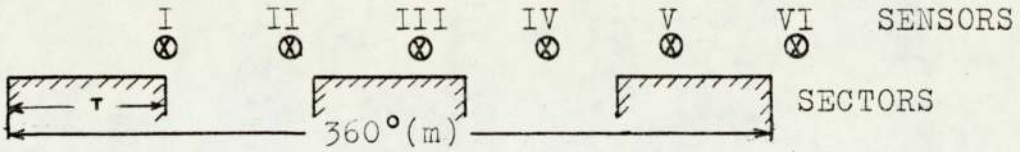

Fig. 4.35 Relative position of sensors and sectors

Rotor position		sensors					
No.	τ	I	II	III	IV	V	VI
1	0 - 1/6	1	0	1	0	1	0
2	1/6 - 2/6	1	0	1	0	1	1
3	2/6 - 3/6	1	0	1	0	0	1
4	3/6 - 4/6	1	0	1	1	0	1
5	4/6 - 5/6	1	0	0	1	0	1
6	5/6 - 6/6	1	1	0	1	0	1
7	6/6 - 7/6	0	1	0	1	0	1
8	7/6 - 8/6	0	1	0	1	0	0
9	8/6 - 9/6	0	1	0	1	1	0
10	9/6 - 10/6	0	1	0	0	1	0
11	10/6 - 11/6	0	1	1	0	1	0
12	11/6 - 12/6	0	0	1	0	1	0

12 steps over 120°(m)
'1': beam broken, '0': beam unbroken
Table 4.3 Switching pulses of opto-switches I to VI

The output signals from the opto-switches are taken to Schmitt triggers (type 7413) since it is important for the transition time between the two logic states to be very short. The connection between the opto-switches on the fixed disc and the Schmitt triggers in the 'logic unit' are made with low-noise, single-core screened cables (10/0.1 mm core, 103 pF/m capacity, 2.54 mm overall diameter).

4.5.3 Decoding of the pulses

Switching signals are required for the measurement of speed and for gating the power transistors. The decoding for each is different and is given in the following two sub-sections.

4.5.3.1 Measurement of speed

Measurement of speed is performed with a counter/driver integrated circuit supplied with pulses from the opto-switches. A single count is performed every 5 seconds, within which the rotor makes 5n/60 revolutions. To obtain a direct reading of speed n, it is therefore required to supply the counter with 12 pulses per revolution. Hence 4 pulses are required over 2τ or $120^{o}(m)$ of rotation.

Several combinations of switching signals can be obtained from Table 4.3 to produce 4 pulses per 120^{o} rotation. But to reduce the error in counting, the 4 pulses are spread out evenly over the 120^{o} as seen from Table 4.4.

Rotor position		sensors					
No.	τ	I	II	III	IV	V	VI
1, 2	0 - 2/6	1		1		1	
4, 5	3/6 - 5/6		0		1		1
7, 8	6/6 - 8/6	0		0		0	
10,11	9/6 - 11/6		1		0		0

Table 4.4 Switching pulses for speed measurement

All signals and their inverse are, therefore, required in decoding the sensor signals for speed measurement. The resultant speed signals fed to the counter are obtained by using 4 NAND gates and 3 NOR gates with the necessary inversion as shown in Fig. 4.36.

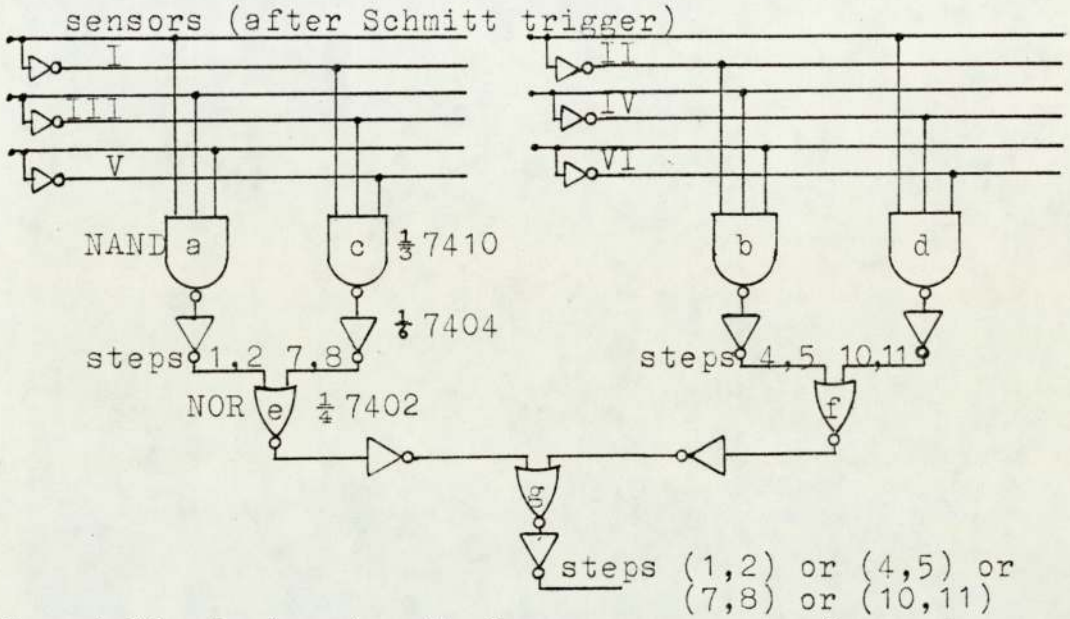

Fig. 4.36 Logic circuit for measurement of speed

The output signals from the circuit in Fig.4.36 are suitable for speed measurement in both directions of rotation. Since positive logic is used, the NOR gates give a low '0' output for a high '1' signal on either or both inputs. This will not affect the resultant pulse as there can be only one pulse at any given time.

The counter/driver is type ZN1040E integrated circuit contained in a 28 pin DIL package. The device is connected to 4 common-anode, light-emitting-diode (LED) indicator units, operating like the counter from the +5 V rail. 7 segment-outputs and 4 digit-select-outputs are connected between the counter and indicator via suitable resistors.

The input signals to the counter are obtained from the output of NOR gate (g) in Fig. 4.36 following an inverter and a Schmitt trigger. It is required to count the signals over a period of 5 seconds, and therefore, a timing pulse is needed to set and reset the counter.

A 1 MHz quartz crystal is used to produce a 1 Hz timing pulse by dividing down the frequency in stages of 10 with six SN7490 counters. A further division by 5 was performed by an SN7490 counter to obtain a frequency of 0.2 Hz, i.e., a timing pulse of 5 seconds.

The width of the timing pulse is 0.5 s as shown in Fig. 4.37 and it is used to trigger an SN74121 monostable multivibrator at the transition from logic 1 to logic 0 of the timing pulse. The width of multivibrator output signal Q1 is about 7.5 μs, being determined by the values of R and C connected across the IC. This output is connected to the 'transfer pin' of the counter/driver, and at the same time triggers a second monostable multivibrator at the transition from logic 1 to 0. The inverted output $\bar{Q}2$ of the second multivibrator is used as the reset signal to the counter/driver.

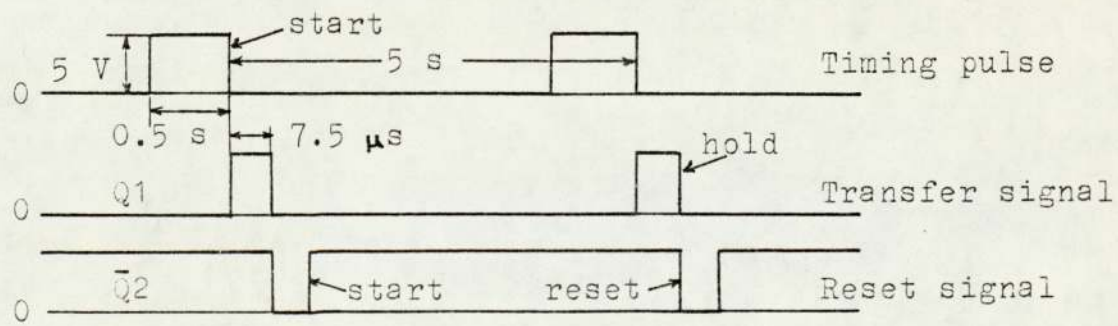

Fig 4.37 Output signals of monostable multivibrators

When the counter is reset by signal $\overline{Q}2$, a single count is started and is transferred to the display 5 seconds later by signal Q1. To display a reading continuously, a 'hold' switch grounds signal Q1 and maintains the 'transfer pin' at logic 0. The combined width of signals $\overline{Q}2$ and Q1 is about 15 μs, and therefore, one pulse would be lost if the leading edge (0 to 1) of the input signal occurs during the reset time, resulting in an error of $\frac{100}{n}\%$. A lamp test of the display units is performed by applying logic level 0 to the test pin of the counter/driver. This is done with a push-button switch to ground.

4.5.3.2 Gating of the power transistors

The pulses from the opto-switches are also used for the gating of the pairs of power transistors forming the electronic commutator. In Section 4.5.2, p. 195, it was mentioned that using 6 switches (I to VI) would give the rotor position to within 10° of rotation. However, to keep the cost down, only 3 of the 6 switches were used, giving the rotor location to 20° or two slot-pitches and providing 6 outputs.

The logic used depends on the type of commutated-winding, i.e., ring, star-connected or star, and on the number of tapping points in use. In the present work, consideration is limited to a star winding with two pairs of diametrically opposite tappings connected to the supply

while one pair is open circuited at any time (v. Fig. 2.23, p. 54).

Signals are therefore required from switches I, III and V only, and the truth table is given in Table 4.5. As in Table 4.3, p. 196, the inverse of the signals is also required.

Rotor position		sensors/logic outputs						
No.	τ	I		III		V		I
1, 2	0 - 2/6	1	i	1	vi	1		1
3, 4	2/6 - 4/6	1	i	1		0	ii	1
5, 6	4/6 - 6/6	1		0	iii	0	ii	1
7, 8	6/6 - 8/6	0	iv	0	iii	0		0
9,10	8/6 - 10/6	0	iv	0		1	v	0
11,12	10/6 - 12/6	0		1	vi	1	v	0

Table 4.5 Truth table for transistor gating

The signals from the opto-switches are decoded using 6 NAND gates and 6 inverters as shown in Fig. 4.38, giving output signals i to vi. These output signals are also given in Table 4.5 where they are at logic 1, formed from the sensor signals appearing on both sides.

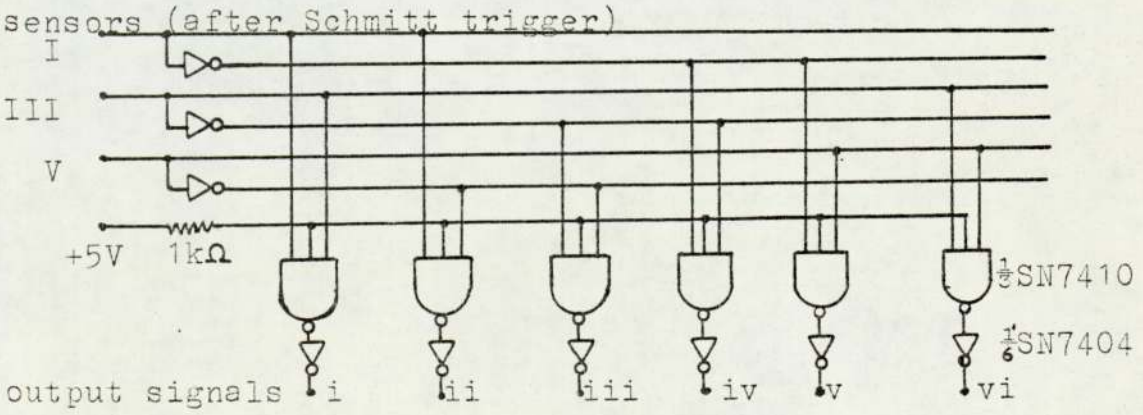

Fig. 4.38 Decoding for transistor gating

The logic controls the sequence and the on/off time of the signals to the base-drive of the power transistors. Output signals i to vi are used as base signals. The switching angle is varied by adjusting the position of the disc with the aluminium sectors relative to the poles.

To guard against a fault condition in which both transistor pairs of a bipolar unit may be provided with base-drive signals at the same time, exclusive OR gates are used. The output signals i to vi from the circuit of Fig. 4.38 are connected to 6 triple-input NAND gates as well as to 3 exclusive OR gates as shown in Fig. 4.39. For positive logic, the output of the exclusive OR gate is at logic 1 only when either input is at logic 1. The output is at logic 0 when both inputs are at either logic 0 or logic 1.

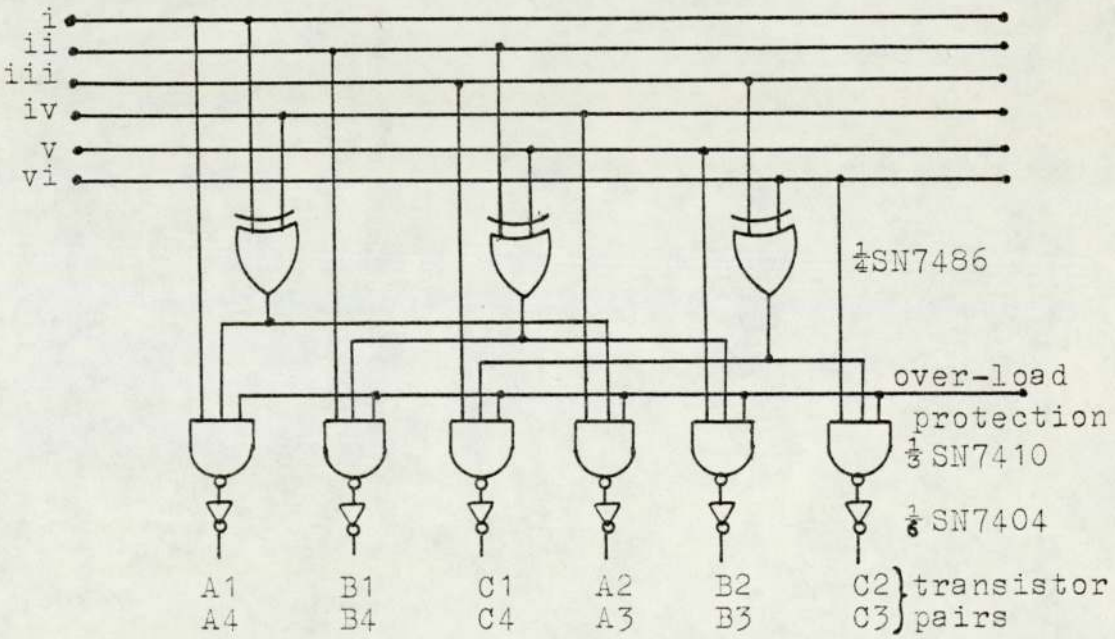

Fig. 4.39 Final logic stage

The two inputs to each OR gate are those for transistor pairs of the same bipolar circuit, e.g., signals i and iv for transistor pairs A1, A4 and A2, A3 of bipolar circuit A. The output signals from the OR gates provide the second input to the NAND gates while the third input is used for removing the output signals, and consequently the base-drive to all transistors, in the event of a current overload, as will be explained in the following Section 4.5.4.

To test the 3 bipolar circuits separately, the board on which the circuit of Fig. 4.39 is connected, is isolated from inputs i to vi, thus isolating the base-drive circuits from the opto-switches. The inputs to the final logic stage are then supplied from the +5 V rail manually via push-button switches on the front panel of the logic unit, (v. Photograph 5a).

4.5.4 Transistor switching and over-load protection

The output signals from the circuit of Fig. 4.39 are required to switch the power transistors as well as the light-emitting-diodes (LED's) serving as indicators. Switching a power transistor on is done by passing current I_D through the diode of the opto-isolator in the base-drive (v. Fig. 4.7, p. 168). This current and the current required for the LED indicator are provided by an NPN transistor as shown in Fig. 4.40. Note that, since each output signal from the circuit of Fig. 4.39 switches

a pair of transistors, e.g., TR1 and TR4, the respective opto-diodes are connected in series. The two diodes, therefore, carry the same current of about 6 mA which is controlled by the 1 kΩ variable resistor.

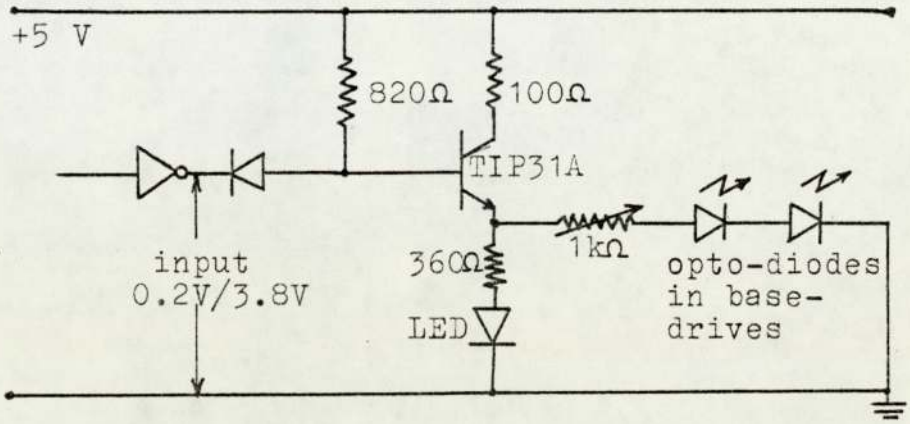

Fig. 4.40 Intermediate stage between logic and base-drive

The over-load protection circuit shown in Fig. 4.41 is connected to the third input of each NAND gate in Fig. 4.39. The output logic state of the Hall-effect IC is normally 1, but it changes to 0 when the supply current through a coil of few turns exceeds a certain level. The maximum value of current is fixed by the number of turns of the coil around a ferrite core and the air-gap between the two halves of the core in which the IC is placed.

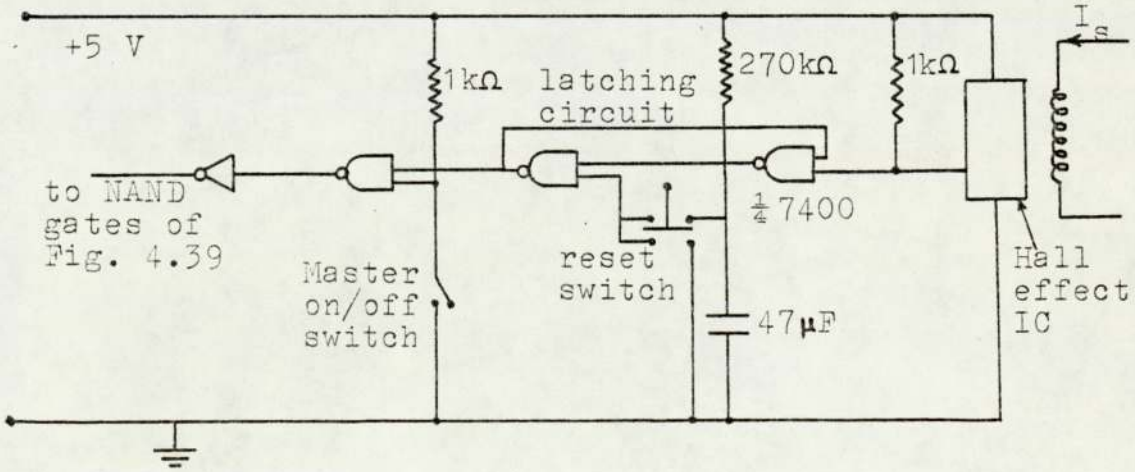

Fig. 4.41 Over-load protection circuit

Base-drive to the power transistors is removed when the output of the IC changes to 0. But to prevent the resumption of the switching signals to the transistors, when current drops slightly below the set value, and the IC output returns to logic 1, a latching circuit is connected between the IC and the output. This consists of two NAND gates. The output of the latching circuit can only be reset by depressing the reset switch which grounds the input to one gate.

4.6 Comments

Three bipolar circuits each consisting of four power transistors form the electronic commutator which is connected to the three pairs of tappings of the commutated-winding. The power transistors are conservatively used, well below the maximum current capability, under normal operation. However, high values of current, which may arise during testing, can be safely carried.

The RC snubber circuits connected across each power transistor improve the turn-off loci and ensure operation within the safe operating area of the transistor. The values of R and C, 3.9 kΩ and 0.47 μF, are selected for the maximum switching period of 20 ms at 1000 rev/min (duty factor = $\frac{1}{3}$) and for the fall time of the transistor.

Decoding the pulses from the opto-switches results in 6 switching pulses for 120°(m) of rotor rotation. Each pulse switches a diagonally opposite pair of transistors for two thirds of a switching cycle. Hence the switching pulses are suitable for a star winding where two pairs of diametrically opposite tappings are connected to the supply at any moment.

CHAPTER 5

MACHINE PERFORMANCE WITH ELECTRONIC COMMUTATOR

5.1 Chapter outline

The brushless motor in this chapter operates with the electronic commutator from a 3-phase diode bridge connected to a 3-phase variac across the a.c. mains. The switching angle of the commutated-winding is discussed in Section 5.2 with the aid of the motor current waveforms. Transistor losses are determined experimentally in Section 5.3 and thermal calculations are performed at extreme load conditions. In Section 5.3, motor operation is examined at no-load and on load and the method of IR compensation to improve motor characteristics is explained. The test results given in this chapter cover selected operating conditions.

5.2 Dynamic performance of the bipolar circuit

The performance of one of the 3 bipolar circuits forming the electronic commutator is discussed with the aid of waveforms obtained during motor operation. The commutated-winding is the star type described in Section 2.6, p. 52, and the power transistors of each bipolar circuit are connected to two coil groups in series, e.g., A and D, (v. Fig. 3.12, p. 76). The rotor position at switching is discussed in Section 5.2.1, and waveforms of voltage, current etc. for motor operation are given in Section 5.2.2.

5.2.1 The switching position

The pulses from the opto-switches are decoded to produce switching signals for the power transistors as explained in Section 4.5.3.2, p. 200. Two pairs of transistors are ON at any moment allowing the supply current to flow through $\frac{2}{3}$ the commutated-winding only. The supply current versus torque curves obtained with a ring winding (v. Fig. 3.45, p. 123) can also be used qualitatively for a star winding. The position of the winding-axis, however, is different for the two windings as seen in Fig. 5.1.

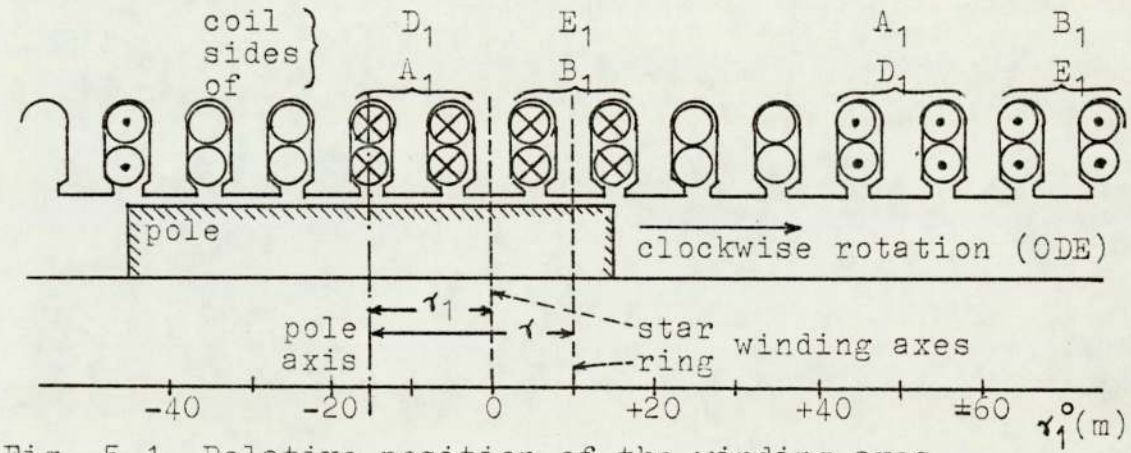

Fig. 5.1 Relative position of the winding axes

The angle γ_1 is the separation angle between the pole-axis and the axis of the two pairs of coil groups of the star winding. The relation between γ_1 and γ, the angle for the ring winding (v. Fig. 3.51, p. 130), is $\gamma_1 = \gamma + 10^{\circ}(m)$, for the same pole position.

In Table 4.5, p. 201, and Fig. 4.39, p. 202, signal 'i' switches transistor pair (A1, A4), and signal 'ii'

switches transistor pair (B1, B4). These two pairs of transistors connect coil groups (A, D) and (B, E) across the supply, respectively. It is also seen from Table 4.5 that the switching signals overlap, resulting in coil groups (B, E) being connected to the supply while coil groups (A, D) are midway through their ON period. Therefore, when transistor pair (B1, B4) is switched on, connecting groups (B, E) to the supply, the coils that are excited are in 4 slots, as shown in Fig. 5.1, and the angle of separation between pole and winding axes that must be considered is then γ_1.

An initial insight into possible values for γ_1 is obtained from the waveforms of the e.m.f. induced in coil groups (A, D) and (B, E) shown in Fig. 5.2. The e.m.f. waveforms are shifted by 20°(m) from each other, resulting in waveform (c) when the two pairs of coil groups are connected in parallel. The difference between the values of e.m.f. causes a circulating current to flow in the two windings as shown in curve (d). This circulating current is minimum when the two e.m.f.'s are of almost equal magnitude.

The e.m.f. across the two pairs in parallel, curve (c), is at the highest value at γ between about -25°(m) and zero (v. angle θ in Fig. 5.2). To limit the winding current to a safe value, it would, therefore, be undesirable to commence conduction in coil groups (A, D) before $\gamma = -25^{\circ}$, and maintain conduction in coil groups

(B, E) after $\gamma = 0^{\circ}$. This limits the range of γ to between -25° and -20° since a conduction period lasts for 20°(m) of pole movement. The equivalent values of γ_1 are therefore -15° to -10°.

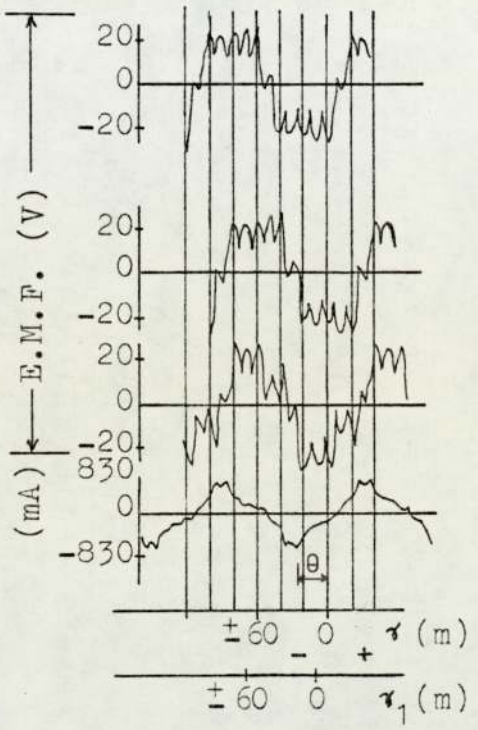

F_f = 450 At, n = 120 rev/min, aligned poles

Fig. 5.2 Induced e.m.f. and current in the star winding

A further indication of possible values for γ_1 is obtained from the curves of output torque for a ring winding shown in Fig. 3.45, p. 123. The highest values of torque are obtained at γ between -14° and -10°. Since these angles refer to the separation between pole and winding axes, the values given can be used directly for the angle γ_1 of the star winding. Since the axes of the ring and star winding are separated from each other by 10°(m), the position of the poles would be shifted by the same angle at switching if $\gamma = \gamma_1$.

5.2.2 Waveforms from motor operation

The waveforms of current i_w in one pair of coil groups (B, E) are shown in Fig. 5.3 at three different values of γ_1. Angle γ_1 is the separation angle between the pole-axis and the resultant axis of the commutated-winding when coil groups (B, E) are switched on as seen in Fig. 5.1. The conduction period t_p in Fig. 5.3a is divided into two parts to identify the other coil groups in parallel with groups (B, E). For the period t_{p1}, groups (A, D) are in parallel, and for t_{p2} groups (C, F).

The effect of different values of γ_1 on the current waveform can be seen from the three waveforms in Fig. 5.3 as changes in the current during periods t_{p1} and t_{p2}. With reference to Fig. 5.2b: at $\gamma_1 = -17.5^\circ$, the e.m.f. induced in groups (B, E) is still increasing from zero, and, hence, results in a high current during t_{p1}; at $\gamma_1 = -15^\circ$ and -12.5° the e.m.f. is higher causing a considerable reduction in the current during t_{p1}.

A reduction in the current during t_{p1} is accompanied by an increase during t_{p2}. This increase maintains motor operation while the current during t_{p1} of the following coil groups (C, F) drops. The current waveforms of the three pairs of coil groups are similar in shape and are shifted from each other by the period $\frac{1}{3} t_p$.

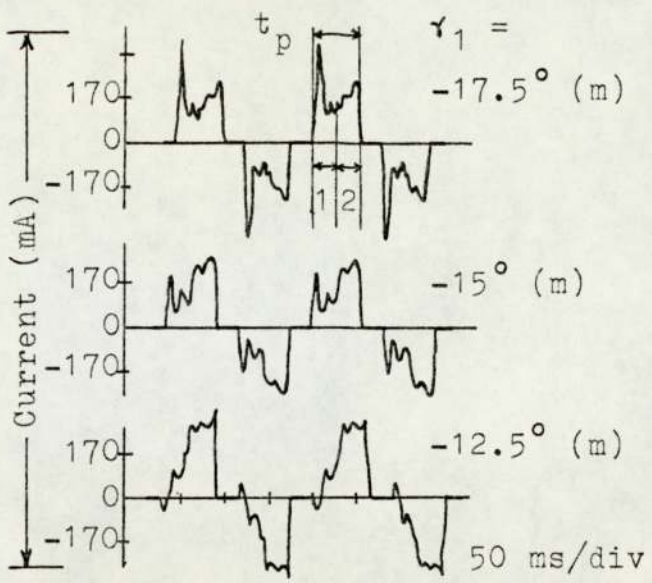

V_s = 25 V, F_f = 450 At, n ≒ 120 rev/min

Fig. 5.3 Current in coil group pair (B, E)

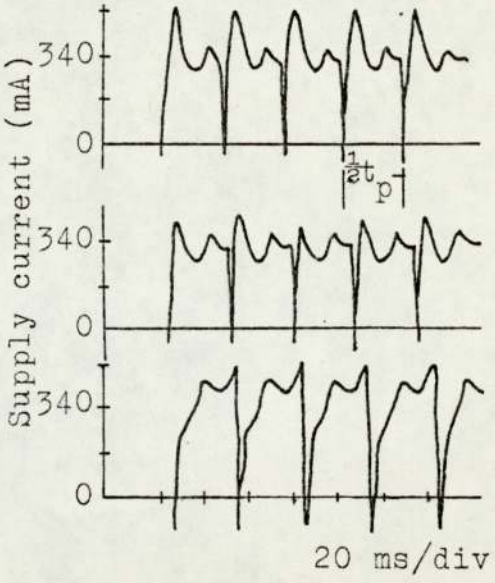

Fig. 5.4 Supply current, I_s

The result of the overlap in current conduction of the three pairs of coil groups is seen in the waveforms of the supply current, I_s, in Fig. 5.4. The waveform of I_s results from the addition of currents in two pairs of coil groups, e.g., (B, E) and (C, F). Since the waveforms of current in the three coil groups are similar, the waveform of I_s is actually the sum of the waveforms during t_{p1} and t_{p2}.

The gradual increase in the winding current seen in Fig. 5.3 at the lower values of γ_1, results in a corresponding gradual increase in supply current waveforms as seen from Fig. 5.4c. The I_s waveform has a period of $\frac{1}{2}$ t_p, equivalent to a rotor movement of two slot-pitches or 20°(m). This coincides with switching one pair of transistors on and switching off another pair. In Section 4.4.5.2, p. 186, it was shown that after

turn-off the energy stored in the winding is released as the winding current flows back into the capacitor C_s across the supply. The waveforms shown there were obtained using only one bipolar circuit. With the complete electronic commutator, the discharge current from one winding at turn-off can circulate through another winding as well as through the supply capacitor. Since the waveforms in Fig. 5.4 are of the current between the electronic commutator and C_s, the current is seen to reverse direction at the end of each $\frac{1}{2} t_p$ period.

The waveforms in Fig. 5.3 show that the winding current can be made more uniform by controlling the switching angle γ_1. High peaks of current and periods of low currents can thus be avoided by adjusting the opto-switches positions detailed in Section 4.5, p. 193. There are, however, other factors affecting the choice of γ_1. These are, (i) the supply voltage V_s, (ii) the excitation level F_f, and (iii) the load on the motor. Figs. 5.5 and 5.6 show these effects on the winding current waveforms at no-load and on load, respectively. All the waveforms were obtained at $\gamma_1 = -15°(m)$.

Regarding the first part of the conduction period t_{p1}, a higher supply voltage does not significantly alter the shape of the waveform at no-load. But when the motor is loaded, a higher supply voltage results in a reduction in the current during t_{p1}. This is attributed to the armature reaction effect, particularly at low field

excitations, which result in a shift of the e.m.f. waveform shown in Fig. 5.2b slightly in the direction opposite to that of rotation. In other words, the angle γ_1 is effectively reduced due to armature reaction effect.

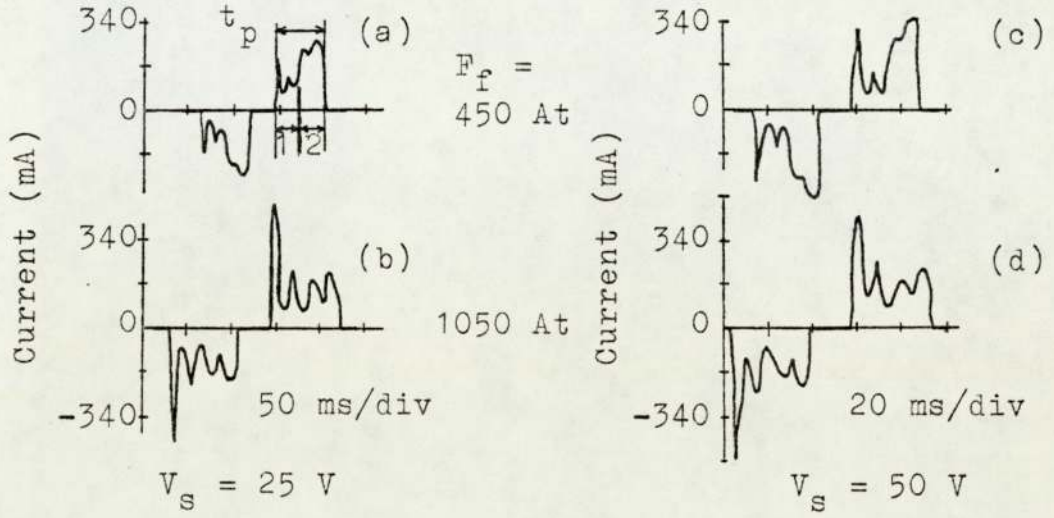

Fig. 5.5 Current in coil group pair (B, E) at no-load, $\gamma_1 = -15°$ (m)

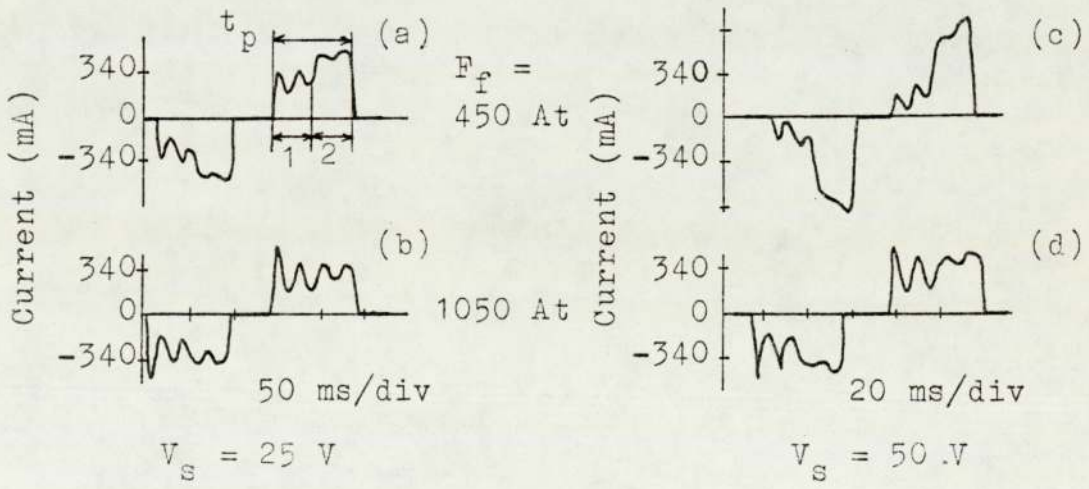

Fig. 5.6 Current in coil group pair (B, E) at load $\gamma_1 = -15°$ (m)

The effect of excitation F_f on the current waveform is much greater than that of the supply voltage as can be judged from the pairs of curves (a) (b), and (c) (d) in Figs. 5.5 and 5.6. Increasing the excitation brings

about changes in the flux paths as the iron is driven further into saturation, resulting in deformations in the waveform of e.m.f. induced in the winding. The effect of higher excitation on the current waveforms is the same as if angle γ_1 is increased. This effect on γ_1 is in the opposite sense as that due to increasing the supply voltage as seen above.

An example of these contradicting effects on γ_1 is seen from a comparison of curves (a) and (c) in Fig. 5.6. The increases in both V_s and F_f maintain a uniformity in the current waveforms in the two periods t_{p1} and t_{p2}.

Alternatively, the switching angle γ_1 can be adjusted to obtain an almost rectangular current waveform for particular values of supply voltage and excitation at which the motor might operate for most of the time. This would result in the minimum fluctuation of the supply current about a mean value.

If the motor is expected to operate at constant V_s and F_f but with a variable load, then it is preferable that γ_1 is made slightly larger than -15^o. This would result in high peaks of current during t_{p1} at light loads, but more important, would reduce the current during t_{p2}, and in particular the current at turn-off. An improved turn-off locus of the power transistor is achieved at the expense of a supply current with some degree of ripple.

5.3 Transistor losses

Using a power transistor in class D entails losses at switching as well as when the device is ON. The turn-on and turn-off losses are the switching losses, and the running losses are those due to the collector-emitter voltage V_{CE} and to the base-drive. Of these 3 losses, only the base-drive loss is fixed in value by the base-emitter voltage V_{BE} and the base current I_B. The other two losses depend upon the collector current I_1 and on the switching times.

All losses, however, are dependent upon the time period t_p a given transistor remains ON. t_p is equal to $\frac{20}{3n}$ seconds, where n is the speed in rev/min. If T is the transistor pulse period then δ, the duty factor, is t_p/T (v. Fig. 5.7) and is equal to 0.33.

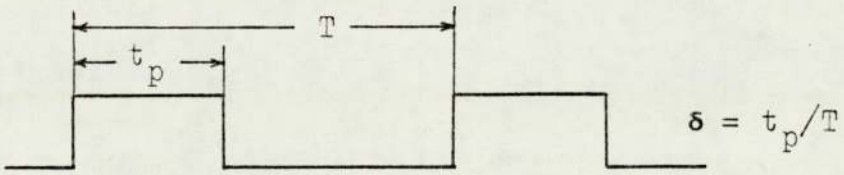

Fig. 5.7 Pulse duration, t_p, and period, T

The safe operation of a power transistor is ensured if the electrical limitations stated in the specification sheet are not exceeded. These limitations are given, as in Appendix A9, as the safe operating area (SOAR) curve enclosed by 4 limits plotted on log/log graph paper. The collector-emitter sustaining voltage $V_{CER(SUS)}$ and

the maximum collector current I_{1max} constitute two boundaries, whereas the third is the power dissipation P_t limit. The fourth and final limit is the second breakdown limit. The power dissipation and secondary breakdown limits of the SOAR curve are affected by two factors: the pulse duration t_p and the duty factor **δ**.

The duty factor **δ** also affects the rate at which power is dissipated from the transistor and hence the limits on the SOAR curves for pulsed operation. For a certain value of t_p, the safe area is larger if the duty factor is reduced. For very small values of **δ**, pulsed operation is practically the same as single-shot pulses and the SOAR boundaries represent the largest possible operating area for particular values of t_p.

In switching inductive loads, as in the electronic commutator, it is possible for either V_{CE} or I_1 to exceed the maximum rating while the power product is still less than P_t. Typical voltage current loci at turn-off are shown in Fig. 5.8.

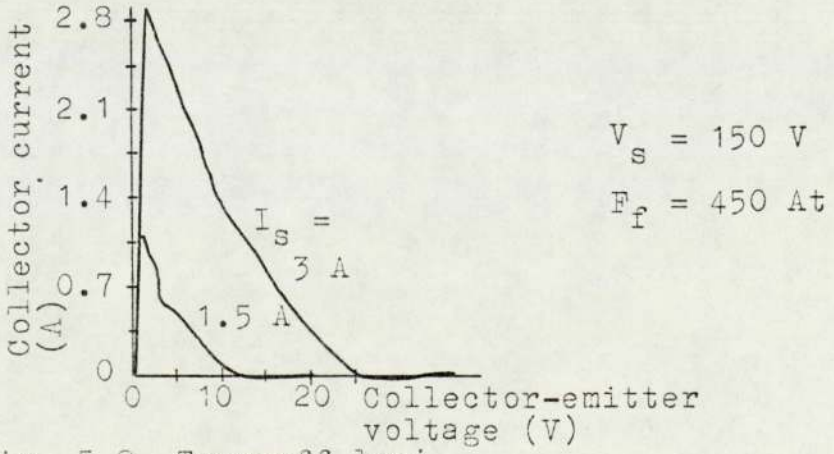

Fig. 5.8 Turn-off loci

5.3.1 Experimental loss curves

At turn-on the rate of rise of the collector current I_1 is considerably less than the rate of fall of the collector-emitter voltage V_{CE} (from $V_s/2$ to $V_{CE(SAT)}$), as expected with inductive loads. V_{CE} drops to a small value (0.4 V) even before the rise of the initial transient current due to the 'short-circuit effect' of the snubber capacitors (v. Section 4.4.3, p. 178). The current/voltage curves in Fig. 5.9a show the relation between I_1 and V_{CE} at turn-on. V_{CE} drops from $V_s/2$ along the line 'i', and eventually settles down to the saturated value $V_{CE(SAT)}$ along curve 'v'.

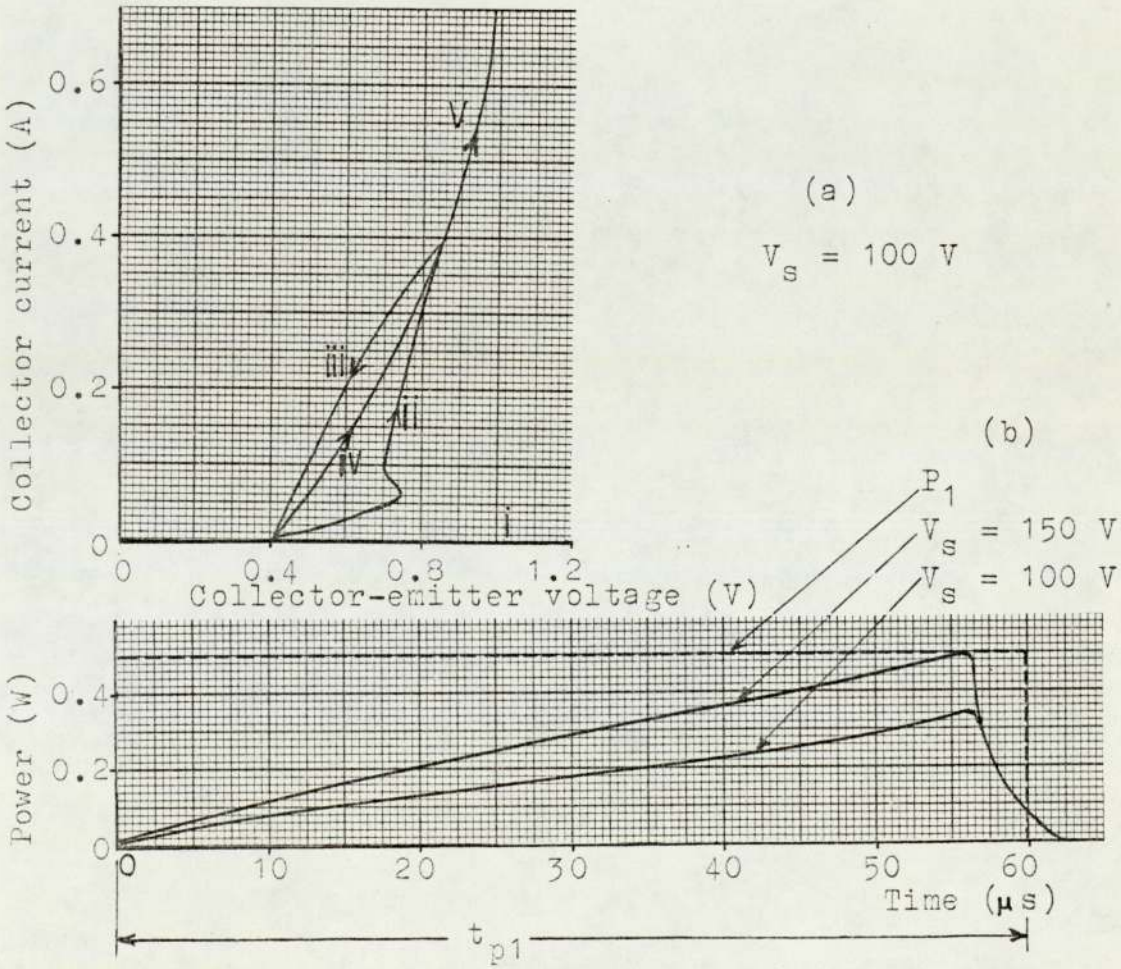

Fig. 5.9 Turn-on curve and losses

The power loss at turn-on is determined from the values of I_1 and V_{CE}, and then plotted against time in Fig. 5.9b. The curve at V_s = 150 V is converted into an equivalent square pulse with the same peak value of power as the actual curve. The equivalent square pulse is shown by the dashed lines in Fig. 5.9b. The peak value is P_1 and the duration is t_{p1}. At V_s = 150 V and 450 At excitation, the supply current I_s is 5 A and the speed is 264 rev/min. At this speed, the pulse period T of the transistor is 75.76 ms giving a pulse duration of 25.25 ms.

The duty factor δ_1 of the equivalent square turn-on pulse is t_{p1}/T and since t_{p1} = 60 μs from Fig. 5.9b, $\delta_1 = 0.8 \times 10^{-3}$. The duty cycle is so small that the single-shot SOAR curves in Appendix A9 are applicable. The values of I_1 and V_{CE} in Fig. 5.9a are well within the safe limits and therefore the turn-on locus is acceptable.

The procedure outlined above is repeated at turn-off. Waveforms of V_{CE} against I_1 similar to those shown in Fig. 5.8 were obtained at various values of supply voltage V_s, excitation F_f and supply current I_s. The values of I_1 at the instant of turn-off (termed I_{1F}) are plotted in Fig. 5.10 against the values of V_{CE} at which I_1 finally falls to zero. It was noted that the relation between I_{1F} and V_{CE} is not affected by V_s, F_f or I_s but is uniquely determined by the power transistor and the components used in the bipolar circuit.

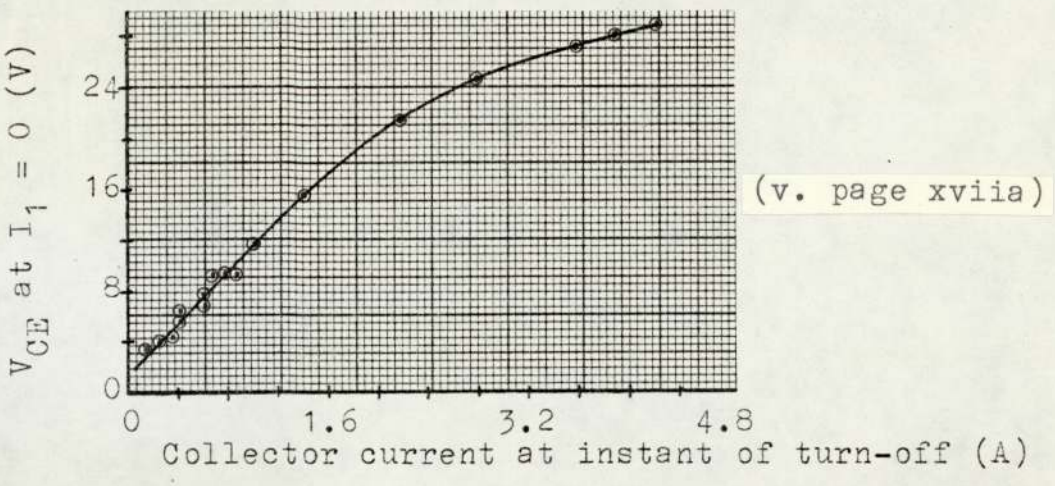

(v. page xviia)

Fig. 5.10 Turn-off voltage vs. collector current curve

The values of V_{CE} and I_1 from the oscilloscope waveforms are used in determining the turn-off power loss, which is then plotted against time. Fig. 5.11 shows power loss curves at 4 values of I_{1F}. The time scale in Fig. 5.11 is fixed by the constant rate of rise of voltage with time (V/t) obtained from Fig. 4.25, p. 187, for the particular values of I_{1F}. In other words, the time scale in Fig. 5.11 corresponds to the increments in voltage V_{CE}. Note that the duration of the curves is approximately the same for the 4 values of I_{1F}. This is due to the almost constant turn-off time of the transistor.

The power loss curve at I_{1F} = 4.2 A in Fig. 5.11 is converted into an equivalent square pulse with a peak value P_3. The pulse duration t_{p3} is 5 μs, and therefore, the duty factor, δ_3, is t_{p3}/T and is equal to 66 x 10^{-6}. Again, the single-shot SOAR curves in Appendix A9 are applicable to the turn-off pulse in view of the small duty factor.

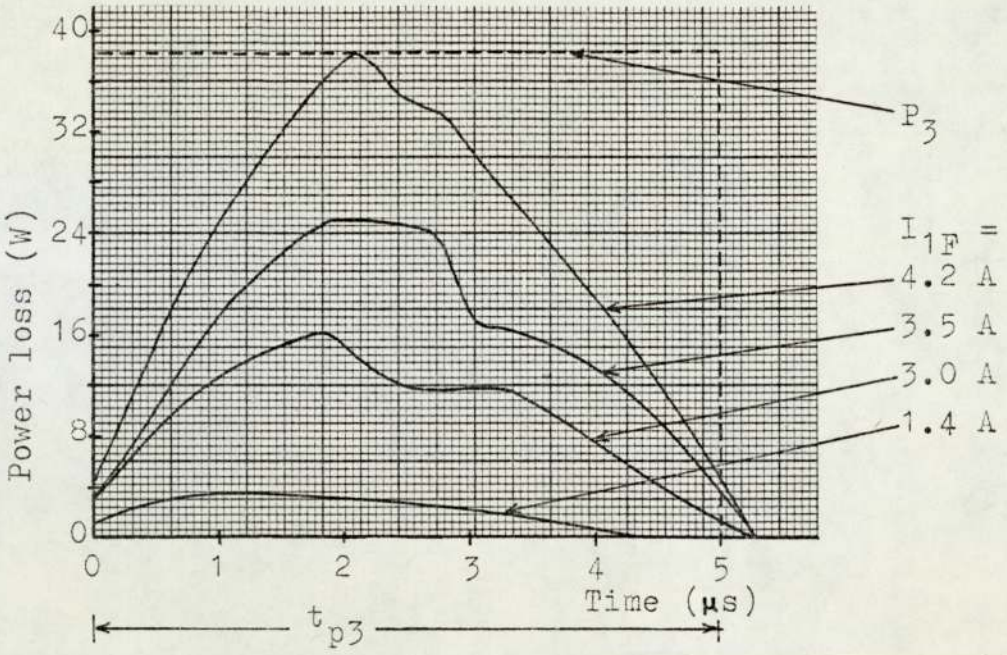

(v. page xviia)

Fig. 5.11 Turn-off power loss, V_s = 150 V, F_f = 450 At

The values of V_{CE} and I_1 from the oscilloscope waveforms are plotted in Fig. 5.12 on log/log graph paper. Operation at V_s = 150 V, F_f = 450 At and a collector current I_{1F} at turn-off of 4.2 A is expected to be about the worst condition for the transistor so far as switching power loss is concerned. The curve in Fig. 5.12 corresponding to these operating conditions is still well within the SOAR limits.

The power loss P_2 when the transistor is saturated and operating between pulses P_1 and P_3 is determined from Equation (5.1).

$$P_2 = V_{CE(SAT)}I_1 + V_{BE}I_B \qquad (5.1)$$

The collector current I_1 is not constant during the conduction time period t_{p2}, as seen previously from

Figs. 5.5 and 5.6, p. 214. But to exaggerate the power loss, I_1 is assumed equal to the highest value for motor operation, i.e., I_{1F} at turn-off. The maximum value of $V_{CE(SAT)}$ is 1.25 V and the base-emitter junction power loss $V_{BE}I_B$ is determined from the values in Section 4.3.3, p. 170. The value of P_2 is, therefore, from Equation (5.1)

$$P_2 = (1.25)(4.2) + (0.75)(0.55) = 5.7 \text{ W}$$

Since t_{p1} and t_{p3} add up to 65 μs only, it is possible to say that $t_{p2} = t_p$ and therefore the duty factor $\delta_2 = \delta = 0.33$.

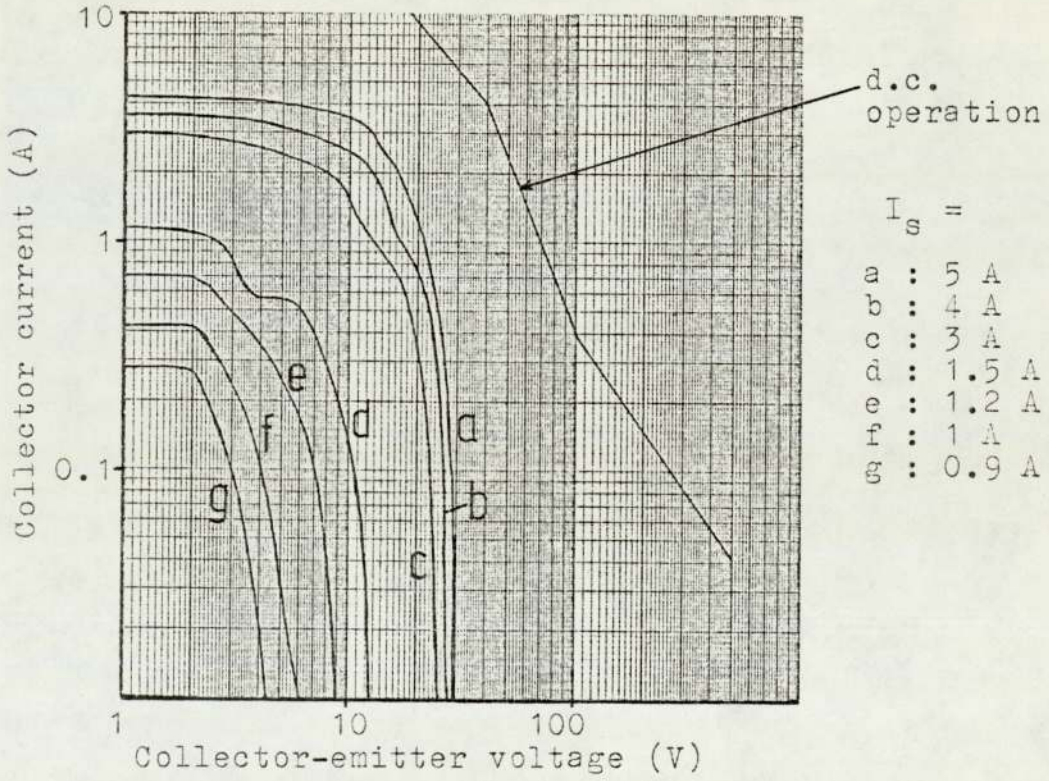

Fig. 5.12 Turn-off curves, V_s = 150 V, F_f = 450 At

To check the acceptability of pulse P_2, the single-shot SOAR curves in Appendix A9 must be reduced for the new duty factor. However, since V_{CE} is only 1.25 V,

operation is within the safe limits even with I_1 up to 10 A and a reduction of the SOAR curves is not required.

The peak values of the equivalent square pulses (P_1, P_2, P_3) and the respective pulse durations (t_{p1}, t_{p2}, t_{p3}) are indicated in Fig. 5.13a (not to scale). The base-emitter power loss $V_{BE}I_B$ which is equal to 0.4 W is added to the values of P_1 and P_3 from Figs. 5.9b and 5.11 (pp. 218 and 221), respectively. This is because the transistor experiences the base-emitter power loss throughout the whole conduction period t_p.

The average power loss per cycle is determined from Equation (5.2)

$$P_{av} = \frac{1}{T}\left(P_1 t_{p1} + P_2 t_{p2} + P_3 t_{p3}\right) \qquad (5.2)$$

$$\doteq \frac{P_2}{3} \doteq 1.9 \text{ W}$$

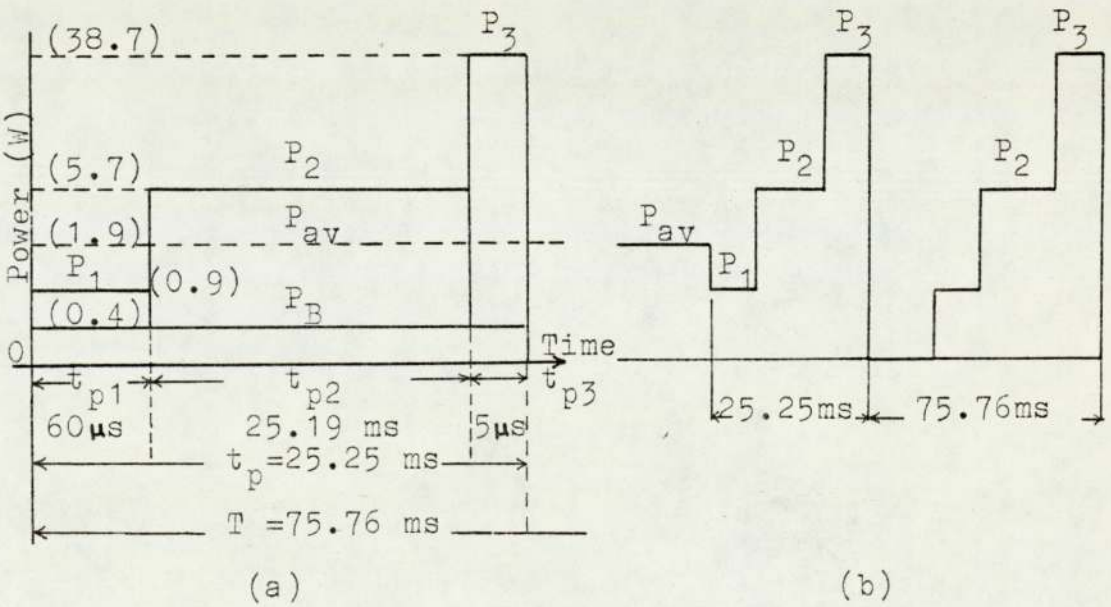

Fig. 5.13 Transistor power dissipation diagrams (not to scale)

5.3.2 Thermal calculations

In the following calculation the temperature rise in the transistor and the accompanying power that must be dissipated by the heat-sink are estimated[54]. The steady state average temperature rise of the transistor junction is determined by superposition, and the final expression based on Fig. 5.13b is as follows:

$$\Delta T_j = P_{av}R_{th} - (P_{av} - P_1)Z_{th(a)} + (P_2 - P_1)Z_{th(b)} + (P_3 - P_2)Z_{th(c)} - P_3Z_{th(d)} + P_1Z_{th(e)} + (P_2 - P_1)Z_{th(f)} + (P_3 - P_2)Z_{th(g)} \qquad (5.3)$$

The symbol Z_{th} represents the transient thermal impedance between junction and mounting base of the transistor. The value of Z_{th} increases with pulse duration t_{px} and reaches the steady state value R_{th} for d.c. operation. The values of $Z_{th(a)}$ to $Z_{th(g)}$ correspond to the following pulse durations, (v. Figs. 5.13a, b):

$Z_{th(a)} : t_p + T$	$Z_{th(e)} : t_{p1} + t_{p2} + t_{p3}$
$Z_{th(b)} : t_{p2} + t_{p3} + T$	$Z_{th(f)} : t_{p2} + t_{p3}$
$Z_{th(c)} : t_{p3} + T$	$Z_{th(g)} : t_{p3}$
$Z_{th(d)} : T$	

The temperature rise is equal to the difference in temperature between the transistor junction and mounting base of the transistor.

$$\Delta T_j = (T_j - T_{mb})_{max} \qquad (5.4)$$

where T_{mb} is the mounting base temperature. The maximum allowable value of T_{mb} can then be determined from the maximum junction temperature $T_{j(max)}$, given in the data sheet, as in Equation (5.5)

$$T_{mb(max)} = T_{j(max)} - (T_j - T_{mb})(max) \qquad (5.5)$$

The maximum allowable value of the thermal resistance of the heat-sink is determined from Equation (5.6),

$$R_{th(h - a)} = \frac{T_{mb(max)} - T_a}{P_{av}} - R_{th(mb - h)} \qquad (5.6)$$

T_a is the ambient temperature and $R_{th(mb - h)}$ is the thermal resistance between mounting base and the heat-sink.

Equations (5.3) to (5.6) are now used to determine the maximum thermal resistance of the heat-sink. The values of Z_{th} are as follows:

$$Z_{th(a)} = Z_{th(b)} = 0.85°C/W$$

$$Z_{th(c)} = Z_{th(d)} = 0.8°C/W$$

$$Z_{th(e)} = Z_{th(f)} = 0.6°C/W$$

and $Z_{th(g)} = (25t)^{0.47} (R_{th}) = 1.5 \times 10^{-2}°C/W$

From Equation (5.3) and Fig. 5.13b,

$$\Delta T_j = 4.5°C$$

Substituting in Equation (5.5), with $T_{j(max)} = 200°C$ (v. data sheet),

$$T_{mb(max)} = 195.5°C$$

In Equation (5.6), the ambient temperature of 30°C is assumed and the thermal resistance between mounting base and heat-sink, $R_{th(mb - h)}$, is assumed equal to 0.1°C/W, which is true only if a heat-sink mounting compound is used. Therefore, the thermal resistance of the heat-sink must not exceed the following value:

$R_{th(h - a)} = 87°C/W$

This value of thermal resistance is well above that of the heat-sinks on which the power transistors are mounted, namely, 0.65°C/W. The power diodes (D9 to D12 in Fig. 4.14, p. 175) in the collector circuit of the power transistors are also mounted on the same heat-sinks.

5.4 Motor operation

In this section, the results of the no-load and load tests are discussed and the losses are determined. The brushless motor is operating with the electronic commutator and the opto-switch disc is set for a switching angle γ_1 of -15°(m) (v. Fig. 5.1, p. 208).

A three-phase diode bridge is used to provide d.c. supply from a three-phase variac. Three single-phase transformers are connected between the variac and the diodes for isolation. The ripple frequency of the supply is 300 Hz and the amplitude is less than 1% of the average voltage.

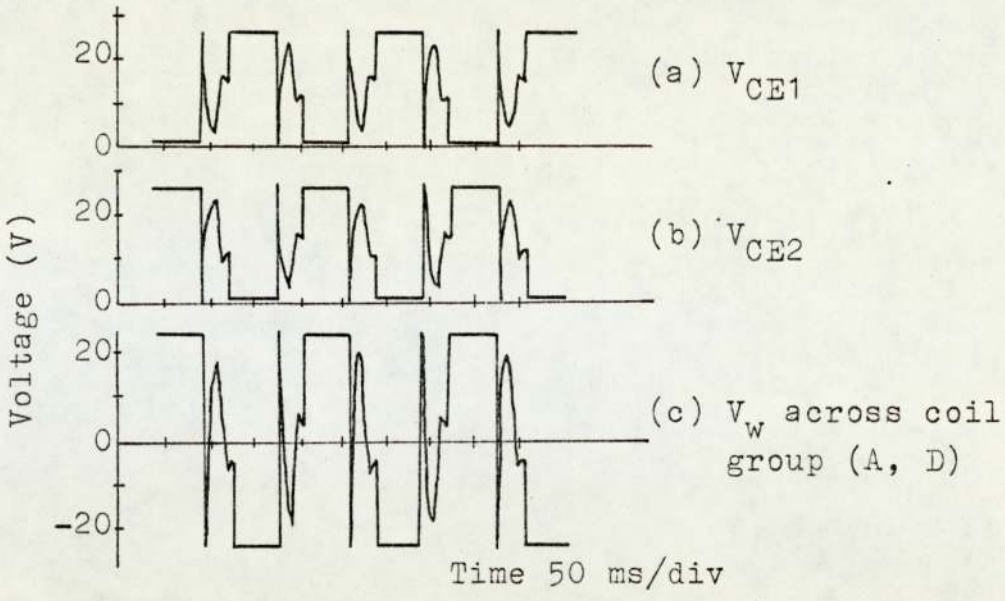

V_s = 25 V, F_f = 450 At, n = 120 rev/min, $\gamma_1 = -15^\circ$

Fig. 5.14 Voltage waveforms

Fig. 5.14 shows typical waveforms of collector-emitter voltage V_{CE} across transistors TR1 and TR2 of the bipolar circuit (v. Fig. 4.14, p. 175) and of the voltage across one pair of coil groups (A, D). As mentioned in Section 4.4.5.3, p. 189, when all the 4 transistors of the bipolar circuit are OFF, the collector-emitter voltages across the transistors are not equal to one-half the supply voltage V_s. This is due to the induced e.m.f. in the winding which charges up diagonally opposite snubber capacitors through the freewheel diodes to a voltage higher than $V_s/2$. However, the switching angle of $\gamma_1 = -15^\circ$(m) coincides with the position at which the e.m.f. in the winding is increasing in value after changing polarity, and consequently V_{CE} is approximately $V_s/2$.

The values of current and voltage were measured with electro-dynamometer instruments and speed was read from the digital display on the logic unit. Torque was measured with a digital voltmeter connected to the strain-gauge transducer via a filter unit (v. Appendix A6). The case temperature of one transistor was continuously monitored with a digital thermometer. For an ambient temperature of 25°C, the case temperature did not exceed about 30°C at full load even with the ventilating fan in the transistor cabinet switched off.

All the following tests were performed with staggered and chamfered rotor poles unless stated otherwise.

5.4.1 No-load test

The no-load tests were performed at various values of supply voltage and excitation and the results are plotted in Figs. 5.15 and 5.16. The generator referred to in these figures is the 1.1 kW d.c. generator used later as a load. Coupling this generator to the brushless motor results in slightly higher values of no-load current, due to the mechanical losses of the generator, as seen from the curves in Fig. 5.15. The variation of the no-load speed with supply voltage shown in Fig. 5.16 is linear as in conventional d.c. motors.

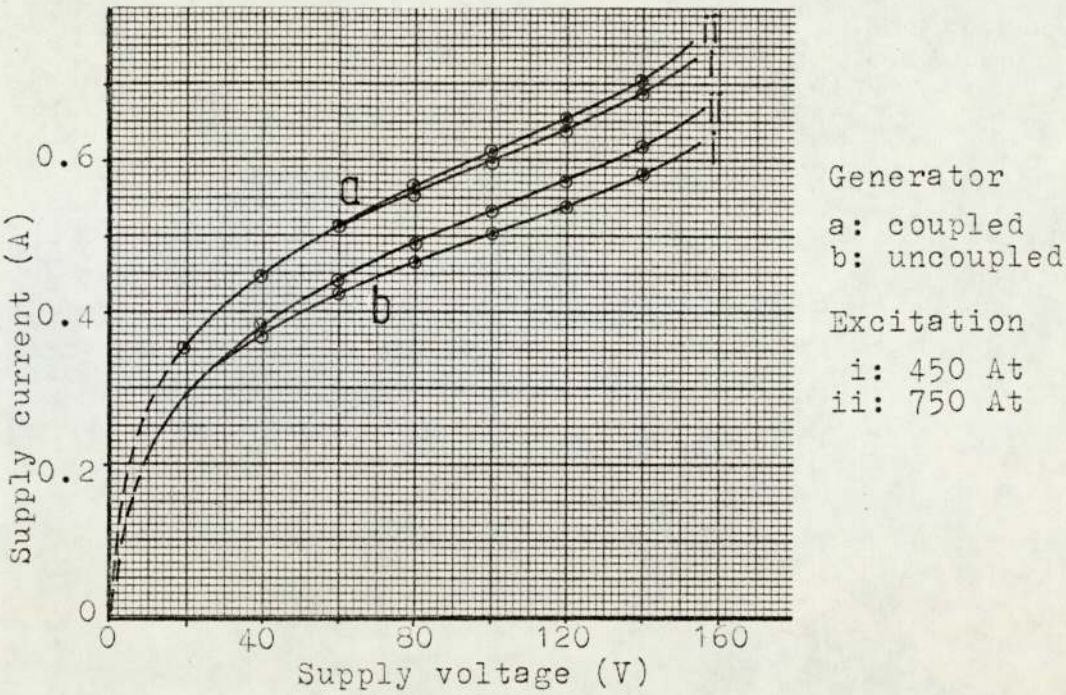

Fig. 5.15 No-load tests, star winding, $\tau_1 = -15^{\circ}$(m)

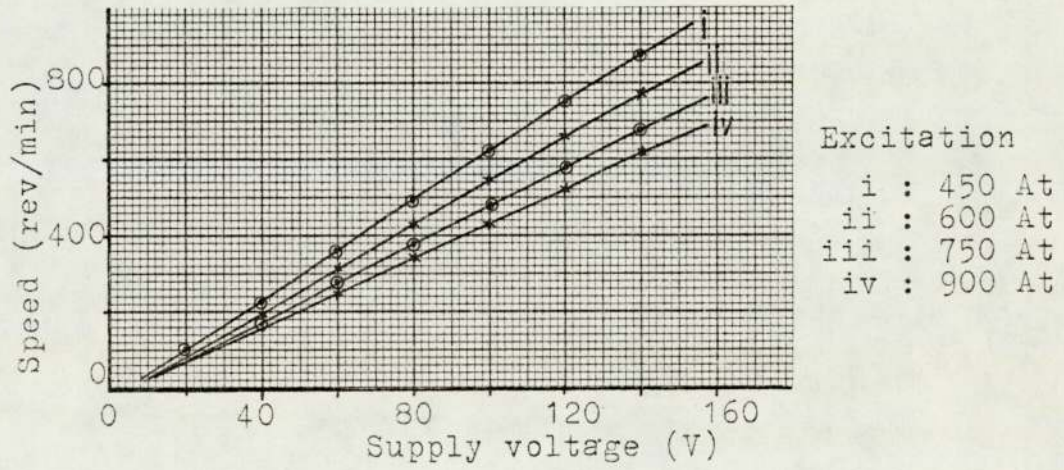

Fig. 5.16 No-load tests, generator uncoupled

Fig. 5.17 shows speed-voltage curves with aligned rotor poles. The speed is higher when the poles are staggered which agrees with a previous observation from Fig. 3.31, p. 103, though for a ring winding, that e.m.f. induced in the winding is higher when the poles are staggered. Changes in speed follow changes in e.m.f. since the air-gap flux is virtually constant at no-load.

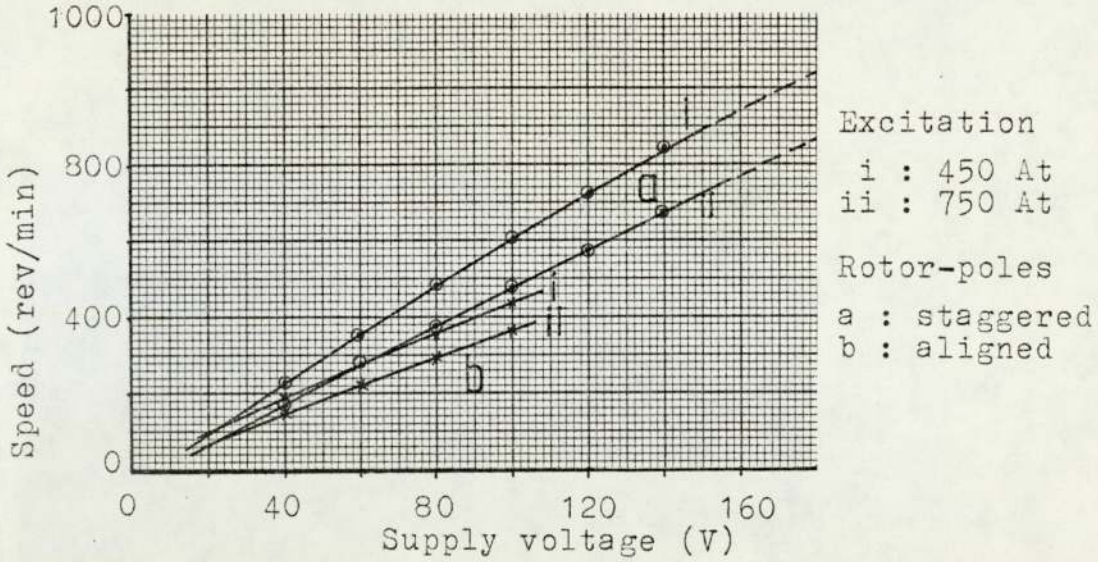

Fig. 5.17 No-load tests, generator coupled, $\tau_1 = -15^\circ$ (m)

To determine the e.m.f. constant U_o for the star winding, the e.m.f. and torque Equations (3.12) and (3.13) given in Section 3.6.1, p. 119, can also be used here. The voltage drop across the saturated transistors and the power diodes of each bipolar circuit is assumed constant at 2.7 V. Equations for the supply current and speed are obtained from the curves in Figs. 5.15 and 5.16, for a field excitation of 750 At and with the d.c. generator uncoupled.

$$I_a = 2 \times 10^{-3} V_s + 0.36 \qquad \text{(A)} \qquad (5.7)$$

$$n = 5\ V_s - 25 \qquad \text{(rev/min)} \qquad (5.8)$$

The value of U_o is 1.9 V/rad/s, or 68% of that for the ring winding, which agrees with the theoretic e.m.f. ratio of 2:3 for star and ring windings as given in Table 2.6, p. 56. The ratio of the air-gap flux-densities corresponding to the two different excitations, is obtained from Fig. 2.20, p. 51, and is included in the U_o ratio.

$$\frac{750 \text{ At}}{1050 \text{ At}} : \frac{B_{g1}}{B_{g2}} = \frac{0.575}{0.64} = 0.9$$

The constants A and K are then determined and the torque equation is given as follows:

$$T = 7.21 \times 10^{-3}\omega + 0.7 \qquad \text{(Nm)} \qquad (5.9)$$

The value of R_a determined from Equations (5.7) and (5.8) is 6.22Ω and is actually $\frac{1}{3}$ the resistance of one pair of coil groups. Although only two pairs are connected to the supply at any moment, the value of resistance obtained from the above calculation is the effective value of 3 pairs in parallel. This is because the currents measured are average values and hence the average winding current is $\frac{1}{3}$ the supply current. The resistance of the star winding is, therefore, $\frac{1}{2}(3 \times 6.22) = 9.33\Omega$ which is 65% of the 14.4Ω for the ring winding.

5.4.1.1 No-load losses

The mechanical and iron losses at no-load are determined from the following relation

$$P_m + P_i = V_s I_s - I_s^2 R_a \qquad (5.10)$$

and plotted against supply voltage V_s and speed n in Figs. 5.18 and 5.19, respectively. At a constant value of V_s in Fig. 5.18, the no-load losses vary within 10% of the maximum value for a wide range of excitation. This small variation is due to a balance between the

increasing mechanical loss at lower excitation (and higher speeds) and the decreasing iron losses.

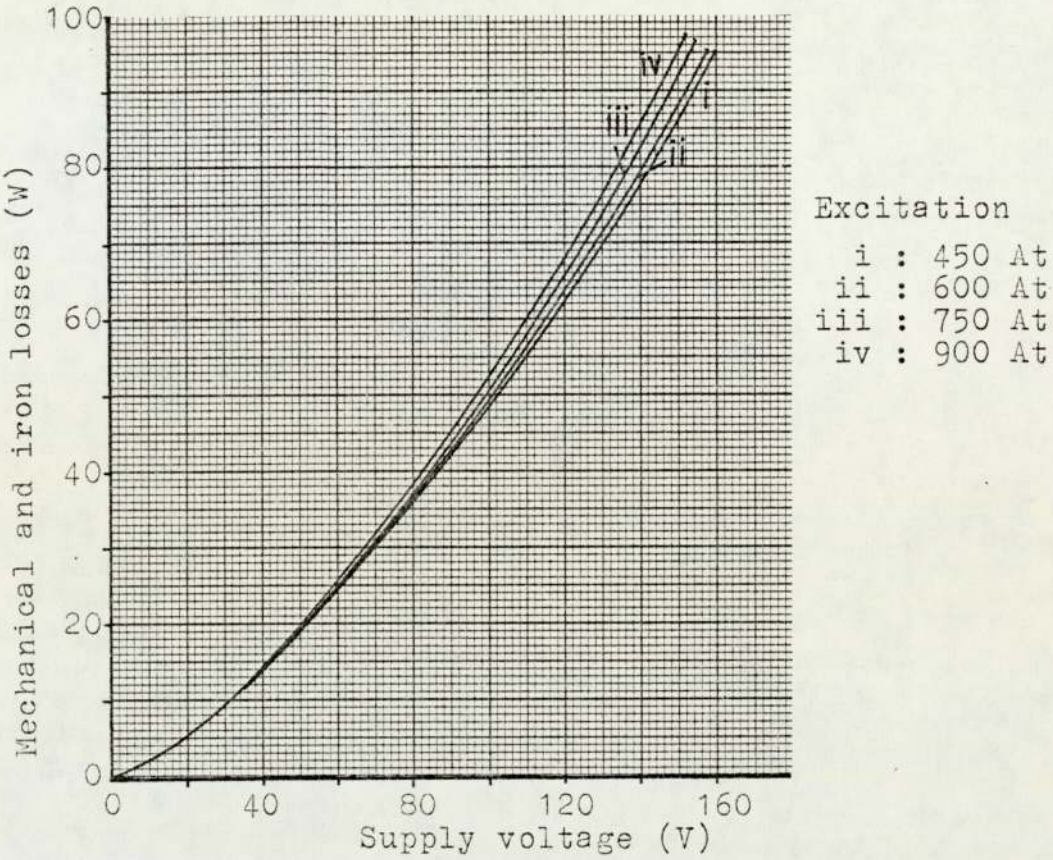

Fig. 5.18 Mechanical and iron losses at no-load

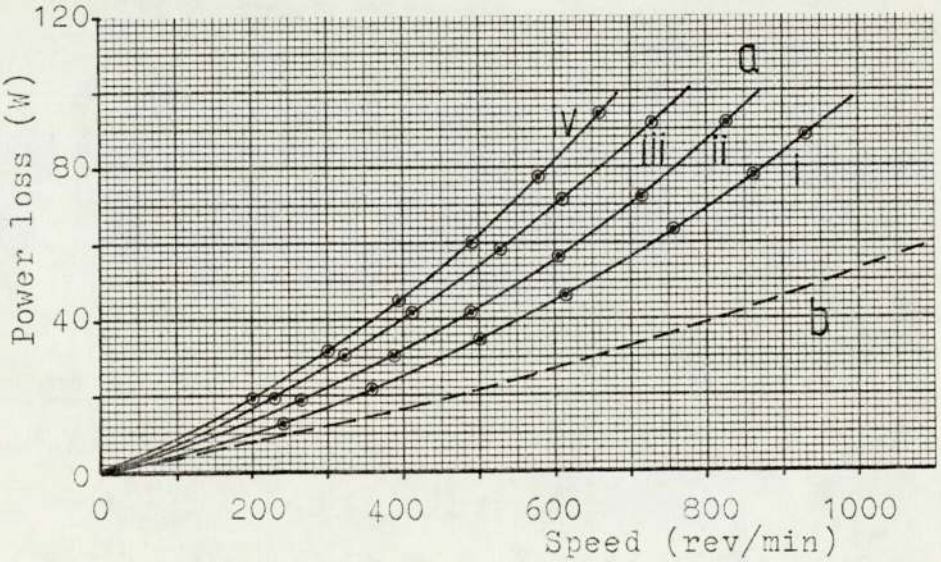

a : mechanical and iron losses
b : mechanical loss

{Excitation values i to iv as above}

Fig. 5.19 No-load losses

In Fig. 5.19, the mechanical loss curve against speed is obtained from Fig. 3.39, p. 113, under exactly the same conditions, i.e., no brushes and not including the mechanical losses of the d.c. generator. The iron losses can, therefore, be determined by subtracting the mechanical loss curve from the curves of the combined mechanical and iron loss. The resultant curves of iron losses are plotted against speed in Fig. 5.20. The expressions for these losses are given in Equation (5.11) at the corresponding values of excitation.

$$
\begin{aligned}
P_i &= 0.25\left(\frac{n}{100}\right) + 0.48\left(\frac{n}{100}\right)^2 \quad (W) \quad 450\ At \\
P_i &= 1.73\left(\frac{n}{100}\right) + 0.53\left(\frac{n}{100}\right)^2 \quad (W) \quad 600\ At \\
P_i &= 3.74\left(\frac{n}{100}\right) + 0.53\left(\frac{n}{100}\right)^2 \quad (W) \quad 750\ At \\
P_i &= 6.00\left(\frac{n}{100}\right) + 0.50\left(\frac{n}{100}\right)^2 \quad (W) \quad 900\ At
\end{aligned}
\qquad (5.11)
$$

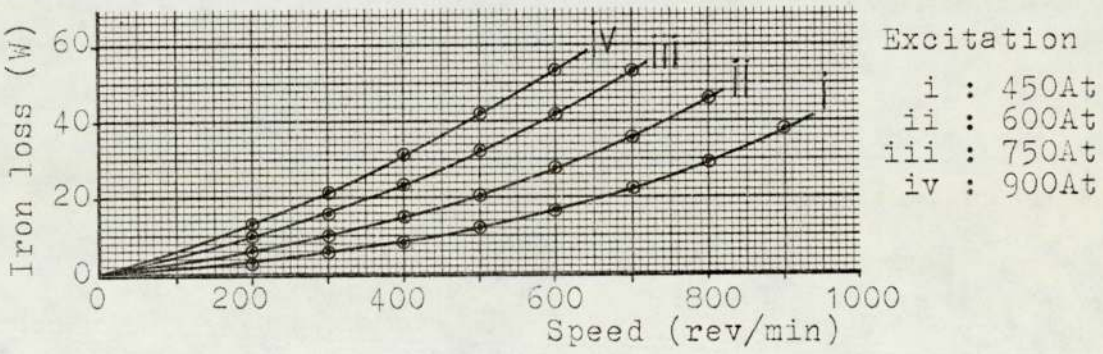

Fig. 5.20 No-load iron losses

A comparison between the curves of Fig. 5.20 and those obtained previously in Fig. 3.42, p. 117, shows that the iron losses in both cases are of the same order of magnitude. The small differences are due to the inclusion of the effect of the winding current on the losses. Since the no-load current is small, this effect is also small.

The expressions in Equation (5.11) also show some similarity with those in Equation (3.11), p. 118. These equations are approximate and are only used for comparison.

5.4.2 Load test

Load tests were performed on the motor at two values of field excitation, 450 At and 750 At, and at 3 values of supply voltage, 50 V, 100 V and 150 V. Readings of speed and torque were recorded at various values of supply current and then plotted in the figures given in Table 5.1. Output power was calculated and plotted against speed and efficiency. All the tests given in this section were performed with staggered and chamfered rotor poles.

Axes		Fig. no.	
Y	X	450 At	750 At
Speed	Supply current	5.21	5.22
Torque	Supply current	5.23	5.24
Speed	Output power	5.25	5.26
Efficiency	Output power	5.27	5.28

Table 5.1 Load characteristics

Figs. 5.21 and 5.22 show a significant drop in the speed as the supply current, I_s, increases. This is due to the increasing voltage drop across the winding resistance and the additional iron losses as I_s increases. A comparison between curves at similar values of supply

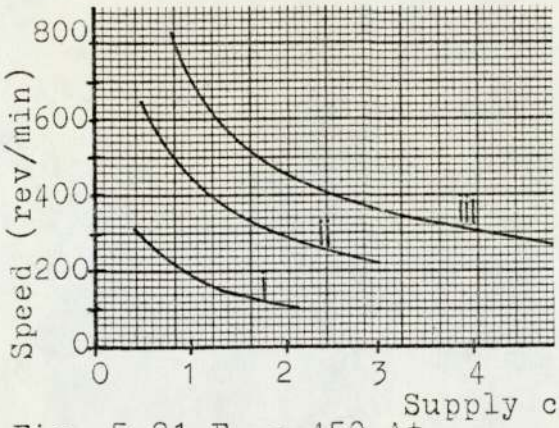

Fig. 5.21 F_f = 450 At

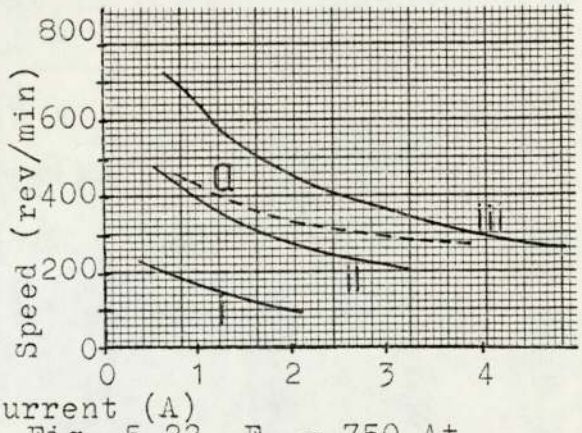

Fig. 5.22 F_f = 750 At

i : 50 V
ii : 100 V Load Tests
iii : 150 V
a : IR compensation (750 At)

(v. page xviia)

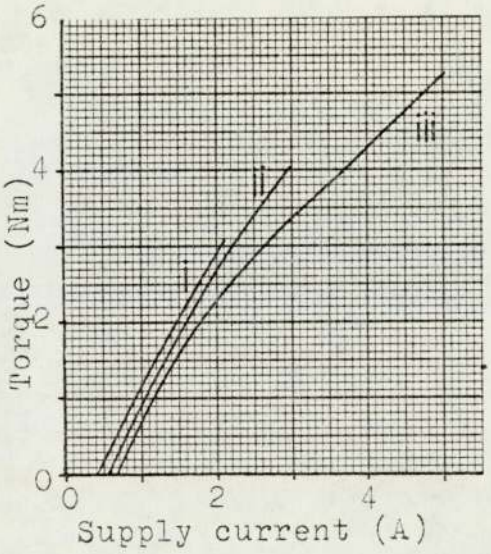

Fig. 5.23 F_f = 450 At

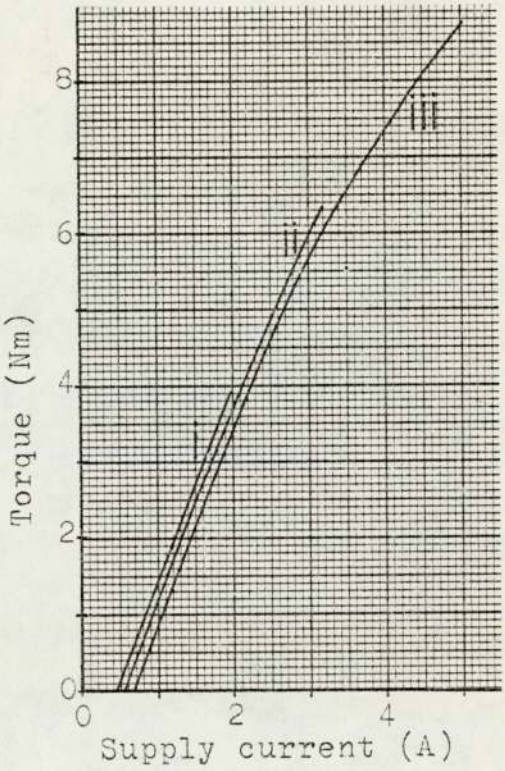

Fig. 5.24 F_f = 750 At

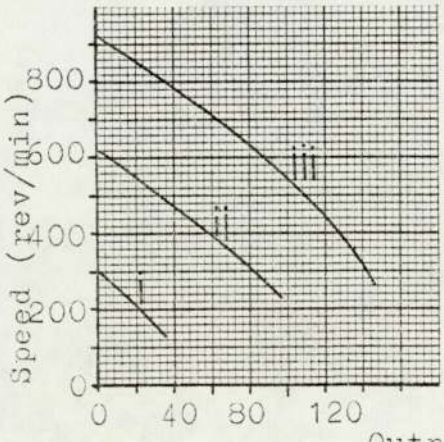

Fig. 5.25 F_f = 450 At

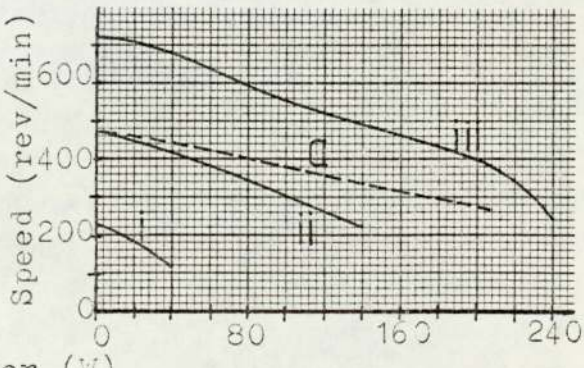

Fig. 5.26 F_f = 750 At

voltage shows higher values of speed at 450 At than at 750 At. This is more so at light loads than at heavy loads where the armature reaction effect, which reduces the air-gap flux, counteracts the effect of the higher excitation level. The result is a very small difference in speed for the two values of excitation at high values of I_s.

The experimental curves in Figs. 5.21 and 5.22 are reasonably close to those determined theoretically in Fig. 3.47, p. 125. However, the type of winding is different in each case (star vs. ring) and, as expected, the experimental values of speed are slightly higher than the theoretic values to compensate for the lower winding-resistance drop and the inherently lower e.m.f. between tappings of a star winding.

In Figs. 5.23 and 5.24, the torque variation with supply current at light loads is linear. But at high values of I_s the armature reaction effect becomes pronounced, reducing the total air-gap flux and resulting in a non-linear torque variation. The nominal maximum torque of 10 Nm specified in Section 2.2, p. 19, was not reached since the supply current was limited to a value well below the maximum nominal value of 10 A.

The experimental values of torque are within the range of values determined theoretically and plotted in Fig. 3.48, p. 125. As expected, the experimental values

of torque are lower than the theoretic values since the latter do not include the load losses, as was explained in Section 3.6.2, p. 122. A reduction in the actual torque was also expected after the observation from the X-Y recorder waveforms in Section 3.3.2, p. 74, where the peak torque with a star winding was about 5% below that of a ring winding at the same conditions of operation.

The curves of speed against output power in Figs. 5.25 and 5.26 show the same rapid drop in speed with load as that seen in Figs. 5.21 and 5.22 for supply current. However, it can now be seen that at the higher excitation of 750 At, the percentage drop in speed with load is much smaller than at 450 At. This is due to the smaller effect of armature reaction on the air-gap flux when the excitation level is high.

(v. page xviia)

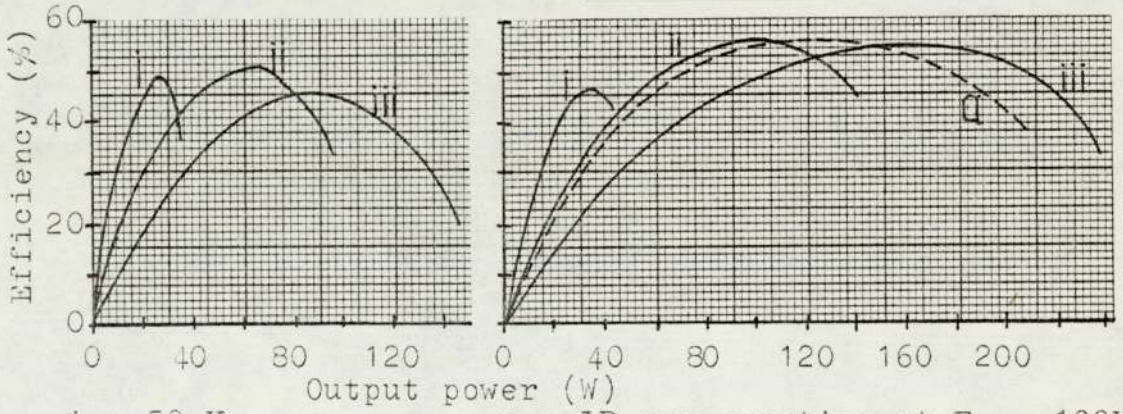

i : 50 V
ii : 100 V
iii : 150 V

Fig. 5.27 F_f = 450 At

a : IR compensation at E_b = 100V and F_f = 750 At

Fig. 5.28 F_f = 750 At

Both power inputs to the commutated-winding and to the field coil are considered in the determination of efficiency, and the results are plotted in Figs. 5.27

and 5.28 for the two levels of excitation. Slightly higher values of efficiency are obtained at 750 At than at 450 At with the maximum efficiency occuring at a higher value of the output power.

Two facts have become clear from the load characteristics in Figs. 5.21 to 5.28. The first is that there is a considerable drop in speed with load and the second is that maximum efficiency is between 50% and 60%. A smaller drop in speed and slightly higher values of efficiency can be achieved by operating at high levels of field excitation.

The reasons for the above two observations are the excessive voltage drop $I_s R_a$ caused by the winding resistance and by the apparently high iron losses at load. The $I_s R_a$ compensation is explained in Section 5.4.3 and the load losses are discussed in the following Section 5.4.2.1.

5.4.2.1 Load losses

The iron losses at load are determined from the input power minus the winding copper losses and the mechanical losses. The star winding resistance, R_a, was taken as 10 Ω, and the values of the mechanical losses versus speed were read off from Fig. 3.39, p. 113. The iron losses are plotted in Figs. 5.29 to 5.34 for two values of excitation as given in Table 5.2.

X - Axis	Fig. no.	
	450 At	750 At
Supply current	5.29	5.30
Supply voltage	5.31	5.32
Output power	5.33	5.34

Table 5.2 Load iron loss curves

For a constant supply voltage, V_s, the iron losses in Figs. 5.29 and 5.30 vary almost linearly with supply current, I_s. However, other parameters are continuously changing, namely, speed and air-gap flux, making it difficult to relate the iron losses to the supply current. It is noticed that iron losses increase rapidly with the increasing supply current despite the considerable drop in the speed. This is attributed to the armature reaction effect which distorts the air-gap flux-density distributions resulting in very high values of flux-density in some of the teeth facing the pole-pieces and in parts of the pole-pieces too. This effect of the armature reaction on the flux-density distribution is minimised by operating at higher levels of excitation as seen from a comparison between the iron losses at the two values of excitation.

The iron losses are also plotted against the supply voltage for constant values of supply current in Figs. 5.31 and 5.32. The dashed curves in these figures

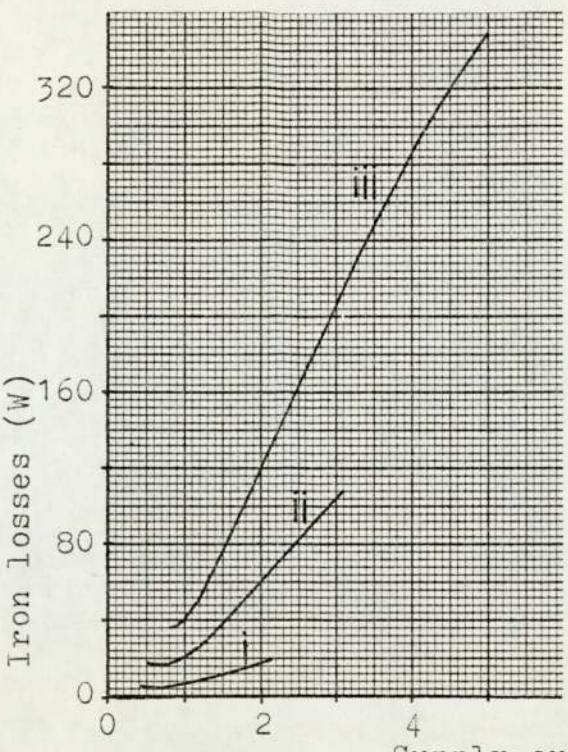

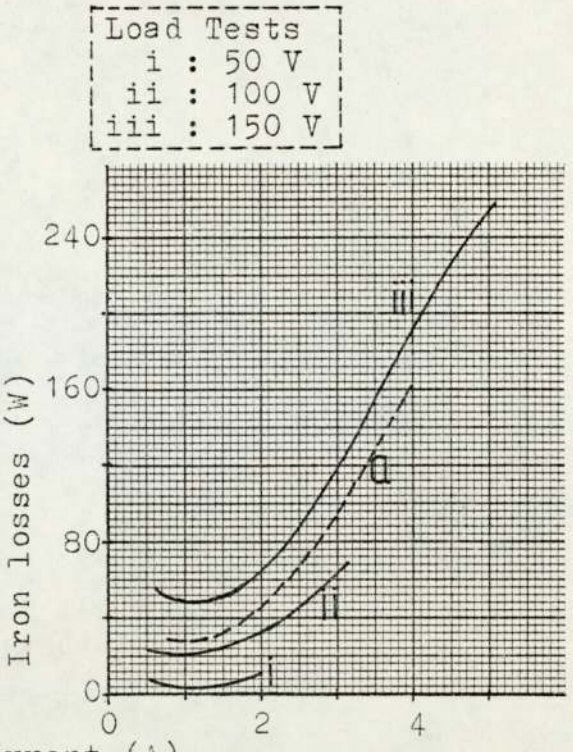

Supply current (A)

a : IR compensation at E_b = 100 V and F_f = 750 At

Fig. 5.29 F_f = 450 At

Fig. 5.30 F_f = 750 At

(v. page xviia)

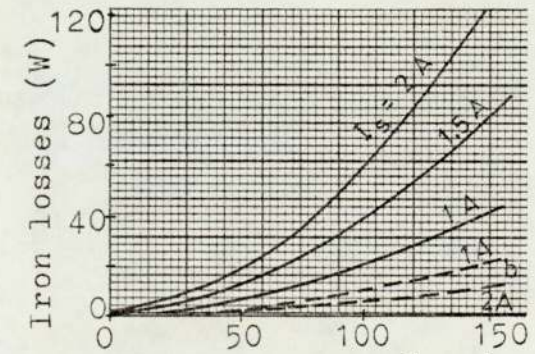

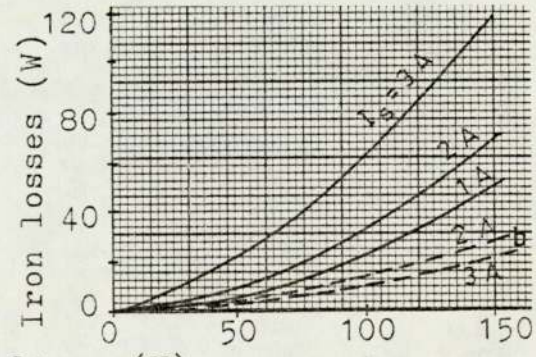

Supply voltage (V)

b: no-load iron losses (for comparison)

Fig. 5.31 F_f = 450 At

Fig. 5.32 F_f = 750 At

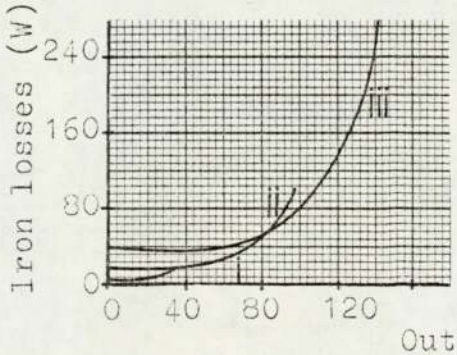

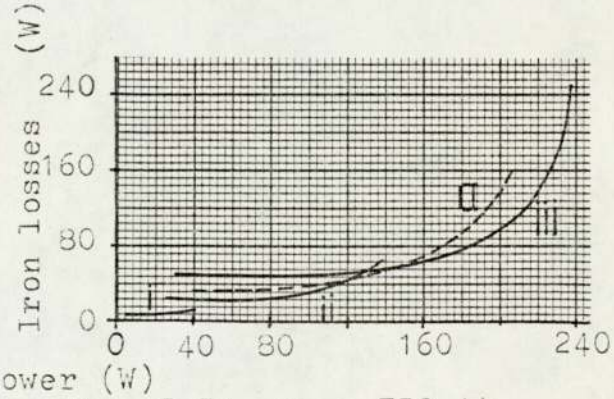

Output power (W)

Fig. 5.33 F_f = 450 At

Fig. 5.34 F_f = 750 At

represent the no-load iron losses obtained from Fig. 5.20, p. 233, at the values of speed corresponding to the particular values of supply current read off the curves in Figs. 5.21 and 5.22, p. 235. The iron losses at load are seen to be several times the values at no-load, which is again attributed to the armature reaction effect.

Figs. 5.33 and 5.34 show the variation in the iron losses with output power. Higher values of output power can be obtained from the motor at higher levels of excitation since the iron losses remain low over a wide range of output power.

5.4.3 IR compensation

To improve the speed characteristics of the brushless motor, the voltage drop across the star winding resistance R_a is compensated for by increasing the supply voltage as the supply current increases. The back e.m.f. is, therefore, held numerically constant as the load changes. A load test was performed at 750 At and the results are plotted in the figures given in Table 5.3.

Since the value of torque depends upon excitation and supply current, changes in the supply voltage have very little effect on the torque as seen in Fig. 5.24, p. 235. The torque curve against supply current with IR compensation remains practically the same as before.

Axes		Fig.	Page
Y	X		
Speed	Supply current	5.22	235
Speed	Output power	5.26	235
Efficiency	Output power	5.28	237
Iron loss	Supply current	5.30	240
Iron loss	Output power	5.34	240

Table 5.3 Load curves with IR compensation

Since speed regulation is much smaller now (Fig. 5.22), higher values of output power can be obtained (Fig. 5.26). The efficiency curve in Fig. 5.28 indicates that with IR compensation it is possible to operate over a wider range of output power with the efficiency at its highest value than before compensation. The iron losses are plotted in Figs. 5.30 and 5.34 versus supply current and output power, respectively. Since the back e.m.f. is kept constant at 100 V, the iron loss curves with IR compensation fall between those for V_s equal to 100 V and 150 V.

The operation at a back e.m.f. of 100 V and an excitation of 750 At is only one example of loading the brushless motor with the IR drop compensated for. This load test was performed by manually adjusting the supply voltage to a new value as the supply current increases with added load. The thyristor power supply which will be explained in Chapter 6, is capable of performing this voltage adjustment automatically as the supply current increases. All that would be needed for IR compensated

operation would be to set the power supply to the required value of back e.m.f., E_b. Operation with the power supply at E_b = 100 V and an excitation of 750 At resulted in exactly the same curves listed in Table 5.3.

The IR drop can also be over-compensated by assuming a value for R_a higher than the actual value. This results in an even smaller difference between the values of speed at no-load and load than that for normal compensation in Fig. 5.26. However, this over-compensation is not very effective with a noticeable fall in speed at very high values of output power. The fall is actually due to the sharp increase in the iron losses at heavy loads as seen from the curves of Fig. 5.34.

5.5 Comments

The switching angle γ_1 for the star winding is related to angle γ for the ring winding (Chapter 3) by the following expression, $\gamma_1 = \gamma + 10^{\circ}(m)$, for the same pole position. Angle γ_1 is set at $-15^{\circ}(m)$ for motor operation with the electronic commutator. This value of γ_1 is selected for the maximum value of developed torque (with the aid of corresponding values of γ) as well as to minimise the high peaks in the waveforms of the winding current.

Power transistor switching at the highest levels of load expected, entails an average power loss of 1.9 W resulting in a junction temperature rise of 4.5°C. For an ambient temperature of 25°C, the heat-sink (R_{th} = 0.65°C/W) is very conservatively used for the temperature rise expected.

Motor operation indicates that the motor has approximately linear torque/speed characteristics particularly at the higher levels of excitation. The shunt characteristics of a conventional d.c. motor are maintained and speed control is satisfactory. The fall in speed from no-load to load is reduced by IR compensation which is performed automatically by the power supply unit (Chapter 6). The maximum efficiency of the motor is limited to about 60% by the rapidly increasing iron losses with the load. This is principally a problem with the present design which uses solid-poles. The replacement by laminated poles would reduce the losses and increase the available shaft torque. The double-stator feature inevitably means more copper loss in the additional overhang winding.

CHAPTER 6

POWER SUPPLY DESIGN AND PERFORMANCE

6.1 Introduction

In common with a conventional d.c. motor, the brushless motor requires a starting method whereby the supply current is limited to a safe value. In this project supply voltage control is adopted, and the power supply unit doubles as a starter and as an IR compensator. Limits on the supply voltage and current are also incorporated.

In principle, a half-controlled SCR bridge is connected across the 50 Hz mains and the smoothed output is fed to the motor. The SCR gates are supplied with controlled trains of triggering pulses. SCR's are preferable to power transistors in the power supply in view of the ability to sustain transients which are usually experienced with mains voltages. The maximum d.c. voltage obtainable from the SCR bridge is $250\sqrt{2}$ or 353 V.

Fig. 6.1 shows the connection diagram of the main circuit to the a.c. mains, and the resistance bridge to the output of the SCR bridge. Four sensing points are shown on the diagram.

(i) The d.c. supply voltage V_s can be measured between this node and ground. A miniature voltmeter (0 - 200 V) is permanently connected

between these two points and mounted on the front panel of the power supply unit.

(ii) The voltage drop across the resistor R_6 is proportional to the supply current I_s and is therefore connected to operational amplifier OA1 in the control circuit of Fig. 6.7, p. 257, for current feedback. This sensing point is also taken out to the front panel.

(iii) Voltage feedback is obtained from the resistance bridge at this node and supplied to the input of op-amp OA2 in Fig. 6.7.

(iv) The d.c. output current of the SCR bridge is proportional to the voltage drop across the sensing resistor R_5.

The various parts of the circuit in Fig. 6.1 are listed below.

(a) A half-controlled bridge-rectifier, type SKB33/12, with a maximum repetitive peak reverse voltage V_{RRM} of 1200 V and a maximum d.c. current I_D at 45° C of 23 A, (v. Appendix A10). The SCR's are common to the d.c. terminal. The bridge is mounted on an 0.65° C/W heat-sink and ventilated with a fan.

(b) A smoothing LC filter consisting of a series choke (L_3 = 5 mH) and a bank of 4 capacitors in parallel making a total of 6000 µF. A 15 kΩ discharge resistor is connected across each capacitor.

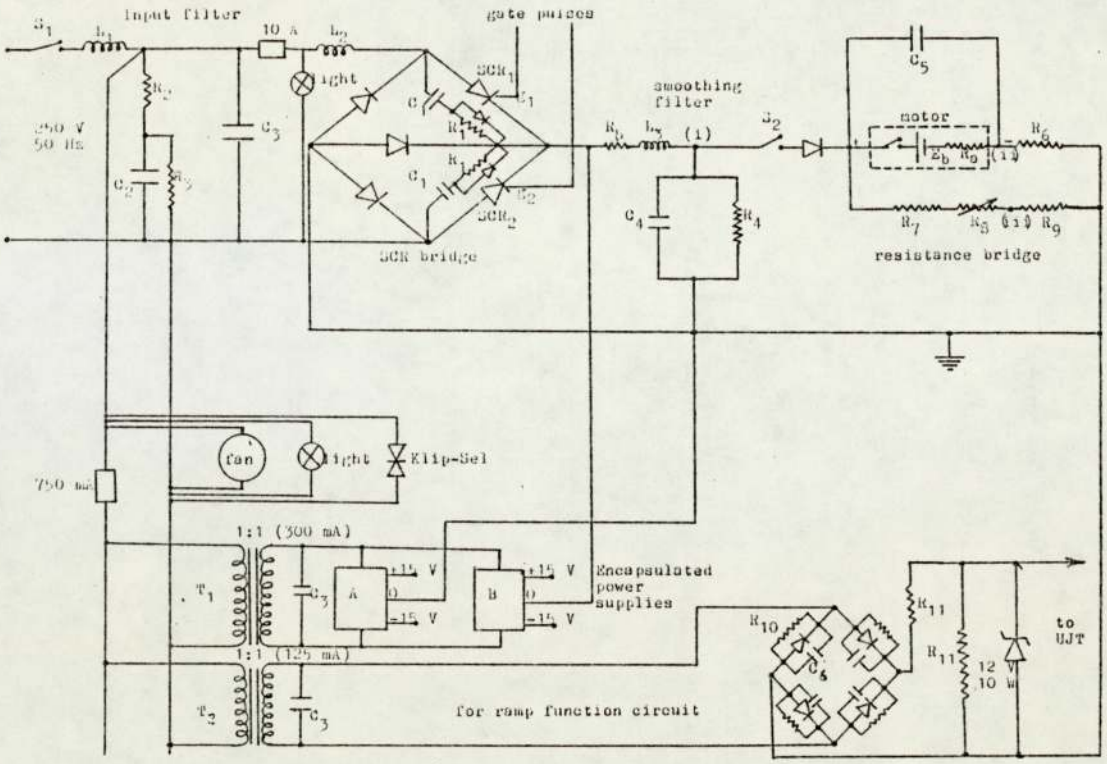

Resistance		Power rating (W)
No.	Value (Ω)	
1	68	7
2	8.2	7
3	22 k	7
4	15 k	10
5	1	25
6	0.1	25
7	8.2 k	7
8	5 k	3
9	100	5
10	200 k	0.5
11	10 k	10

Capacitance		d.c. voltage (V)
No.	Value (μF)	
1	0.22	1000
2	4	1000
3	0.47	1000
4	1500	450
5	8	400
6	0.01	750

Inductance		Remarks
No.	Value (H)	
1	205 μ	65 turns, 22 S.W.G.
2	350 μ	85 turns, 22 S.W.G.
3	5 m	0.125 Ω, 1.5 mm^2

Fig. 6.1 Power supply main circuit

(c) Transient suppression:

(i) An RC snubber circuit is connected across each SCR.

(ii) An input filter to suppress mains-borne voltage transients consists of L_1, R_2, C_2. The maximum rate of rise of voltage $(\frac{dv}{dt})$ is controlled by the input filter as well as by the parallel capacitor C_3 and series choke L_2. The maximum value of $(\frac{dv}{dt})$ is determined later in Section 6.1.1.

(iii) A stack of 14 cells forming a voltage surge protector ('Klip-Sel') is connected across the a.c. mains. The r.m.s. operating voltage of the stack is about 364 V and the clipping voltage is about 875 V.

(d) Two isolating transformers:

(i) Transformer T_1 provides additional isolation for the two encapsulated power supplies A and B. These power supplies provide the ±15 V supplies for the two control boards A and B.

(ii) Transformer T_2 provides isolation for the full-wave rectifier bridges of the ramp function circuit.

(e) The limbs of the resistance bridge comprise the brushless motor winding R_a, a combination of a fixed resistor R_7, and a variable resistor R_8, R_6, and R_9.

The resistance bridge provides a voltage that is proportional to the back e.m.f., E_b, of the motor which can be compared with a set reference voltage and

maintained constant. The equations of the voltages at nodes (ii) and (iii) are given in Equations (6.1) and (6.2), respectively.

$$V_{ii} = \frac{R_6}{R_a + R_6} (V_s - E_b) \tag{6.1}$$

$$V_{iii} = \frac{R_9}{(R_7 + R_8) + R_9} V_s \tag{6.2}$$

Since R_8 is a variable resistor, the resistance bridge can be balanced for a given value of R_a as in Equation (6.3).

$$\frac{R_a}{R_6} = \frac{(R_7 + R_8)}{R_9} \tag{6.3}$$

The potential difference between nodes (ii) and (iii) is, therefore,

$$V_{iii} - V_{ii} = \frac{R_6}{R_a + R_6} (E_b) \tag{6.4}$$

which is proportional to the back e.m.f.

6.1.1 dv/dt calculation

Fig. 6.2 shows the circuit diagram of the input filter with V as the peak value of the mains supply voltage and V_o the output voltage.

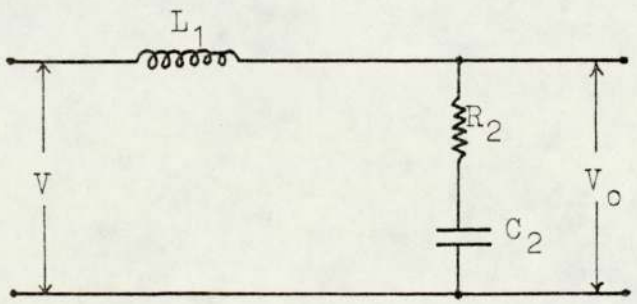

Fig. 6.2 Input filter

The instantaneous output voltage is given by[55]:

$$V_o = V\left(1 - \frac{\cos(\omega_n t\sqrt{1 - \xi^2} + \theta)}{\sqrt{1 - \xi^2}} e^{-\xi\omega_n t}\right) \qquad (6.5)$$

where ω_n is the natural frequency of the circuit, and ξ is the damping factor:

$$\omega_n = \frac{1}{\sqrt{L_1 C_2}} \quad \text{rad/s} \qquad (6.6)$$

$$\xi = \frac{R_2}{2\omega_n L_1} \text{ or } \frac{\omega_n C_2 R_2}{2} \text{ or } \sqrt{C_2/L_1}\left(\frac{R_2}{2}\right) \qquad (6.7)$$

Angle θ is a function of the damping factor:

$$\theta = \text{arc sin}\xi \qquad (6.8)$$

The voltage V_o reaches the maximum value when:

$$t = \frac{(\pi - \theta)}{\omega_n\sqrt{1 - \xi^2}} \qquad (6.9)$$

Substituting (6.9) in (6.5) results in

$$V_{omax} = V\left(1 + \frac{1}{\sqrt{1 + \xi^2}} e^{-(\pi - \theta)(\xi/\sqrt{1 - \xi^2})}\right) \qquad (6.10)$$

The rate of rise of v_o can be obtained by differentiating Equation (6.5), thus

$$\frac{dv_o}{dt} = V\left(\frac{\omega_n}{\sqrt{1 - \xi^2}} \sin(\omega_n t\sqrt{1 - \xi^2} + 2\theta) e^{-\xi\omega_n t}\right) \qquad (6.11)$$

The maximum value of $\frac{dv_o}{dt}$ occurs when:

$$t = \frac{(\pi/2 - 3\theta)}{\omega_n\sqrt{1 - \xi^2}} \qquad (6.12)$$

Substituting (6.12) in (6.11) gives:

$$\left(\frac{dv_o}{dt}\right)_{max} = V\,\omega_n\, e^{-(\pi/2 - 3\theta)(\xi/\sqrt{1 - \xi^2})} \qquad (6.13)$$

To determine the voltage overshoot at switch-on, ω_n, ξ and θ are calculated from Equations (6.6) to (6.8) and substituted in Equation (6.10).

For $L_1 = 205\ \mu H$, $R_2 = 8.2\ \Omega$, and $C_2 = 4\ \mu F$:

$$\omega_n = 34.9 \times 10^3 \text{ rad/s}, \quad \xi = 0.573, \quad \theta = 35^\circ$$

Therefore, $V_{omax} = 1.208\ (250)(\sqrt{2}) = 427$ V, which means that the voltage appearing across the SCR bridge when the mains switch is closed is 20% above the peak value of the mains voltage. This value of voltage is acceptable since it is within the SCR rating.

The other important calculation is the rate of rise of v_o at switch-on. This value is determined from Equation (6.13),

$$\left(\frac{dv_o}{dt}\right)_{max} = 14.8 \text{ V/}\mu\text{s}$$

and is seen to be well below the maximum rated value of 200 V/μs (v. Appendix A10).

The voltage overshoot and the rate of rise of voltage can also be determined for the smoothing filter when one of the SCR's is triggered into conduction. The circuit of the smoothing filter and the components between the filter and the supply are shown in Fig. 6.3a. The values of the components are as follows:

$L_1 = 205\ \mu H$, $L_2 = 350\ \mu H$, $L_3 = 5$ mH,

$R_5 = 1\ \Omega$, $4 \times C_4 = 6000\ \mu F$

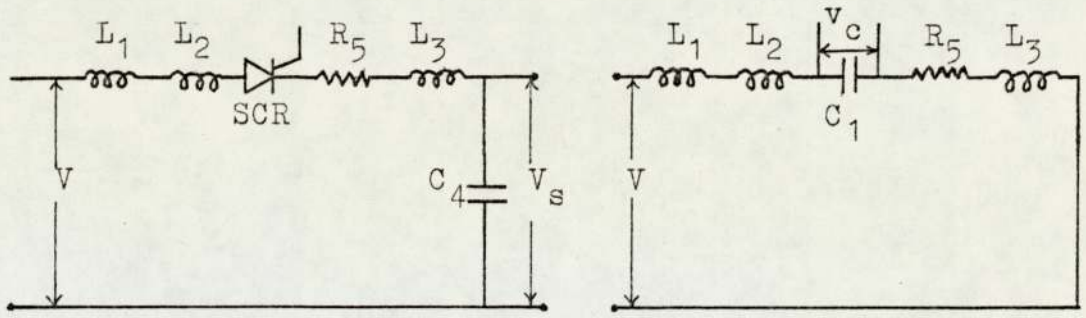

(a) smoothing filter and supply circuit

(b) snubber capacitor C_1 circuit at turn-off

Fig. 6.3 Circuit diagrams at switching

For a total inductance of 5555 μH and a resistance of 1.125 Ω, (including the coils):

ω_n = 173.2 rad/s, ξ = 0.585, θ = 35.8°

Substituting in Equation (6.10),

V_{smax} = 1.201 (250)($\sqrt{2}$) = 427 V is the maximum overshoot voltage across the capacitor (minus the voltage drop across R_5) when an SCR is triggered at the crest of the alternating voltage waveform.

The maximum rate of rise of voltage is determined from Equation (6.13) and the value is:

$$\left(\frac{dv_s}{dt}\right)_{max} = 76.2 \text{ mV/μs}$$

which is very small and acceptable.

Finally, the rate of rise of voltage across the SCR when it returns to the blocking state is determined. The circuit is given in Fig. 6.3b with the SCR replaced by C_1 = 0.22 μF.

$\omega_n = 28.6 \times 10^3$ rad/s, $\xi = 3.54 \times 10^{-3}$, θ = 0.2°

From Equation (6.10) and for this small value of ξ, V_{cmax} is approximately 2 x V or 707 V which is below the maximum rated voltage of the SCR, i.e., 1200 V.

The maximum rate of rise of voltage from Equation (6.13) is:

$$\left(\frac{dv_c}{dt}\right)_{max} = 10.1 \text{ V}/\mu\text{s}$$

This value of $\frac{dv_c}{dt}$ is below the maximum rated value and is, therefore, acceptable.

The maximum inrush current into the capacitors of Figs. 6.2 and 6.3a can be estimated from the maximum voltage at switch-on, or firing, and the circuit resistance for critical damping. Thus, for the circuit of Fig. 6.2:

$$I = \frac{V_{omax}}{2\sqrt{L_1/C_2}} = 30 \text{ A}$$

which is the value of current into C_2 for the extreme condition of closing the mains switch at the crest of the voltage waveform.

For the circuit of Fig. 6.3a, the inrush current is:

$$\frac{V_{smax}}{2\sqrt{L/C}} = 222 \text{ A}$$

This value of current is within the maximum non-repetitive 10 ms surge current of 400 A tolerated by the SCR bridge. However, it is very unlikely that this value is reached since the SCR triggering does not commence at

the crest of the sinusoidal waveform but at the zero-crossing points of the voltage waveform. In the event of triggering at a high voltage, the 10 A fuse in the supply circuit provides adequate protection.

6.1.2 Triggering requirements

To achieve control over the output voltage of the half-controlled bridge, phase-control is used. Each SCR is triggered at an angle α in the positive half-cycle of the supply as shown in Fig. 6.4. The SCR remains in the conduction state until the anode-cathode voltage reverses polarity. This period is equivalent to the conduction angle λ, and is the time period for which current flows in the SCR. The power supplied to the circuit can, therefore, be controlled by varying λ which is also $(180 - \alpha)^\circ$.

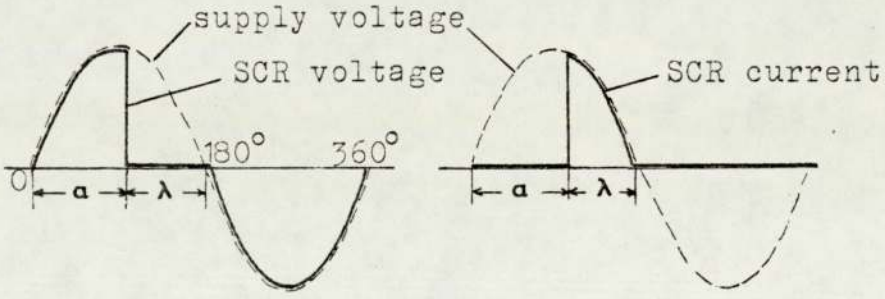

Fig. 6.4 SCR voltage and current waveforms

An SCR can be triggered by one pulse of sufficient voltage and duration. The maximum value of pulse duration can be estimated assuming a purely inductive load on the SCR. Thus, from the relation $e = L\frac{di}{dt}$, the pulse duration is

$$t_p = \frac{L}{V_s} I_L \qquad (6.14)$$

where I_L is the latching current of the SCR which is typically 50 mA. For the minimum value of V_s of, say, 10 V, and an inductance L_3 of 5 mH, the maximum value of t_p required is 25 μs.

The limits on the gate input are a maximum gate-cathode voltage of 3 V and a maximum gate current of 100 mA. To ensure SCR triggering at the desired value of α, a train of triggering pulses is used in case the SCR does not latch with one pulse, especially when the load on the SCR is inductive.

The same train of pulses is simultaneously applied to the gates of both SCR's of the half-controlled bridge shown in Fig. 6.5. The waveform of the output voltage of the bridge is shown in Fig. 6.6 as part of the 50 Hz sinusoidal supply voltage waveform[55].

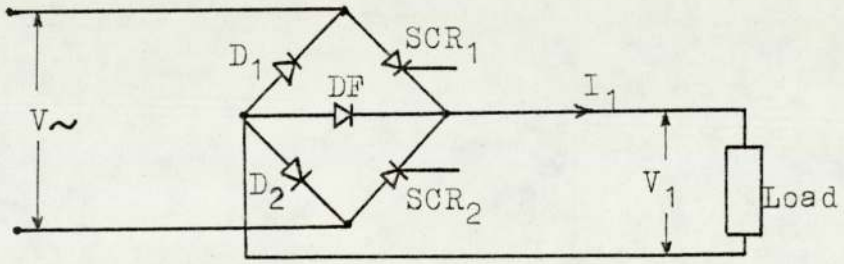

Fig. 6.5 Half-controlled SCR bridge

The load in Fig. 6.5 is assumed a combination of R and L only. But in the actual power supply circuit of Fig. 6.1, a smoothing filter consisting of L and C is

connected across the SCR bridge. The effect of C in the load in Fig. 6.5 is to make V_x positive and equal to the voltage across the capacitor. At time t_1, after the SCR reverts to the blocking state, the voltage V_1 across the load becomes that of the capacitor. This is shown as the dashed curve in Fig. 6.6.

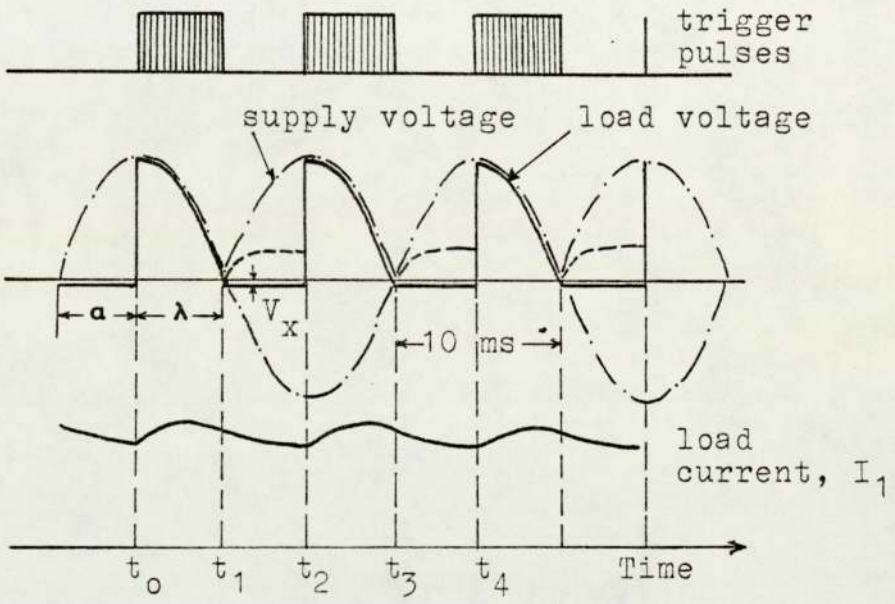

Fig. 6.6 Waveforms for the circuit of Fig. 6.5

6.2 Control circuitry

The block diagram of the control circuitry is shown in Fig. 6.7 and the actual arrangement on strip-boards A and B is shown in Fig. 6.8 (v. Photograph 6b). The general-purpose operational-amplifier used is an integrated-circuit type 741. Amplifier OA10 is the only exception and is type 531 which has higher input resistance, higher slew rate and wider band-width than the 741 type. The operating modes of the op-amps are explained in the following sections.

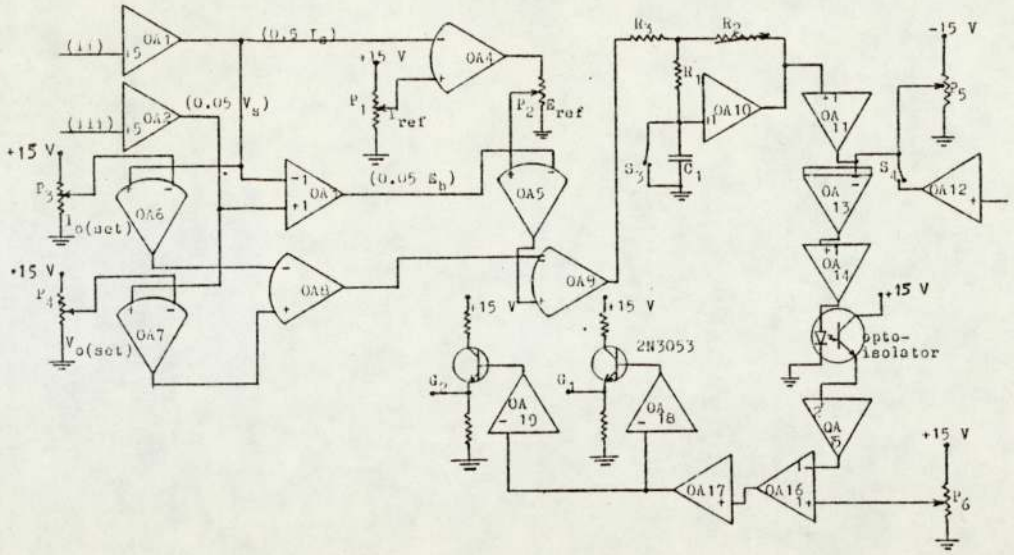

Fig. 6.7 Block diagram of control circuitry

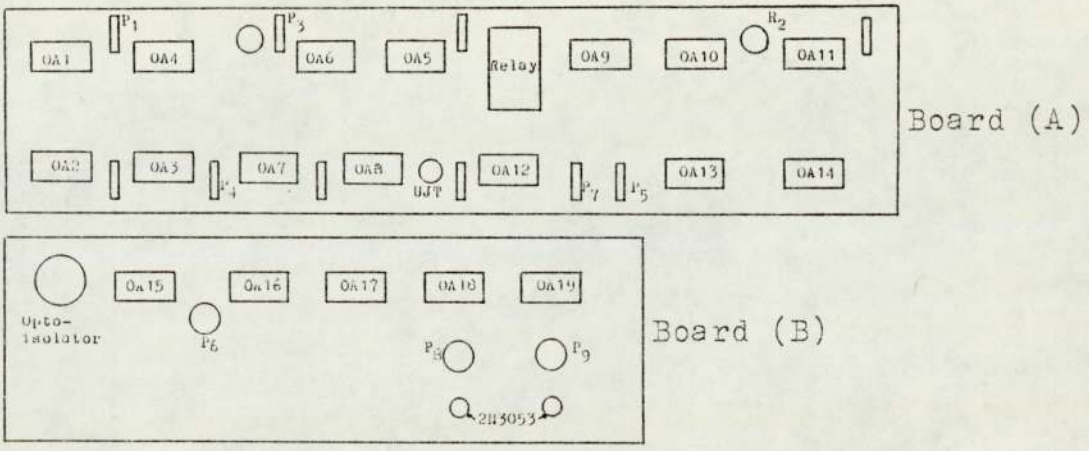

Fig. 6.8 Arrangement of components of control circuit

6.2.1 Key features

The key features of the control circuitry are listed below and later explained with the aid of truth tables.

(a) The supply current to the motor can be set to a maximum value (up to 4 A) by adjusting potentiometer P_1 at the input of OA4.

(b) IR compensation is performed by setting the back e.m.f. to any value between zero and 200 V. This is achieved by adjusting the potentiometer P_2 at the output of OA4.

(c) To prevent an uncontrolled increase in the output d.c. voltage when the power supply is switched on while the electronic commutator is off, the circuit consisting of OA6, OA7 and OA8 limits the voltage to a low value set by the potentiometer P_4.

(d) The rate at which the conduction angle λ increases from zero is controlled with the values of the resistors and the capacitor connected to OA10. This is equivalent to controlling the output voltage of the power supply.

The operation of the control circuitry requires feedback signals from the motor circuit corresponding to the supply current I_s and the supply voltage V_s. These two signals are obtained from nodes (ii) and (iii) in Fig. 6.1. The current feedback node (ii) is connected to OA1 and the voltage feedback node (iii) to OA2, (v. Fig. 6.7). The two op-amps are connected to differential amplifier OA3 and the output of OA3 satisfies the requirement of Equation (6.4), p. 249. If the winding resistance is assumed as 10 Ω then, since R_6 is 0.1 Ω, $V_{iii} - V_{ii} = 0.01\ E_b$. Since the gains of OA1 and OA2 are equal to 5, the output of OA3 is $0.05\ E_b$. For a maximum value of 200 V for E_b, the output of OA3 would be 10 V which is an acceptable value.

The output of current feedback amplifier OA1 is also taken to comparator OA4 where it is compared with the voltage from a reference potentiometer P_1. The voltage at node (ii) can be written as $R_6 I_s$ or $0.1\ I_s$. The output of OA1 is, therefore, $+0.5\ I_s$ and would be equal to 2 V at the maximum required value of I_s = 4 A. Hence the output of potentiometer P_1 can be varied between zero and 2 V for values of current-setting between zero and 4 A. If the supply current I_s is below the reference current I_{ref}, the output voltage of OA4 is positive and vice versa.

The outputs of OA3 and OA4 are now combined in comparator OA5 to check the value of the back e.m.f. E_b. Since the output of OA3 varies between zero and 10 V for values of E_b between zero and 200 V, the output of OA4 is also controlled with potentiometer P_2 between zero and 10 V. Therefore, the output of OA5 is positive provided that I_s is less than I_{ref}, and that E_b is less than E_{ref}. If either I_s or E_b reaches the reference value, the output from OA5 would be negative, as can be seen from Truth Table 6.1.

$I_s < I_{ref}$	$E_b < E_{ref}$	OA5 output (V)
Yes (N)	Yes (N)	+15 (N)
No	Yes (N)	-15
Yes (N)	No	-15
No	No	-15

Table 6.1 Truth table for OA5, N: normal

Hence the output of OA5 can be used as an indication of the requirement for triggering pulses to the SCR. However, in the case of switching the supply on with the electronic commutator still OFF, the output of OA5 remains positive until the supply voltage reaches the value E_{ref}. This situation is unacceptable in case the electronic commutator is switched on with the supply voltage at a high value, resulting in a high inrush current which would damage the power transistors.

The combination of op-amps OA6, OA7, OA8 and potentiometers P_3 and P_4 senses the absence of the supply current and operates to prevent the supply voltage from increasing above a certain value. Potentiometer P_3 is set at 0.04 V representing $I_{o(set)}$ which is equivalent to 80 mA, while potentiometer P_4 can be adjusted to the desired value of open-circuit voltage $V_{o(set)}$. The voltage at potentiometer P_4 should be $V_{o(set)}/20$ V. Table 6.2 is the truth table for the output of op-amp OA8 showing that normal operation (N) is obtained when the output voltage is -15 V. The error output is obtained when the supply voltage exceeds the set value. Note that when I_s exceeds the very small value of 80 mA, an indication of motor operation, the output of OA8 is normal, thus not affecting the output of OA5.

The outputs of both OA5 and OA8 are combined in comparator OA9 and the truth table is given in Table 6.3.

The normal output (N) of +15 V occurs when 80 mA $< I_s < I_{ref}$ and $E_b < E_{ref}$, and also when $I_s <$ 80 mA but $V_s < V_{o(set)}$.

0.5 $I_s <$ 0.04 V	0.05 $V_s < V_{o(set)}$	OA8 output (V)
Yes (N)	Yes (N)	-15 (N)
No	Yes (N)	-15 (N)
Yes (N)	No	+15
No	No	-15 (N)

Table 6.2 Truth table for OA8, N: normal

OA5 (V)	OA8 (V)	OA9 (V)
+15 (N)	-15 (N)	+15 (N)
-15	-15 (N)	-15
+15 (N)	+15	-15
-15	+15	-15

Table 6.3 Truth table for OA9, (output voltages), N: normal

The fourth feature of the control circuit is the control over the rate of rise of supply voltage to provide the motor with a smooth start. This is performed with op-amp OA10 and the circuit connected to it whose values are given below.

R_1 = 75 kΩ $\qquad$ R_3 = 21 kΩ

R_2 = 100 Ω to 10 kΩ $\qquad$ C_1 = 22 μF

Capacitor C_1 starts to charge up once the output voltage of OA9 goes positive. A zener diode limits the voltage across C_1 to +8.5 V and, when the output of OA9 goes

negative, to -0.5 V. The charging rate of C_1 and hence the output of OA10 are controlled by the value of the variable resistor R_2 as in Equation (6.15).

$$\tau = C_1 R_1 \left(1 + \frac{R_3}{R_1} + \frac{R_1}{R_2}\right) \quad \text{seconds} \qquad (6.15)$$

Therefore, for values of R_2 between 100 Ω and 10 kΩ, the time constant τ can be varied between 20.7 minutes and 14.5 seconds. This range of τ provides a wide choice of rates of rise of the supply voltage, V_s, at start. In any case, if V_s rises rapidly the starting current is limited to the value I_{ref} while the motor speed builds up.

The remainder of the control circuitry deals with the generation of the triggering pulses for the SCR's.

6.2.2 Generation of the triggering pulses

Triggering pulses are produced by the regenerative action of op-amp OA13 which is connected as shown in Fig. 6.9. The input to OA13 consists of 3 parts:

(a) a constant negative voltage of -4.7 V from potentiometer P_5

(b) a 100 Hz ramp function input with a maximum value of +4.7 V

(c) the varying output voltage from OA10 (following unity-gain buffer amplifier OA11) with a maximum value of +3.8 V.

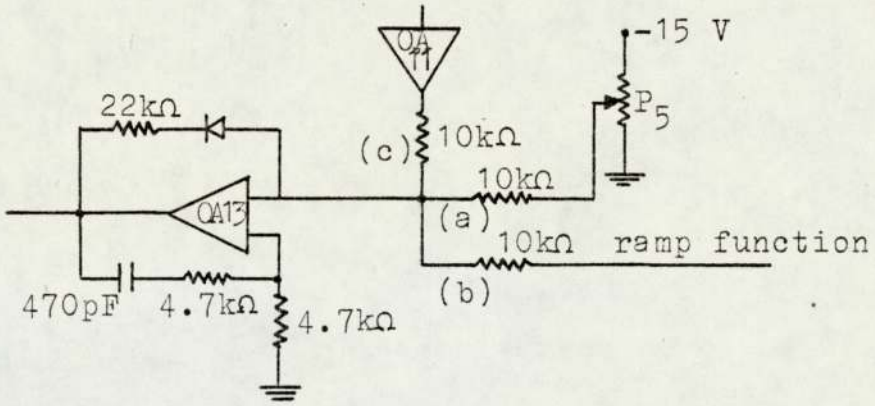

Fig. 6.9 Pulse generator OA13

In Fig. 6.10, inputs (a) and (b) are represented as a constant value and a ramp function, respectively. The sum of these two inputs is then shown at 3 values of input (c), V_c = 0 V, 1 V and at the maximum value of 3.8 V. The total input is seen to be positive over larger angles starting from zero at V_c = 0 V, and increasing to about 150° at the maximum value of V_c from OA11. The rate at which this increase in the angle takes place is determined by τ of OA10 as was explained in the previous section.

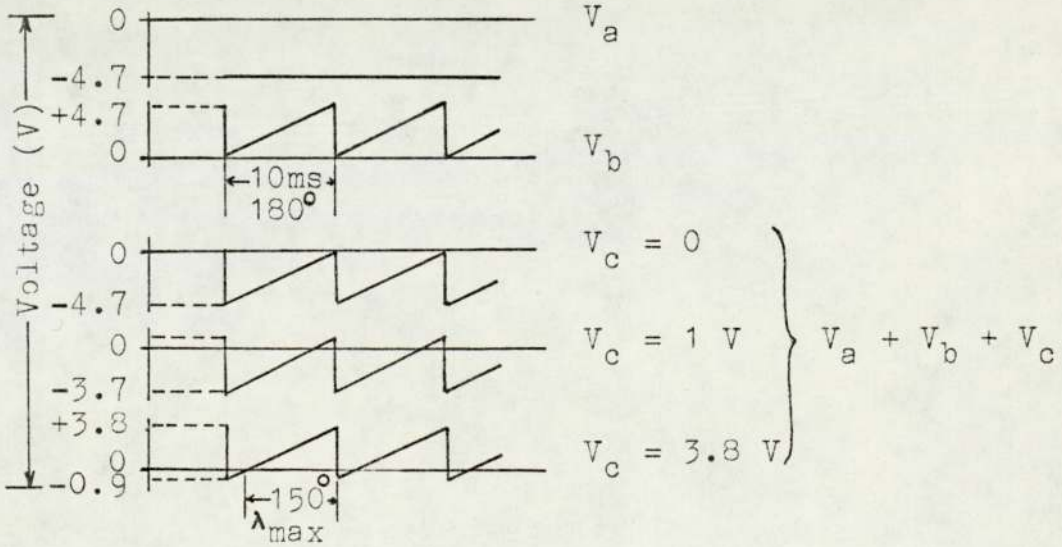

Fig. 6.10 Input voltages to OA13

The output pulses are obtained from OA13 as long as the sum of the 3 input voltages to it is positive. These pulses are eventually used to trigger the SCR and hence the start of a train of pulses signifies the conduction angle λ of the SCR. A conduction angle between 0° and 150° is quite adequate for this application. In fact, since the capacitor at the output of the SCR bridge charges up to the maximum value of voltage at the start of the conduction period, a much smaller λ is sufficient to obtain the supply voltage required. The value of the supply voltage is determined from the peak value of the mains voltage and the conduction angle λ as in Equation (6.16).

$$V_s = (250\sqrt{2}) \sin \lambda \qquad (6.16)$$

As an example, the required value of λ is about 35° for a voltage V_s of 200 V. This means that the voltage at input (c) to op-amp OA13 would be about 1 V for this condition, (v. Fig. 6.10).

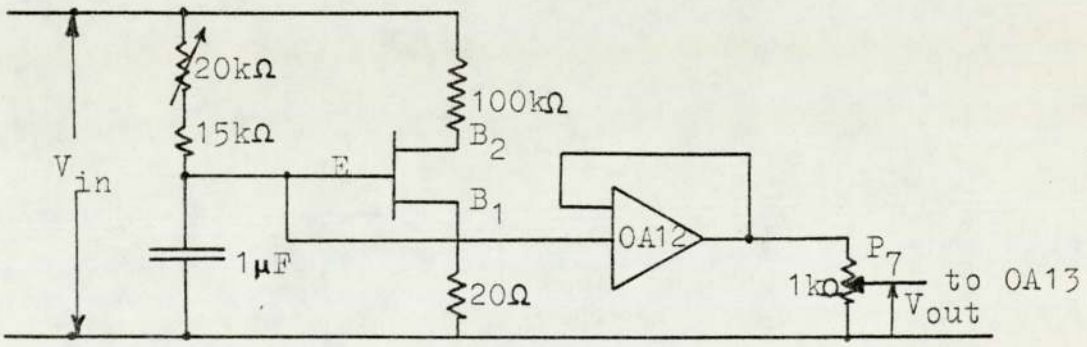

Fig. 6.11 Ramp function circuit

The circuit of the ramp function generator is given in Fig. 6.11. The output voltage from the full-wave diode bridge in Fig. 6.1, p. 247, is used as the supply. The

zener diode limits the voltage to 12 V resulting in the waveform given in Fig. 6.12a where the voltage falls to zero at 10 ms intervals (due to the 50 Hz supply). The output ramp function from the emitter of the unijunction transistor (type 2N2646) which is shown in Fig. 6.12b, is fed to OA13 through the buffer OA12. The non-linearity in the ramp function introduces negligible non-uniformity in the rate of increase in the conduction angle λ.

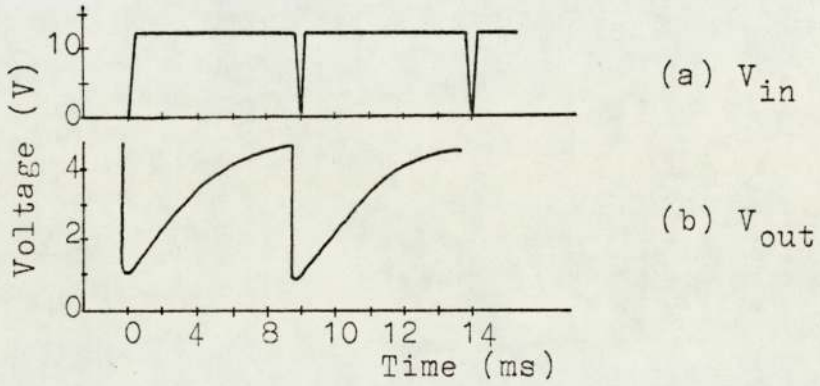

Fig. 6.12 Waveforms of voltages in Fig. 6.11

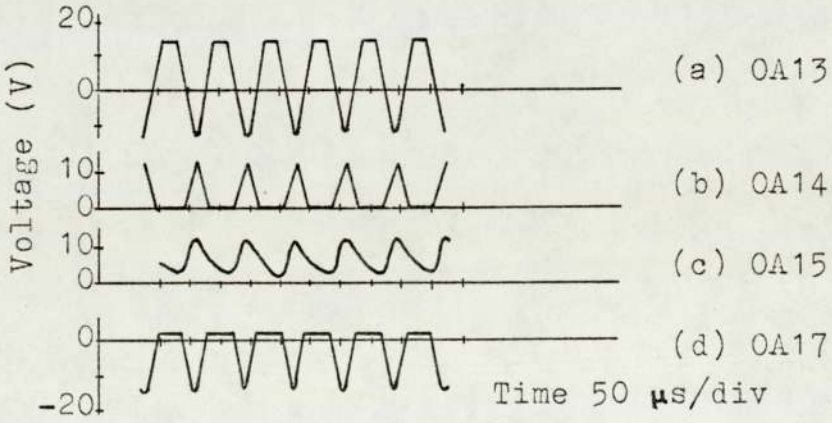

Fig. 6.13 Output voltage waveforms of op-amps

The frequency of the triggering pulses at the output of OA13 is about 12 kHz and a few of these pulses are shown in Fig. 6.13a. These pulses cannot be used directly to trigger the SCR's for the reasons given in the following section.

6.2.3 Processing of the triggering pulses

The pulses produced by op-amp OA13 must be processed before they can be used to trigger the SCR for the following reasons:

(a) The output voltage alternates between ±15 V, whereas the gate requirement is for positive pulses only.

(b) Since different points of the control circuit are at different potentials, isolation must be provided between the feedback nodes and the triggering pulses.

(c) The power requirements of the gates are beyond the rating of the op-amps.

Op-amp OA14 is a unity-gain amplifier, connected to remove the negative parts of the pulses produced by OA13. The resultant waveform is shown in Fig. 6.13b.

Isolation is provided by an opto-isolator at the output of OA14. The pulses cause a maximum current of about 6 mA to flow in the opto-diode. The opto-transistor and the remaining op-amps are supplied from power supply B indicated in Fig. 6.1, p. 247. whereas the circuit prior to the opto-diode was supplied from power supply A.

The output of the opto-transistor is connected to op-amp OA15 which operates as a buffer amplifier with a gain of 2. The waveform is shown in Fig. 6.13c, and the

voltage is seen to change between +2 V and +14 V. To remove the constant d.c. level of 2 V, differential amplifier OA16 (with a gain of 0.5) is connected to the output of OA15. The positive input to OA16 is adjusted with potentiometer P_6 so that the output of OA16 varies between ±14 V. The positive parts of the output signals are removed with op-amp OA17 resulting in the waveform shown in Fig. 6.13d. A positive voltage of about 1.9 V is deliberately introduced in the output of OA17 as shown in Fig. 6.14. This small positive voltage results in a negative voltage at the output of OA18 and OA19 so that the base circuits of the transistors are reverse biased in the absence of the triggering pulses.

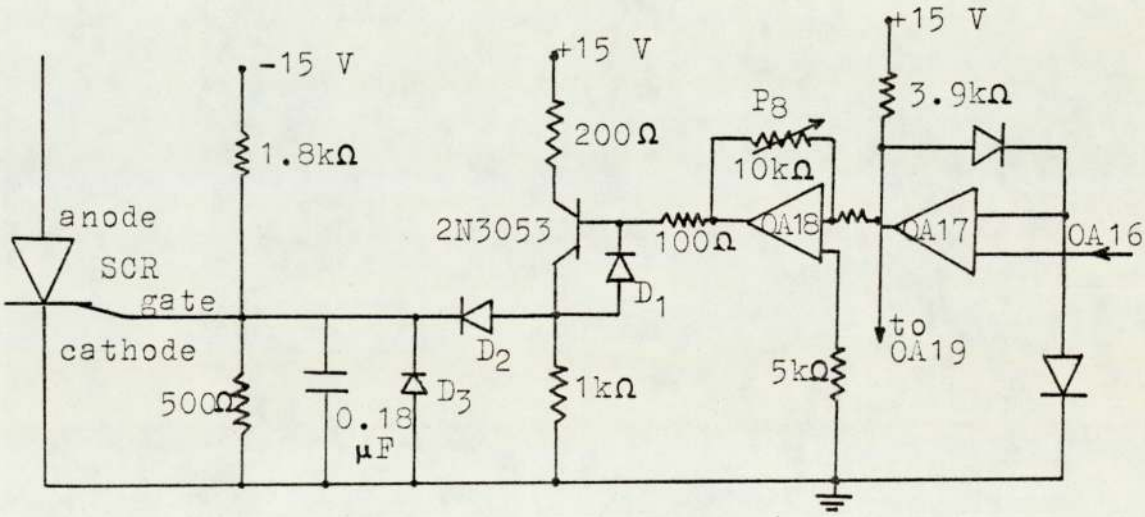

Fig. 6.14 SCR gate circuit

These pulses are now suitable to drive the transistors supplying the gates of the SCR's after inversion and attenuation to a maximum of 5 V performed by op-amps OA18 and OA19. One gate circuit is shown in more detail in Fig. 6.14.

The output pulses of OA18 and OA19 forward bias the base drives of the transistors allowing triggering pulses to be applied to the gate-cathode junction of the SCR. The voltage between gate and cathode is about 2.2 V dropping to about 1.5 V when the SCR is triggered into conduction. The gate current then is about 60 mA.

Applying a negative voltage to the gate circuit in Fig. 6.14 results in a small negative voltage of about -0.6 V across the gate-cathode junction corresponding to the forward voltage drop across diode D_3. This negative voltage makes it more difficult for the SCR to be triggered by transients from the control circuit.

Fig. 6.15a shows typical gate pulses before they are applied to the SCR. The width of the pulses at the base is about 25 µs, which is sufficient to trigger the SCR, (v. Section 6.1.2, p. 254). The waveform in Fig. 6.15b shows the gate-cathode voltage during SCR conduction. These and other waveforms of the SCR's and the mains voltage are discussed in the following section.

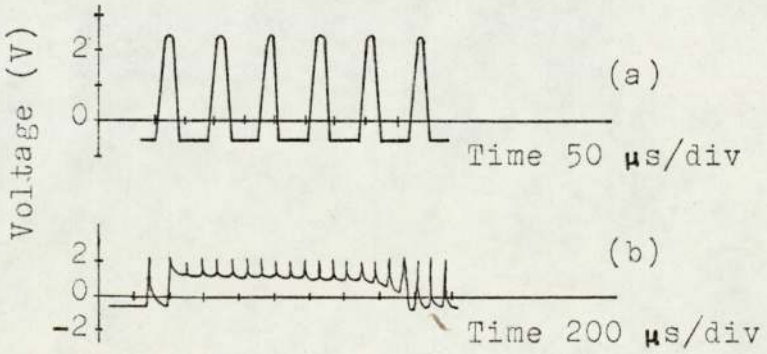

Fig. 6.15 SCR triggering pulses

6.3 Power supply performance

The following initial adjustments are carried out:

(a) The maximum value of supply current allowed to flow to the motor is fixed by setting the output voltage of potentiometer P_1 to the corresponding value read off from Fig. 6.16a. The actual maximum values of current allowed are slightly below the theoretical values for the same setting of the potentiometer. This is due to the adjustment of the op-amps.

(b) The desired value of the back e.m.f. E_b for the motor to operate at, is chosen by setting potentiometer P_2 to the required value. P_2 is a 10-turn potentiometer mounted on the front panel of the power supply with an indicator for the reference value of E_b, (v. Photograph 6a).

(c) The maximum value of the no-load voltage, $V_{o(set)}$, is fixed by adjusting potentiometer P_4 to the necessary value determined from Fig. 6.16b. The voltage can actually be set to any value up to 200 V, but naturally 5 V or 10 V is more realistic, since the purpose of this control is to limit the no-load voltage to a very small value.

(d) The rate at which the supply voltage V_s increases from zero is controlled with resistor R_2 across op-amp OA10 (v. Fig. 6.7, p. 257). It is best to choose a value for R_2 experimentally, i.e., by gradually increasing the value of R_2 from the minimum and observing the rate of rise of V_s until

an acceptable rate is reached. A very slow rise of V_s results in an oscillation of the voltage about the reference value E_{ref} which might take some time before settling down to the final value. This would be experienced every time the supply current changes as the load changes. A fast rise in V_s, on the other hand, causes the motor to draw a high current at start. However, there is no danger in a high starting current since it would be limited to the value of I_{ref} fixed in (a).

(e) The final setting, before switching on, is that of R_8 in the resistance bridge shown in Fig. 6.1, p. 247. This setting depends upon the value of the commutated-winding resistance R_a. To satisfy Equation (6.3), p. 249, the total resistance of $(R_7 + R_8)$ must be equal to 1000 R_a, e.g. 10 kΩ if R_a is taken as 10 Ω. The 'Set Resistance' knob on the front panel of the power supply can be adjusted to any position opposite 115 divisions which correspond to the values of $(R_7 + R_8)$ given in Fig. 6.16c.

The brushless motor is not connected directly to the power supply d.c. terminal, but through the transient suppression circuit shown in Fig. 6.17. A 1:1 transformer is connected so that current flows in opposite directions in the two windings, eliminating the inductive effect of the transformer under normal operation, but more important not allowing transient

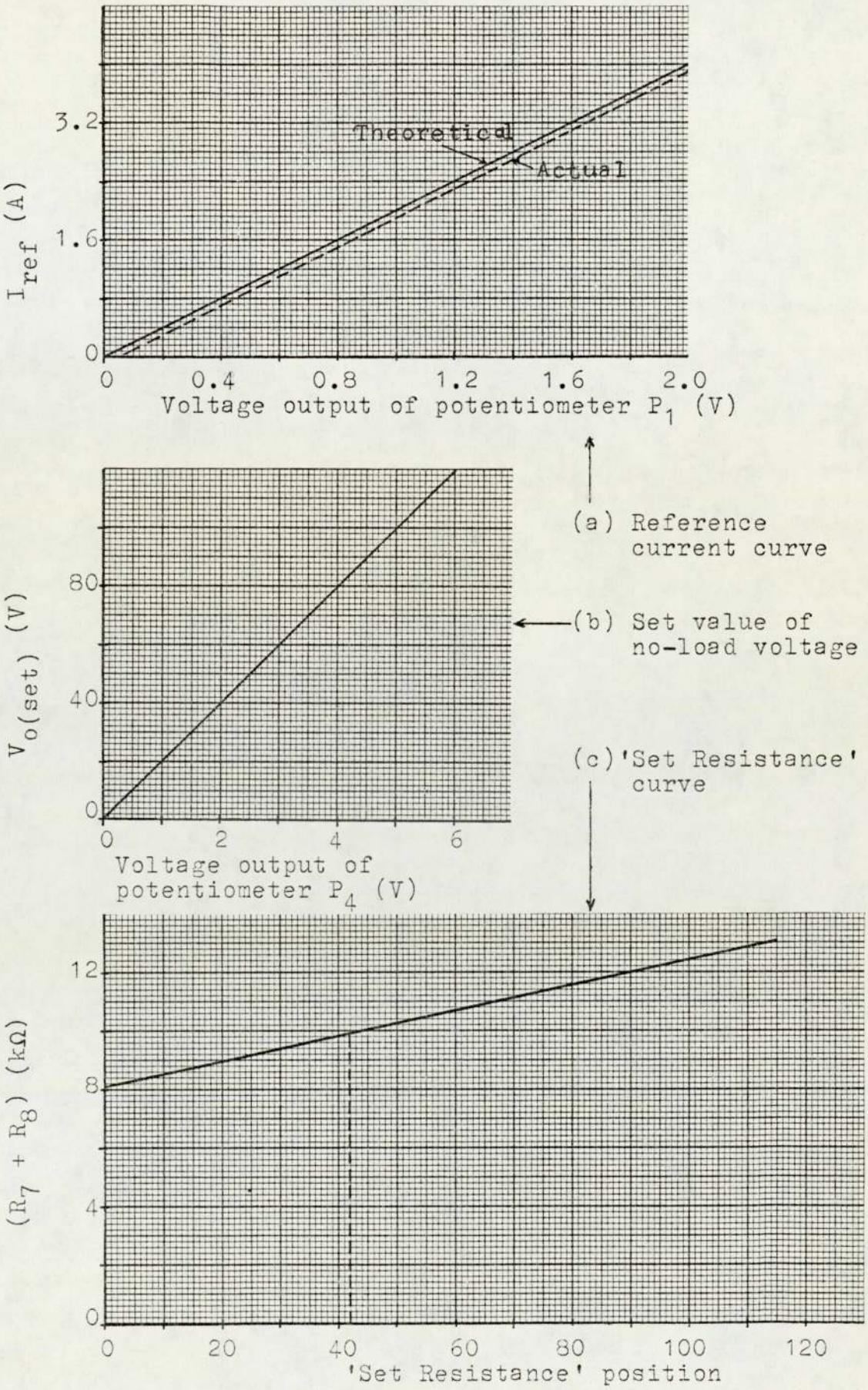

Fig. 6.16 Power supply adjustment curves

voltages through to the motor. A 3000 μF capacitor across the motor winding is connected for the same purpose of transient suppression.

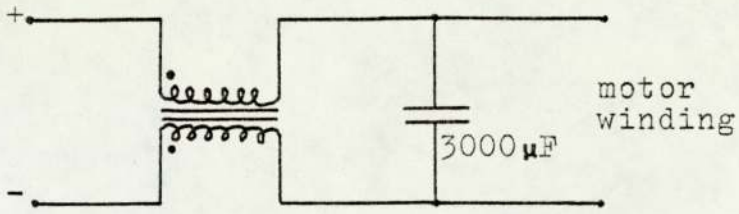

Fig. 6.17 Transient suppression circuit

6.3.1 Voltage and current waveforms

The waveform of the output voltage, V_s, from the power supply is satisfactorily smooth with a typical ripple factor of about 2%. The value of the ripple factor actually depends upon both supply voltage and current since energy is stored in the filter capacitor, C_4, during SCR conduction and is then released to the load until the following period of SCR conduction. The value of the supply current I_s determines the rate of discharge of the capacitor voltage while the value of supply voltage V_s affects the percentage ripple.

The conduction period λ of the two SCR's was seen to be different at constant values of V_s. This is mainly due to differences between the SCR's of the half-controlled bridge. However, the values of V_s and I_s also affect the difference between conduction angles of the two SCR's. At low values of V_s, for example, only one SCR conducts despite the availability of triggering pulses for both SCR's.

Another effect of the varying supply voltage is the position of the conduction period in relation to the zero crossing point of the mains supply voltage waveform. The train of triggering pulses always ends at the zero crossing point as was seen from Fig. 6.10, p. 263. However, in Fig. 6.15b, p. 268, SCR conduction angle λ is smaller than the width of the pulse train. Angle λ can also be greater than the width of the pulse train or, at a certain value of V_s, be equal to it.

Fig. 6.18a shows waveforms of the voltage across each of the two SCR's along with the waveform of the mains voltage. In Fig. 6.18b, one of the waveforms is inverted showing that the mains voltage is equal to the sum of the voltages across the SCR's. It can be seen from both waveforms that conduction ceases before the zero crossing of the mains waveform. These waveforms were obtained at

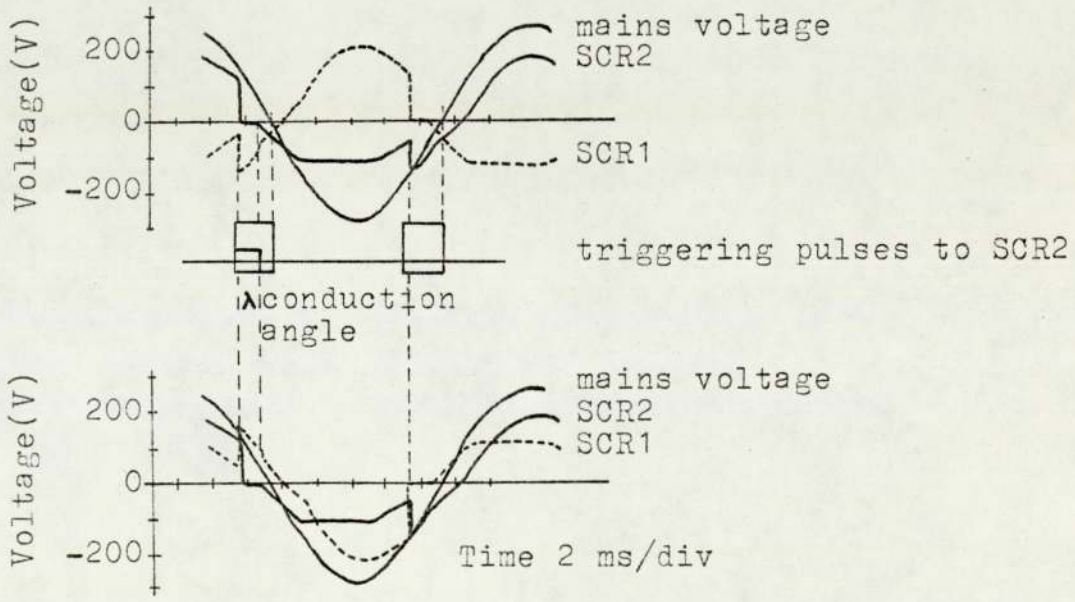

Fig. 6.18 Voltage waveforms across the SCR's and the mains, V_s = 120 V

V_s of about 120 V. At low values of V_s, SCR conduction continues after the zero crossing point. Conduction appears to end at the zero crossing point at V_s equal to about 50 V.

Fig. 6.19 shows waveforms of the input a.c. current to the complete power supply unit, at no-load and at load. Curve (a) shows that the peak current supplying the control circuitry and the SCR bridge at no-load is about 0.5 A. The r.m.s. value of current is 0.31 A. The non-sinusoidal shape of this waveform is due to the inductive circuits of the power supply unit. Curve (b) is the input current waveform with the power supply loaded by the brushless motor, at the following values:

E_b = 20 V, V_s = 25 V,

I_s = 0.5 A, n = 102 rev/min.

Note that even at this light load, the supply current during SCR conduction reaches about 10 A. This is the type of disturbance caused by SCR operation in which harmonics are fed back into the mains. There are methods of limiting this harmonic contribution but they are outside the scope of this project.

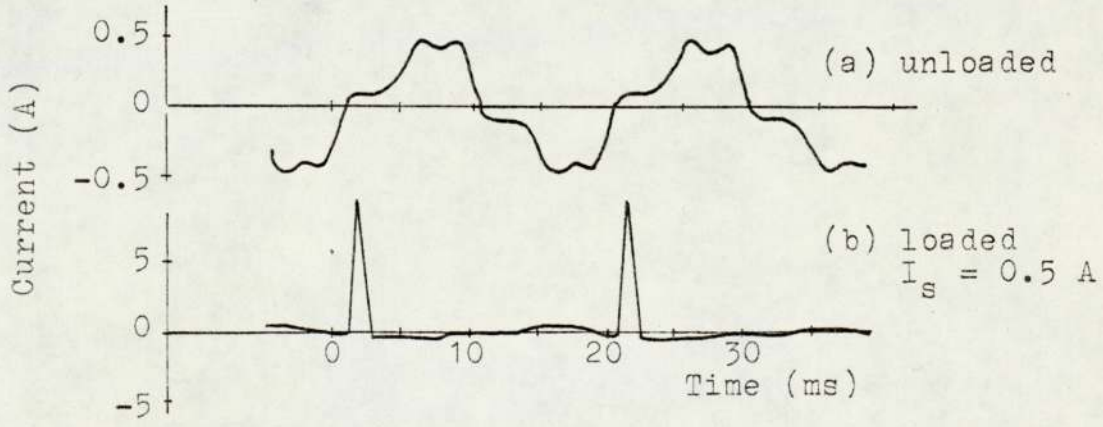

Fig. 6.19 Input current to power supply, E_b = 20 V

The rate of rise of current in the SCR at turn-on is about 20 mA/μs. This is well below the maximum rated value of 200 A/μs.

6.3.2 Crowbar protection circuit

The input LC filter connected at the a.c. side of the SCR is intended to suppress mains-borne transients before these reach the SCR's and the control circuitry. However, this filter becomes ineffective when a triggering pulse is erroneously generated in the control circuitry causing sudden SCR conduction. Such pulses can be due to an op-amp malfunction or, more likely, to a pick-up transient.

Because of the unacceptable consequences of false triggering, a crowbar thyristor protection circuit is connected across the output d.c. terminals of the power supply. The circuit diagram is given in Fig. 6.20, and the values of the components are given below.

Resistance		Power rating (W)
No.	Value(Ω)	
1	1	25
2	100	0.5
3	4.7 k	17
4	100	11
5	820	0.5
6	1 k	0.5
7	68	0.5
8	1 k	0.5

C_1 = 1500 μF, 450 V

D_1: Rs - 26 A

D_2, D_3: IN4004

SCR_3: THY 500-26

SCR_4: BTX 30-400

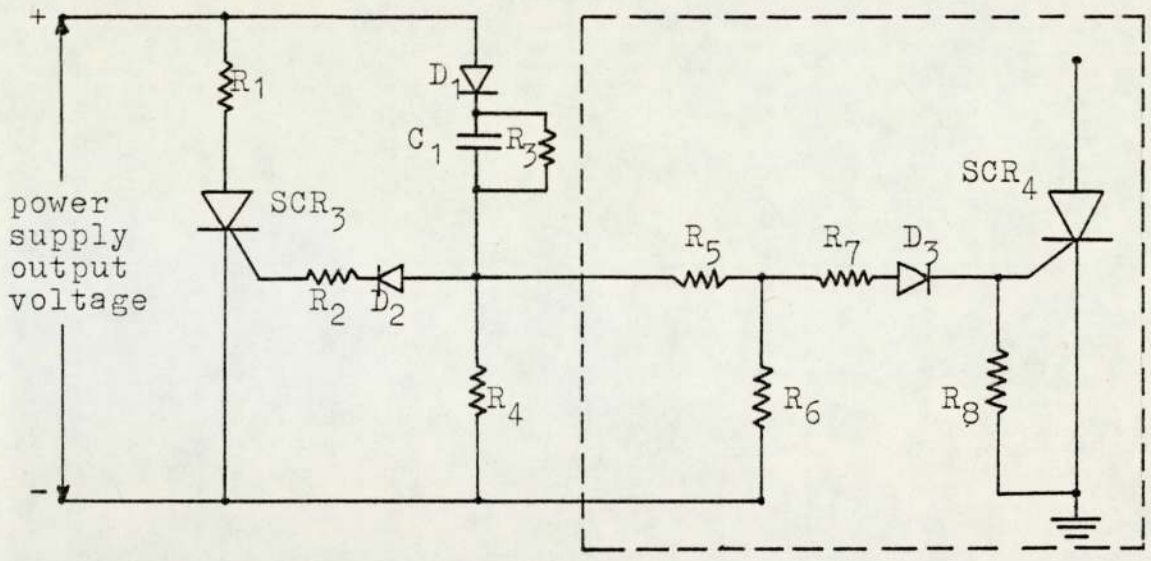

Fig. 6.20 Protection circuit

The crowbar thyristor is SCR_3 and the triggering circuit consists of the components outside the dotted lines in Fig. 6.20. Thyristor SCR_3 is triggered when the voltage across resistor R_4 reaches about 6 V, thus shorting the output voltage with resistor R_1 and protecting the motor winding from the sudden rise in voltage. This short-circuit current can blow the 10 A fuse in the mains circuit if the supply voltage V_s at firing is high enough.

The presence of the capacitor C_1 ensures that for normal operation, the voltage across R_4 does not rise to 6 V to trigger SCR_3. This is because C_1 constantly charges up to the value of the supply voltage V_s leaving no voltage drop across R_4. However, in the case of false triggering of the SCR's in the main bridge, the rate of rise of V_s with time $(\frac{dv_s}{dt})$ can be quite substantial, resulting in enough voltage across R_4 to trigger the crowbar thyristor SCR_3.

The maximum rate of rise of V_s was determined in Section 6.1.1, p. 249, when SCR_1 or SCR_2 is triggered at the crest of the mains voltage waveform, i.e., at $\lambda = 90^\circ$.

$$\left(\frac{dv_s}{dt}\right)_{max} = 76.2 = (250\sqrt{2} \sin \lambda)(0.2155) \qquad mV/\mu s$$

Therefore, the time t which elapses before the voltage across R_4 reaches 6 V is given by:

$$t = \frac{6}{(250\sqrt{2} \sin \lambda)(0.2155)} \qquad ms$$

The values of t are plotted in Fig. 6.21 against the conduction angle λ and against the voltage at which the false triggering occurs, i.e., $250\sqrt{2} \sin \lambda$. Note that at low values of voltage, t is only a few milliseconds falling rapidly to microseconds at higher voltages. This means that very little heat is developed before the transient is suppressed.

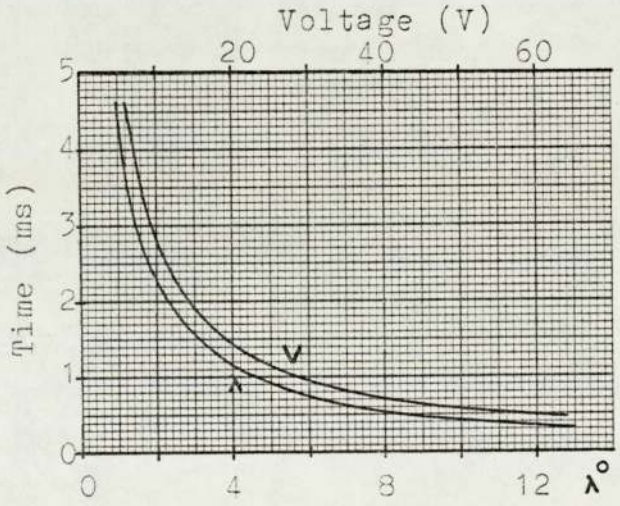

Fig. 6.21 Crowbar thyristor SCR_3 triggering time

The rate of rise of the collector-emitter voltage V_{CE} across the power transistors at turn-off was seen from

Fig. 4.25, p. 187, to reach about 9 V/μs at the maximum winding current of 5 A. Although this value is much higher than the value on which the above calculation was based, it does not affect the operation of the transient protection unit, since this rise in V_{CE} is seen by the power transistors only. At transistor turn-off, V_{CE} rises from $V_{CE(SAT)}$ to V_s, while capacitor C_1 is continuously charged at voltage V_s and hence remains unaffected.

The circuit enclosed by dotted lines in Fig. 6.20, p. 276, consists of SCR_4 and the components required to trigger it once the crowbar thyristor SCR_3 is triggered, i.e. both thyristors require about 6 V across resistor R_4 to be triggered into conduction. Thyristor SCR_4, however, is much smaller than SCR_3 and is only required to short the coil of an electromagnetic relay.

This relay has two pairs of contacts, one normally closed and the other normally open. The normally closed pair is represented in Fig. 6.7, p. 257 as S_3 and the normally open pair as S_4. S_3 is connected across capacitor C_1 and normally shorts it so that no triggering pulses can be produced even if the output of OA9 is positive, (v. Section 6.2.1, p. 257). S_4 ensures that the circuit is broken between the ramp function circuit and the pulse generating op-amp OA13, so that the input to OA13 remains negative to prevent false triggering when the power supply is OFF (v. Section 6.2.2, p. 262).

The ON button on the front panel is pressed to start the production of the triggering pulses, thus energising the coil of the electromagnet and changing the states of S_3 and S_4, i.e., allowing C_1 to charge and connecting the ramp function to OA13. When the power supply is switched off the coil is shorted and the switches revert to the normal states.

The switching off action can be done by thyristor SCR_4 since it is connected across the relay coil. In the event of a voltage transient, the crowbar thyristor SCR_3 is triggered, shorting the supply voltage, and at the same time thyristor SCR_4 would remove the triggering pulses. This is important since without SCR_4, triggering pulses would continue to be produced even when capacitor C_1 across OA10 is discharging after a fault. Allowing C_1 to discharge slowly results in a sudden rise in the supply voltage before it falls to zero.

Since SCR_4 remains conducting after having been triggered, the OFF button must be pressed to commutate it off before the power supply can be switched on again by pressing the ON button.

6.4 Comments

Owing to the sensitivity of the crowbar thyristor protection circuit to voltage transients resulting from false triggering, starting the brushless motor sometimes

requires several attempts. This occurs because thyristor SCR_4 removes the triggering pulses in the case of a fault and must be reset before the ON button is pressed again. However, the occurence of false triggering is much less likely during normal operation of the motor than at starting. This problem needs further investigation.

In Section 5.4.3, p. 241, the results given referred to load tests performed with IR compensation. Similar tests were performed with the motor supplied from the power supply unit and the results obtained were in excellent agreement.

It is also possible to over-compensate the IR drop by the simple adjustment of the 'Set Resistance' knob. The advantage of this is to increase the supply voltage V_s by an additional amount dependent upon the value of $(R_7 + R_8)$ and on V_s. This additional amount ΔV_s is determined from the bridge circuit in Fig. 6.1, p. 247, and is given by

$$\Delta V_s = \left(\frac{\left[(R_7 + R_8) - 1000\, R_a \right] \left[R_6 (R_7 + R_8) \right]}{10\, R_a \left[R_a + R_6 \right] \left[R_9 + (R_7 + R_8) \right]} \right) V_s \qquad (6.17)$$

The supply voltage can then be given as

$$V_s = E_b + I_s R_a + \Delta V_s \qquad (6.18)$$

For a winding resistance of 10 Ω, ΔV_s was determined from Equation (6.17) and plotted in Fig. 6.22 against $(R_7 + R_8)$. Naturally, when $(R_7 + R_8)$ = 10 kΩ, the resistance bridge is balanced and ΔV_s is zero.

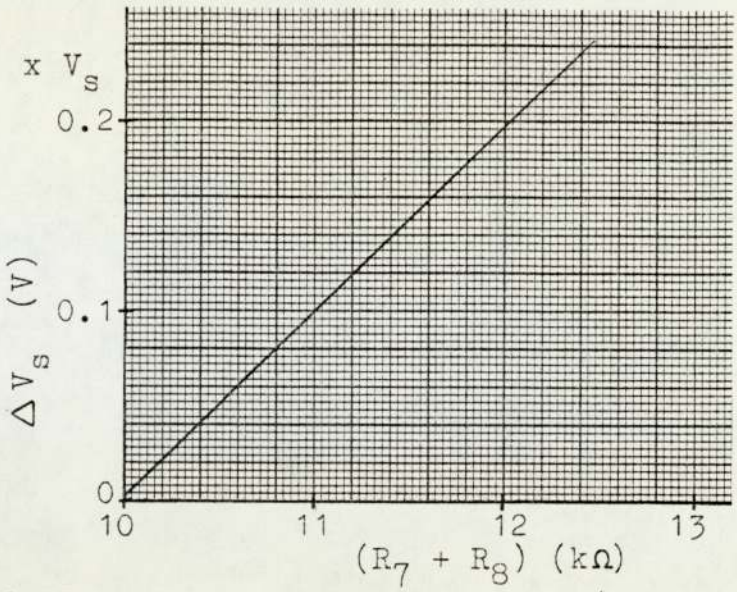

Fig. 6.22 ΔV_s for IR compensation (R_a = 10 Ω)

To demonstrate the effect of over-compensation on the voltages, V_s is determined from Equation (6.18) for a resistance setting $(R_7 + R_8)$ of 10.5 kΩ. The corresponding value of ΔV_s from Fig. 6.22 is 0.05 V_s. The back e.m.f. setting is assumed at 100 V resulting in the value of V_s plotted in Fig. 6.23 against supply current I_s. The true value of the back e.m.f. can now be determined by subtracting $I_s R_a$ from the calculated value of V_s. The normal values of E_b and V_s without over-compensation are also given in Fig. 6.23. Therefore, over-compensation not only raises the value of E_b from that of the reference value but also increases it as the load current increases. This results in an improved shunt characteristic by maintaining the speed within a smaller range of values between no-load and full-load than those in Figs. 5.22 and 5.26, p. 235.

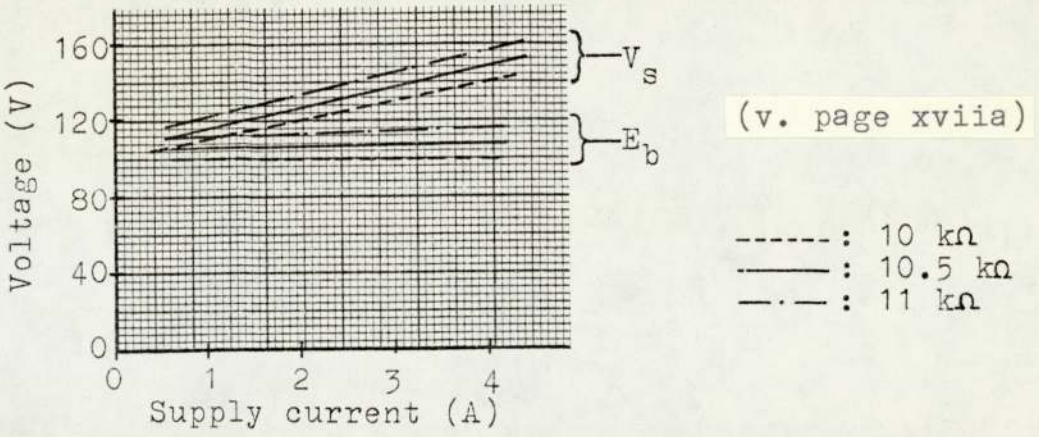

Fig. 6.23 Effect of over-compensation on voltage

The curves in Fig. 6.24 show the experimental values of the speed versus the output power with normal and over-compensation. The fall in speed between no-load and load is smaller with over-compensation even though compensation is only 5% above normal.

The use of a current limit in the power supply means that, during the starting period, the motor has a constant torque characteristic. With the limit set at 4 A and with a field excitation of 750 At, the shaft torque is 7.5 Nm. This value can be increased because the current limit is set quite low.

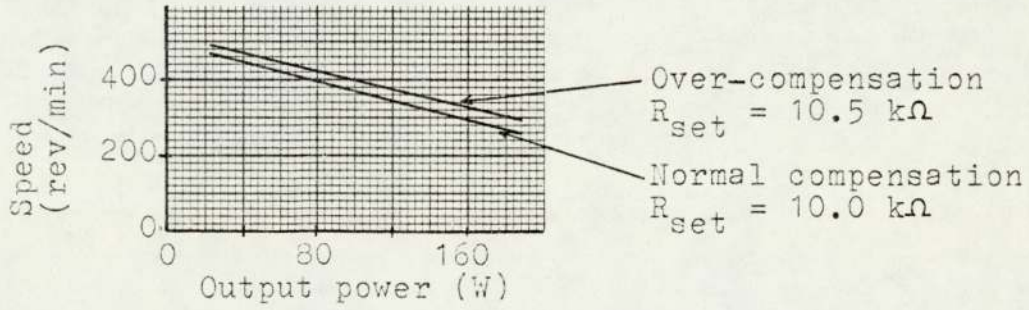

Fig. 6.24 Load test, F_f = 750 At, E_{set} = 100 V

CHAPTER 7

CONCLUDING REMARKS

7.1 Power requirements

The power requirements of 3 of the main units of the test rig are estimated from the respective voltage and current measurements. The 3 units are: power supply, logic unit and transistor cabinet. The waveform of the input current to the power supply was given in Fig. 6.19, p. 274, at no-load and at load. The current waveform for the logic unit and the transistor cabinet are given in Fig. 7.1.

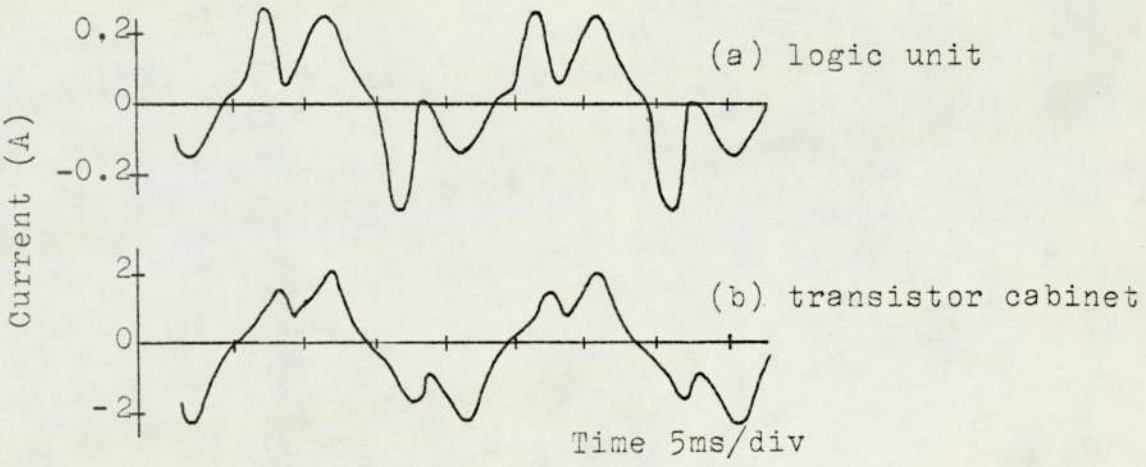

Fig. 7.1 Input current from a.c. mains

The r.m.s. values of current to each of these units as well as to the cooling fan in the transistor cabinet are given in Table 7.1. The average power in VA, also given in the table, was calculated at a mains voltage of 250 V. A total of about 500 VA is required to operate these

units and about $\frac{2}{3}$ of this amount is consumed by the transistor cabinet. This high power consumption was expected in view of the 12 individual base power supplies for each of the power transistors.

Unit	$I_{r.m.s.}$ (A)	P (VA)	%P
Power supply	0.31	77.5	16
Logic unit	0.14	35.0	7
Transistor cabinet	1.31	327.5	67
Cooling fan	0.19	47.5	10
Total	1.95	487.5	100

Table 7.1 Power requirements

If the above total power requirement is included in the efficiency calculation of the brushless motor (v. Figs. 5.27 and 5.28, p. 237) the overall efficiency does not exceed about 30%. A few examples are given in Table 7.2.

F_f (At)	V_s (V)	P_o (W)	η(motor) (%)	η(overall) (%)
450	100	66	50	12.4
450	150	90	44	14.9
750	100	120	53	19.3
750	150	200	52	25.7

Table 7.2 Overall efficiency values

7.2 Cost estimates

The material cost of the rig is based on the prices at the time of purchase. Due to the large number of different components and items, some of the cheaper ones were combined and their price estimated. Table 7.3 shows the cost of the 4 main parts of the rig and the two accesory units in Pounds and as a percentage of the total cost. The additional items used which were already available in the laboratory are estimated at an additional 15% of the total cost.

Unit	Cost	
	£	%
Brushless motor	180	12.5
Logic unit	135	9.4
Transistor cabinet	778	54.2
Power supply	282	19.6
Timer unit	30	2.1
100 Hz filter	32	2.2
Total	1437	100.0

Table 7.3 Cost distribution

The transistor cabinet is by far the most expensive unit. The 12 power transistors, power diodes and their heat-sinks cost about £300 and the 12 base-drives an estimated £432.

7.3 Conclusions

The brushless motor with an electronic commutator has similar characteristics to those of a conventional d.c. motor. The linear torque/speed characteristics are controlled with a variable supply voltage from the power supply unit. The power supply can be set to provide a constant voltage or compensate continuously for the voltage drop across the winding resistance ($I_s R_a$). This voltage compensation was devised primarily to offset the drop in speed between no-load and load, by ensuring a constant value of back e.m.f. However, due to the rapid rise of iron losses with load, IR compensation becomes ineffective at heavy loads. These losses are concentrated in the stator teeth and rotor poles.

The double-stator feature of the brushless motor results in an axial flux path which is longer than the circumferential path of a conventional motor. However, the m.m.f. required for equal values of the air-gap flux-densities becomes noticeably higher in the brushless motor only when the rotor-core reaches saturation. An air-gap flux-density between 0.6 T and 0.7 T is obtained at field excitations below 1000 At.

Starting the brushless motor is done by controlling the rate of rise of the supply voltage. This is performed by controlled triggering of the thyristors in the power supply unit. In addition to this control, the supply

current is limited to a safe value either at start or in the case of a fault or an overload. This is mainly to protect the power transistors from exceeding their safe operating limits.

Other protective measures include transient suppressors and snubber circuits. The RC snubber circuits are essential in shaping the switching loci of the transistors, and reducing the switching losses. In fact, the average power loss of a transistor at the highest expected value of winding current is less than 2 W, and the heat-sink provided is considerably larger than required.

The switching sequence of the transistors is controlled by the logic unit which receives the pulses from the opto-switches. These pulses are decoded to switch the transistors in a sequence suitable for a star-type commutated-winding, whereby two-thirds of the winding is connected to the supply at any moment. Each power transistor is provided with a separate base-drive circuit to ensure isolation between the bipolar circuits and between the switching pulses fed into the base circuits.

The commutated-winding has 3 pairs of diametrically opposite tappings and can be connected as a ring as well as a star winding. However, the switching sequence at the present is suitable for a star winding only. Testing in the earlier stages with the ring winding connected to a

mechanical commutator, showed in comparison that the peak values of torque are only about 5% lower with a star winding. The star winding was eventually selected since a more effective use of the power transistors can be made with it.

The maximum value of developed torque depends upon the angle between pole and winding axes at the switching instant of the supply to a particular pair of tappings. This angle γ for a ring winding lies between -10° and -20°(m) depending upon the excitation and the supply voltage. The range of values is approximately the same for angle γ_1 for a star winding. Angle γ_1 is set at -15°(m) but can be altered by the position sensors to suit any other operating condition. The criteria for selecting a value for γ_1 are maximum developed torque and minimum peaks in the winding current waveform.

Selecting a value for the switching angle in the brushless motor is of particular importance in view of the small number of switching pulses per revolution (18) compared with the normally large number of commutator segments in a conventional d.c. motor (which are equivalent to switching points). The number of tappings in a brushless motor is subject to economic considerations involving the relatively expensive power transistors and the associated circuitry. However, experimental results show that even with a limited number of switching points, the developed torque is

satisfactorily smooth. This is naturally due in part to the moment of inertia of the rotor member. The inductive nature of the commutated-winding also reduces wide variations in the developed torque.

The ease and flexibility with which the brushless motor in the project can be controlled makes it suitable wherever the use of a conventional d.c. motor is objectionable, yet variable speed characteristics are required. Using power transistors in the electronic commutator is successful and proves to be a viable substitute for thyristors in the medium power range, in view of the simpler switching circuitry. Various voltage and current controls are easily interfaced with a switching system in which the switching pulses are produced outside the motor.

7.4 Suggestions for future work

It was found from the load tests on the brushless motor that the main reason for the sudden drop in speed at heavy loads is the sharp increase in the electric and iron losses. The electric loss depends upon the winding resistance and is partially offset by the IR compensation. The iron loss, however, is dependent upon the magnetic circuit and the changes in flux distribution with load. A reduction in the eddy-current losses caused by air-gap flux pulsations can be made by cutting grooves on the surface of the pole-pieces. Alternatively, the poles can

be laminated to achieve the same purpose without changing the air-gap surface.

The m.m.f. calculations in Chapter 3 showed that a substantial amount of m.m.f. is required by the rotor-core especially at high values of air-gap flux-density. This indicates high levels of flux-density in the rotor-core which can be lowered by increasing the cross-sectional area of the core in a future design.

Although the cross-section of the rotor-core should be increased, in its present form the machine would be ideal as a vehicle drive. The rotor is rugged and simply made. The stator would be increased in length, thereby increasing the available torque and reducing the proportion of losses in the overhang winding. The drive would be direct to the road wheels. Some redesign of ancillary equipment would be necessary as the power supply would be from batteries.

In a modified design, considerable saving of both the space and power consumption of the transistor cabinet is possible. Smaller heat-sinks can be used and the base-drive circuits modified to halve the number of transformers (thereby almost halving the cabinet losses). The cabinet would also become portable.

Control over the duty factor of the power transistors can be exercised by using 6 additional opto-switches (a - f).

These switches would be mounted on the same disc supporting switches (I - VI) but placed in slots, thus enabling position-adjustments within 15°(m) to be made.

Additional control over the motor characteristics can be achieved with a variable-voltage power supply for the field coil(s). This power supply can be coupled to the control circuitry in the main power supply unit. The supply voltage can then be reduced immediately in the case of a fault in the field circuit. Constant speed operation can also be made possible with a variable field excitation.

These control features can best be performed by using a microprocessor to regulate the firing angle of the SCR's in the power supply unit to obtain the supply voltage required for constant speed operation. Indeed, constant torque operation can also be obtained using the microprocessor since a torque feedback signal is easily available. Another very useful operation using the microprocessor would be delaying or advancing the switching angle γ_1 by an amount corresponding to, say, the commutated-winding current. This would facilitate motor operation at the optimum angle regardless of load or excitation, eliminating the need to adjust the position sensors mechanically. In general, microprocessor control of the brushless motor would result in a more efficient use of the motor and in achieving specialised conditions of operation.

APPENDIX A1

THE E.M.F. INDUCED IN A STATOR COIL

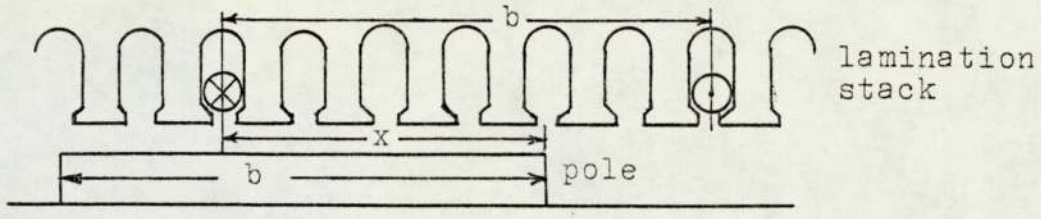

Fig. A1.1 Relative positions of a coil and a pole

Consider a full-pitch coil of N-turns in the lamination stack opposite a rotating pole as shown in Fig. A1.1. From Faraday's Law, the e.m.f. induced in one turn is:

$$e_t = -\frac{d\psi}{dt} \quad \text{V} \qquad \text{(A1.1)}$$

where ψ is the magnetic flux linkage of the coil with the circuit. The negative sign refers to the direction of e.m.f. induced and may be ignored if only the magnitude of the e.m.f. is required.

Equation (A1.1) can be expressed as

$$e_t = \frac{d\psi}{dx} \cdot \frac{dx}{dt} \quad \text{V} \qquad \text{(A1.2)}$$

where x is the portion of the pole-arc, b, covering the coil. If ϕ_p is the flux per pole, then

$$\psi = \phi_p \frac{x}{b} \qquad \text{(A1.3)}$$

where

$$x = \frac{2pbn}{60} t \qquad \text{(A1.4)}$$

Differentiating (A1.3) and (A1.4) and substituting into (A1.2), the e.m.f. per turn is

$$e_t = \frac{2pn\phi_p}{60} \quad \text{V} \qquad \text{(A1.5)}$$

and for an N-turn coil

$$e_c = \frac{2pnN\phi_p}{60} \quad \text{V} \qquad \text{(A1.6)}$$

APPENDIX A2

THE OUTPUT EQUATION

It is assumed that the direction of current in each conductor in the lamination stack does not change sign while the pole opposite to it moves over a complete pole-pitch. Maximum work done by each conductor depends upon the air-gap flux and the current in the conductor. Therefore, total work done due to the conductors of one lamination stack over one revolution is:

W_1 = total flux x electric loading

$$W_1 = p\phi_p \times I_c Z_a \qquad \text{J} \qquad \text{(A2.1)}$$

Since flux in the interpolar zone is practically zero, the total flux in (A2.1) is $p\phi_p$ instead of $2p\phi_p$. The total work done by the motor is $2W_1$, or

$$W_T = 2p\phi_p \times I_c Z_a \qquad \text{J} \qquad \text{(A2.2)}$$

The power developed by the motor is:

$$P = \frac{n}{60} W_T = \frac{2pn\phi_p}{60} I_c Z_a \qquad \text{W} \qquad \text{(A2.3)}$$

Power developed can also be expressed in terms of the specific electric and magnetic loading. The electric loading of the machine is $I_c Z_a$ ampere conductors, and the specific electric loading per unit of circumference is:

$$q = \frac{I_c Z_a}{\pi d} \qquad \text{A.C./m} \qquad \text{(A2.4)}$$

The magnetic loading per lamination stack is $p\phi_p$ and can be written as:

$$p\phi_p = \frac{\pi d \ell_a}{2} B_{av} \quad \text{Wb} \qquad \text{(A2.5)}$$

where

$$B_{av} = K_f B_g \quad \text{Wb} \qquad \text{(A2.6)}$$

If the pole-arc and pole-pitch are equal, then the form factor K_f is unity and $B_{av} = B_g$.

Substituting (A2.4) and (A2.5) into (A2.3), the power developed for the two lamination stacks is given by:

$$P = d^2 \ell_a \frac{\pi^2}{60} nq B_{av} \quad \text{W} \qquad \text{(A2.7)}$$

or

$$\frac{P \times 10^{-3}}{n} = C_o d^2 \ell_a \qquad \text{(A2.8)}$$

where C_o is the output coefficient,

$$C_o = \frac{\pi^2}{60} qB_{av} \times 10^{-3} \qquad \text{(A2.9)}$$

APPENDIX A3

CONFORMAL TRANSFORMATIONS FOR FIELD FORM

The flux-density distribution at the stator surface of the air-gap can be determined using conformal transformations. For this purpose the following assumptions are made.

(1) Since air-gap length and slot openings are small compared with the diameter at the air-gap, the curvature at the surface of the air-gap is negligible.

(2) Since the field does not penetrate very far into the slot opening, the slot depth is assumed infinite.

(3) The analysis is two-dimensional, end effects being neglected.

(4) The smooth surface is an equipotential surface at potential V, and the slotted surface (except for the opening) is an equipotential surface at zero potential.

(5) The effect of adjacent slots on the slot being investigated is neglected.

The slot-tooth configuration is represented in Fig. A3.1 in the X-Y plane and in Fig. A3.2 in the z plane with suitable values for ω. The transformation from the z plane to the ω plane of Fig. A3.3 is made by the Schwarz-Christoffel Equation (A3.1) and then the constants of the equation are determined as in ref. 46.

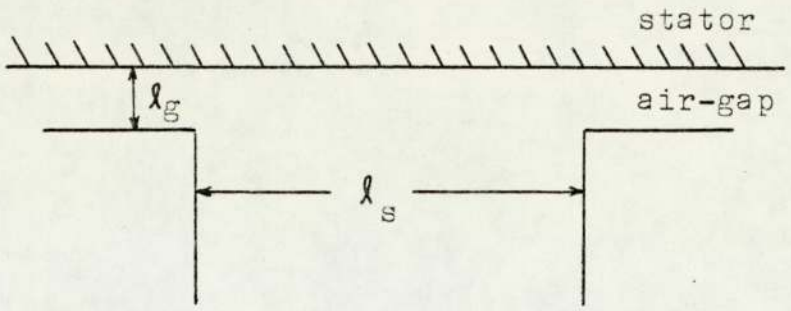

Fig. A3.1 X-Y plane

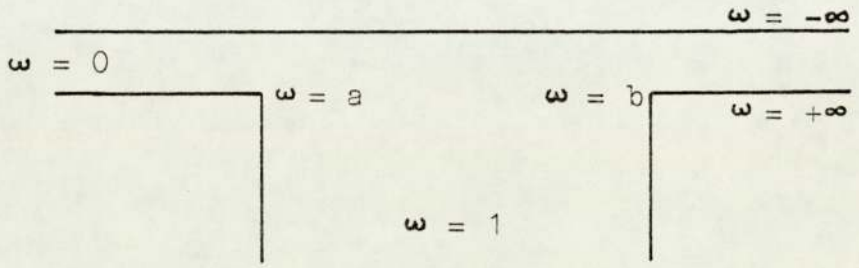

Fig. A3.2 z plane

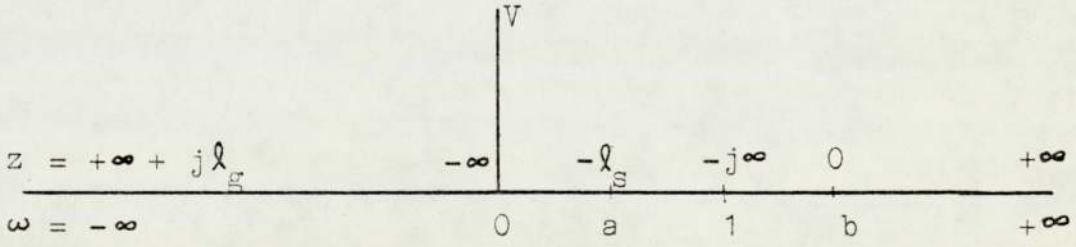

Fig. A3.3 ω plane

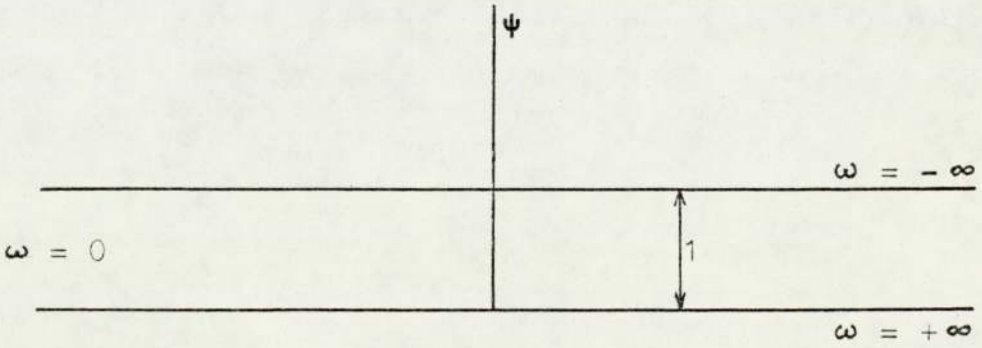

Fig. A3.4 ψ plane

$$\frac{dz}{d\omega} = \frac{A(\omega - a)^{\frac{1}{2}} (\omega - b)^{\frac{1}{2}}}{(\omega - 1)} \qquad (A3.1)$$

The constants are determined from the following equations:

$$A = \ell_g/\pi \qquad (A3.2)$$

$$ab = 1 \qquad (A3.3)$$

$$\frac{b - 1}{\sqrt{b}} = \frac{\ell_s}{\ell_g} \qquad (A3.4)$$

z is determined by integrating Equation (A3.1)

$$z = \frac{\ell_g}{\pi} \left(\log \left| \frac{1 + p}{1 - p} \right| - \log \left| \frac{b + p}{b - p} \right| - \frac{2(b - 1)}{\sqrt{b}} \tan^{-1} \frac{p}{\sqrt{b}} \right) \qquad (A3.5)$$

where

$$p = (b - \omega)^{\frac{1}{2}} / (a - \omega)^{\frac{1}{2}} \qquad (A3.6)$$

To determine the flux-density distribution, the points on the ω plane are transformed to the ψ plane shown in Fig. A3.4 by the following relation

$$\psi = \frac{V}{\pi} \log \omega \qquad (A3.7)$$

This leads to the following expressions for the flux-densities:

$$\frac{B}{B_{max}} = \frac{1 - \omega}{(a - \omega)^{\frac{1}{2}} (b - \omega)^{\frac{1}{2}}} \qquad (A3.8)$$

$$\frac{B_{min}}{B_{max}} = \frac{2}{(a + b + 2)^{\frac{1}{2}}} \qquad (A3.9)$$

The maximum value of B from the z plane in Fig. A3.2 is at $\omega = 0$. If the differential of the equation of B in the ψ plane is equated to zero, the minimum value of B is seen to occur when $\omega = -1$. Hence flux-density calculations are made at values of ω between 0 and -1. But first the constants a and b are determined from

(A3.3) and (A3.4) for the particular configuration. Then p is calculated from (A3.6) and used in determining the position z in the X-Y plane from (A3.5). The flux-density ratio B/B_{max} at this position is determined from (A3.8).

In the first calculation in Section 2.3.3, p. 32, the stator surface is assumed smooth and the variation in flux-density at a pole-tip is investigated. ℓ_s in (A3.4) is, therefore, replaced by the pole-arc.

The constants for calculating flux-density variations due to slotting are determined by substituting for ℓ_s, the slot opening, in (A3.4), and then the procedure explained above is followed. In this second calculation, the effect of adjacent slots is neglected. Normally, the inclusion of adjacent slots results in a drop in the flux-density at the tooth surface. Since in the motor the slot opening is much greater than the air-gap length, this effect is negligible.

APPENDIX A4

STORED ENERGY AND SALIENCY TORQUE FROM THE FLUX PATH MODEL

The flux path model for saliency torque in Fig. A4.1 is based on the diagrams of Fig. 2.12, p. 37, and the relevant details in Section 2.3.4.2, p. 36. A full-pitch coil of N turns is assumed in each lamination stack. The pole-arc subtends an angle 'b' equal to $\pi/3$ mechanical radians, which is divided into two angles 'b_1' and 'b_2'.

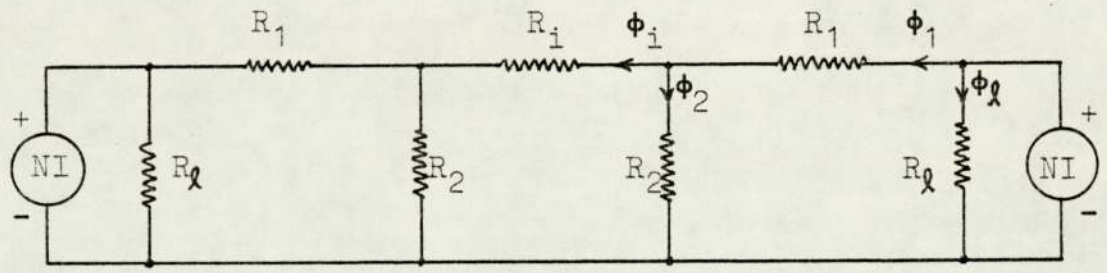

Fig. A4.1 Flux path model

The two coils are connected so that the m.m.f.'s produced assist each other. The leakage flux path is represented by the equivalent leakage reluctance R_ℓ. R_1 and R_2 correspond to the reluctances of the air-gaps (1) and (2), respectively. Flux and flux-density in these sections are Φ_1, Φ_2 and B_1, B_2. The reluctance of the rotor-core is represented by R_i.

Flux path (i) in Fig. 2.12a consists of R_1 and R_2, and flux path (ii) in Fig. 2.12b is through R_1, R_i and R_1 at the other end. The reluctance of the stator yoke is small due to the large cross-sectional area, and in any case is included in the value for R_i.

The diagram of Fig. A4.1 is treated like an electric circuit and hence the loop equation can be given as in (A4.1).

$$\begin{bmatrix} NI \\ - \end{bmatrix} = \begin{bmatrix} R_1 & R_2 \\ R_i & -R_i - 2R_2 \end{bmatrix} \begin{bmatrix} \phi_1 \\ \phi_2 \end{bmatrix} \qquad (A4.1)$$

Since R_1, R_2 and R depend upon the cross-sectional area of the air-gap, they vary with the angles b_1 and b_2 as in the following expressions:

$$R_i = \beta \frac{\pi/3}{b_1} R \qquad (A4.2)$$

$$R_2 = \beta \frac{\pi/3}{b_2} R \qquad (A4.3)$$

$$R_\ell = \gamma \frac{\pi/3}{b_2} R \qquad (A4.4)$$

where R is the reluctance of the air-gap facing the pole-arc.

$$R = \frac{2K\ell_g}{\mu_o \ell_a d \ \pi/3} \qquad (A4.5)$$

β is a factor chosen to compensate for the effect of slotting on the air-gap reluctance and γ is an experimentally determined correction factor. The reluctance of the iron path R_i is represented by R and a factor α:

$$R_i = \alpha R \qquad (A4.6)$$

Since $\frac{b_1}{\pi/3} + \frac{b_2}{\pi/3} = 1$, the relation between R_1, R_2 and R can be written as:

$$\frac{1}{R_1} + \frac{1}{R_2} = \frac{1}{\beta R} \qquad (A4.7)$$

From (A4.1) and making the necessary substitutions,

$$\Phi_1 = \frac{NI(\frac{b_1}{\pi/3})(1 + \frac{\alpha}{2\beta} \cdot \frac{b_2}{\pi/3})}{R\beta\ (1 + \alpha/2\beta)} \qquad (A4.8)$$

and,

$$\Phi_2 = \frac{NI(\frac{b_1}{\pi/3})(\frac{\alpha}{2\beta} \cdot \frac{b_2}{\pi/3})}{R\beta\ (1 + \alpha/2\beta)} \qquad (A4.9)$$

A_1 and A_2 are the areas of the air-gaps subtended by angles b_1 and b_2, respectively.

$$A_1 = \frac{\pi d}{6}\ \ell_a\ \frac{b_1}{\pi/3} \qquad (A4.10)$$

and,

$$A_2 = \frac{\pi d}{6}\ \ell_a\ \frac{b_2}{\pi/3} \qquad (A4.11)$$

Flux-densities B_1 and B_2 can, therefore, be written as:

$$B_1 = \frac{\mu_o NI\ (1 + \frac{\alpha}{2\beta}\ \frac{b_2}{\pi/3})}{K\ell_g\beta(1 + \alpha/2\beta)} \qquad (A4.12)$$

and,

$$B_2 = \frac{\mu_o NI(\frac{\alpha}{2\beta}\ \frac{b_1}{\pi/3})}{K\ell_g\beta(1 + \alpha/2\beta)} \qquad (A4.13)$$

since flux in the iron is $(\Phi_1 - \Phi_2)$, then from (A4.8) and (A4.9),

$$\Phi_i = \frac{NI\ \frac{b_1}{\pi/3}}{R\beta\ (1 + \alpha/2\beta)} \qquad (A4.14)$$

Leakage flux can be determined from the following equation,

$$NI = R_\ell \Phi_\ell \qquad (A4.15)$$

hence

$$\Phi_\ell = \frac{NI\ \frac{b_2}{\pi/3}}{R\gamma} \qquad (A4.16)$$

Energy stored in the magnetic circuit is the sum of that stored in the n sections of the circuit. The energy expression can be written in several forms:

$$E_T = \Sigma \tfrac{1}{2} B_n H_n \cdot v_n \qquad \text{(A4.17)}$$

$$= \Sigma \tfrac{1}{2} B_n A_n \cdot H_n \ell_n \qquad \text{(A4.18)}$$

$$= \Sigma \tfrac{1}{2} \phi_n \cdot (NI)_n \qquad \text{(A4.19)}$$

$$= \Sigma \tfrac{1}{2} \phi_n^2 \cdot R_n \qquad \text{(A4.20)}$$

$$= \Sigma \tfrac{1}{2} (NI)_n^2 / R_n \qquad \text{(A4.21)}$$

(A4.20) is used in determining the energies E_1, E_2, E_i and E_ℓ stored in the sections of the circuit shown in Fig. A4.1. Since there are 3 coils in each lamination stack and the rotor-core is divided into 3 sections of 120°(m), then the total energy stored in the machine is 6 times that of E_1, E_2 and E_ℓ plus 3 times that of E_i. (A4.22) gives the expression for the total energy stored using 6 coils.

$$E_T = \frac{3}{8} \frac{N^2 I^2}{R_1^2} \frac{R_i^2}{(1 + \alpha/2\beta)^2} \left(2\left(\frac{1}{R_2} + \frac{2}{R_i}\right)^2 R_1 + 2\left(\frac{1}{R_2}\right)^2 R_2 + \left(\frac{2}{R_i}\right)^2 R_i \right) + \frac{3N^2 I^2}{R_\ell} \qquad \text{(A4.22)}$$

(A4.22) can be simplified to (A4.23)

$$E_T = \frac{3}{2} \frac{N^2 I^2}{R_1} \frac{R_i}{(1 + \alpha/2\beta)} \left(\frac{1}{R_2} + \frac{2}{R_i}\right) + \frac{3N^2 I^2}{R_\ell} \qquad \text{(A4.23)}$$

Substituting for R_1, R_2, R_ℓ and R_i using (A4.2), (A4.3), (A4.4), and (A4.6), the energy expression in joules becomes:

$$E_T = \frac{3N^2I^2}{R}\frac{b_1}{\beta\pi/3}\frac{(1 + \frac{\alpha}{2\beta}\frac{b_2}{\pi/3})}{1 + \alpha/2\beta} + \frac{3N^2I^2}{R}\frac{b_2}{\gamma\pi/3} \qquad (A4.24)$$

Torque developed is equal to the rate of change of stored energy with rotor position. This is expressed as:

$$T_s = \frac{\partial E_T}{\partial b_1} \qquad \text{(negative sign ignored)} \qquad (A4.25)$$

$$T_s = \frac{3N^2I^2}{R\pi/3}\left(\frac{1}{\beta(1 + \alpha/2\beta)}\left(1 + \frac{\alpha}{2\beta}\frac{b_2}{\pi/3} - \frac{\alpha}{2\beta}\frac{b_1}{\pi/3}\right) - \frac{1}{\gamma}\right) \qquad (A4.26)$$

Rearranging (A4.26), the expression for torque T_s in Nm becomes:

$$T_s = \frac{3N^2I^2}{R\pi/3}\left(\frac{1}{\beta}\left(1 - \frac{\frac{\alpha}{\beta}\frac{b_1}{\pi/3}}{1 + \alpha/2\beta}\right) - \frac{1}{\gamma}\right) \qquad (A4.27)$$

A stable position of the rotor is when the pole-axis is in line with the coil-axis. In Equation (A4.27), therefore, T_s is zero when $b_1 = \pi/3$ and hence γ can be written as in (A4.28).

$$\gamma = \beta\left(\frac{1 + \alpha/2\beta}{1 - \alpha/2\beta}\right) \qquad (A4.28)$$

Substituting (A4.28) into (A4.27) gives the final expression for saliency torque due to 6 coils.

$$T_s = \frac{3N^2I^2}{R\beta\pi/3}\frac{\frac{\alpha}{\beta}\cdot\frac{b_2}{\pi/3}}{(1 + \alpha/2\beta)} \qquad \text{(Nm)} \qquad (A4.29)$$

α at a particular value of winding m.m.f. per pole can be read from the curve in Fig. A4.2. This curve is based on the values of m.m.f. determined in Table 2.4, p. 50. If β is assumed 1.1, γ can then be calculated from Equation (A4.28).

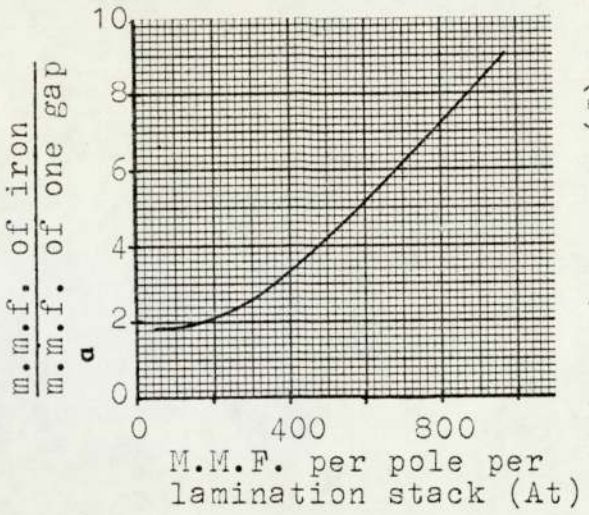

Fig. A4.2 a curve

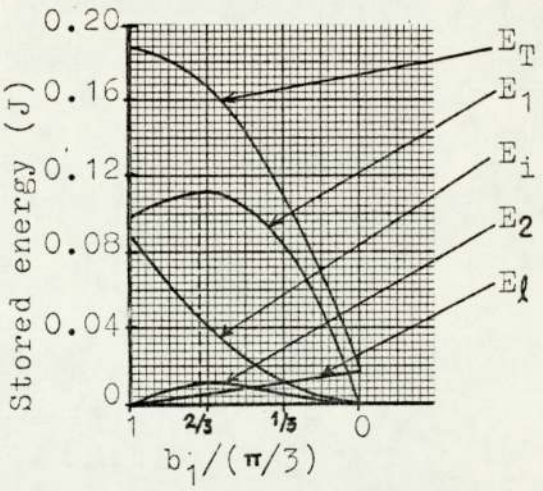

Fig. A4.3 Stored energy curves

Energy stored in the different sections of Fig. A4.1 is calculated from (A4.22) at the values of α, β and γ given in Section 2.3.4.2, p. 36. The curves are plotted in Fig. A4.3 against rotor position represented by $b_1/(\pi/3)$. The total energy E_T is the arithmetic sum of the individual energies. But it can also be calculated directly from (A4.24).

To see the relation between E_T and $b_1/(\pi/3)$, (A4.24) is rewritten in a simplified form as in (A4.30):

$$E_T = K_1 + K_2 \left(\frac{b_1}{\pi/3}\right) - K_3 \left(\frac{b_1}{\pi/3}\right)^2 \qquad \text{(A4.30)}$$

where K_1, K_2 and K_3 are constants which depend upon α, β, γ, R and NI. The relation between E_T and T_s is given in (A4.25) and, therefore, T_s can be written as:

$$T_s = K_2 - 2K_3 \left(\frac{b_1}{\pi/3}\right) \qquad \text{(A4.31)}$$

which is a simplified form of (A4.29). Hence the linear variations of T_s in Fig. 2.13, p. 39, are in agreement with (A4.31).

The values of $b_1/(\pi/3)$ at which E_1 and E_2 are maximum can be determined by differentiating the respective equations from (A4.22) and equating them to zero. For E_1, the maximum value occurs at

$$b_1/(\pi/3) = \frac{1}{3}\left(1 + \frac{2\beta}{\alpha}\right) \qquad \text{(A4.32)}$$

At $\alpha = 2$ and $\beta = 1.1$, $b_1/(\pi/3) = 0.7$ as indicated on the curve in Fig. A4.3. The maximum value of E_2, however, occurs at $b_1/(\pi/3) = \frac{2}{3}$ regardless of the values of the constants α and β.

APPENDIX A5

DIMENSIONS OF THE MAGNETIC CIRCUIT

The cross-sectional area of the various parts of the magnetic circuit are given in Table A5.1. To include the effect of stacking, the sectional area of the lamination stack given is 0.9 the overall area.

The flux-density is assumed uniform over the cross-sectional area of the flux path and hence only one value of area is given for the complete cross-section.

The length of the flux path in each part is that of the path midway between the boundaries of the X-Y plane of the path. Carter's correction coefficient for the effect of slotting is 1.26, determined for the values of slot and tooth widths, and air-gap length.

The assumption made in the magnetic circuit is that contact between the surfaces of adjacent iron parts is perfect. In practice, flux-densities are reduced by the extra reluctance presented by these gaps.

Part	Material	Diameter mm	Area/pole mm^2	Mean length mm
Gap	Air	127.0	3290	0.25
Tooth	Laminations	A 127.25 B 128.8 D 143.9 E 165.1 F 168.3	* 362.9 235.9 235.9 312.7 671.4	A-B 1.6 B-D 15.1 D-F 4.4
Back of teeth	Laminations	F 168.3 203.2	4028 4864	17.5
Stator yoke	Mild steel I	228.6 to 279.4	6756	88.9
Pole-pieces	Mild steel II	127.0 to 88.9	§ 3290 2284	19.1
Rotor-core	Mild steel II	88.9 to 38.1	2284 **1689	13.3 + 79.4

* Area per tooth

** Area per $\frac{1}{3}$ core. For segmented core A = 1410 mm^2

§ 60° pole-arc

Table A5.1 Dimensions of the magnetic circuit

APPENDIX A6

100 Hz FILTER UNIT

Fig. A6.1 shows the twin 'T' network of the filter and the associated voltage followers A3 and A4. It also shows amplifier A1 at the input and buffer A2 preceding the filter. The output of the filter is taken to a second buffer A5 and an RC circuit, before it can be connected to a digital voltmeter, DVM.

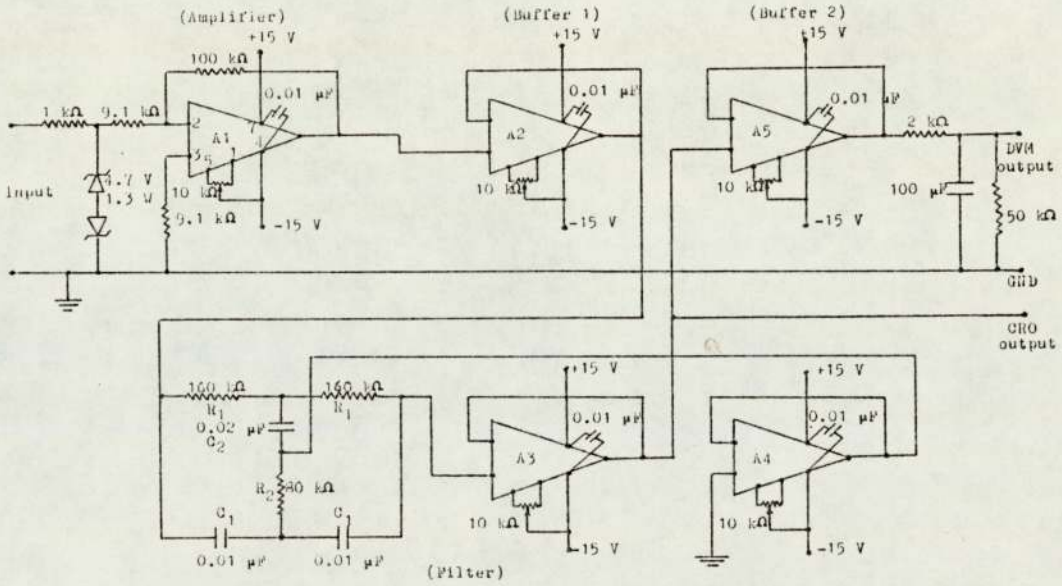

Fig. A6.1 100 Hz filter unit (op-amps type 741)

To protect the unit from voltage transients, two zener diodes are connected back to back at the input. Buffer (1) provides a high input resistance and a low output resistance, thus preventing the filter network from loading the preceding stages.

The parameters of the twin 'T' network are related to each other as in the following relations:

$$R_1 = 2R_2 \qquad (A6.1)$$

$$C_2 = 2C_1 \qquad (A6.2)$$

The frequency at which the maximum attenuation occurs is

$$f_o = \frac{1}{2\pi C_1 R_1} \quad \text{Hz} \qquad (A6.3)$$

The frequency response of this filter is similar to that shown in Fig. A6.2. The 'Q' or sharpness of the notch is at the highest possible value in this circuit since the non-inverting input to A4 is grounded. For lower values of Q, different amounts of signal are fed to this input from A3.

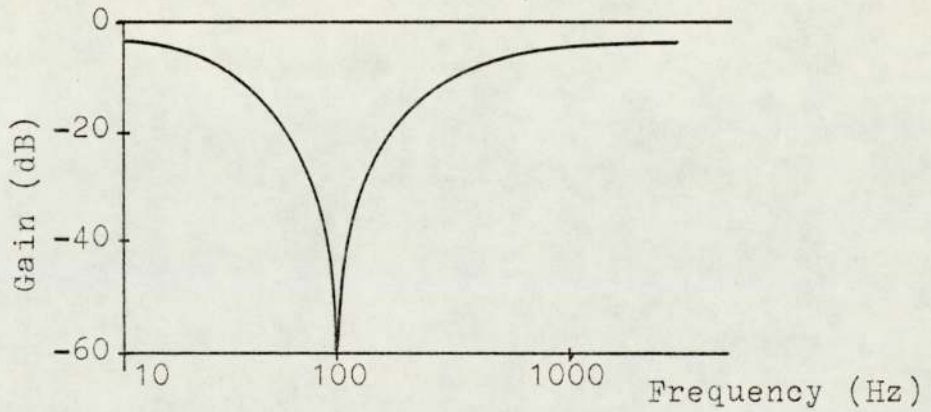

Fig. A6.2 Frequency response

Silver mica capacitors are used in the network to minimise notch frequency shift with temperature. To obtain the value of notch frequency required, the resistor and capacitor pairs are matched in value to better than 0.1% and 1%, respectively.

The integrated circuits (IC's) used in the circuit are operational amplifiers type 741 DIL package. To ensure

stability of operation, 0.01 μF capacitors are connected across the supply terminals to each IC.

The input signal to the unit is obtained from a commercial unit comprising a strain-gauge torque transducer and an external amplifier. The output signals can be displayed on either an oscilloscope (CRO) screen or measured with a digital voltmeter (DVM). The relation between the input and output signals of both commercial and filter units is linear.

Static calibration of the final voltage output against shaft torque over the range of the strain-gauge gave the following relation:

$$T = 3.07\ (V) \qquad \text{Nm} \qquad \text{(A6.4)}$$

APPENDIX A7

THE E.M.F. WAVEFORM

Suppose that the waveform of the e.m.f. induced between opposite fixed tappings of the ring commutated-winding is approximated to a triangular form. Equation (A7.1) is the expression for a triangular waveform of maximum value h.

$$e = \frac{8h}{\pi^2}\left(\frac{\sin\theta}{1^2} - \frac{\sin 3\theta}{3^2} + \frac{\sin 5\theta}{5^2} - \text{etc.}\right) \qquad \text{(A7.1)}$$

The r.m.s. value of 'e' is the square root of the mean value of e^2. Since the mean value is taken over π electric radians, only the sum of the squares of the separate terms of Equation (A7.1) need be considered.

$$e^2 = e_1^2 + e_2^2 + e_3^2 + \text{etc.}$$

$$e^2 = \frac{64h^2}{\pi^4}\left(\frac{\sin^2\theta}{1^4} + \frac{\sin^2 3\theta}{3^4} + \frac{\sin^2 5\theta}{5^4} + \text{etc.}\right) \qquad \text{(A7.2)}$$

The mean value of (A7.2) is $\frac{1}{\pi}\int_0^{\pi} e^2 \, d\theta$,

$$(e^2)_{\text{mean}} = \frac{64h^2}{2\pi^4}\left(\frac{1}{1^4} + \frac{1}{3^4} + \frac{1}{5^4} + \text{etc.}\right) \qquad \text{(A7.3)}$$

The r.m.s. value of the triangular waveform is therefore,

$$e_{\text{r.m.s.}} = \frac{8h}{\pi^2\sqrt{2}}\sqrt{\frac{1}{1^4} + \frac{1}{3^4} + \frac{1}{5^4} + \text{etc.}}$$

If all the harmonics up to infinity are considered, then

$$e_{\text{r.m.s.}} = 0.57735\ h \qquad \text{(A7.5)}$$

and the maximum value h is:

$$h = \sqrt{3}\, e_{r.m.s.} \qquad \text{(A7.6)}$$

or $e_{max}/e_{r.m.s.} = 1.73$

Since slotting harmonics are the main source of ripple in the e.m.f. waveform of Fig. 3.26d, p. 97, then the harmonics involved are mainly the $(n \pm 1)$th harmonics where n is equal to 12 slots per 120° (m).

The 11th and 13th harmonics are further assumed equal in amplitude and of value (sh). The magnitudes of these harmonics in Equation (A7.1) are, therefore, increased by $\frac{8h}{\pi^2}$ (s), and the mean value in Equation (A7.3) by:

$$\frac{64h^2}{2\pi^4}\left[(2s^2) + 2s\left(\frac{1}{11^2}+\frac{1}{13^2}\right)\right]$$

From Fig. 3.28a, p. 99,

$$s = \frac{\frac{1}{2}(130.0 - 81.1)}{100.0} = 0.245$$

Therefore $e_{r.m.s.} = 0.6124\ h$ (A7.7)

The actual height of the e.m.f. waveform including the 11th and 13th harmonics is:

$$e_{peak} = \frac{130.0}{100.0}\, h = 1.3\ h \qquad \text{(A7.8)}$$

From (A7.7) and (A7.8),

$$e_{peak}/e_{r.m.s.} = \frac{1.3}{0.6124} = 2.12 \qquad \text{(A7.9)}$$

When the rotor poles at the ends of the machine are staggered by $\frac{1}{2}$ a slot pitch, the ideal triangular

waveform is replaced by a trapezoidal as shown in Fig. A7.1.

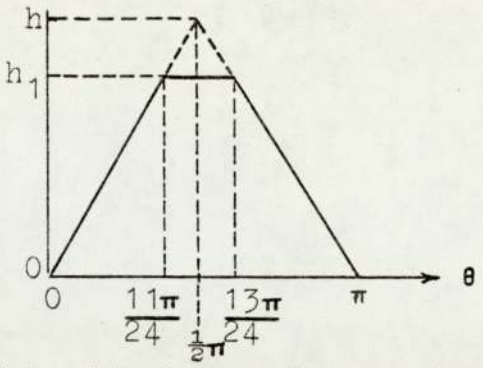

Fig. A7.1 Ideal e.m.f. waveforms

$h_1 = \frac{11}{12}\,h$, and the equation of the line between the origin and $\frac{11}{24}\pi$ is $e = \frac{2}{\pi}\theta h$.

The mean value of the square of the waveform is given by

$$(e^2)_{mean} = \frac{2}{\pi}\left(\int_0^{\frac{11}{24}\pi} (\tfrac{2}{\pi}\,\theta\,h)^2\,d\theta + \int_{\frac{11}{24}\pi}^{\frac{1}{2}\pi} (\tfrac{11}{12}\,h)^2\,d\theta\right) \qquad (A7.10)$$

and the r.m.s. value is

$$e_{r.m.s.} = 0.57164\ h \qquad (A7.11)$$

Compared with (A7.5), the r.m.s. value of the trapezoidal voltage waveform is about 1% lower than the original triangular waveform. In terms of the actual height h_1, the r.m.s. value is,

$$e_{r.m.s.} = 0.6236\ h_1 \qquad (A7.12)$$

From (A7.12), h_1 or the maximum value of the trapezoidal waveform is given by

$$h_1 = 1.604\ e_{r.m.s.} \qquad (A7.13)$$

APPENDIX A8

TIMER UNIT

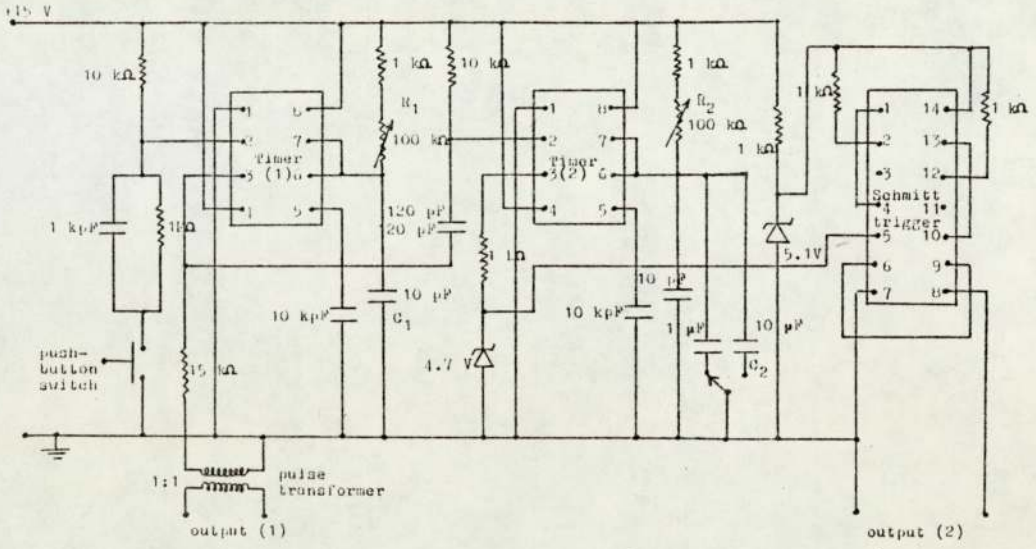

Fig. A8.1 The timer unit

The circuit diagram of the timer unit is given in Fig. A8.1. The unit provides two output signals whose time periods can be varied by R_1 and R_2. Also, the second output is dependent upon the first as shown ideally in Fig. A8.2. Output signal (1) is used to trigger an oscilloscope externally at t = 0, prior to the application of the second signal at $t = t_1$ to the circuit being tested.

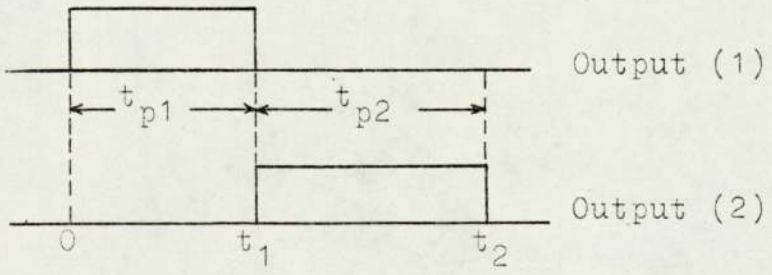

Fig. A8.2 Ideal output pulses of the timer

Two 555 timers constitute the core of this unit. The first timer is manually started by a push-button switch, whereas the second is started automatically when the output of the first falls to zero. A timer is started by grounding its input. The periods t_{p1} and t_{p2} are equal to 1.1 R_1C_1 and 1.1 R_2C_2, respectively. t_{p1} is actually less than one µs and t_{p2} can be varied between 1.10 ms and 1.11 s by changing R_2 and/or C_2.

A pulse transformer is used on output (1) to provide isolation between the trigger pulse and the test circuit. The output of the timer (2) is fed to a Schmitt trigger to obtain a higher output current at output (2) capable of supplying the test circuit.

WESTCODE SEMICONDUCTORS

Technical Publication
WT52A
Issue 1
June 1976

HIGH VOLTAGE NPN POWER TRANSISTORS

WT5201 WT5202 WT5203 WT5209

This range of triple diffused NPN silicon power transistors is designed for high voltage power switching, switching regulator, converter, inverter and power amplifier applications.

- **FAST SWITCHING** – Fall Time 1μs max
- **HIGH SUSTAINING VOLTAGE** – V_{CER} 400 - 500 Volts
- **HIGH COLLECTOR VOLTAGE** – V_{CBO} 650 - 750 Volts
- **HIGH CURRENT** – 30 Amperes Peak
- **HIGH POWER** – 175 Watts

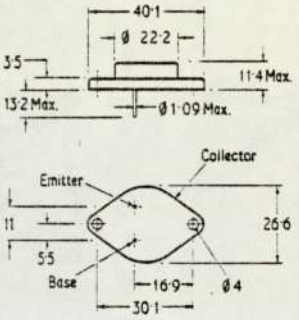

MAXIMUM RATINGS

		WT5209	WT5201	WT5202	WT5203	
Collector-to-Base Voltage	V_{CBO}	750	750	700	650	V
Collector-to-Emitter Sustaining Voltage						
with base open	$V_{CEO(SUS)}$	400	350	300	250	V
with base-to-emitter resistance R_{BE} = 10Ω	$V_{CER(SUS)}$	500	500	450	400	V
Emitter-to-Base Voltage	V_{EBO}			10		V
Collector Current, continuous	I_C			10		A
Collector Current, peak	I_{CM}			30		A
Base Current, continuous	I_B			10		A
Base Current, peak	I_{BM}			20		A
Transistor Dissipation at T_{case} = 25°C	P_T			175		W
Junction Temperature, Operating and Storage	T_j			200		°C

ELECTRICAL CHARACTERISTICS

CHARACTERISTIC	SYMBOL	TEST CONDITIONS V V_{CE}	TEST CONDITIONS V V_{EB}	TEST CONDITIONS A I_C	TEST CONDITIONS A I_B	TEST CONDITIONS °C T_{case}	LIMITS Type WT5209	LIMITS Type WT5201	LIMITS Type WT5202	LIMITS Type WT5203	UNITS
Collector Cut-off Current With base-emitter reverse biased or base short.	I_{CEV}, I_{CES}	750				25	2	2	-	-	mA max
		750				150	5	5	-	-	mA max
		700				25	-	-	2	-	mA max
		700				150	-	-	5	-	mA max
		650				25	-	-	-	2	mA max
		650				150	-	-	-	5	mA max
With base-emitter resistance R_{BE} = 10Ω	I_{CER}	450				25	2	2	-	-	mA max
		400				25	-	-	2	-	mA max
		350				25	-	-	-	2	mA max
With base open	I_{CEO}	350				25	2	-	-	-	mA max
		300				25	-	2	-	-	mA max
		250				25	-	-	2	-	mA max
		200				25	-	-	-	2	mA max
Emitter Cut-off Current	I_{EBO}		8	0		25 & 150	1	1	1	1	mA max
Collector-to-Emitter Sustaining Voltage With base-emitter resistance R_{BE} = 10Ω	$V_{CER(SUS)}$			0.5		25 & 150	500	500	450	400	V min
With base open NOTE 1	$V_{CEO(SUS)}$			0.5	0	25 & 150	400	350	300	250	V min
Emitter-to-base Voltage	V_{EBO}			0	5mA	25 & 150	10	10	10	10	V min
Base-to-Emitter Saturation Voltage NOTE 2	$V_{BE(SAT)}$			10	1.5	25 & 150	2	2	2	2	V max
Collector-to-Emitter Saturation Voltage NOTE 2	$V_{CE(SAT)}$			10	1.5	25	1.25	1.25	1.25	1.25	V max
				10	1.5	150	3.5	3.5	3.5	3.5	V max
D.C. Forward Current Transfer Ratio NOTE 2	h_{FE}	5		10		25	10	10	10	10	min
		5		10		150	7	7	7	7	min
Gain-Bandwidth Product	f_T	10		0.2		25	2	2	2	2	MHzmin
Turn-on Time NOTE 3	t_{on}	200		10	1.5	25	1.5	1.5	1.5	1.5	µs max
				10	1.5	150	3	3	3	3	µs max
Storage Time NOTE 3	t_s	200		10	1.5	25 & 150	2.5	2.5	2.5	2.5	µs max
Fall Time NOTE 3	t_f	200		10	1.5	25	1	1	1	1	µs max
				10	1.5	150	2	2	2	2	µs max
Second Breakdown Collector Current (with base forward biased) NOTE 4	$I_{S/b}$	38				25	4.6	4.6	4.6	4.6	A min
Second Breakdown Energy (with base reverse biased, R_{BE} = 50Ω, L = 50µH)	$E_{S/b}$		4	10		25	2.5	2.5	2.5	2.5	mJ min
Thermal Impedance, Junction to case	R_{j-c}						1.0	1.0	1.0	1.0	°C/W max

Note 1 The Sustaining Voltages $V_{CEO(SUS)}$ and $V_{CER(SUS)}$ must not be measured on a Curve Tracer, but by means of the Test Circuit shown in Figure 1

Note 2 Pulse Test - 300µS duration, repetition rate 50Hz

Note 3 $I_{B_{on}} = I_{B_{off}}$ The Switching Times are measured by means of the Test Circuit shown in Figure 2

Note 4 Pulse Test - 1 second duration non-repetitive

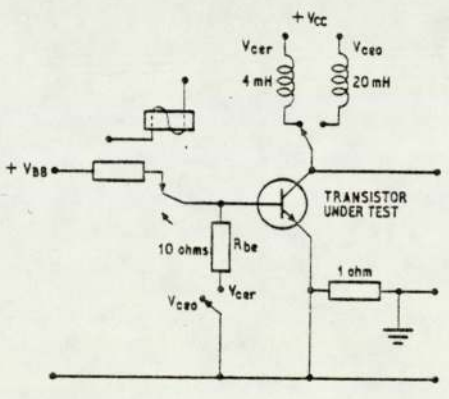

Figure 1 Test Circuit Sustaining Voltage

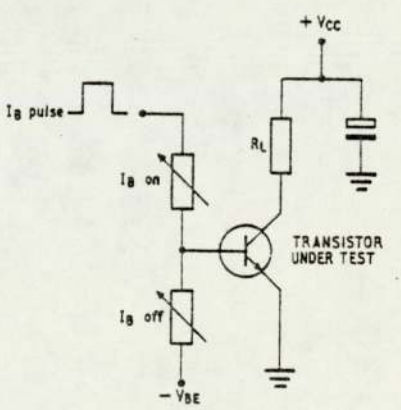

Figure 2 Test Circuit Switching Times

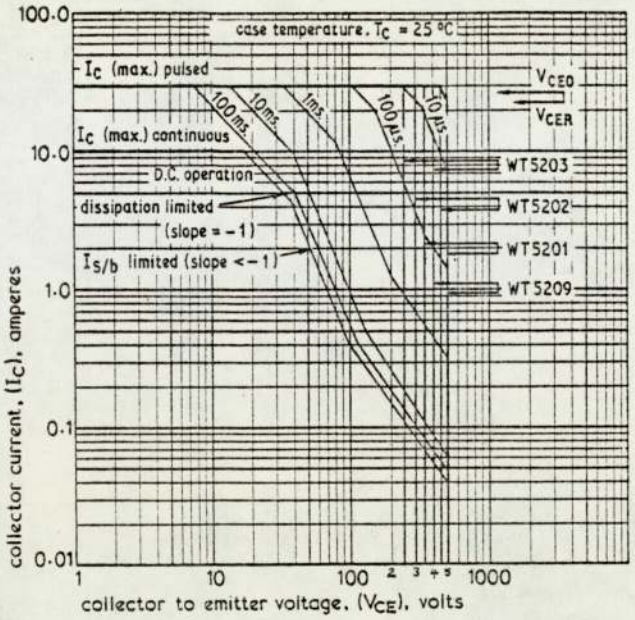

Figure 3 Maximum Safe Operating Areas, Forward Bias

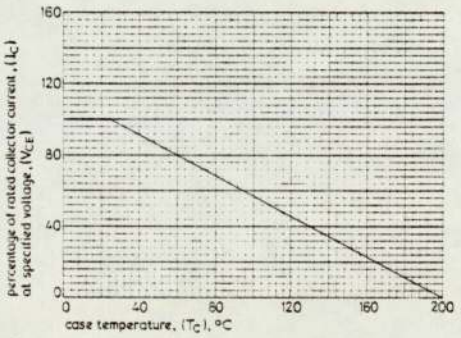

Figure 4 Dissipation Derating Curve

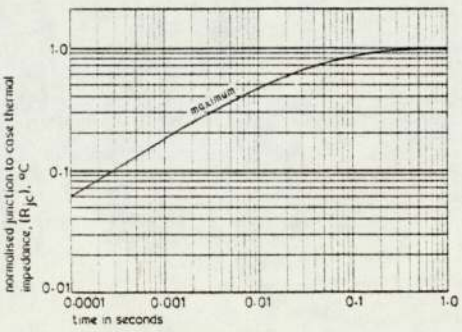

Figure 5 Transient Thermal Impedance

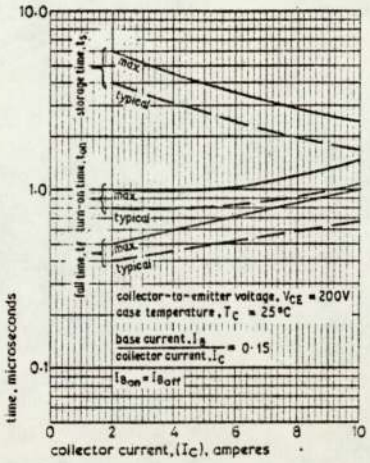

Figure 6 Switching Time Characteristics

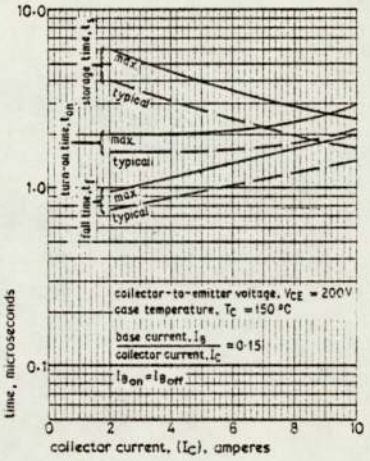

Figure 7 Switching Time Characteristics

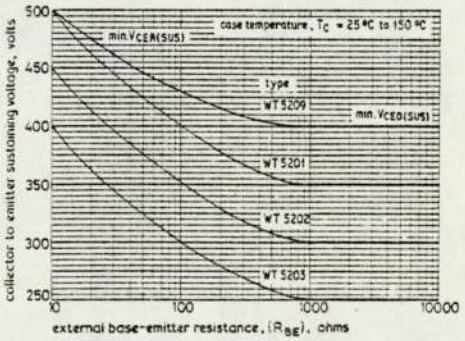

Figure 8 Collector-To-Emitter Sustaining Voltage Characteristics

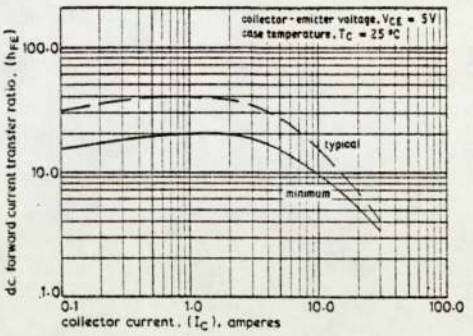

Figure 9 D.C. Forward Current Transfer Ratio Characteristics

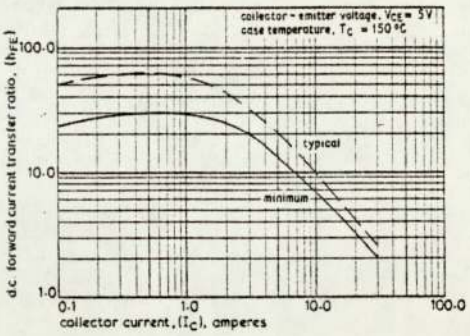

Figure 10 D.C. Forward Current Transfer Ratio Characteristics

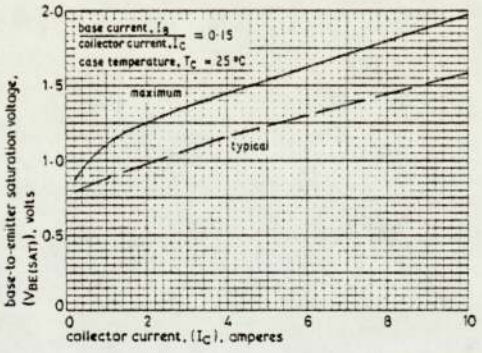

Figure 11 Base-To-Emitter Saturation Voltage Characteristics

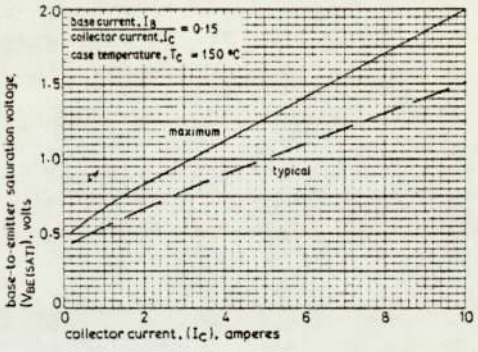

Figure 12 Base-To-Emitter Saturation Voltage Characteristics

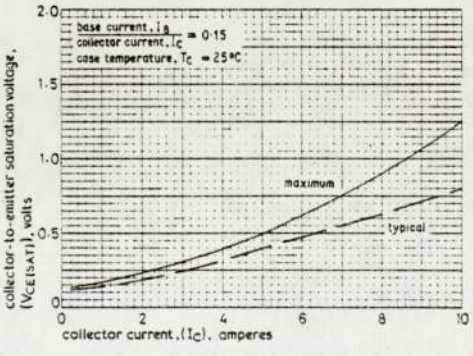

Figure 13 Collector-To-Emitter Saturation Voltage Characteristics

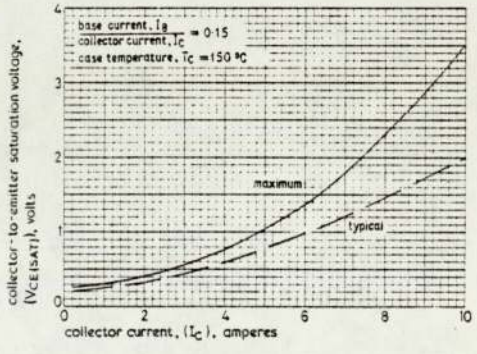

Figure 14 Collector-To-Emitter Saturation Voltage Characteristics

Semiconductor Division
Westinghouse Brake and Signal Co. Ltd.
Chippenham SN15 1JD England

	Telephone	*Telex*
Chippenham	*0249 4141*	*44751*

Steuerbare Kompaktgleichrichter
Half controlled bridge rectifiers
Ponts monophasés mixtes moulés

SKB 33

	SKB 33/02	SKB 33/04	SKB 33/06	SKB 33/08	SKB 33/10	SKB 33/12
V_{RSM}	300 V	500 V	700 V	900 V	1100 V	1300 V
V_{RRM}	200 V	400 V	600 V	800 V	1000 V	1200 V

		P 1/120 F (T_{amb} = 35 °C)	P 1/120	M	I
			(T_{amb} = 45 °C)		
I_D	(rec. 180)	36 A	24 A	14 A	6.5 A
	(sin. 180)	34 A	23 A	13.5 A	6 A
I_{FSM}	(T_{vj} = 25 °C)	400 A			
	(T_{vj} = 130 °C)	350 A			
i^2t	(T_{vj} = 25 °C)	800 A^2s			
	(T_{vj} = 130 °C)	600 A^2s			
$(di/dt)_{cr}$	(f = 50 Hz)	200 A/µs			
$(dv/dt)_{cr}$	(T_{vj} = 130 °C)	200 V/µs			
t_q	(T_{vj} = 130 °C)	typ. 80 µs			
I_H	(T_{vj} = 25 °C)	typ. 20 mA max. 200 mA			
I_L	(T_{vj} = 25 °C)	typ. 80 mA max. 700 mA			
V_{GT}	(T_{vj} = 25 °C)	3 V			
I_{GT}	(T_{vj} = 25 °C)	100 mA			
V_{GD}	(T_{vj} = 130 °C)	0.25 V			
I_{GD}	(T_{vj} = 130 °C)	2 mA			
$R_{th\,j-c}$		0.65 °C/W			
$R_{th\,c-s}$		0.06 °C/W			
T_{vj}		– 40 ... + 130 °C			
T_{stg}		– 55 ... + 150 °C			
V_{isol}		2500 V~			
RC		Siehe S. 3	See p. 5	Voir p. 7	
Fig.		$V_{VRMS} \leq 220$ V: 36 A	$V_{VRMS} > 220$ V: 25 A		
W		≈ 250 g			
Ex		SKB 33/06 + P 1/120			

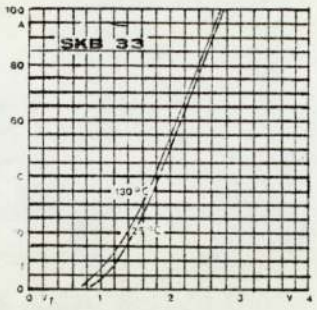

Fig. 1

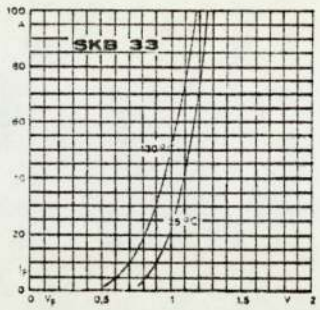

Fig. 1a

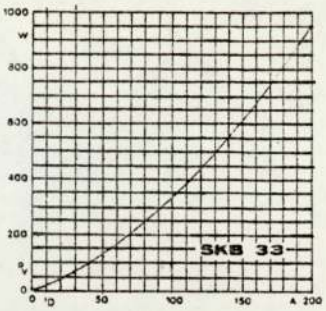

Fig. 2a

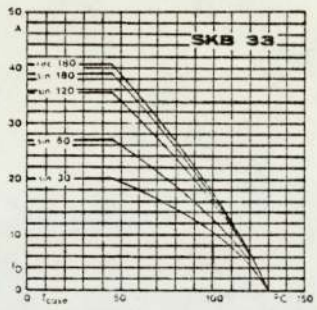

Fig. 3a

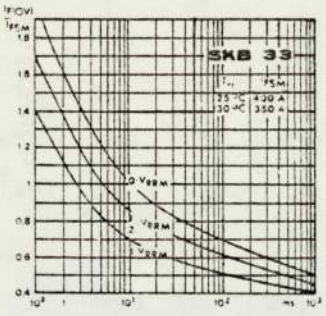

Fig. 4a

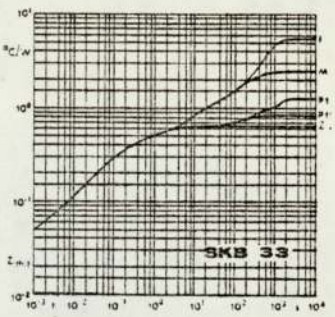

Fig. 5b

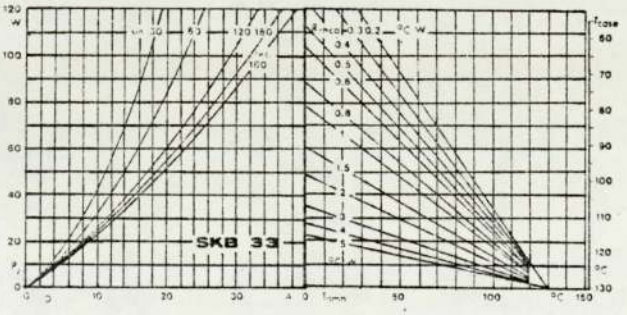

Fig. 5a

	R_{thca}
P 1/120 F	0.20 °C/W
P 1/120	0,65 °C/W
M	1,8 °C/W
I	5 °C/W

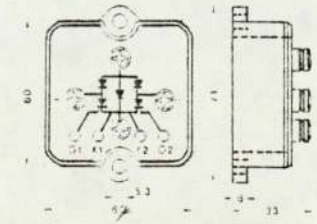

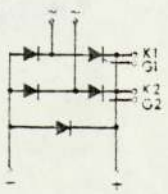

Fig. 6

SKB 33

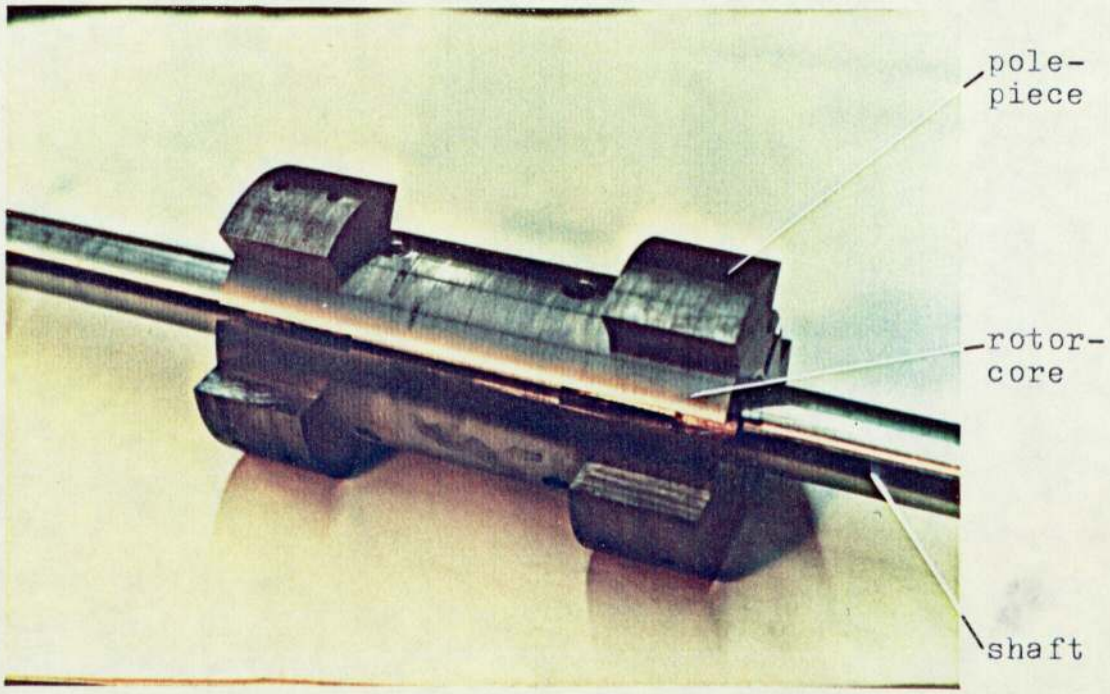

Photograph 1a The rotor member

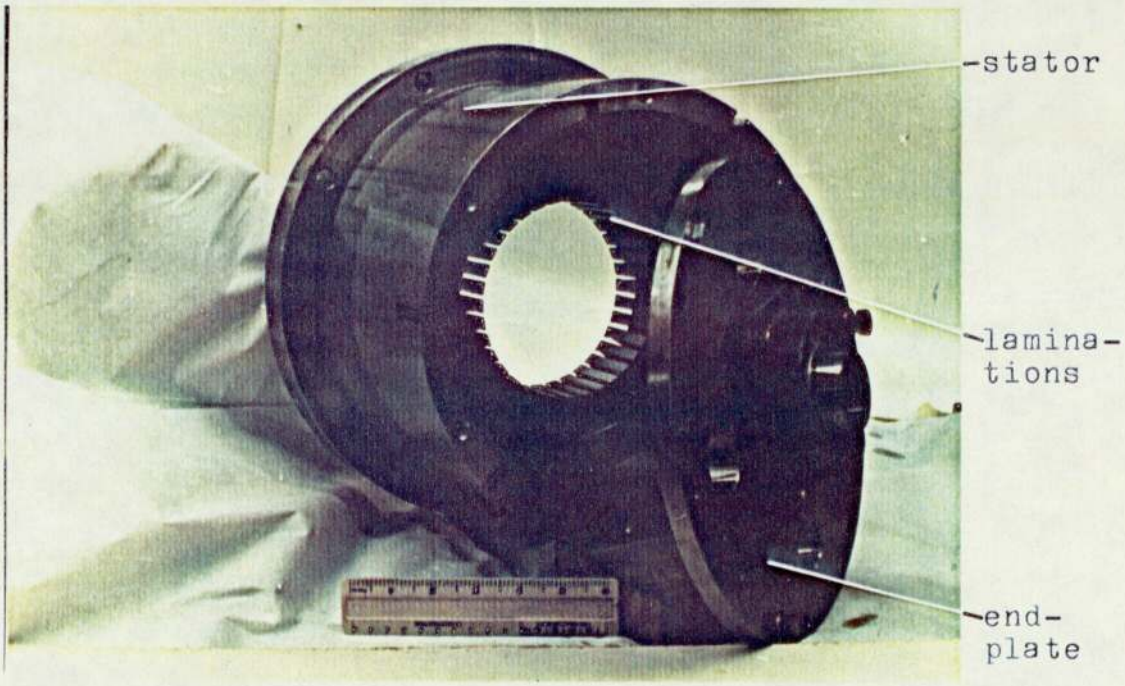

Photograph 1b Stator and end-plate (ODE)

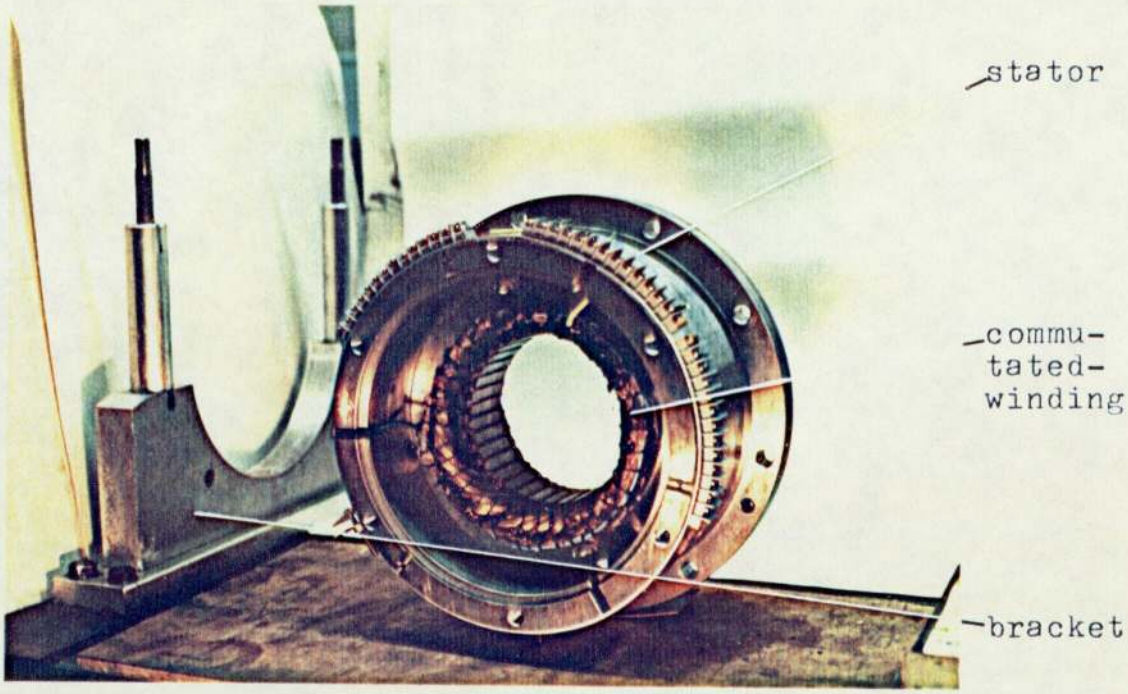

Photograph 2a Stator and commutated-winding (ODE) end view

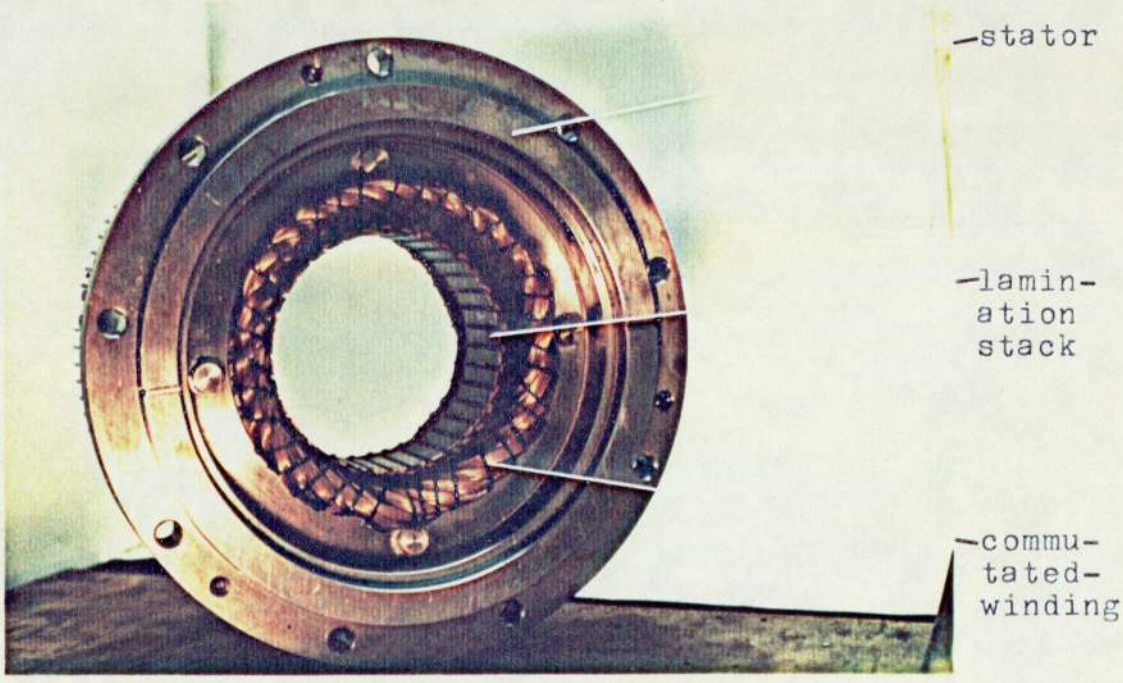

Photograph 2b Stator and commutated-winding (ODE) inside view

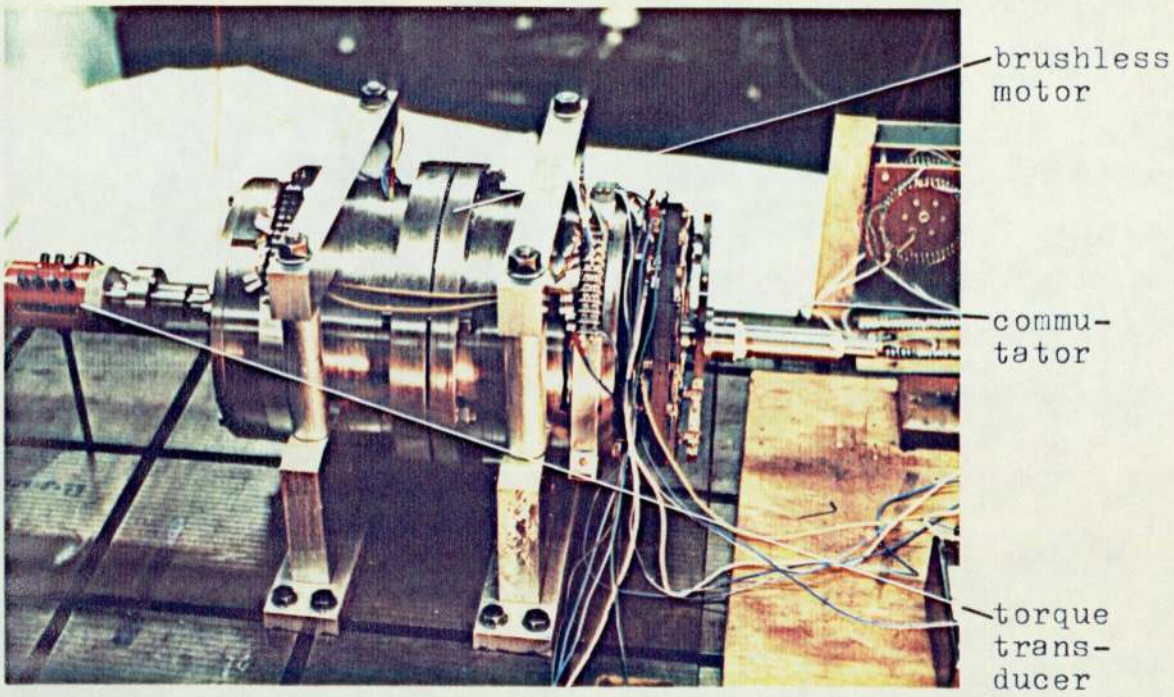

Photograph 3a Brushless motor with mechanical commutator

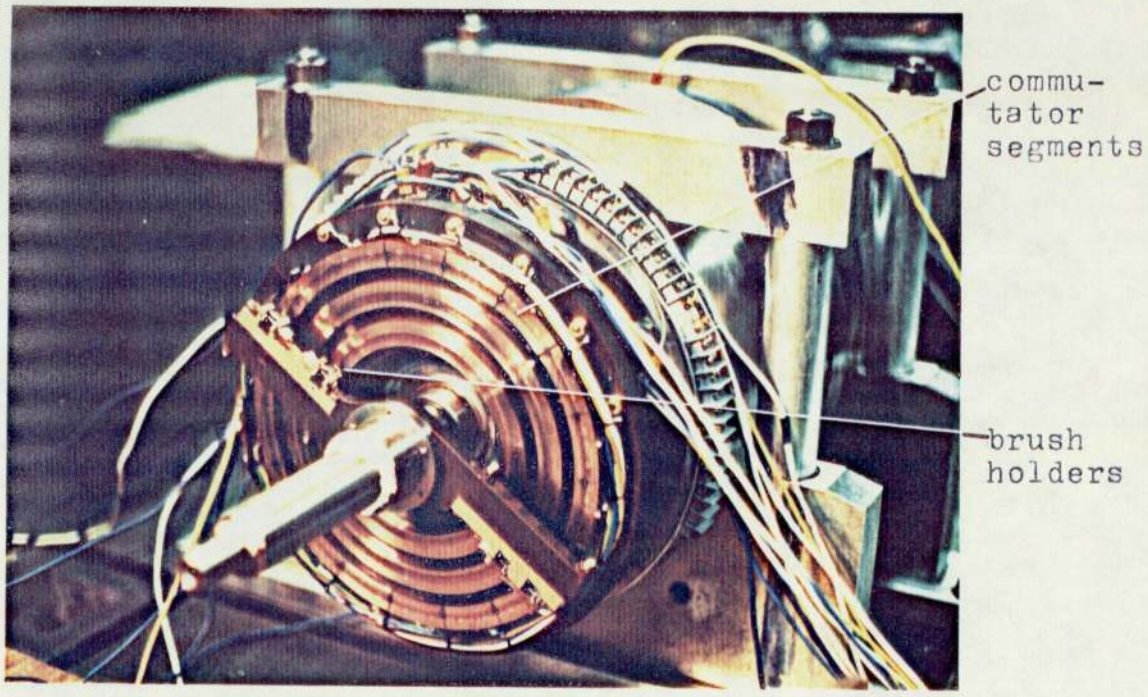

Photograph 3b Faceplate commutator and brushes

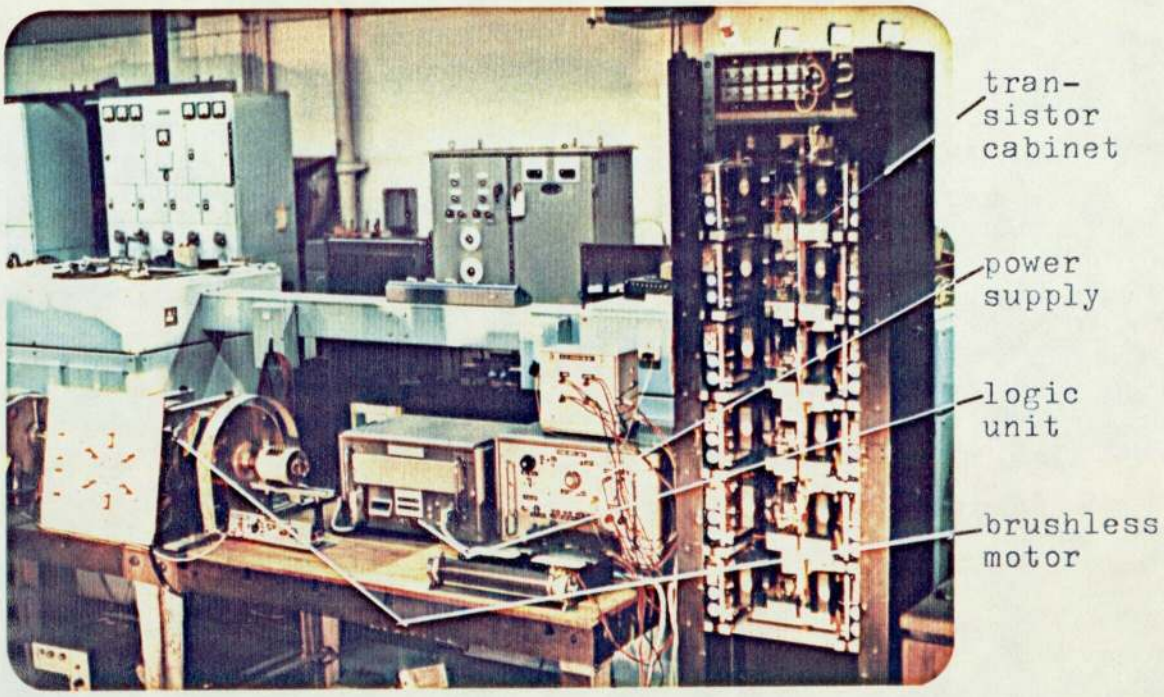

Photograph 4a Complete rig

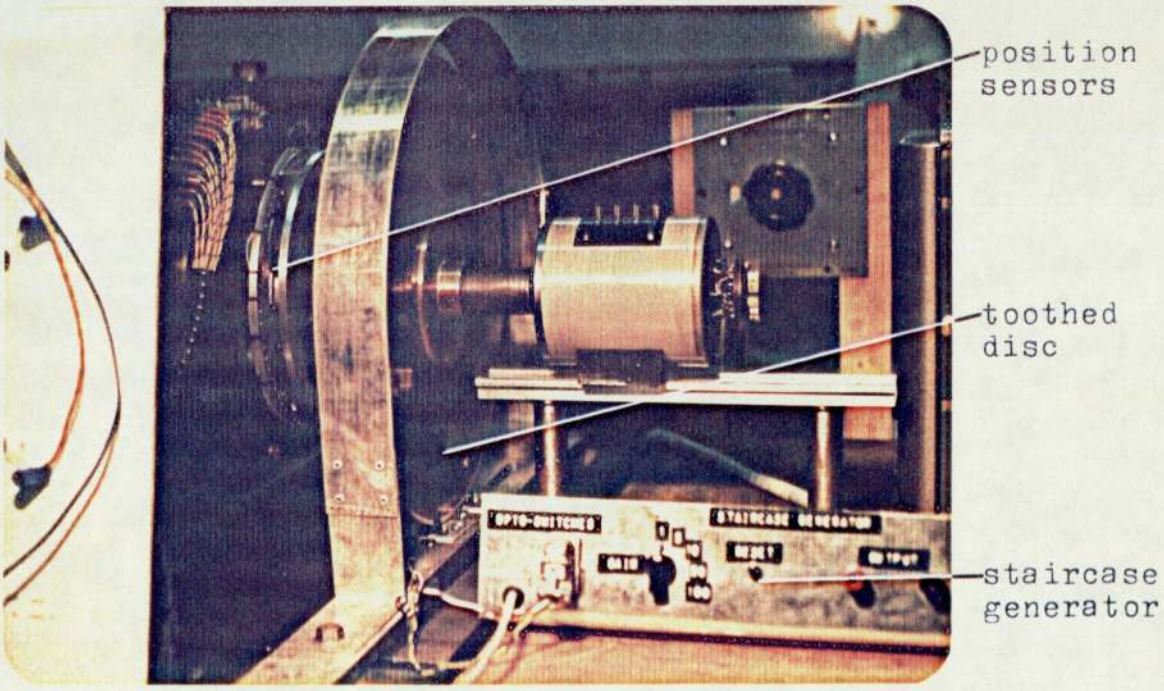

Photograph 4b Position-sensors and toothed disc

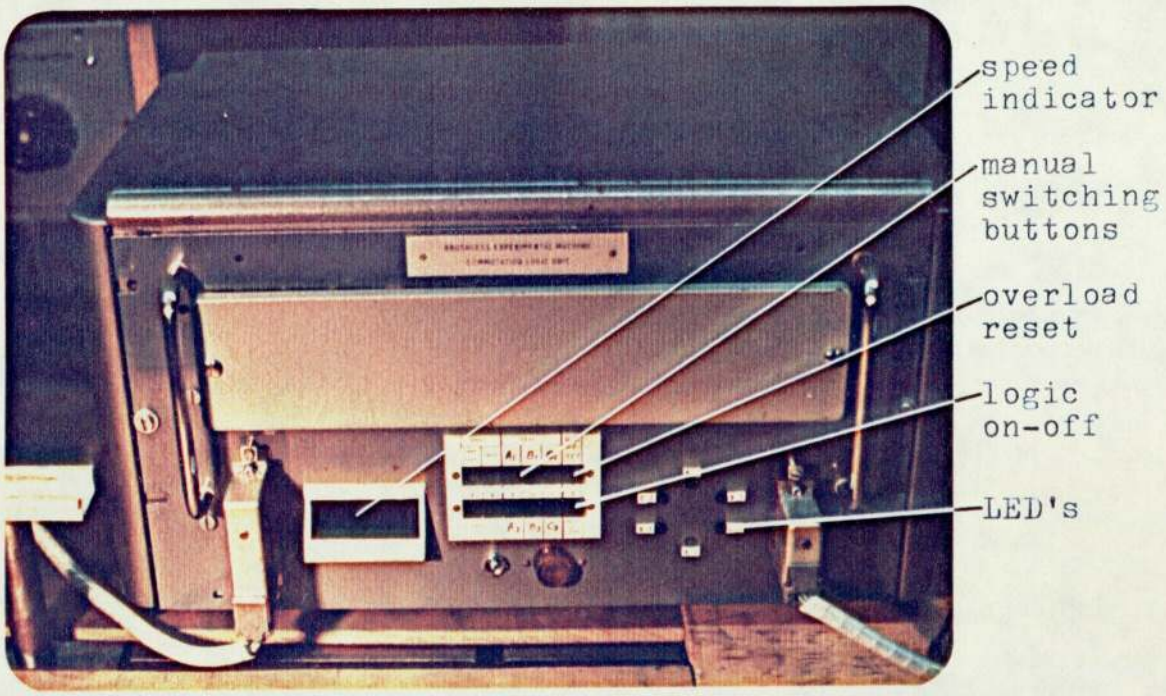

Photograph 5a Logic unit (outside view)

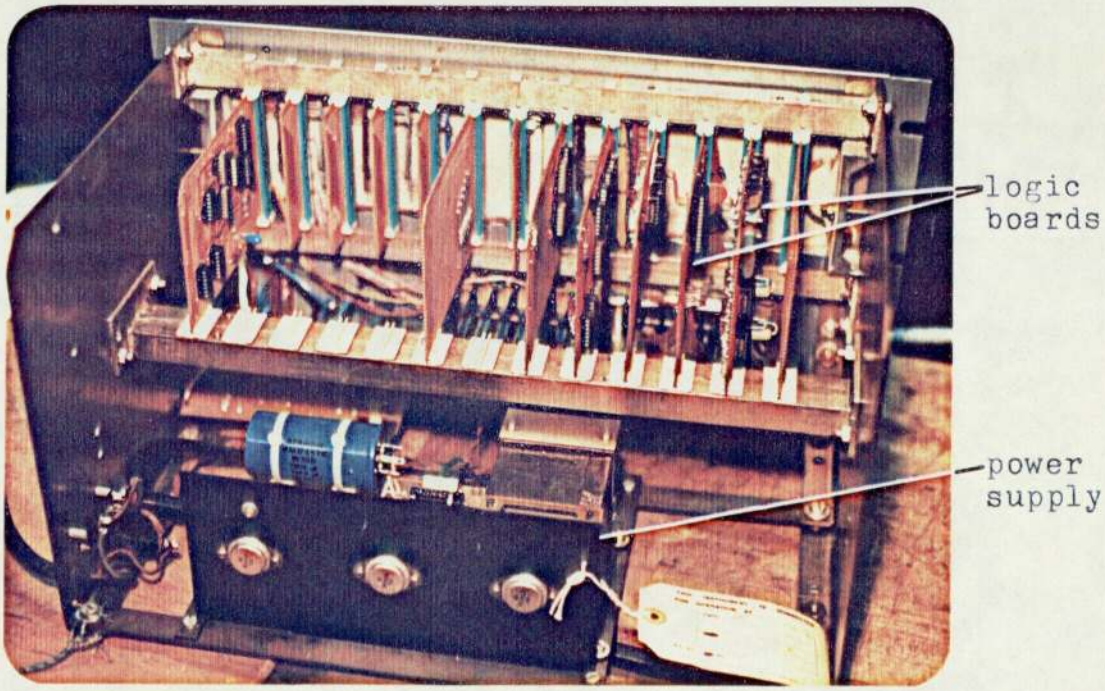

Photograph 5b Logic unit (inside view)

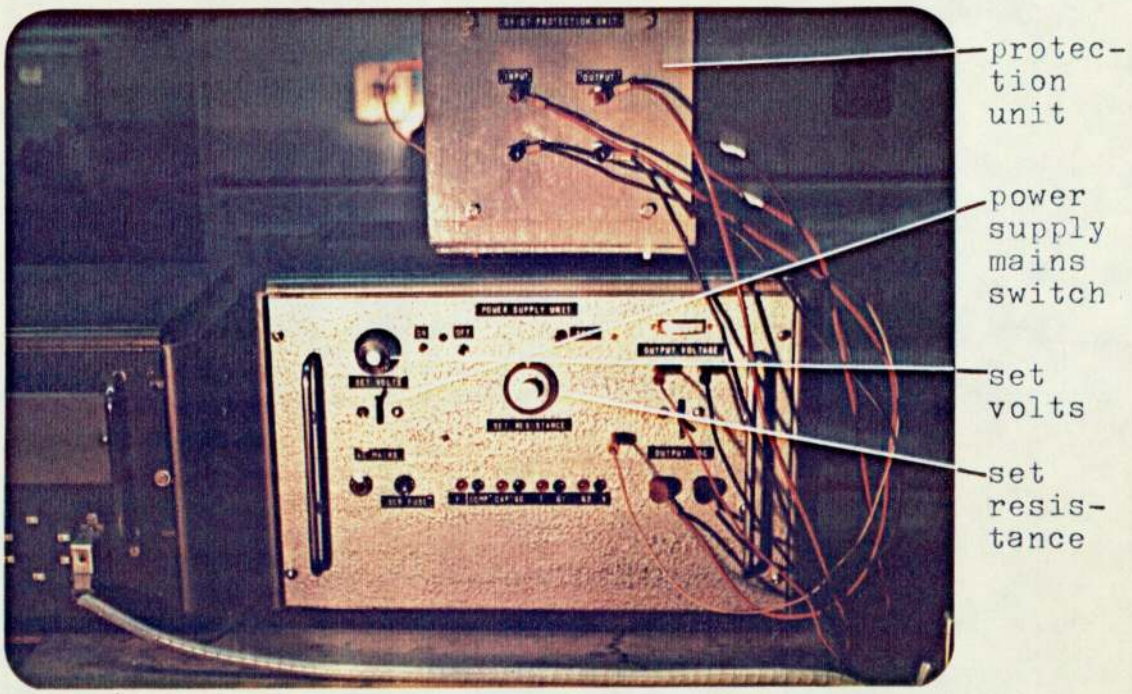

Photograph 6a Power supply (outside view)

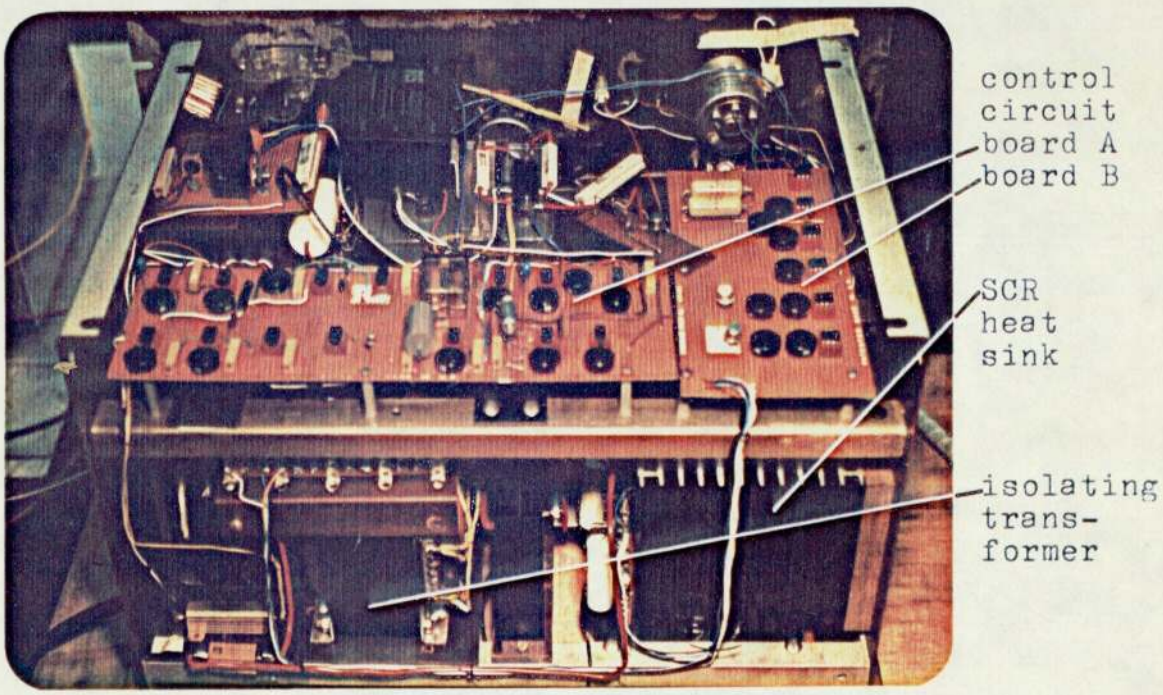

Photograph 6b Power supply (inside view)

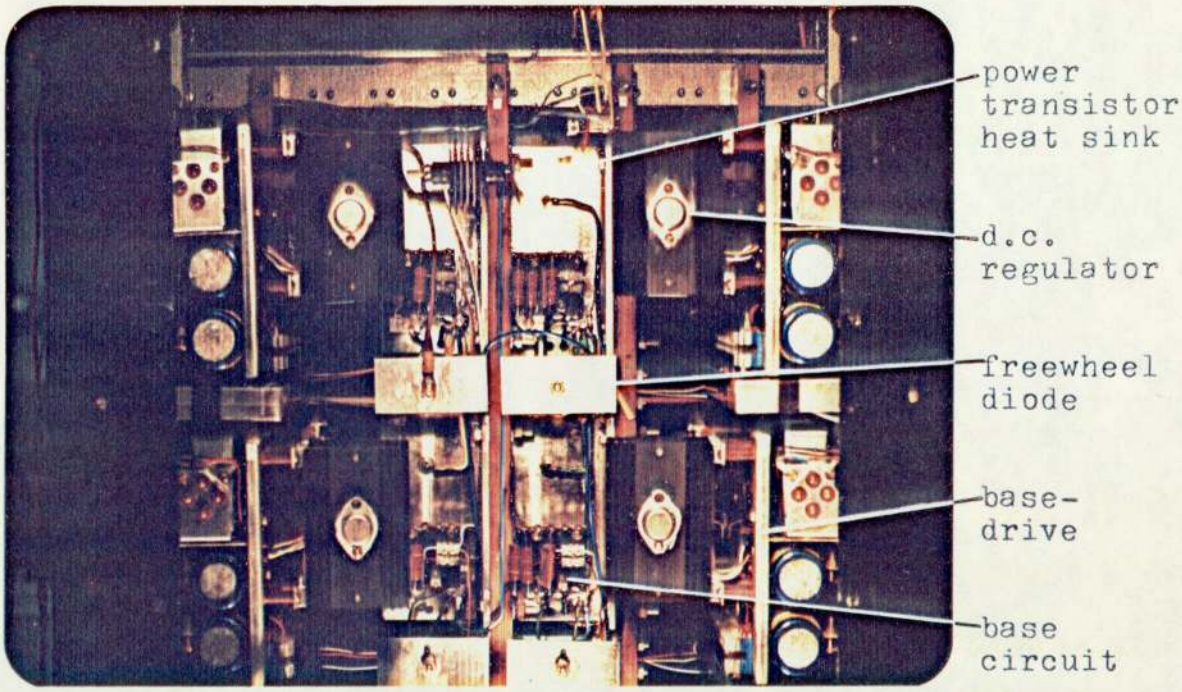

Photograph 7a Bipolar circuit

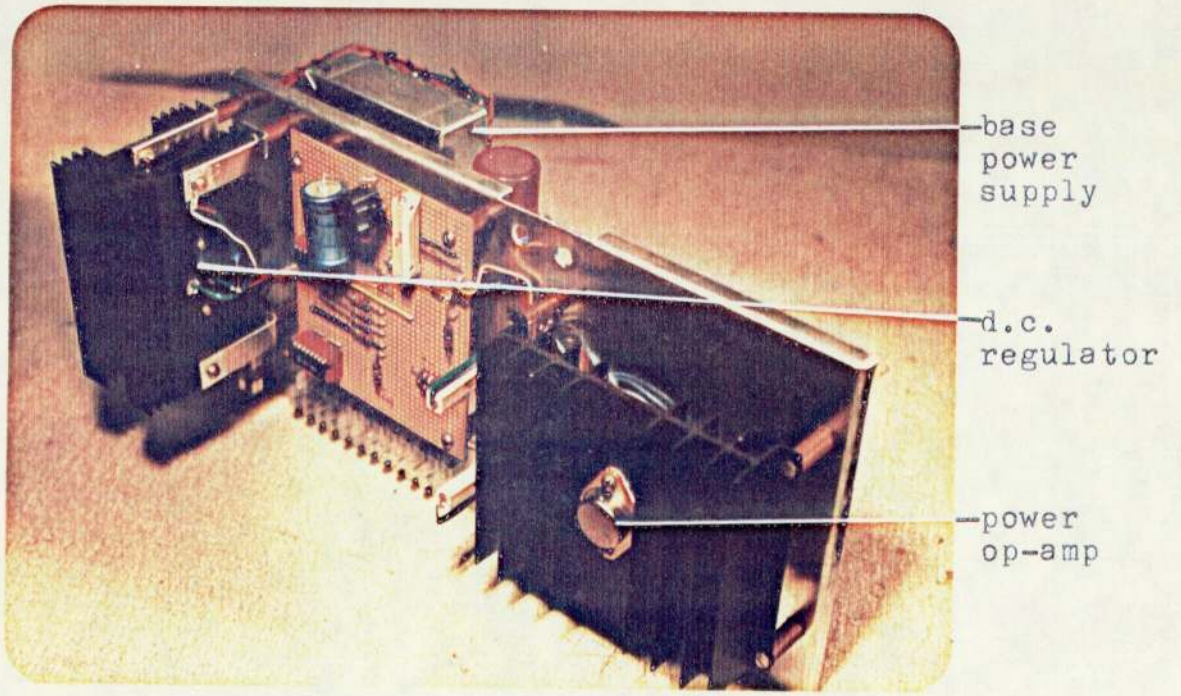

Photograph 7b Base-drive

REFERENCES

1. Alexanderson, E. F. W., Mitag, A. H.
   The thyratron motor
   Elect. Engng., 1934, Vol. 53, pp. 1517-23

2. Lamb, C. St. J.
   Machine commutation using thyristors
   IEE Conf. Pub. No. 11, 1964, pp. 98-104

3. Burton, G. E.
   Commutation system for satellite motors
   ibid., pp. 114-7

4. Brailsford, H. D.
   Solid state commutation for direct current motors
   Proc. of Intermag. Conf. (IEEE New York) T-159,
   1964, paper no. 7-4

5. Wolfendale, E.
   A d.c. motor with SCR commutator and synchronous
   speed control
   Control, 1965, Vol. 9, pp. 497-9

6. Werninck, E. H.
   Stepper motors
   Electromechanical prime-movers: Electric motors
   (MacMillan, 1971), pp. 72-7

7. Proceedings of the international conference on
   stepping motors and systems,
   University of Leeds, 13-15 July 1976

8. Liska, M., Ulrich, B.
Magnetic stepper motors and brushless d.c. motors: principles and applications in drive units
Conf. on Small Elect. Machines, London, 30-31 March 1976, pp. 15-8

9. Walker, J. H.
The theory of the inductor alternator
J. IEE, 1942, Vol. 89, part II, pp. 227-41

10. Thomson, S. P.
Polyphase electric current and alternating-current motors
(Spon, 1900), pp. 111-9

11. Fink, R. A.
The brushless d.c. motor: link to system versatility
Control Engng., June 1970, Vol. 17, pp. 75-8

12. Fink, R. A.
The brushless motor: types and sources
ibid., Aug. 1970, pp. 42-5

13. Frankel, J. M.
Brushless d.c. torque motors
Instr. Control Systems, 1968, Vol. 41, No. 10, pp. 115-6

14. Radziwill, W.
A highly efficient small brushless d.c. motor
Philips Tech. Rev., 1969, Vol. 30, pp. 7-12

15. Watanabe, T., Inagaki, J., Tadakuma, S., Tanaka, S.
Transistor motor, a brushless d.c. motor
Toshiba Rev. (Internat. Ed.), Jan./Feb. 1970, No. 46, pp. 50-4

16. Mazda, F. F.
Electronic commutation for small motors
Elect. Times, 17 Sep. 1971, Vol. 160, pp. 45-9

17. Ogawa, T., Yoneda, S.
Electronically commutated d.c. motor with Hall elements
Fuji Elect. Rev. (Jap.), 1974, Vol. 20, No. 3, pp. 120-8

18. Persson, E. K.
Brushless low inertia motors
Conf. on Small Elect. Machines, London, 30-31 March 1976, pp. 19-22

19. Radziwill, W.
Brushless d.c. machines for space applications
ibid., pp. 23-6

20. Ashen, R. A., Bolton, H. R.
Performance and design of brushless d.c. torque motor
ibid., pp. 27-30

21. Janonis, V. F.
HV d.c. brushless torpedo propulsion motor
Trans. IEEE, 1966, Vol. IGA-2, pp. 297-301

22. Inagaki, J., Kuniyoshi, M., Tadakuma, S.
Commutators get the brush-off
IEEE Spectrum, June 1973, Vol. 10, pp. 52-8

23. Kazuno, H.
Low frequency inductor type rotating machines
Elect. Engng. in Japan, 1973, Vol. 93, No. 4,
pp. 74-83

24. Ichihara, A., Nawa, M., Nakamura, M.
CL motor
Medensha Rev. (Internat. Ed.), Japan, 1974, No. 2,
pp. 18-24

25. Miyairi, S., Tsunehiro, Y.
Analysis and the characteristics of a commutatorless
motor as a d.c. motor
Elect. Engng. in Japan, 1965, Vol. 85, No. 9,
pp. 51-62

26. Bauerlein, G.
A brushless d.c. motor with solid state commutation
IRE Conv. Rec., 1962, Vol. 10, part 6, pp. 184-90

27. Lujic, A.
Controlling brushless d.c. motors
Machine Design, 30 Oct. 1969, Vol. 41, pp. 113-5

28. Liska, M.
A new brushless variable speed d.c. drive for 60,000 rev/min and torque output up to 50 NCM
Conf. on Elect. Variable Speed Drives, London, 10-12 Oct. 1972, IEE Pub. No. 93, pp. 74-8

29. Wise, J. F., Simons, F. O.
A brushless Hall generator d.c. servomotor
Trans. IEEE, 1974, Vol. IECI-21, No. 2, pp. 75-7

30. Clayton, A. E.
The performance and design of direct current machines
(Pitman, 1959), Chapter 16

31. Kawasaki, A.
Existing state and future trends of brushless motors
Elect. Engng. in Japan, May 1973, No. 78, pp. 43-6

32. Hughes, E.
Errors in the magnetic testing of ring specimens
J. IEE, 1927, Vol. 65, pp. 932-43

33. Walker, M.
Conjugate functions for engineers
(Oxford Univ. Press, 1933), pp. 73-87

34. Mitchell, R. R., Ciccanti, A. D., Bartlemay, J. M.
High voltage solid state switches for space applications
IEEE Power Conditioning Specialists Conf., 1970, pp. 65-76

35. Hetterscheid, W. Th.
Turn-on and turn-off behaviour of high voltage switching transistors
Electron Appl. Bull. (Netherlands), Oct. 1975, Vol. 33, No. 2, pp. 59-72

36. Walker, R. J., Yu, R.
Horizontal output transistor base circuit design
Trans. IEEE, Aug. 1974, Vol. BTR-20, No. 3, pp. 185-191

37. Bowler, P.
A wide bandwidth servo amplifier
IEE Conf. on Power Electronics, Dec. 1974, pp. 122-6

38. Allan, R.
Power semiconductors
IEEE Spectrum, Nov. 1975, Vol. 12, No. 11, pp. 37, 40-4

39. Gutzwiller, F. W.
Thyristors and rectifier diodes - the semiconductor workhorses
IEEE Spectrum, Aug. 1967, Vol. 4, pp. 102-11

40. Persson, E. K.
Brushless d.c. motors in high performance servo systems
Proc. 4th Annual Symposium Incremental Motion Control Systems and Devices, 1-3 April 1975, p. T1

41. Hanitsch, R.
On the reliability of brushless d.c. machines
Internat. Conf. on Elect. Machines, Vienna, 1976,
paper I 17

42. I.R. Application note GBAN-SSR - 1:
'Introduction to solid state relays'.

43. VMOS Power FET's
Design Catalogue
Siliconix Semiconductor Devices
Nov. 1977

44. Schafft, H. A.
Second breakdown - a comprehensive view
Proc. IEEE, 1967, Vol. 55, No. 8, pp. 1272-88

45. Pascoe, R. D.
Solid state switching
(Wiley, 1973)

46. Gibbs, W. J.
Conformal transformations in electrical engineering
(Chapman and Hall, 1958), Chapter 9

47. International Rectifier Bulletin No. SCR-155

48. Calkin, E. T., Hamilton, B. H.
Circuit techniques for improving the switching loci
of transistor switches in switching regulators
Trans. IEEE, July/Aug. 1976, Vol. IA-12, No. 4,
pp. 364-9

49. Calkin, E. T., Hamilton, B. H.
A conceptually new approach for regulated d.c. to d.c. converters employing transfer switches and pulsewidth control
ibid., pp. 369-77

50. van Beekvelt, A. P. A., van Heuklom, F. A., Wolf, G.
A switched mode power supply with mains isolation for TV receivers
Mullard Tech. Comm., July 1978, No. 139, pp. 319-42

51. Locher, R. E.
On switching inductive loads with power transistors
Trans. IEEE, 1970, Vol. IECI-17, pp. 256-62

52. Westinghouse Power Transistor Manual
(Westinghouse, 1967, first edition), Chapter 5

53. Digital integrated circuit, operational amplifier and opto-electronic circuit design
(Texas Instruments, 1976), p. 11

54. SCR Manual
(General Electric Co., 1977, fifth edition), Chapter 3

55. Power engineering using thyristors
(Mullard Ltd., 1970, Vol. 1), Chapter 7